The Dissertation Committee for Alberto Mendoza Chávez
certifies that this is the approved version of the following dissertation:

Rapid Numerical Simulation and Inversion of Nuclear Borehole

Measurements Acquired in Vertical and Deviated Wells

Committee:

Carlos Torres-Verdín, Supervisor

William E. Preeg, Co-Supervisor

Kamy Sepehrnoori

Quoc P. Nguyen

Erich A. Schneider

Rapid Numerical Simulation and Inversion of Nuclear Borehole Measurements Acquired in Vertical and Deviated Wells

by

Alberto Mendoza Chávez, B.S.; M.S.

Dissertation

Presented to the Faculty of the Graduate School of

The University of Texas at Austin

in Partial Fulfillment

of the Requirements

for the Degree of

Doctor of Philosophy

The University of Texas at Austin

May 2009

Dedication

To my parents Margarita and Rogelio

Acknowledgements

I would like to express my deepest gratitude to my supervising professor Dr. Carlos Torres-Vérdin for his excellent technical guidance and support. The lessons learned from his example will be a continuous driving force and an invaluable asset in my career. Special thanks to Dr. Bill Preeg for his supervision and encouragement, and for sharing his valuable experience. He was an eminent source of support. I would like to extend my most sincere appreciation to the members of my dissertation committee: Dr. Kamy Sepehrnoori, Dr. Erich A. Schneider, and Dr. Quoc P. Nguyen for taking the time to review my dissertation. I would like to thank John C. Rasmus and R.J. Radtke from Schlumberger as well as Ed Stockhausen from Chevron for their constructive comments and valuable input on density measurements in high-angle and horizontal wells. A note of gratitude is also extended to Reynaldo Casanova for his administrative support.

I was very fortunate to have the mentorship of Dr. Darwin Ellis during my summer internship at Schlumberger-Doll Research from whom I learned valuable lessons. I would also like to thank my tutors Dr. Ahmed Badruzzaman and Dr. Pingjun Guo for sharing their experience during summer internships.

Special thanks to my colleagues Echezona A. Uzoh, Jesus Salazar, Robert Mallan, Jorge Sanchez, David Wolf, Malek Lemkecher, Olabode Ijasan, Zoya Heidari, Jordan Mimoun, German Merletti, Ben Voss, Renzo Angeles Omer Alpak, Emmanuel Toumelin, Javier Miranda, and Thaimar Ramirez for their comments, suggestions or programming assistance.

I would like to acknowledge the faculty of the Petroleum and Geosystems Engineering Department and Dr. Erich Schneider from The Department of Mechanical Engineering for valuable courses and encouraging technical discussions. I thank Cheryl Kruzie and Dr. Roger Terzian for their assistance with graduate studies and computing.

Special thanks go to the friends I made in our department, Hee Jae, Mayank, Nathan, Narayan, Abraham, Maylin, Elena, Silvia, Toby, Elif, and Serkan, and my friends who stood with me through graduate school away from the office, Sonia, Tania, and Maria.

I would like to thank Schlumberger, Chevron, and ExxonMobil for the opportunity of collaboration and learning with the industry through summer internships as well as the UT Cockrell School of Engineering for bestowing me with a scholarship.

The work reported in this dissertation was possible because of the funding of The University of Texas at Austin's Research Consortium on Formation Evaluation, jointly sponsored by Aramco, Anadarko Petroleum Corporation, Baker-Hughes, BG Group, BHP Billiton, BP, Chevron, ConocoPhillips, ENI, ExxonMobil, Halliburton Energy Services, Marathon Oil Corporation, Mexican Institute for Petroleum, Petrobras, Schlumberger, Shell International E&P, StatoilHydro, TOTAL, and Weatherford.

Finally, I sincerely dedicate this dissertation to my parents and my brothers and their families for their support.

Rapid Numerical Simulation and Inversion of Nuclear Borehole Measurements Acquired in Vertical and Deviated Wells

Publication No._____

Alberto Mendoza Chávez, Ph.D.

The University of Texas at Austin, 2009

Supervisor: Carlos Torres-Verdín

Co-Supervisor: William E. Preeg

The conventional approach for estimation of in-situ porosity is the combined use of neutron and density logs. These nuclear borehole measurements are influenced by fundamental petrophysical, fluid, and geomtrical properties of the probed formation including saturating fluids, matrix composition, mud-filtrate invasion and shoulder beds. Advanced interpretation methods that include numerical modeling and inversion are necessary to reduce environmental effects and non-uniqueness in the estimation of porosity.

The objective of this dissertation is two-fold: (1) to develop a numerical procedure to rapidly and accurately simulate nuclear borehole measurements, and (2) to simulate nuclear borehole measurements in conjunction with inversion techniques.

Of special interest is the case of composite rock formations of sand-shale laminations penetrated by high-angle and horizontal (HA/HZ) wells. In order to quantify shoulder-bed effects on neutron and density borehole measurements, we perform Monte Carlo simulations across formations of various thicknesses and borehole deviation angles with the multiple-particle transport code MCNP. In so doing, we assume dual-detector tool configurations that are analogous to those of commercial neutron and density wireline measuring devices. Simulations indicate significant variations of vertical (axial) resolution of neutron and density measurements acquired in HA/HZ wells. In addition, combined azimuthal- and dip-angle effects can originate biases on porosity estimation and bed boundary detection, which are critical for the assessment of hydrocarbon reserves.

To enable inversion and more quantitative integration with other borehole measurements, we develop and successfully test a linear iterative refinement approximation to rapidly simulate neutron, density, and passive gamma-ray borehole measurements. Linear iterative refinement accounts for spatial variations of Monte Carlo-derived flux sensitivity functions (FSFs) used to simulate nuclear measurements acquired in non-homogeneous formations. We use first-order Born approximations to simulate variations of a detector response due to spatial variations of formation energy-dependent cross-section. The method incorporates two- (2D) and three-dimensional (3D) capabilities of FSFs to simulate neutron and density measurements acquired in vertical and HA/HZ wells, respectively.

We calculate FSFs for a wide rage of formation cross-section variations and for borehole environmental effects to quantify the spatial sensitivity and resolution of neutron and density measurements. Results confirm that the spatial resolution limits of neutron measurements can be significantly influenced by the proximity of layers with large contrasts in porosity.

Finally, we implement 2D sector-based inversion of azimuthal logging-while-drilling (LWD) density field measurements with the fast simulation technique. Results indicate that inversion improves the petrophysical interpretation of density measurements acquired in HA/HZ wells. Density images constructed with inversion yield improved porosity-feet estimations compared to standard and enhanced compensation techniques used commercially to post-process mono-sensor densities.

Table of Contents

List of Tables

List of Figures

Chapter 1: Introduction

This dissertation first describes petrophysical and environmental effects on neutron and density borehole measurements acquired across laminated sequences penetrated by deviated wells. Second, this dissertation develops and validates a linear iterative refinement technique for the rapid simulation of nuclear borehole measurements acquired in both, vertical and highly-deviated wells. Finally, we implement two-dimensional inversion of sector-based azimuthal density measurements in conjunction with the fast simulation method.

1.1 BACKGROUND

Estimation of in-situ porosity and true stratigraphic thickness (TST) in laminated formations has an enormous impact on the calculation of hydrocarbon reserves. The conventional approach for the estimation of in-situ porosity is the combined use of neutron and density logs. These nuclear borehole measurements are affected by formation and borehole environmental effects, including shoulder beds, mud-filtrate invasion, saturating fluids, salt concentration, matrix composition, and dip and azimuth angles between the well and formation layering (Ellis and Singer, 2007).

Numerical simulation of borehole nuclear measurements has been extensively used to quantify effects of porosity and invasion on neutron and density logs (Ellis et al., 2003, 2004; Ellis and Chiaramonte, 2002; Mendoza et al., 2007). Although recent developments promote reductions in computational time with deterministic methods (Aristodemou, 2006), for nuclear-log simulations, the Monte Carlo method is the most

widely used approach because of its detailed geometrical capabilities, high numerical accuracy, and versatility to incorporate complex tool configurations and arbitrary spatial distributions of material properties. Likewise, recent implementations of advanced variance-reduction techniques, such as importance sampling, have considerably reduced the computer time required by Monte Carlo simulations of borehole nuclear measurements (Booth and Hendricks, 1984; Hendricks, 1982; Mickael, 1992; Liu and Gardner, 1997). However, currently the Monte Carlo simulation method is not efficient either for application of inversion techniques (Patchett and Wiley, 1994) or for quantitative integration of nuclear measurements with other well logs.

Several techniques have been developed to process raw single-detector responses to obtain the best vertical resolution of density and neutron porosity logs in vertical wells (Galford et al., 1986; Flaum et al., 1987). In high-angle and horizontal (HA/HZ) wells, because the formation layering is not perpendicular to the borehole axis, both detection of bed boundaries and porosity estimation are functions of the vertical (axial) resolution, the radial length of investigation, and the azimuthal sensitivity of the measurements.

Groundwork research addressing nuclear-measurement interpretation and processing in HA/HZ wells is relatively recent (Ellis and Chiaramonte, 2002; Mendoza et al., 2006; Yin et al., 2006; Radtke et al., 2007; Uzoh et al., 2007; Badruzzaman et al., 2007; Yin et al, 2008;). The above studies used the Monte Carlo method to demonstrate the impact of geometry between wellbore and formation on density and neutron porosity measurements.

Neutron flux distribution maps have been used to quantify variations of neutron borehole measurements due to mud-filtrate invasion (Parsons, 1983). Similarly, density detector response functions have described gamma-ray paths in the formation (Flaum, et al., 1991) and quantified the radial length of investigation (Ellis, 2003) for dual-detector density tools. Watson (1984) introduced the concept of Monte Carlo-derived differential sensitivity functions for nuclear detector responses due to Compton and photoelectric gamma-ray interactions. This technique provided important information for tool design and improved post-processing of measured single-detector responses. It also initiated fast nuclear log simulation with the use of linear sensitivity functions (Watson, 1992; Couët and Watson, 1992; Couët and Watson, 1993; Case et al., 1994). However, none of the previously published methods have reported successful results for the simulation of neutron measurements with linear sensitivity functions. In this dissertation, I show that Monte Carlo-derived flux sensitivity functions can be used in an iterative method to rapidly and accurately simulate nuclear borehole measurements. Additionally, by simulating density measurements with the fast method, I am bale to implement inversion techniques to improve interpretation of logging-while drilling (LWD) measurements acquired with multiple azimuthal sectors across highly-laminated sequences.

1.2 PROBLEM STATEMENT

The focus of this dissertation is primarily on the development of fast simulation procedures for neutron and density measurements with the objective of implementing inversion techniques as improved post-processing methods for raw field measurements.

Fundamental formation petrophysical and geometrical properties such as thin laminations, shoulder beds, mud-filtrate invasion, saturating fluids, non-uniform salt concentration, and layering deviation angle with respect to the wellbore (tool), can cause standard interpretation methods to yield incorrect calculations of porosity from neutron and density measurements. Such effects cannot be understood intuitively; it is necessary to quantify them with numerical modeling.

A fast numerical method is essential to simulate nuclear borehole measurements in conjunction with inversion techniques as well as for their quantitative integration with other borehole measurements. This was not done before for nuclear measurements, such as formation neutron porosity and active gamma-ray, primarily because of implicit high computational requirements. At the outset of this dissertation I use the Monte Carlo method to quantify basic formation petrophysical and environmental effects on neutron and density measurements acquired in HA/HZ wells. These effects and the particular case of logging while drilling (LWD) measurements in highly-deviated wells (which entail simulations over long depth intervals and multiple azimuthal sectors) are used as motivation for the development of fast and reliable approximation techniques

Subsequently, I use Monte Carlo-derived flux sensitivity functions (FSFs) to develop an iterative refinement rapid approximation technique. In so doing, I study spatial variations of FSFs due to variations of formation energy-dependent cross-section, shoulder beds in HA/HZ wells, mud-filtrate invasion, and borehole environmental effects. Finally, I use the new fast simulation method in conjunction with inversion

techniques for improved interpretation of LWD density measurements acquired in laminated sequences in HA/HZ wells.

1.3 RESEARCH OBJECTIVES

The thrust of this dissertation is the development of a new fast numerical procedure to simulate nuclear borehole measurements that can be used in conjunction with inversion techniques. General objectives are as follows:

- Quantitatively describe effects of thin laminations penetrated by HA/HZ wells on raw nuclear borehole measurements via Monte Carlo simulations of neutron and density logs acquired with generic source-sensor tool configurations.
- Develop an accurate and rapid three-dimensional (3D) forward modeling technique to perform reliable simulations of nuclear borehole measurements in vertical and HA/HZ wells, across laminated formations with large contrast of porosity, saturating fluids, and matrix composition.
- Apply two-dimensional (2D) inversion techniques in conjunction with the new fast simulation method to improve post-processing and quantitative interpretation of azimuthal density measurements acquired in laminated sequences penetrated by HA/HZ wells.
- Verify the applicability of the developed simulation and inversion procedures on field measurements for the specific case of a commercial logging while drilling (LWD) density tool.

1.4 METHOD AND APPROACH OVERVIEW

The first stage of this dissertation uses the Monte Carlo code MCNP (X-5 Monte Carlo Team, 2003) to perform a systematic sensitivity analysis of petrophysical and environmental effects of neutron and density measurements acquired in highly-deviated wells that penetrate sand-shale highly-laminated formations. The objective is to quantify the effect of complicated formation conditions, such as thin laminations and high-deviation angle of the wellbore with respect to the formation, on raw nuclear measurements.

The second stage of the dissertation develops and tests a linear iterative refinement technique to accurately and rapidly simulate nuclear borehole measurements. The approximation stems from Monte Carlo-derived geometrical response factors referred to as flux sensitivity functions (FSFs) for specific density and neutron tool configurations. Subsequently, I use MCNP to calculate the associated detector response function and the particle flux included in the integral form of Boltzmann's equation. The linear iterative refinement method accounts for spatial variations of the response functions due to spatial perturbations of energy-dependent cross-section in the numerical simulation of neutron- and density-porosity logs via first-order Born approximations. In so doing, I construct a library of FSFs for a range of homogeneous formation porosity-matrix-fluid mixtures (base cases). The variety of geometric factors contained in the library enables the iterative refinement method to select the most appropriate base-case FSF for the simulation of nuclear borehole measurements across non-homogeneous formations. In the library of FSFs, I include three-dimensional (3D) spatial variations of

FSFs of neutron and density measurements due to basic borehole environmental effects (i.e., mudcake and tool standoff) and spatial variations of formation properties.

To appraise the accuracy of linear iterative refinement approximations, I first concentrate on the case of vertical wells with the assumption of symmetry about the axis of the borehole. I consider shoulder beds and piston-like mud-filtrate invasion to asses the performance of the approximations on radial and vertical spatial formation perturbations. Combined vertical and radial variations of formation properties benchmark the two-dimensional (2D) capabilities of the rapid approximations. Next, I incorporate the 3D (radial, vertical and azimuthal) spatial capabilities of FSFs in the approximation of nuclear measurements across horizontal layers penetrated by deviated wells. Comparisons between MCNP simulations and iterative refinement approximations benchmark the reliability of the iterative refinement technique in both, vertical and HA/HZ wells.

The final stage of this dissertation implements sector-based 2D inversion of azimuthal density measurements in conjunction with the fast simulation method. To that end, I use a correlation algorithm to estimate dip and azimuth from density images, and refine the location of bed boundaries previously selected at inflection points of measurements. At the outset, I perform inversion assuming synthetic azimuthal density measurements simulated with a commercial LWD density tool configuration. Next, I use field density images to perform inversion in conjunction with the fast simulation method. Comparison of porosity-feet calculated with inversion results quantifies the relative

improvement with respect to standard techniques that use standard cutoffs on field-processed compensated density.

1.5 OUTLINE OF THE DISSERTATION

Following the introductory chapter, the dissertation consists of five additional chapters. Chapter 2 comprises a systematic sensitivity analysis of petrophysical and environmental effects of neutron and density measurements acquired in highly-deviated wells that penetrate sand-shale laminated sands.

Chapter 3 develops a new method to rapidly simulate density and neutron borehole measurements with the use of Monte Carlo-derived flux sensitivity functions (FSFs). Simulations use linear first-order Born approximations, assume axial symmetry with respect to the axis of the borehole, and consider 2D variations of formation properties. The main technical contribution is the development of a linear iterative refinement procedure that accounts for spatial variations of the response function due to non-homogeneous formations and presence of key borehole environmental effects.

Chapter 4 makes use the new method to simulate neutron and density measurements acquired across laminated sequences in HA/HZ, which incorporates the 3D (radial, vertical and azimuthal) spatial capabilities of FSFs.

Chapter 5 implements the rapid simulation of density measurements for the 2D inversion of logging while drilling (LWD) density images. Inversion techniques consider measurements acquired with azimuthal sectors located around the perimeter of the borehole.

Finally, Chapter 6 summarizes the general conclusions and future research recommendations stemming from this dissertation.

1.6 LIST OF PUBLICATIONS

Several journal and conference papers were published or submitted for review as a result of the research work developed in this dissertation:

Refereed Journal Publications

Mendoza, A., Torres-Verdín, C., and Preeg, W. E., 2009, "Linear iterative refinement technique for the rapid simulation of borehole nuclear measurements, part I: vertical wells," *Geophysics* (submitted for review).

Mendoza, A., Torres-Verdín, C., and Preeg, W. E., 2009, "Linear iterative refinement technique for the rapid simulation of borehole nuclear measurements, part II: high-angle and horizontal wells," *Geophysics* (submitted for review).

Mendoza, A, Torres-Verdín, C., Rasmus, J. C., and Stockhausen, E., J., 2009, "Sector-based inversion of density measurements acquired in laminated sequences penetrated by high-angle and horizontal wells," *Petrophysics* (submitted for review).

Uzoh, E. A., Mendoza, A., Torres-Verdín, C., Preeg, W. E., and Stockhausen, E. J.: "Quantitative Studies of Relative Dip Angle and Bed Thickness Effects on LWD Density Images Acquired in High-Angle and Horizontal Wells," *Petrophysics* (submitted for review).

Mendoza, A., Torres-Verdín, C., and Preeg, W. E., 2007,"Monte Carlo modeling of borehole nuclear measurements in vertical and horizontal wells in the presence of mud-filtrate invasion and salt mixing," *Petrophysics*, vol 48. no.1, pp. 28 – 44, February.

Refereed Conference Proceedings

Mendoza, A., Torres-Verdín, C., and Preeg, W. E.: "Rapid Simulation of Borehole Nuclear Measurements with Approximate Flux Scattering Functions," paper O presented at the 48th Society of Petrophysicists and Well Log Analysts (SPWLA) Annual Logging Symposium, Austin, Texas, June 3 – 6, 2007.

Uzoh, E. A., Mendoza, A., Torres-Verdín, C., Preeg, W. E., and Stockhausen, E. J.: "Quantitative Studies of Relative Dip Angle and Bed Thickness Effects on LWD Density Images Acquired in High-Angle and Horizontal Wells," paper M presented at the 48th Society of Petrophysicists and Well-Log Analysts (SPWLA) Annual Logging Symposium, Austin, Texas, June 3 – 6, 2007.

Liu, Z., Torres-Verdín, C., Wang, G. L., Zhu, P., Mendoza, A., and Terry, R..: "Joint Inversion of Density and Resistivity Logs for the Improved Petrophysical Assessment of Thinly-Bedded Clastic Rock Formations," paper VV presented at the 48th Society of Petrophysicists and Well-Log Analysts (SPWLA) Annual Logging Symposium, Austin, Texas, June 3 – 6, 2007.

Mendoza, A., Preeg, W. E., Torres-Verdín, C., and Alpak, F.: "Monte Carlo Modeling of Borehole Nuclear Measurements in Vertical and Horizontal Wells in the Presence of Mud-filtrate invasion and salt mixing," *Petrophysics*, vol. 48. no. 1, p. 28-44. Feb. 2007.

Mendoza, A., Torres-Verdín, C., and Preeg, W. E.: "Environmental and Petrophysical Effects on Density and Neutron Porosity Logs Acquired in Highly Deviated Wells," paper EEE presented at the 47th Society of Petrophysicists and Well-Log Analysts (SPWLA) Annual Logging Symposium, Veracruz, Mexico, June 4 - 7, 2006.

Chapter 2: Environmental and Petrophysical Effects on Density and Neutron Porosity Logs Acquired in Highly Deviated Wells

Conventional interpretation methods of nuclear measurements for vertical wells can produce incorrect calculations of porosity in complex rock formations. The case of logs acquired in highly deviated wells relative to sand beds may yield inaccurate estimates of bed boundary depth and porosity. In this chapter we describe a systematic sensitivity analysis of petrophysical and environmental effects of neutron and density measurements acquired in highly deviated wells that penetrate sand-shale laminated sands. The focus is primarily on the effects caused by the angle between the wellbore and formation layering. Raw nuclear tool responses are simulated with Monte Carlo simulations of generic source-sensor configurations via the code MCNP. Results from this study indicate that shoulder beds can have a significant impact on the nuclear response of thin layers penetrated by high-angle wells. Simulations strongly suggest that improved interpretation methods are necessary to accurately estimate the porosity of laminated formations penetrated by high-angle wells.

2.1 INTRODUCTION

Existing neutron and density porosity tools were designed primarily for measurement acquisition in vertical wells; their calibration is performed in pits of uniform petrophysical properties. Complicated formation conditions such as thin laminations, shoulder beds, invasion, non-uniform salt concentration (Ellis et al., 1987), and formation geometry with respect to the wellbore (tool), can cause standard

interpretation methods to yield incorrect calculations of porosity from raw neutron and density measurements. Factors affecting tool response in deviated wells near adjacent shale beds, or simply across sands with high variations of porosity, include the radial length of investigation, the vertical resolution, and the tool location around the perimeter of the wellbore (azimuthal sensitivity). Passey et al. (2005) reported biases in porosity calculations as high as 6% porosity, over 50% uncertainty in water saturation, and significant ambiguity in bed thickness estimation. Such effects cannot be understood intuitively; it is necessary to quantify them with numerical modeling.

In this chapter, we make use of previously introduced generic nuclear tool models referred to as the "Longhorn Nuclear Well Logging Tools" (LNLT) (Mendoza et al., 2007) to simulate neutron and density logs in vertical and deviated wells. We use the Monte Carlo method (MCNP) for the numerical simulation of neutron and density measurements. The simulations consider synthetic formations of sand-shale laminations penetrated by vertical wells, and by wells deviated 70 and 85 degrees from the vertical. Moreover, we assume homogeneous water-saturatesd sand beds of 25% porosity bounded by shale beds. Our objective is to assess the effects, on calculated density and porosity logs, of geometric factors between the wellbore and the formation, namely angle of deviation, using conventional processing techniques.

The vertical resolution of nuclear tools as well as their radial length of investigation play an important role on the processing of raw measurements to calculate final density and neutron porosity logs. Because the vertical resolution and radial length of investigation is different for each detector, the process of combining their individual

responses has an important effect on the resolution of the estimated density and neutron porosity logs.

In vertical wells, several techniques have been used to process the near- and far-detector response to obtain the best vertical resolution for density and porosity logs acquired in laminated formations. The bed boundary detection capability of neutron and density logs in thin beds can be degraded beyond the intrinsic vertical resolution of the tool due to under sampling. This capability is improved by increased sampling and by calculating density with the near detector as the primary source of the measurements (Dodge, 1994). McCall et al. (1989) listed values of vertical resolution of density and neutron tools of 18 and 24 inches, respectively. They also described the corresponding vertical resolutions for alpha-processed (1.2 in. sampled) measurements equal to 4 inches for density and 8 inches for neutron. Galford et al. (1986) introduced a processing method to amplify the vertical resolution of neutron porosity measurements by matching the resolution of the near- and far-detectors. This latter work was followed by Flaum et al. (1987), who introduced a similar technique to improve the vertical resolution of density logs. Their method consists of combining the response of the near-detector with the compensated density response. With the application of such a processing technique, Flaum et al. (1987) report a vertical resolution of less than 6 inches.

In general, the above techniques have shown positive results in vertical wells. However, work on similar or new processing techniques applicable to highly deviated wells is in order. Chapter 5 analyzes an inversion-based processing technique for logging while drilling (LWD) density measurements acquired in highly-deviated wells.

2.2 METHOD

We simulated the raw neutron and density logs using the Monte Carlo method via the code MCNP (X-5 Monte Carlo Team, 2003). As illustrated in **Figures 2.1** and **2.2**, for both neutron and density tools, the radial length of investigation and vertical response are different and spatially complex for short- and long-spaced detectors.

Ellis (2003) described density response maps for a hypothetical tool which exhibited highest sensitivity to the formation near the tool, in particular close to the source and detectors. **Figure 2.1** shows the map of normalized sensitivity for the thermal neutron porosity tool in a homogenous 25% porosity water-saturated sand. Similarly, **Figure 2.2** shows the normalized sensitivity map for the density tool. For each tool, the depth shift necessary to match the mid-point between the source and the near- and far-detectors is shown in the center of the figure. The functions are discretized in cylindrical cells. Each cell quantifies the normalized sensitivity integrated over the azimuthal direction. In the case of the neutron tool, it can be observed that high sensitivity to the formation concentrates near the detectors. For the density tool, higher importance is observed near the source region.

Given that radial length of investigation plays an important role in deviated wells, **Figure 2.3** compares this capability by way of normalized sensitivity maps for the thermal neutron porosity tool in porous rocks of different petrophysical properties. We observe a longer radial length of investigation for the lower porosity formation (5%). Moreover, higher sensitivity concentrates near the detector at elevated values of hydrogen index (higher porosity formations). Similarly, as shown in the right-hand panels of

Figure 2.3, for the case of equal-porosity formations, different fluid saturations would also have a measurable effect on the radial length of investigation of the thermal neutron tool. In the case of density measurements, the response capabilities remain nearly invariant to variations of petrophysical properties.

We estimate neutron porosity from the near- to far-detector ratio. **Figure 2.4** shows the calibration curves for the thermal neutron porosity tool for the case of a homogeneous water-saturated sandstone formation. Relative particle counts were calculated to an average relative error of approximately 1% for each detector after running 1 million particle histories with MCNP.

Density measurements for each detector as well as the density correction, $\Delta\rho$, are calculated using the "spine and rib" plot shown in **Figure 2.5** following the procedure described by Bigelow (1995). The formation bulk density (compensated density), ρ_b, is then calculated by

$$\rho_b = \rho_{LS} + \Delta\rho, \tag{2.1}$$

where ρ_{LS} is the density estimated from the far-detector response.

Formation bulk density is calculated after depth-matching the near- and far-detectors as described in **Figures 2.1** and **2.2**. We also calculate the formation bulk density resulting from the "enhanced vertical resolution," ρ_{enh}, using the procedure described by Flaum et al. (1989), i.e.

$$\rho_{enh} = \rho_b + \left(\rho_{near} - \overline{\rho}_{near}\right), \tag{2.2}$$

where ρ_{near} is the near- detector density and $\overline{\rho}_{near}$ is the near-detector density averaged to match the resolution of the far-detector density.

We assumed a synthetic rock formation consisting of a 30-inch homogeneous water-saturated sandstone of 25% porosity bounded by shale (illite) beds to simulate neutron and density logs. Calculated neutron and density logs in a vertical well are compared to logs simulated in wells penetrating the same formation at angles of deviation of 70 and 85 degrees. This procedure is repeated for the case of a formation consisting of 16-inch sand-shale beds of the same petrophysical properties as in the previous case. Also, simulated logs for a vertical well are compared to the logs for wells deviated 70 and 85 degrees from the vertical. In all cases, neutron and density measurements were simulated with a 1.2-inch sampling rate. Additionally, to illustrate fluid effects on density and neutron porosity logs, we show simulations for the case of a 30-inch sand bed fully saturated with gas (CH_4), bounded by a shale. Measurements in the gas-saturated sand bed are simulated in a well deviated 70 degrees from the vertical, and compared to logs simulated in a vertical well penetrating the same formation.

For the cases described above, the tool position against the borehole wall is assumed at the bottom of the wellbore. However, we assess the effect of azimuthal tool position by comparing the case of a 70-degree deviated well for the maximum change in tool rotation of 180 degrees. In all cases, the assumed borehole fluid was a fresh water-base mud with the same properties as formation water. To improve statistical accuracy in the calculations, we used superimposed importance grids consisting of 1600 cells for

neutron simulations, and 3920 cells for density simulations, in a three-dimensional (3D) cylindrical coordinate frame.

2.3 SIMULATION RESULTS

Figure 2.6 shows a comparative plot of the simulated neutron porosity logs for the single 25% porosity water-saturated sand bed, for a vertical well and for wells deviated 70 and 85 degrees from the vertical. The plots describe the neutron porosity calculated using the mid-point depth-matching procedure described in **Figure 2.1** and the neutron porosity calculated from raw measurements (no depth shift). Using this processing technique, we observe a better vertical resolution in the log for the vertical well. However, the tracks in the center- and right-hand panels of **Figure 2.6** show less influence from depth matching at high wellbore angles with respect to the formation described in vertical depth. It can be observed that the vertical resolution of the neutron tool is adequate to calculate the true porosity for the 30-inch sand bed. Nevertheless, there are clear shoulder-bed effects in the shale-sand and sand-shale transitions. Similar effects can be observed in the 16-inch laminated case shown in **Figure 2.7**. Again, for the case of a highly-deviated well we note a decrease of sensitivity of the calculated neutron porosity to depth-matching of the far-detector response. Shoulder-bed effects are clear for both cases. However, as in the single-bed case, an apparent increase in resolution is observed in the deviated well case due to the longer exposure of the tool to the sand bed. The logs also show non-symmetrical shale-sand and sand-shale transitions.

The above results are shown versus vertical depth. There is a degradation of the vertical resolution if the comparisons are made along the direction of the borehole as a logging tool would acquire the measurements.

The simulation of every sample point in depth for the neutron logs resulted in average relative errors of 1.1% and 0.9% for the near- and far-detectors, respectively, after running 1 million particle histories with MCNP.

Figures 2.8, 2.9, and **2.10** show the simulated density logs for the case of a vertical well and wells deviated at 70 and 85 degrees. The track on the left-hand panel shows the near-detector density, the depth-matched far-detector density, and the compensated formation bulk density. In the center panel we show the density correction, $\Delta\rho$, and the track on the right-hand panel shows the near-detector density, ρ_{near}, the near resolution-matched density, $\overline{\rho}_{near}$, and the resulting "enhanced" bulk density, ρ_{enh}. Since no near borehole environmental effects (mudcake, borehole rugosity) are included in the models, $\Delta\rho$ is solely due to the difference of resolution between the near- and far-detectors across bed boundaries, whereas the near response shows the best estimate of density. The log of ρ_{enh} differs from the compensated density by sharpening the boundaries across beds in the three well cases. **Figures 2.11** and **2.12** show the simulated density logs for the 16-inch sand-shale laminated formation. As in the neutron porosity case, we observe a degraded effect when depth matching the far density at high angles of wellbore deviation. Moreover, an apparent higher resolution, attributed to the longer

exposure of the tool to the sand beds, is observed in vertical depth for the case of a deviated well.

The simulation of every sample point in depth for the density logs, after running 10 million particle histories with MCNP resulted in average relative errors of 1.4% and 1% for the far and near detectors, respectively.

2.4 DISCUSSION AND INTERPRETATION

As shown in **Figures 2.1, 2.2** and **2.3** for both neutron and density tools, the radial length of investigation and vertical resolution are different and complex for short- and long-spaced detectors. Various techniques have been used to process the near- and far-detector measurements acquired in vertical wells to obtain the most accurate porosity and vertical response. In truly horizontal wells, beds can be detected away from the borehole at different distances depending on the detector's radial length of investigation. In high-angle wells, the assessment of bed boundary and bed thickness is non-trivial.

In highly deviated wells, the vertical resolution of the detectors is enhanced when the results are compared in vertical depth and the amount of change in vertical resolution is a function of the angle of deviation. Also, the change in vertical resolution will be different between the near- and far-spaced detectors since they exhibit different radial lengths of investigation. The above results are shown with respect to vertical depth. There is a degradation of the vertical resolution if the comparisons are made along the direction of the borehole as a logging tool would acquire the measurements.

When simulation results are transformed into vertical depth, the response to bed boundaries becomes much sharper at large values of deviation angle because (a) the

distance along the borehole is much longer than the vertical depth and (b) the tool resolution is determined by the distance along the borehole. **Figures 2.13** and **2.14** show results from this exercise.

To concisely describe a case of combined fluid and formation geometrical effects on density and neutron porosity measurements, **Figure 2.15** shows the effect of gas in a 30-inch gas-saturated sand bed penetrated by a well deviated 70 degrees from the vertical. These results are compared to logs simulated in a vertical well. For density measurements, we observe similar effects on bed boundary transitions and vertical resolution as in the case of a water-saturated sand. In this case, the sharpening of sand-shale and shale-sand transitions as well as the apparent increase in vertical resolution of the far-detector is more pronounced due to the higher density contrast between the gas-saturated sand and the bounding shale beds. Neutron porosity logs exhibit significant gas-effect in both the vertical and 70-degree deviated wells. However, in the case of the deviated well we observe more accurate bed boundary transitions.

Given that we assumed a single tool position around the perimeter of the wellbore (bottom face) for all the simulations presented above, it is important to quantify the effect of azimuthal tool position on the symmetry of the logs acquired across bed boundaries for the case of deviated wells. **Figure 2.16** shows the symmetrical variations of logs simulated across bed boundaries between the cases of tool location against the bottom face of the wellbore, and against the top face (rotated 180 degrees from the bottom). We observe a shift in the detection of bed boundaries of approximately 2.8 inches for the neutron porosity log and 2.4 inches for the density log. Moreover, these results exhibit an

approximate shift of 0.8 inches in the far-detector density response. Despite the geometrical shifts in bed boundary detection because of azimuthal tool location, the vertical resolution of the near- and far-detectors for both neutron and density tools remains approximately constant.

2.5 CONCLUSIONS

Individual detector responses for neutron and density measurements are spatially complex. Each of these responses exhibits different vertical resolutions and radial lengths of investigation. Accounting for such properties of nuclear measurements is essential for estimating actual formation porosity. In the case of highly deviated wells, optimum combination of multi-detector responses is a more complicated process than in the case of vertical wells. Several techniques have been used to enhance the vertical resolution of neutron and density logs in laminated formations penetrated by vertical wells. However, these techniques have not been proven successful in deviated wells. In this chapter, we quantified the effect of high-angle wells penetrating sand-shale laminated formations on neutron porosity and density logs via numerical modeling.

Results from our study show that, for the case of a 30-inch water-saturated sand bounded by shale beds, depth-matching the far-detector response improves the detection of bed boundaries with the neutron tool. However, shoulder-bed effects bias the calculated porosity by approximately 2.5% porosity through most of the sand bed thickness. Nevertheless, the resolution of the measurement was high enough to sense the true porosity (25%) of the sand bed. For the case of 16-inch sand-shale laminations, both neutron and density measurements exhibited sharper bed boundary transitions as well as

reduced shoulder-bed effects in a well deviated 70 degrees from the vertical when transformed into vertical depth.

At high angles of deviation, the response of both neutron and density measurements was sharper than for the case of a vertical well, and we observed an apparent enhancement in vertical resolution. These effects are attributed to the much longer distance along the borehole of the response compared to the case of a vertical well.

Because of their sensitivity to hydrogen index, neutron porosity measurements are substantially more affected than density measurements by the combined effects of gas saturation and geometrical factors between the wellbore and laminated formations.

Rotation of the tool around the borehole caused a geometrical shift in bed boundary detection from simulated neutron and density logs. However, the vertical resolution remained approximately constant for both neutron and density measurements.

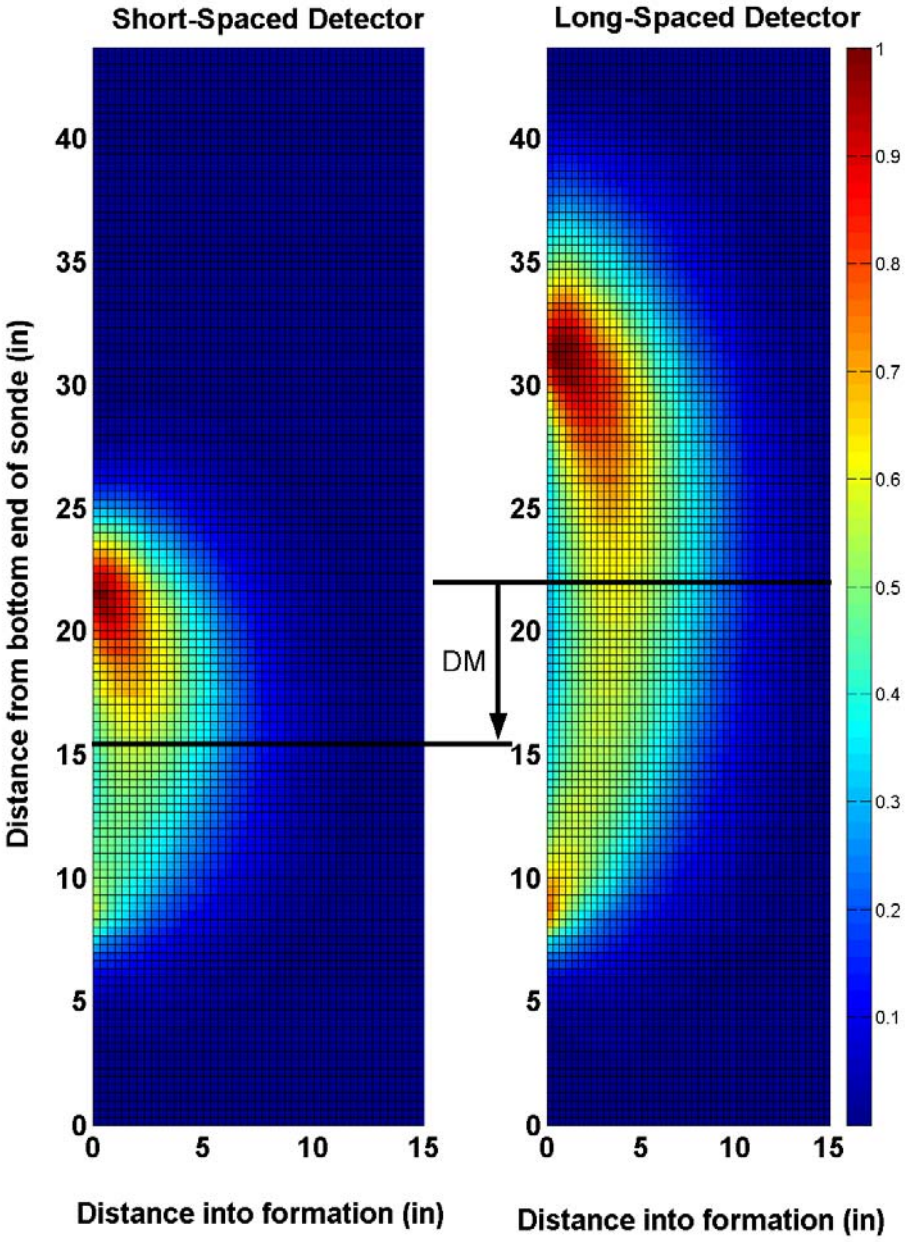

Figure 2.1: Sensitivity functions for the thermal neutron porosity tool. Colors describe the normalized formation sensitivity of the neutron tool response as a function of the distance from the bottom of the sonde (vertical resolution) and distance into the formation (radial length of investigation). The depth shift necessary to match the middle distance between the source and each detector is shown in the center of the figure.

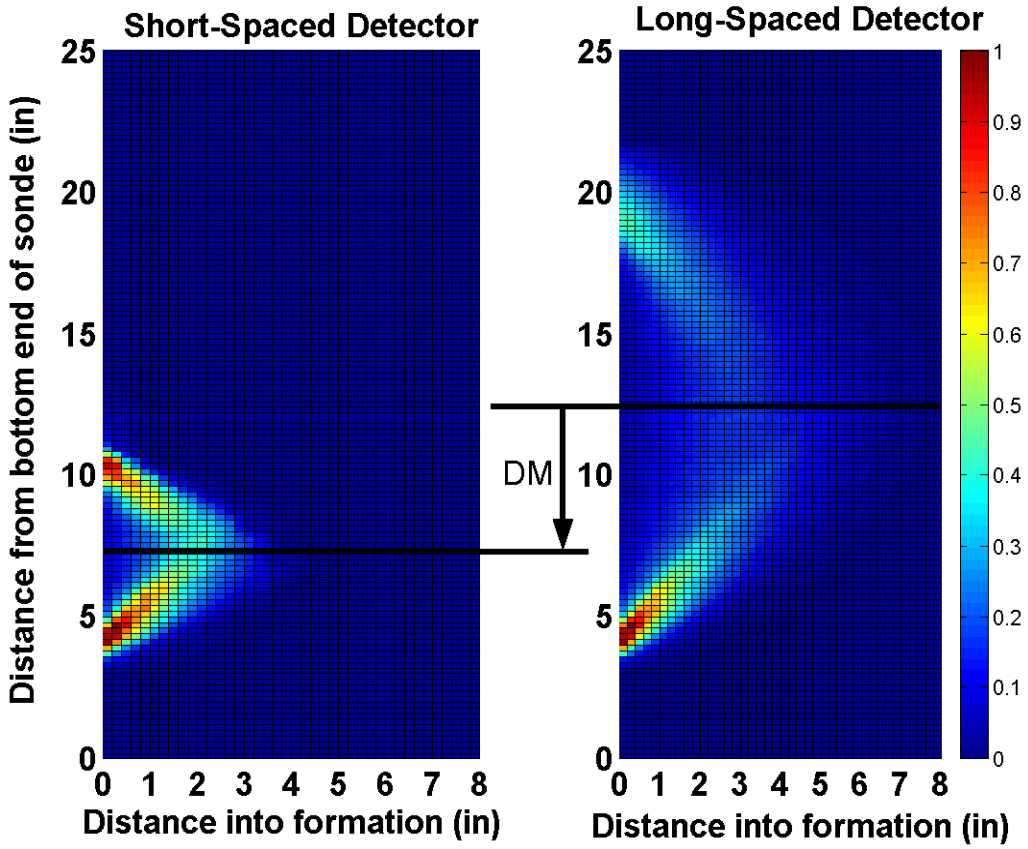

Figure 2.2: Sensitivity functions for the density tool. Colors describe normalized formation sensitivity of the density tool response as a function of the distance from the bottom of the sonde (vertical resolution) and distance into the formation (radial length of investigation). The depth shift necessary to match the middle distance between the source and each detector is shown in the center of the figure.

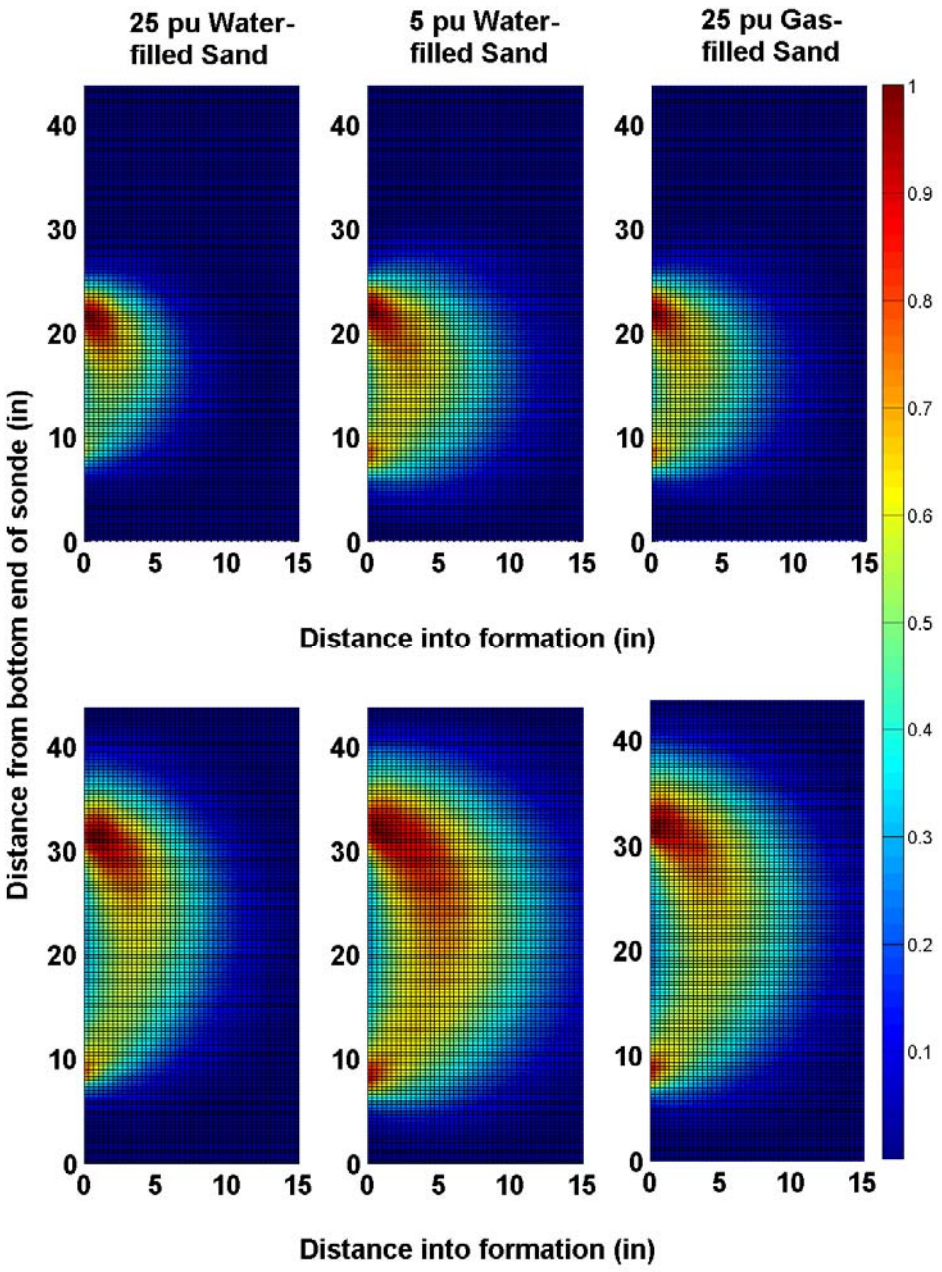

Figure 2.3: Comparative plot of sensitivity functions for the thermal neutron porosity tool. Colors describe the normalized formation sensitivity of the neutron tool response as a function of the distance from the bottom of the sonde (vertical resolution) and distance into the formation (radial length of investigation). Top and Bottom panels show sensitivity maps for the near- and far-detectors, respectively.

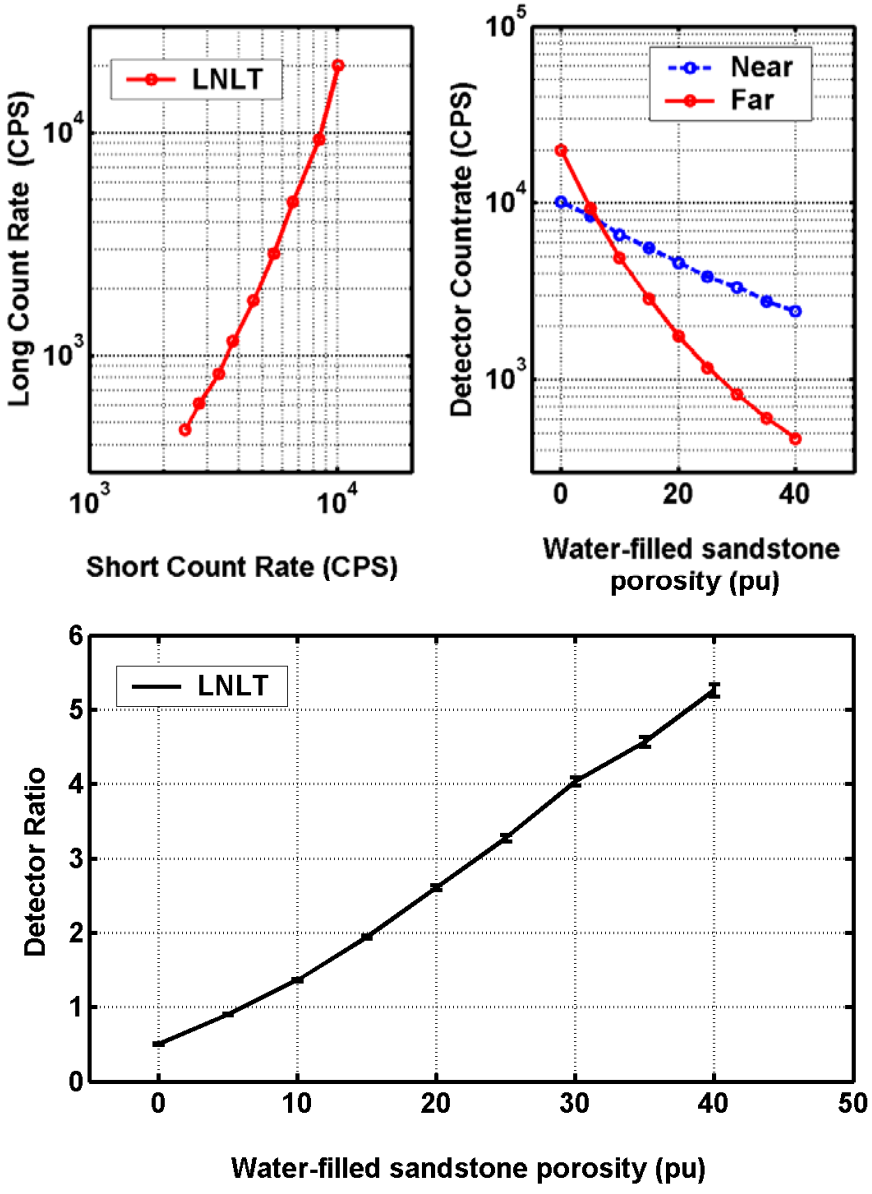

Figure 2.4: Calibration curves for the thermal neutron porosity tool in water-filled sandstone. The top-left panel shows the log-log plot of the detectors' count-rate and the top-right panel shows the count rate of each detector per sandstone porosity. The bottom panel shows the near to far detector-count ratio as a function of sandstone porosity units.

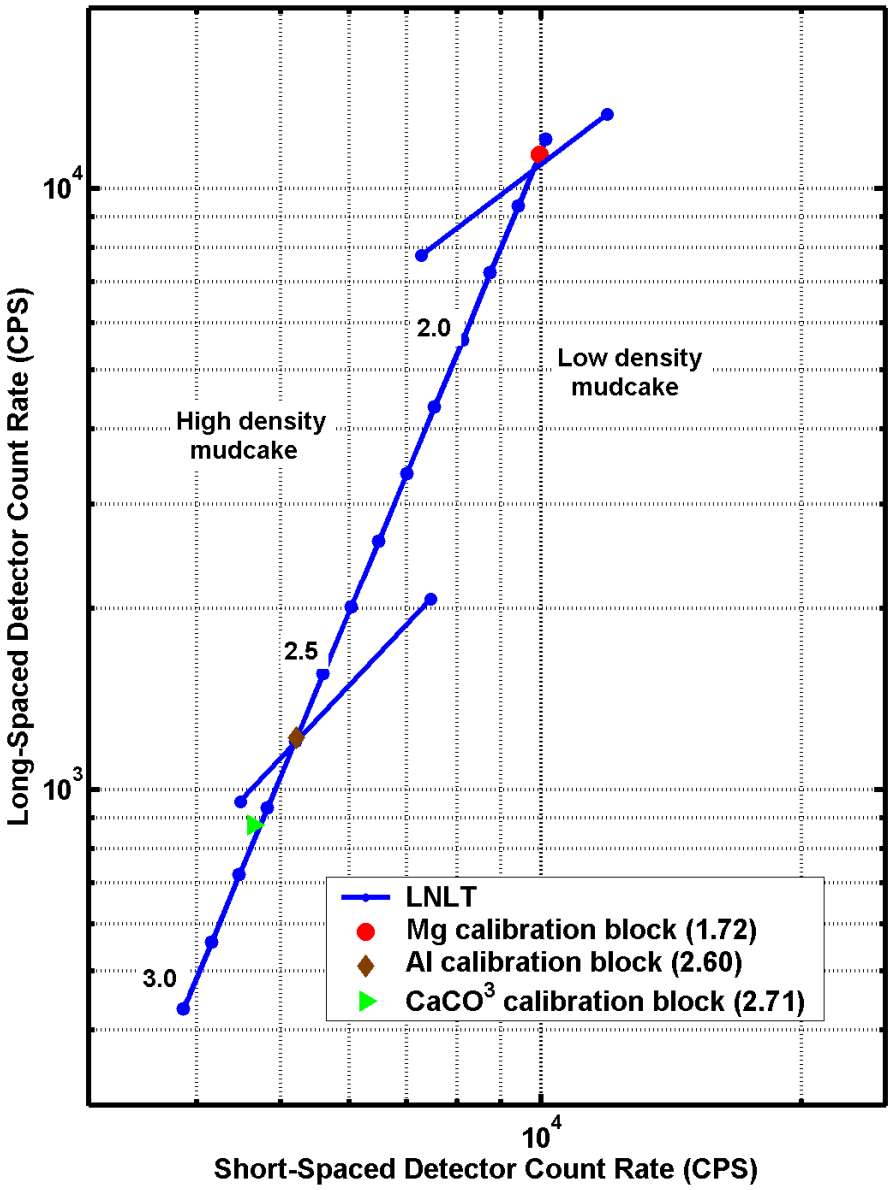

Figure 2.5: "Spine and rib" cross-plot plot describing the relationship between photon counts at the short- and long-spaced detectors for the density porosity tool. The spine from the Longhorn Nuclear Logging Tool (LNLT) is displayed with ribs for "light" and "heavy" mudcake (Mendoza et al., 2007).

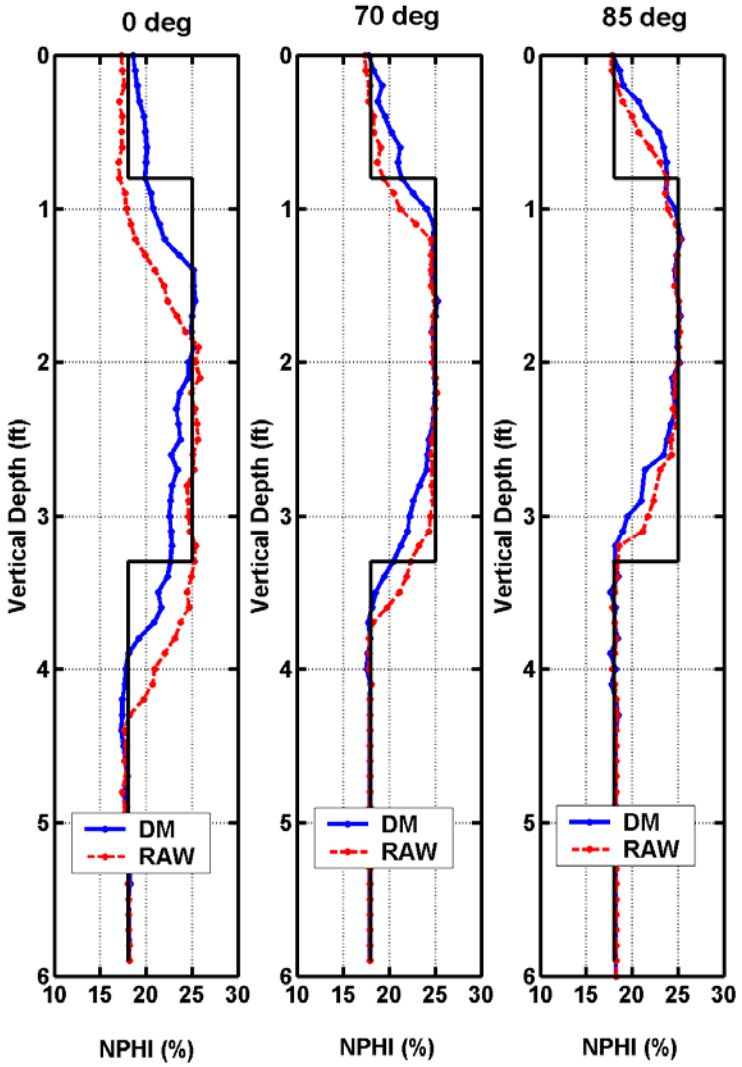

Figure 2.6: Simulated neutron tool measurements for a 30-inch, 25% porosity water-saturated sandstone bed, bounded by shale beds. The left panel shows the synthetic neutron log for a vertical well. On the center, we show the neutron log of the same formation, simulated for a well deviated 70 degrees from the vertical, and on the right we show the log simulated for a well deviated 85 degrees from the vertical. Depth-matched neutron porosity and raw neutron porosity are shown in blue and red, respectively. The black line describes the actual porosity of the formation.

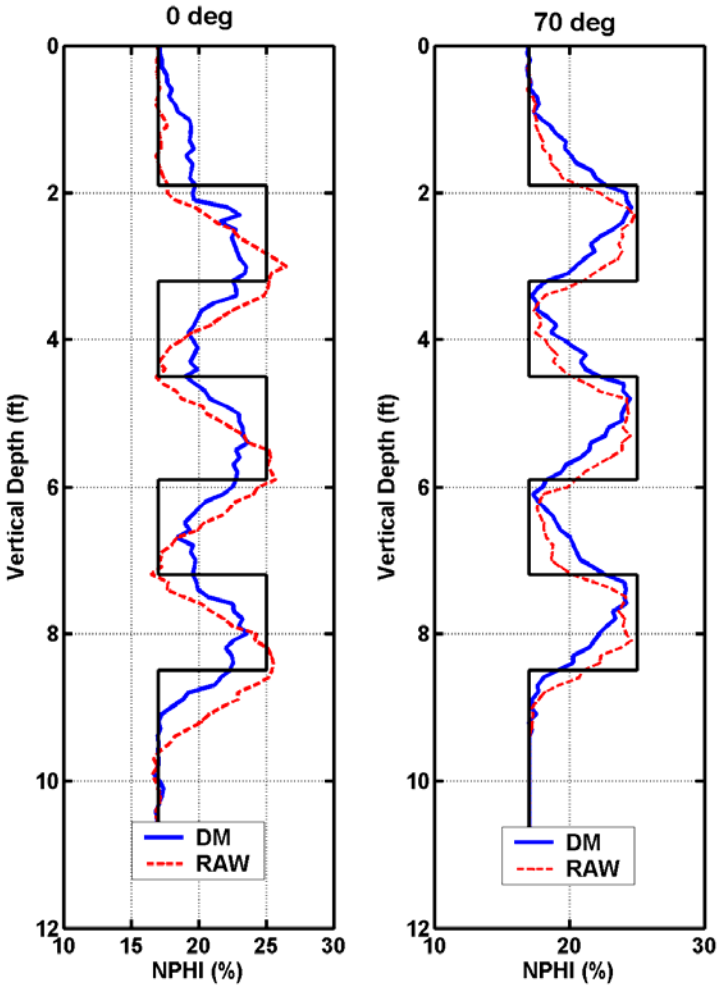

Figure 2.7: Neutron porosity logs simulated on a sand-shale sequence penetrated by a vertical well and a well deviated 70 degrees form the vertical. The left panel shows the simulated neutron porosity processed after depth-matching the far-detector (in blue) and the raw neutron porosity without depth-matching processing (in red). The right panel shows similar neutron porosity logs simulated in a 70-degree deviated well penetrating the same formation. The formation consists of 16-inch, 25% porosity water-saturated sand beds, bounded by 16-inch shale beds. The black line describes the true porosity of the formation.

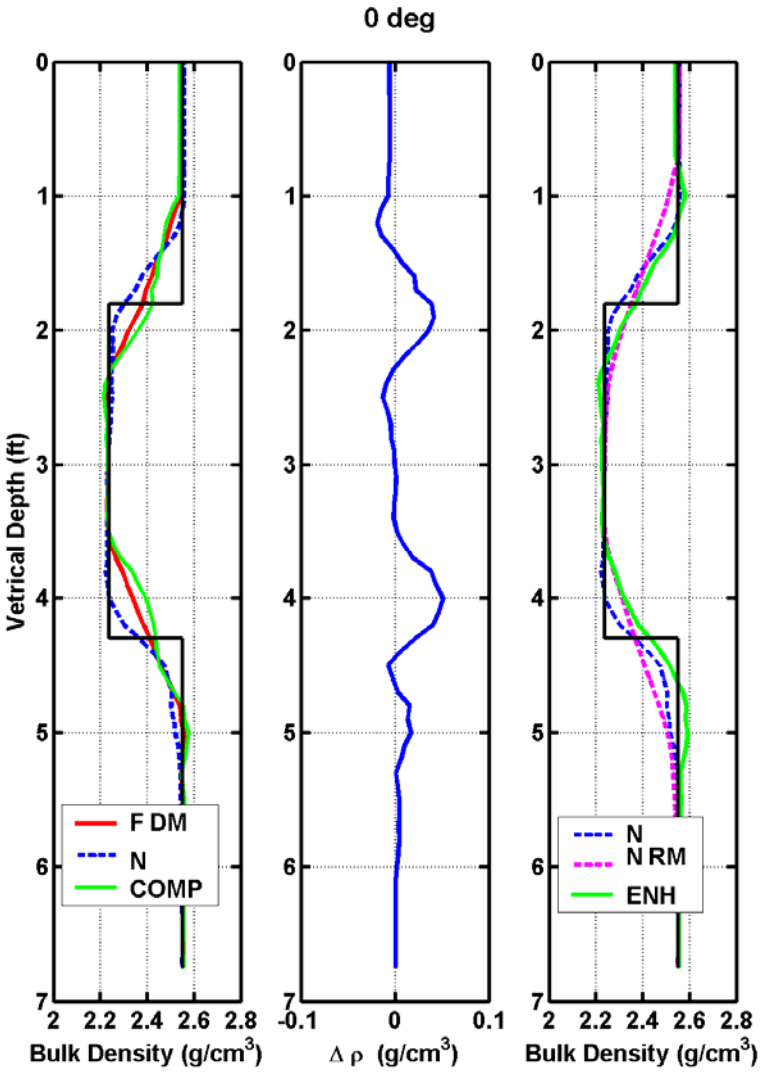

Figure 2.8: Simulated density log for a 30-inch, 25% porosity sandstone bed, bounded by shale beds in a vertical well. The panel on the left shows the near-detector density in blue, the depth-matched far-detector density in red, and the compensated density in green. The density correction is plotted in the center track, and the panel on the right shows the near-detector density in blue, the averaged density (resolution-matched) in magenta, and the resulting "enhanced" density in green. The black line describes the actual density of the formation.

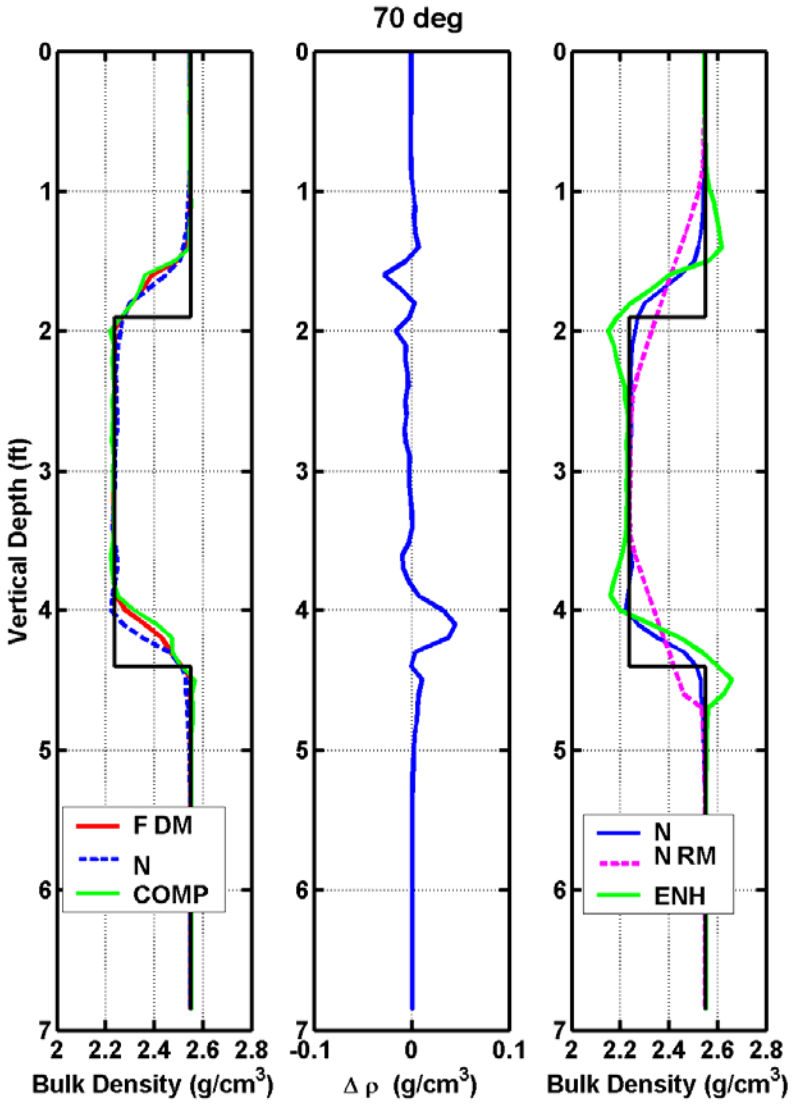

Figure 2.9: Simulated density log for a 30-inch, 25% porosity sandstone, bounded by shale beds in a well deviated 70 degrees from the vertical. The left panel shows the near-detector density in blue, the depth-matched far-detector density in red, and the compensated density in green. The density correction is plotted in the center panel, and the right panel shows the near-detector density in blue, the averaged density (resolution-matched) in magenta, and the resulting "enhanced" density in green. The black line describes the actual density of the formation.

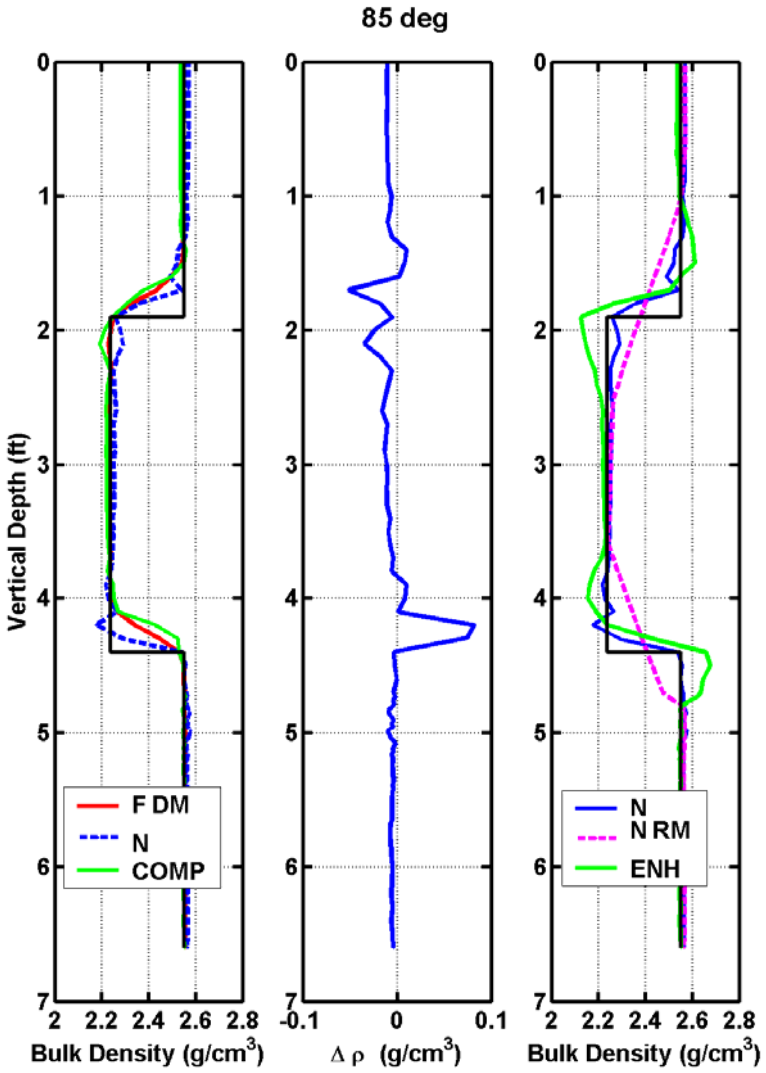

Figure 2.10: Simulated density log for a 30-inch, 25% porosity sandstone, bounded by shale beds in a well deviated 85 degrees from the vertical. The left-hand panel shows the near-detector density in blue, the depth-matched far detector density in red, and the compensated density in green. The density correction is shown in the center panel, and the right-hand panel shows the near detector density in blue, the averaged (resolution-matched) density in magenta, and the resulting "enhanced" density in green. The black line describes the actual density of the formation.

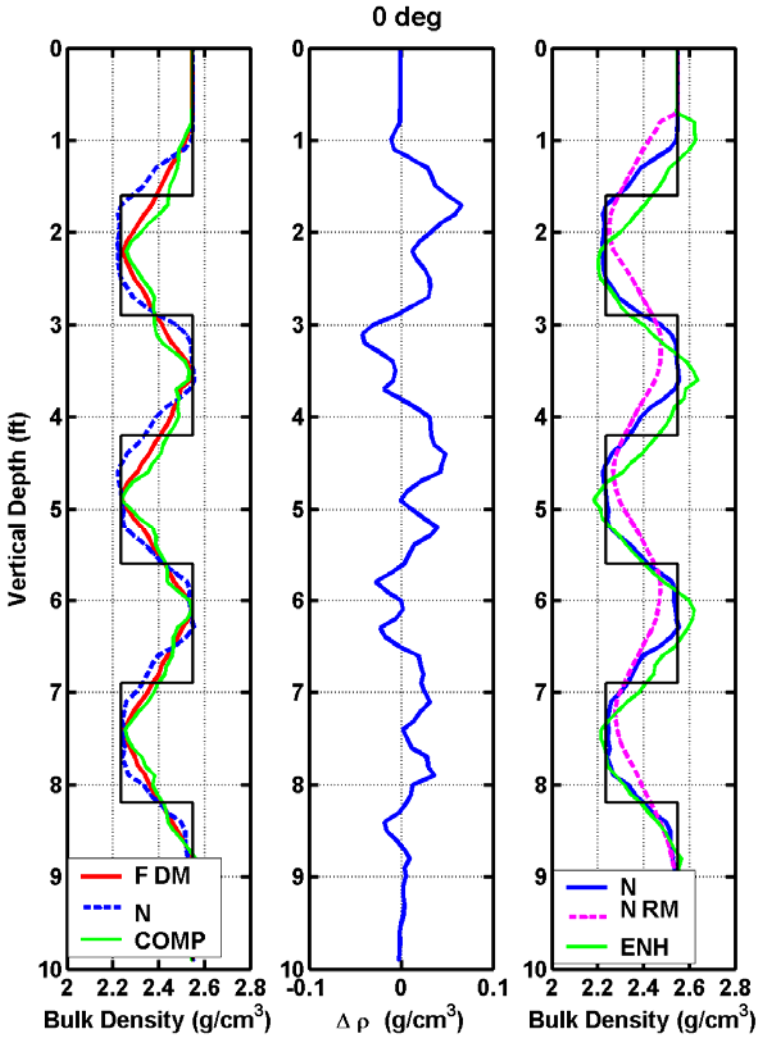

Figure 2.11: Density logs simulated in a sand-shale sequence penetrated by a vertical well. The left-hand panel shows the near-detector density in blue, the depth-matched far-detector density in red, and the compensated density in green. The density correction is shown in the center panel, and the right-hand panel shows the near-detector density in blue, the averaged (resolution-matched) density in magenta, and the resulting "enhanced" density in green. The formation consists of 16-inch, 25% porosity water-saturated sand beds, bounded by 16-inch shale beds. The black line describes the actual density of the formation.

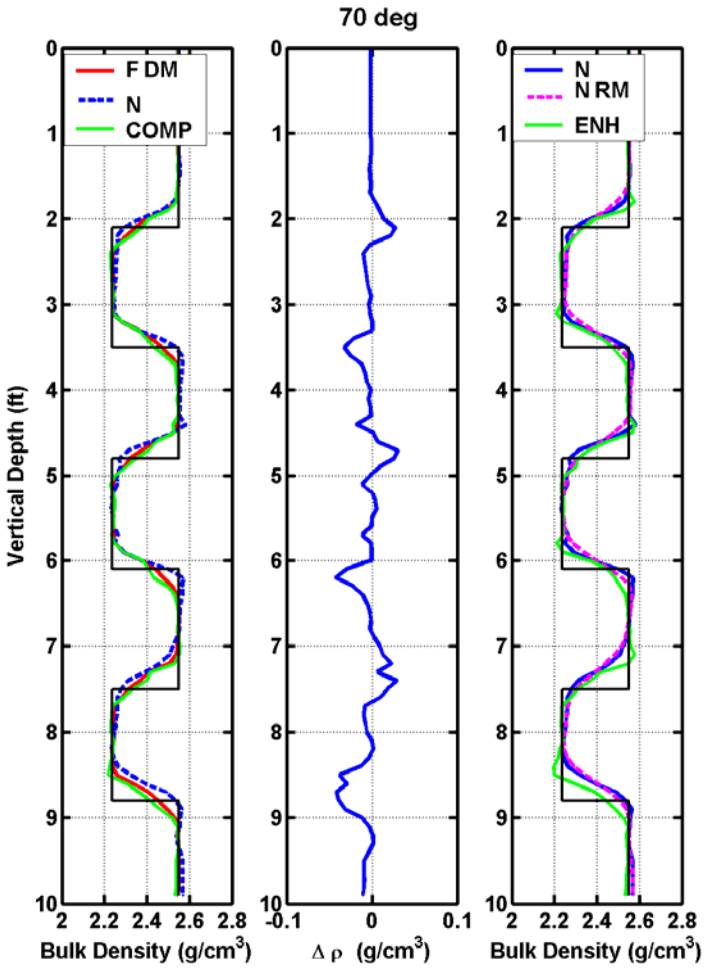

Figure 2.12: Density logs simulated in a sand-shale sequence penetrated by a well deviated 70 degrees from the vertical. The left-hand panel shows the near-detector density in blue, the depth-matched far-detector density in red, and the compensated density in green. The density correction is shown in the center panel, and the right-hand panel shows the near-detector density in blue, the averaged (resolution-matched) density in magenta, and the resulting "enhanced" density in green. The formation consists of 16-inch, 25% porosity water-saturated sand beds, bounded by 16-inch shale beds. The black line describes the actual density of the formation.

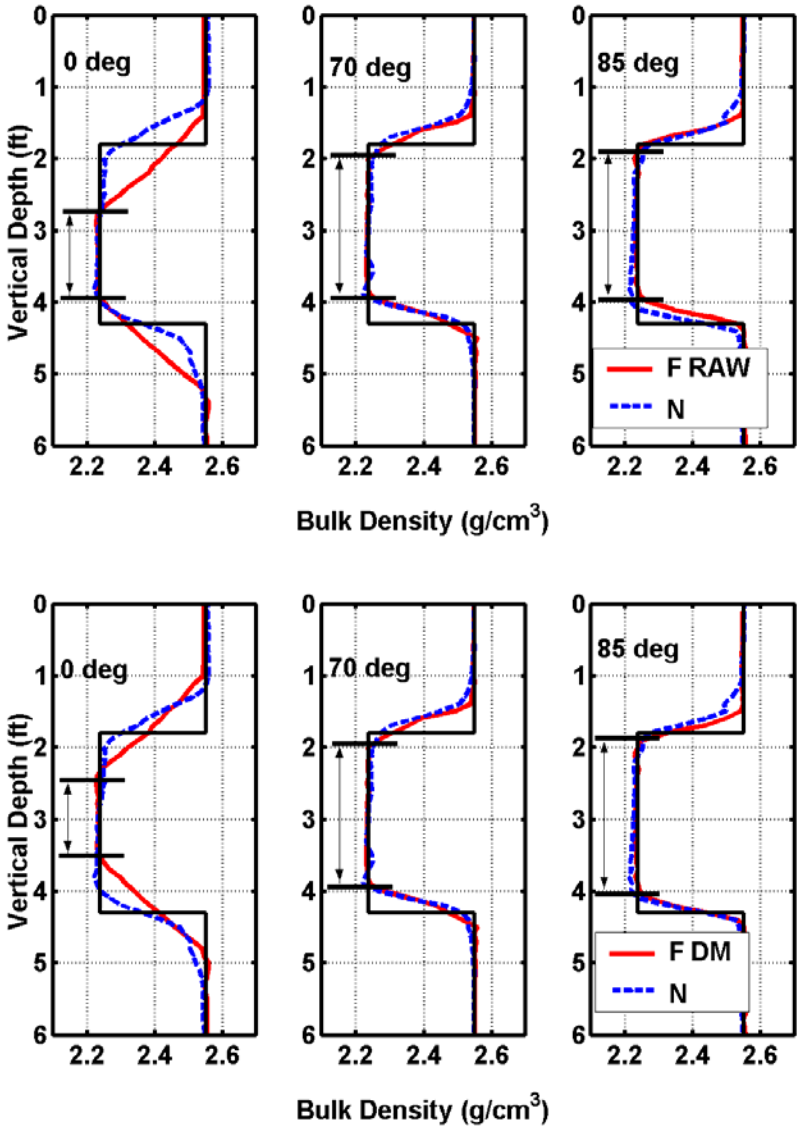

Figure 2.13: Comparative plots of the raw and depth-matched single-detector density logs describing shifts in vertical resolution corresponding to a vertical well and wells deviated 70 and 85 degrees from the vertical. Top panels show the raw far-detector density in red, and the near-detector density in blue. Bottom panels show depth-shifted far-detector density in red and near-detector density in blue.

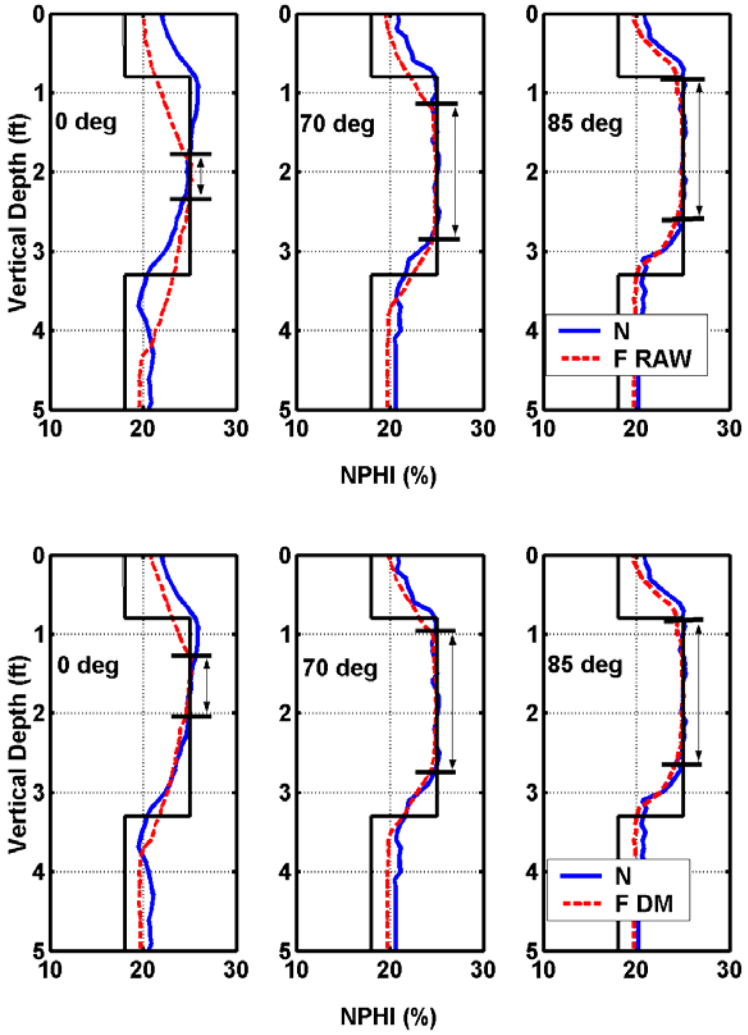

Figure 2.14: Comparative plot of the raw and depth-matched single-detector neutron porosity logs describing shifts in vertical resolution corresponding to a vertical well and wells deviated 70 and 85 degrees from the vertical. Top panels show the raw far-detector neutron porosity in red, and the near-detector neutron porosity in blue. Bottom panels show depth-shifted far-detector neutron porosity in red and near-detector neutron porosity in blue.

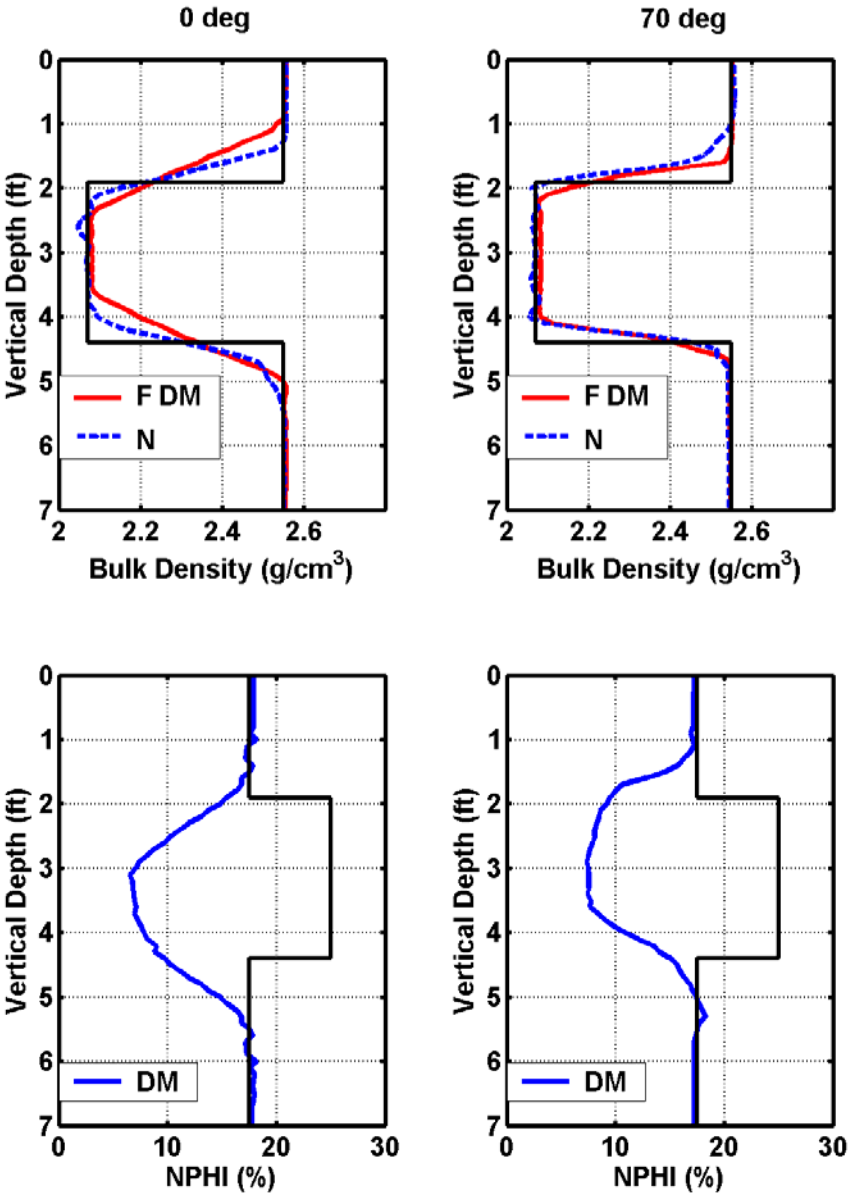

Figure 2.15: Comparative plot of simulated neutron and density logs for the case of a gas-saturated sand. The top panels show the single-detector density logs and the bottom panels show the simulated neutron porosity. All the logs correspond to the case of a well deviated 70 degrees from the vertical, penetrating a 30-inch gas-saturated sand bounded by shale beds.

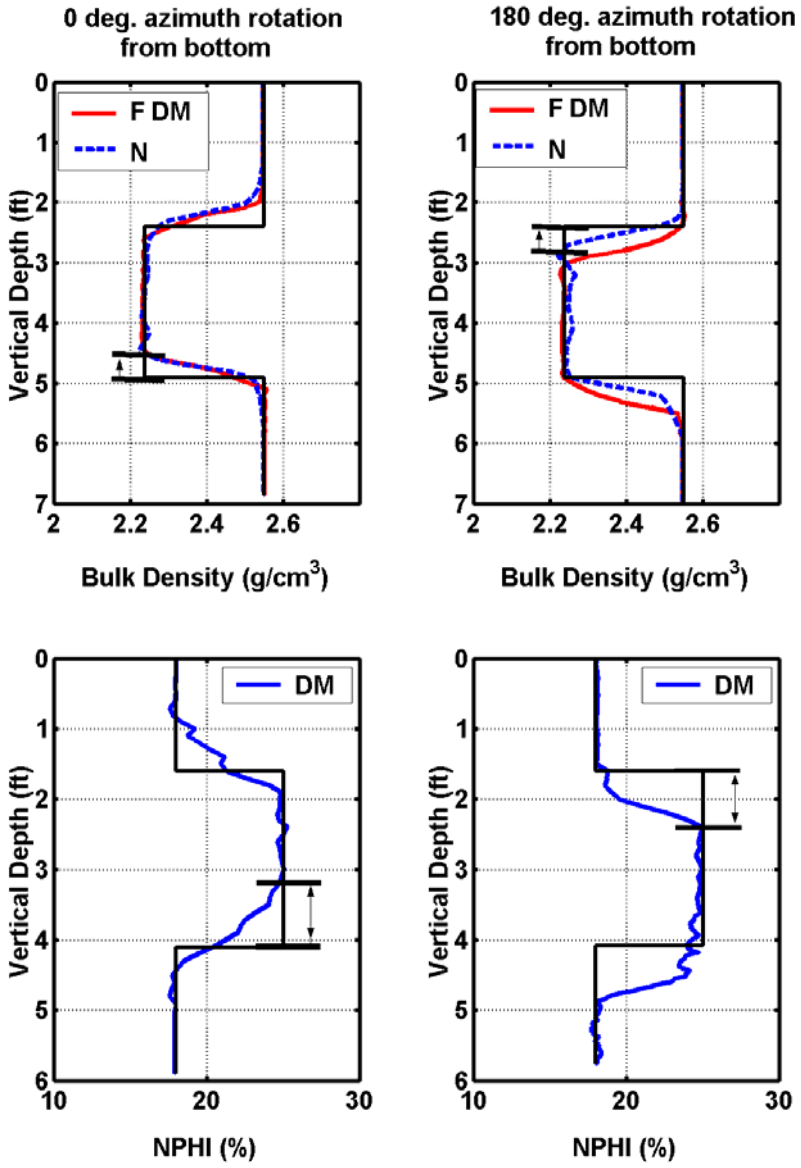

Figure 2.16: Comparative plot of simulated neutron and density logs for azimuthal tool locations of 0 and 180 degrees from the bottom face of the borehole. The top panels show the single-detector density logs and the bottom panels show the simulated neutron porosity. All the logs correspond to the case of a well deviated 70 degrees from the vertical, penetrating a 30-inch water-saturated sand bounded by shale beds.

Chapter 3: Linear Iterative Refinement Technique for the Rapid Simulation of Borehole Nuclear Measurements Acquired in Vertical Wells

We develop and successfully test a new linear iterative refinement technique to accurately and rapidly simulate nuclear borehole measurements. The approximation stems from Monte Carlo-derived geometrical response factors referred to as flux sensitivity functions (FSFs) for specific density and neutron tool configurations. First, we invoke an integral representation of Boltzmann's transport equation to describe the detector response due to the flux of particles emitted by the radioactive source. Subsequently, we use the Monte Carlo code MCNP to calculate the associated detector response function and the particle flux included in the integral form of Boltzmann's equation.

The linear iterative refinement method accounts for variations of the response functions due to local perturbations of energy-dependent cross-section in the numerical simulation of neutron and density porosity logs via first-order Born approximations. We quantify variations in the flux sensitivity functions of neutron and density measurements due to borehole environmental effects and changes of formation properties. Comparisons between MCNP simulations and iterative refinement approximations are shown for property perturbations in the radial (mudcake, standoff, invasion), and vertical (formation layering) directions.

3.1 INTRODUCTION

The conventional approach for in-situ porosity estimation is the combined use of bulk density and neutron porosity logs. Borehole nuclear measurements are influenced by fundamental petrophysical and geometrical properties such as saturating fluids, matrix composition, mud-filtrate invasion, and shoulder beds (Ellis and Singer, 2007). Therefore, advanced interpretation methods that include numerical modeling are necessary to reduce environmental effects and non-uniqueness in the estimation of porosity to secure reliable interpretations. Our ultimate objective is twofold: (1) to simulate borehole nuclear measurements in conjunction with inversion techniques, and (2) quantitatively integrate nuclear logs with other borehole measurements for estimation of petrophysical properties.

A fast numerical method is essential to simulate nuclear borehole measurements in conjunction with inversion techniques as well as for their quantitative integration with other borehole measurements. This is not currently done for nuclear logs, such as neutron and active gamma-ray, mainly because of the associated high computational requirements. Although recent developments promote reductions in computational time with deterministic methods (Aristodemou, 2006), the Monte Carlo method is the most widely used approach to simulate borehole measurements because of its versatility, variable numerical precision, and detailed three-dimensional (3D) geometrical capabilities. However, currently the Monte Carlo simulation method is not efficient either for application of inversion techniques (Patchett and Wiley, 1994) or for quantitative integration of nuclear measurements with other well logs.

Importance sampling of Monte Carlo codes has improved the efficiency of the calculations of the contribution flux for arbitrary spatial distribution of material properties (Booth and Hendricks, 1984; Hendricks, 1982; Mickael, 1992; Liu and Gardner, 1997). Neutron flux distribution maps have been used to quantify variations of neutron borehole measurements due to mud-filtrate invasion (Parsons, 1983). Similarly, density detector response functions have described gamma-ray paths in the formation (Flaum, et al., 1991) and quantified the radial length of investigation (Ellis, 2003) for dual-detector density tools. Subsequently, Watson (1984) introduced the concept of Monte Carlo-derived differential sensitivity functions for nuclear detector responses due to Compton and photoelectric gamma-ray interactions. This technique not only provided important information for tool design and improved post-processing of measured single-detector responses, but it opened the door to fast nuclear log simulation with the use of linear sensitivity functions (Watson, 1992; Couët and Watson, 1992; Couët and Watson, 1993; Case et al., 1994). However, none of the previously published methods have reported successful results for the simulation of neutron measurements with linear sensitivity functions.

In this chapter, we develop new fast approximate linear numerical procedures to simulate density and neutron well logs with the use of Monte Carlo-derived flux sensitivity functions (FSFs) of neutron and density measurements. We use linear first-order Born approximations to simulate nuclear measurements acquired in formations with arbitrary spatial distributions of a wide range of material property contrasts (i.e., energy-

dependent cross-section, migration length, mass density, porosity, and fluid saturations). The main technical contribution is the development of a linear iterative refinement procedure that accounts for spatial variations of the response function due to non-homogeneous formations and key borehole environmental effects. Our approximations differ from previous work on differential sensitivity functions both in the way we calculate the sensitivity function and in the implementation of FSFs for the simulation of nuclear borehole measurements.

We describe the physical variables involved in our approximation technique starting with the integral form of Boltzmann's transport equation (Greenspan, 1976). The formulation identifies geometrical properties of the model and describes the basic components of Monte Carlo-derived spatial FSF approximations. To quantify the flux sensitivity function due to specific variations of the total energy-dependent cross-section of the material, we perform a sensitivity analysis over a wide range of porosity values and rock matrix properties. Finally, we simulate neutron and density measurements with the use of the FSFs and the iterative refinement technique. To benchmark these approximations, we compare fast simulation results against synthetic nuclear logs calculated with MCNP (X-5 Monte Carlo Team, 2003). Simulations include 1D cases of vertical variations of formation properties (layering perpendicular to the borehole). In addition, to asses the two-dimensional (2D) capabilities of the rapid approximations, we include results with horizontal variations of formation properties (invasion, tool standoff, mudcake) and shoulder-bed effects. Chapter 4 verifies the reliability of the

approximations for the case of three-dimensional (3D) variations of formations properties.

3.2 FORMULATION

To establish terminology, and to describe the general formulation of the approximations introduced in this chapter, we begin with a concise description of nuclear particle transport via the time-independent Boltzmann's equation, given by

$$\left[\boldsymbol{\Omega}\cdot\nabla+\Sigma_t\left(\mathbf{r},E\right)\right]\psi\left(\mathbf{r},E,\boldsymbol{\Omega}\right)=\int dE'\int d\boldsymbol{\Omega}'\;\;\Sigma_s\left(\mathbf{r},E'\boldsymbol{\Omega}'\rightarrow E\boldsymbol{\Omega}\right)\psi\left(\mathbf{r},E',\boldsymbol{\Omega}'\right)+q\left(\mathbf{r},E,\boldsymbol{\Omega}\right),\quad(3.1)$$

where ψ is energy angular particle flux at position $\mathbf{r}$ of energy E and direction $\boldsymbol{\Omega}$, Σ_t is total macroscopic energy-dependent cross-section (i.e., $\Sigma_t=\Sigma_s+\Sigma_a$), Σ_s is macroscopic energy-dependent scattering cross-section, Σ_a is macroscopic absorption energy-dependent cross-section, and q is the nuclear particle source. The direction of particles is described by $\boldsymbol{\Omega}=\mathbf{v}/\|\mathbf{v}\|$, where $\mathbf{v}$ is particle velocity.

Figure 3.1 illustrates the geometrical and formulation conventions used for the calculation of FSFs and for the approximation of nuclear borehole measurements. We assume a fixed background medium, $\mathscr{R}^3$, of known total energy-dependent cross-section, $\Sigma_B\left(\mathbf{r},E\right)$, and a scatterer region, $\mathscr{T}$, of total energy-dependent cross-section $\Sigma\left(\mathbf{r}_0,E\right)$ (the total macroscopic energy-dependent cross-section is appropriate to describe variations of formation petrophysical properties, i.e., porosity, fluid saturations, rock matrix). In this chapter, we concentrate on the specific situation of axial-symmetric variations of formation properties about the axis of the borehole. Consequently, the

position vector **r** is a function of the radial direction ρ, and the vertical location, z. **Figure 3.2** illustrates the geometrical assumptions for a base-case formation that includes basic borehole environmental effects. In both situations, with and without borehole environmental effects, the base-case includes both borehole and tool configuration, and assumes a formation of constant total energy-dependent cross-section Σ_B with infinite boundaries away from the borehole and tool location.

The detector response is proportional to the number of particles entering the detector per unit time (counting rate). The sum over all the particles emitted by the radioactive source, each weighted by its contribution to the detector count rate (Lewins, 1965) can be written as

$$N_B(\mathbf{r}_R) = \int d\mathbf{r} \int dE \int d\mathbf{\Omega}\, \psi_B(\mathbf{r}_S, \mathbf{r}, E, \mathbf{\Omega}) S_B^+(\mathbf{r}_R, \mathbf{r}, E, \mathbf{\Omega}), \tag{3.2}$$

where N_B is the detector response at the observation point inside the tool due to the radioactive source in a base-case formation of constant total energy-dependent cross-section Σ_B. In this expression, $\psi_B(\mathbf{r}_S, \mathbf{r}, E, \mathbf{\Omega})$ is energy-dependent angular flux at location $\mathbf{r}$ due to a particle source; $q(\mathbf{r}_S, \mathbf{r}, E, \mathbf{\Omega})$ located at $\mathbf{r}_S$, and $S_B^+(\mathbf{r}_R, \mathbf{r}, E, \mathbf{\Omega})$ is the response function for the detector located at $\mathbf{r}_R$ and is given by

$$S^+(\mathbf{r}_R, \mathbf{r}, E, \mathbf{\Omega}) = \int dE' \int d\mathbf{\Omega}' \Sigma_s(\mathbf{r}, E\mathbf{\Omega} \to E'\mathbf{\Omega}') \psi^+(\mathbf{r}_R, \mathbf{r}, E', \mathbf{\Omega}'), \tag{3.3}$$

where $\psi^+(\mathbf{r}_R, \mathbf{r}, E, \mathbf{\Omega})$ is the importance function related to the solution of the integro-diferential adjoint equation (Greenspan, 1976; Lewins, 1965).

The counting rate at each detector due to a radioactive particle source is influenced by the material properties of the formation (Ellis and Singer, 2007), specifically by the total macroscopic energy-dependent cross-section. We invoke the first-order Born approximation to calculate the excess detector response (which is proportional to the detector secondary count rate) due to spatial variations of total energy-dependent cross-section (Torres-Verdín and Habashy, 2001). The approximation is given by

$$\Delta N\left(\mathbf{r}_R\right) \cong$$
$$N_B\left(\mathbf{r}_R\right)\int d\mathbf{r}_0 \int dE\left[\int d\mathbf{\Omega}\left(\frac{1}{N_B\left(\mathbf{r}_R\right)}\right)\psi\left(\mathbf{r}_S,\mathbf{r}_0,E,\mathbf{\Omega}\right)S^{+}\left(\mathbf{r}_R,\mathbf{r}_0,E,\mathbf{\Omega}\right)\right]\frac{\Delta\Sigma\left(\mathbf{r}_0,E\right)}{\Sigma_B\left(\mathbf{r}_0,E\right)}, \tag{3.4}$$

under the assumption that $\Delta N << N_B$. In the above equation, the expression between brackets "weights" the relative variation of Σ away from the assumed base-case model i.e.,

$$\Delta\Sigma\left(\mathbf{r}_0,E\right)=\Sigma_B\left(\mathbf{r}_0,E\right)-\Sigma\left(\mathbf{r}_0,E\right), \tag{3.5}$$

and the dependence of $\Delta N\left(\mathbf{r}_R\right)$ on the source location, $\mathbf{r}_S$ is implicit. In the above expressions $\mathbf{r}_R$ is the location of the detector, and $\mathbf{r}_0$ is an arbitrary location inside the perturbed space (i.e., $\Delta\Sigma\left(\mathbf{r}_0,E\right)=0$).

We define the flux sensitivity function for a particular base-case formation (FSF_B) (in analogy to the response sensitivity function defined by Greenspan (1976)) as

$$\mathrm{FSF}_B\left(\mathbf{r}_R,\mathbf{r},E\right)\equiv\int d\mathbf{\Omega}\left(\frac{1}{N_B\left(\mathbf{r}_R\right)}\right)\psi_B\left(\mathbf{r}_S,\mathbf{r},E,\mathbf{\Omega}\right)S_B^{+}\left(\mathbf{r}_R,\mathbf{r},E,\mathbf{\Omega}\right). \tag{3.6}$$

Substituting Equation (3.7) into Equation (3.4) gives

$$\Delta N(\mathbf{r}_R) \cong N_B(\mathbf{r}_R) \int d\mathbf{r}_0 \int dE \quad \mathrm{FSF}_B(\mathbf{r}_R, \mathbf{r}_0, E) \cdot \frac{\Delta\Sigma(\mathbf{r}_0, E)}{\Sigma_B(\mathbf{r}_0, E)}. \tag{3.7}$$

The iterative refinement technique described in this chapter locally adapts the FSF_B at each sample point by means of fixed-point iterations. Therefore, FSF_B in Equation (3.7) is space-shift invariant only at a fixed-point. Using the concept of superposition, we approximate the detector response (which is proportional to the counting rate) due to a point source inside the tool assuming a base-case of constant energy-dependent cross-section, Σ_B, and consider Σ variations away from the original formation. The estimated detector response, *N*, in a perturbed formation can then be written as

$$N(\mathbf{r}_R) = N_B(\mathbf{r}_R) + \Delta N(\mathbf{r}_R) = N_B(\mathbf{r}_R)\left(1 + \frac{\Delta N}{N_B}(\mathbf{r}_R)\right), \tag{3.8}$$

where $\Delta N(\mathbf{r}_R)$ is the change in detector response due to a spatial variation of Σ in the formation (Equation 3.7).

An alternative approximation of $N(\mathbf{r}_R)$ can be written as

$$\frac{\Delta N}{N_B}(\mathbf{r}_R) \cong \ln\left[N(\mathbf{r}_R)\right] - \ln\left[N_B(\mathbf{r}_R)\right], \tag{3.9}$$

(Habashy et al., 1993) or equivalently,

$$N(\mathbf{r}_R) \cong N_B(\mathbf{r}_R) \exp\left(\frac{\Delta N}{N_B}(\mathbf{r}_R)\right) \tag{3.10}$$

where Equation 3.8 is the first two terms of a Taylor expansion of Equation 3.10.

The integral in Equation (3.6) is solved numerically for specific energy windows base on a spatial grid constructed in a cylindrical coordinate system via the Monte Carlo code MCNP. Calculations assume a spatial mesh that includes the borehole and the tool configuration. The radial grid is coarsened in the region away from the borehole, whereas in the vertical direction the grid spacing is constant. We calculate the spatial flux $\psi_B(\mathbf{r}_S, \mathbf{r}, E)$ in the formation due to a specified source in a reference medium (which includes the borehole). Furthermore, for each neutron and gamma-ray detector, we calculate the corresponding detector response function, $S^+(\mathbf{r}_R, \mathbf{r}, E)$, with the use of the forward-adjoint generator implemented in MCNP to calculate space and energy-dependent weight windows (Booth and Hendricks, 1984; Hendricks, 1992, Mickael, 1982; Gardner and Liu, 1999). Moreover, we modify the MCNP code to optimize the calculation of the geometrical response functions with the use of superimposed geometry to reduce the input of a fine spatial grid (Liu and Gardner, 1997), and to render the FSF as a direct output of MCNP.

To illustrate the concept of flux sensitivity functions, **Figure 3.3** shows the three-dimensional (3D) spatial functions involved (total flux and detector's response function) in the calculation of the FSF for the case of a neutron tool detector. **Figures 3.4** and **3.5** show 2D maps of density and neutron flux sensitivity functions, respectively. For density measurements, we calculate separate functions for Compton (density) and photoelectric effect (PEF) assuming a 1.5-curie 662 keV ^{137}Cs gamma-ray source and the tool configuration described in **Table C.1**. In so doing, we discriminate gamma rays with

energies below 200 keV from the particles that contribute to the detector response. Conversely, in the FSF simulations for PEF we include only gamma rays with energies below 200 keV in the detector count rate. For the case of neutron FSF calculation, we include all neutron energies assuming a 16-curie AmBe neutron source and the tool configuration described in **Table C.2**. **Figure 3.5** indicates that the neutron spatial response exhibits a more pronounced peak in the vicinity of the detector than near the source. This behavior remains consistent with the neutron sensitivity functions calculated by Couët and Watson (1993). By comparison, **Figure 3.4** shows a more symmetric geometric response function for the case of density measurements.

The application of sensitivity functions for simulations of nuclear borehole measurements is poorly documented in the open technical literature. Using a superimposed geometry importance function generator recently implemented in MCNP, we construct the FSF in a faster manner than the differential sensitivity functions described by Watson (1984). Our approximations differ from the sensitivity functions described by Watson (1992) and Case et al., (1994) primarily in the use of the FSF for the simulation of nuclear borehole measurements. We implement a linear iterative refinement technique that approximates spatial variations of the FSF due to spatial perturbations of formation properties (this procedure is described in a subsequent section of this chapter). In addition, we successfully test the accuracy of 2D FSF approximations in the presence of shoulder beds, mud-filtrate invasion, and borehole environmental effects.

3.3 DEPENDENCE OF THE FSF ON FORMATION PROPERTIES

The principle behind the rapid simulation of nuclear borehole measurements via Equations (3.2), (3.6), and (3.8), is to define a base-case formation (which includes the borehole and is not necessarily a homogeneous formation) for the calculation of the flux sensitivity functions. Since the FSF weights spatial variations of formation properties (i.e., variations of energy-dependent cross-section due to spatial variations of petrophysical properties) to approximate the corresponding variation of detector response in the perturbed medium, the spatial properties of the sensitivity function are critical to the simulations. Therefore, to appraise the performance of the spatial response approximations for different choices of base-case formation, we calculate flux sensitivity functions for density and neutron measurements for a wide range of homogeneous formations that include the borehole.

Figure 3.6 and **Table 3.1** describe the spatial dependence of the density-measurement FSF to formation density in an 8-inch borehole for an assumed density tool configuration (Mendoza et al., 2007, b). In the vertical direction, we observe that the maximum variation occurs in the region between the source and the detector. In addition, the maximum vertical spatial variation (integral of the FSF when normalized with respect to its maximum value) is less than 3% for both long-spaced (LS) and short-spaced (SS) detectors. Similarly, in the radial direction, the geometric factors show a maximum variation of approximately 1.2 inches for 90% of the response at the LS detector, and smaller for the case of the SS detector. For 90% of the response, the radially-integrated FSF referred to as J-factor (Sherman and Locke, 1975) exhibits average radial lengths of

investigation of 3.33 and 2.02 inches for the LS and SS detectors, respectively. From the radially-integrated FSF at 100% of the response the total radial length of investigation is 6 inches. By comparison, for a different density tool model and for the maximum penetration distance of the contribution flux, Liu and Gardner (1997) reported a radial length of investigation of 20 cm (7.874 inches).

Figure 3.7 and **Table 3.1** describe the spatial dependence of the neutron-measurement FSF to formation migration length in an 8-inch borehole for the assumed neutron tool configuration (Mendoza et al., 2007, b). In the vertical direction, maximum FSF variations occur in the vicinity of the source and detector. Moreover, the total vertical spatial variation (integral of the FSF when normalized with respect to its maximum value) of the FSF is as large as 36% for the far detector, and as large as 62% for the near-detector. In the radial direction, the geometric factors exhibit maximum variations of 4.10 and 3.80 inches for 90% of the near- and far-detector responses, respectively. By comparison, Liu and Gardner (1997) reported a change of radial length of investigation of 8 cm (3.15 inches) for 100% of the response between a 1pu limestone (L_m = 25.85) and a 20pu limestone (L_m = 14.13 cm) formation assuming a different neutron tool configuration.

3.4 BOREHOLE ENVIRONMENTAL EFFECTS ON FSFs

By design, density tools are nearly insensitive to the borehole environment (i.e., borehole size, mud type, etc.). However, the most common formation density measurement in vertical wells is the *compensated* or corrected density given by $\rho_b = \rho_{LS} + \Delta\rho$, where $\Delta\rho$ is the density correction due to the difference between the

density measured by the short-spaced detector, ρ_{SS}, and the long-spaced detector, ρ_{LS}. This density difference between detectors is due to a perturbation in the counting rate caused by a radial layer of material (mudcake) between the tool and the borehole wall (Ellis and Singer, 2007). Consequently, a perturbation in the counting rate modifies the flux sensitivity function. The radial geometric factor (J-factor) decreases not only depending on mudcake (tool standoff) thickness, but also on the contrast between formation density and mudcake density. A streaming effect can occur as gamma rays channel through the radial water layer (tool standoff) causing a substantial change in the spatial shape of the FSF (**Figure 3.8**). By contrast, in addition to formation porosity, lithology and saturating fluids, neutron-porosity measurements are influenced by the borehole environment. The neutron flux sensitivity function is also perturbed by tool standoff (**Figure 3.9**), borehole size, mud weight, and borehole salinity.

3.5 LINEAR ITERATIVE REFINEMENT TECHNIQUE

In addition to the perturbations on the J-factor caused by borehole environmental effects, formation petrophysical properties can influence the resolution limits (vertical and azimuthal geometric factors) of the measurement. The principle behind the linear iterative approximation technique is to simulate nuclear logs in non-homogeneous formations using multiple flux sensitivity functions pre-computed in homogeneous formations (that also include the borehole). The linear iterative refinement technique accounts for variations of the spatial FSF due to perturbations of formation and borehole environment properties. This procedure locally updates the flux sensitivity function at each sample point based on the results of a previous pass. To that end, we previously

construct a library of FSFs for a range of porosity-matrix-fluid mixtures. This library consists of a set of pre-computed FSFs, each simulated in homogeneous formations (base-case formations) of different petrophysical properties. The variety of geometric factors contained in the library enables the selection of the most appropriate base-case FSF_B for the simulation of nuclear borehole measurements across non-homogeneous formations.

The vertical and radial geometric factors of the neutron response function can change significantly depending on the volumetric proportions and chemical composition of the rock and saturating fluids. To account for a wide range of rock matrix, porosity, and saturating fluid combinations that would result in an approximate effective value of migration length, the library of neutron FSFs includes gas- and water-saturated base-case formations for several values of porosity. **Table 3.1** summarizes the petrophysical properties of the base-case formations used to compute neutron FSFs for a range of migration length values between 44.87 cm and 10.74 cm. Because the density FSF is much less affected by the characteristics of the medium (**Figure 3.6**), a limited library of sensitivity functions is sufficient. The benefit of iterating for updates of density FSFs is only significant in cases of high contrasts of material properties in the radial direction (invasion of water in a high porosity gas-saturated formation). However, in the presence of borehole environmental effects, it is necessary to use flux sensitivity functions that include tool standoff or mudcake. Hence, in addition to the homogeneous base-case formations, the library of density FSFs incorporates several non-homogeneous base-case formations that include tool standoff and mudcake of up to one inch in a borehole filled

with water-base mud. **Table 3.1** summarizes the density FSFs included in the library. In both neutron and density measurement approximations, linear interpolation is used to compute FSFs that correspond to values of tool standoff and/or migration length that are between available pre-computed functions.

The first step is to assume a matrix type and an average porosity value to select an initial flux sensitivity function for nuclear log simulation. A second step consists of simulating tool response (i.e., detectors count rate) which correlates to porosity under specific assumptions about fluid and matrix type. In a third step, at each sample point a new FSF is calculated by linear interpolation between available functions corresponding to the closest neighbors of the simulated porosity. Finally, the updated FSF is used to simulate a new value of porosity. The procedure repeats until the simulated porosity matches the sensitivity function used for the simulation (**Figure 3.10**). This fixed-point iteration converges when the difference between values of the simulated porosity and that corresponding to the assumed base-case is below a pre-specified threshold. For situations that include borehole environmental effects, simulations use flux sensitivity functions that contain mudcake or standoff. In such cases, the linear optimization is based on interpolations to match both mudcake thickness and formation density contrast.

3.6 RAPID SIMULATION OF NUCLEAR BOREHOLE MEASUREMENTS: NUMERICAL RESULTS

This section describes examples of the simulation of neutron and density measurements with the approximations described above.

3.6.1 Neutron Measurements

The large variability of neutron FSFs around the source and detectors for different porosity and matrix formations indicate that a constant FSF will not, in general, yield accurate approximations of neutron measurements for large contrasts of material properties. This observation is especially critical across boundaries between contrasting formations. **Figure 3.11** describes the 1D spatial behavior of the neutron FSF in the vertical direction across a boundary between water-filled sandstone formations of 25% and 2% porosity. We consider cases where the tool is moving along the borehole, from the low-porosity into the high-porosity layer and the reverse order of porosities. In addition, we calculate the neutron porosity from the depth-matched near-to-far detector ratio. The relative distance between the boundary (proportional to the source-detector spacing) and the midpoint between source and detector is equivalent for the near- and far-detectors. For those cases where the boundary is close to one end of the tool, we observe limited variation in the FSF regardless of the location of the low- and high-porosity formations. However, when the boundary is near the midpoint between source and detector, the formation around the detector dominates the value of porosity. Moreover, the FSF exhibits a spatial distribution approximately equal to that of the FSF of a base-case formation (i.e., FSF_B) corresponding to the average formation property around the detector. Results shown in **Figures 3.7** and **3.11** indicate that, when used for the simulation of neutron logs across a layered (perturbed) formation, the spatial neutron FSF_B must be iteratively changed from that of a starting base-case formation to one of similar properties of the adjacent bed.

In Equations (3.4) and (3.5) the nuclear sensitivity parameter is expressed in terms of formation total energy-dependent cross-section, Σ. This property of the material is related to nuclear parameters such as hydrogen index, slowing-down length, diffusion length, and migration length (Ellis and Singer, 2007). Correlations enable the selection of specific sensitivity nuclear parameters in Equations (3.4) and (3.5) for the rapid approximation of nuclear borehole measurements (**Appendix A**) and subsequent porosity estimations. We choose the migration length, L_{m}, as the appropriate weighted formation parameter in Equations (3.4) and (3.5) because it retains dependence on material cross-section (Ellis et al. 1987). Furthermore, the logarithm of the neutron flux correlates with the reciprocal of L_{m}. In so doing, we use the code SNUPAR (McKeon and Scott, 1989) for the calculation of L_{m} starting from volumetric compositions of the formation. With the use of equation (3.4) and a constant base-case FSF_B of 5% porosity water-saturated sand (L_m equal to 24.07 cm), we simulate variations of the near- and far-detector responses across four adjacent 16-inch thick layers of 5% and 30% porosity sandstone formation bounded by shale shoulder beds. The bottom sands are fully water-saturated whereas the top sands are gas-saturated. **Table 3.2** lists the petrophysical properties of the multi-layer model used in the simulations. **Figure 3.12** shows that the Born approximation, Equation (3.8), and a constant FSF_B, yield a maximum difference of 4.40% porosity or 22% error with respect to the same neutron log simulated with the Monte Carlo method. By contrast, with the implementation of linear iterative refinement, simulations improve yielding a maximum porosity difference with respect to MCNP of 1.59% or 8% error. For this particular case, Monte Carlo simulations required 160 hours

of CPU time (for 112 sample points and 2 detectors) while the linear iterative refinement approximation required 1.4 minutes.

To quantify the performance of the approximations in the presence of spatial variations of formation properties in the radial direction only, we consider a case of invasion of water in a fully gas-saturated 30% porosity sandstone (**Figure 3.13**). The model assumes piston-like invasion wherein the invading water displaces 100% of the original saturating gas. For this situation, the Born approximation, Equation (3.8), and a constant FSF_B, yield a maximum difference of 7.16% porosity with respect to Monte Carlo simulations. By comparison, the linear iterative refinement approximation improves the simulations to a difference of 2.47% porosity with respect to MCNP.

Because of borehole environmental effects (**Figure 3.14**), and formation properties in the case of neutron measurements (**Figure 3.7**), the shape of FSFs is not constant. The linear iterative refinement technique accurately approximates variations in the J-factor (1D radial) due to tool standoff with a maximum difference of 1.67% porosity with respect to MCNP results (**Figures 3.15**). In the case of neutron measurements, formation layering perturbs the vertical geometrical factor. Shoulder-bed effects combined with tool standoff causes a 2D perturbation of material properties which can still be accurately approximated in vertical wells with the linear iterative refinement technique. For this case, the maximum difference between the rapid approximation and MCNP simulations was 3.05% porosity (**Figures 3.16**). Results for 1-inch tool standoff represent an extreme case. For smaller effects, the accuracy of the approximation

improves. **Table 3.2** compares the results obtained with the iterative refinement technique and MCNP.

3.6.2 Density and PEF Measurements

For the case of rapid simulation of density measurements via the Born approximation (Equations 3.2, 3.4, and 3.8), we choose density of the formation as the weighted nuclear sensitivity parameter. **Figure 3.17** compares numerical simulations performed with the rapid approximation and the Monte Carlo method for the case of periodic 4-inch thick beds of density values equal to 2.0 g/cm^3 and 2.6 g/cm^3. The fast approximation yields a maximum difference of 0.012 g/cm^3 for the filtered SS detector density, and of 0.008 g/cm^3 for the depth-matched LS detector density. After conventional density log processing (Evans et al., 1995) of the single-detector responses, the compensated density exhibits a maximum difference of 0.018 g/cm^3 between the rapid FSF approximation and the Monte Carlo simulation. Similarly, for the volumetric photoelectric factor (U) comparison between the rapid FSF and the Monte Carlo simulation indicates a maximum difference of 0.2 (PEF was derived from division of the simulated volumetric photoelectric factor, U, by the simulated SS detector density, ρ_{SS}).

To quantify the accuracy of the rapid density simulation method for the case of spatial variations of formation properties in the radial (horizontal) direction, we consider the case of water invasion in a fully gas-saturated 30% porosity sandstone (**Figure 3.18**). For this situation, the Born approximation, Equation (3.8), and a constant FSF_B, yield a maximum difference of 0.0398 g/cm^3 with respect to Monte Carlo simulations of the final compensated density. By contrast, the iterative refinement technique yields a maximum

difference in compensated density equal to 0.0194 g/cm^3 with respect to MCNP simulations.

The linear iterative refinement technique accurately approximates variations of the J-factor (1D radial) due to mudcake. Because the density contrast between formation and mudcake or borehole fluid impacts the shape of the FSF, we consider simulations of density measurements with presence of heavy (ρ = 2.74 g/cm^3) and light (ρ = 1.0 g/cm^3) mudcake (**Figure 3.19**, and **Tables 3.3**, **3.4**, and **3.5**). In most cases, the difference between the rapid approximation and MCNP simulations is less than 0.03 g/cm^3. In addition, numerical noise implicit in Monte Carlo calculations contributes to the difference in the simulations with respect to the rapid approximations. **Tables 3.3**, **3.4**, and **3.5** quantitatively compare rapid approximation results for SS, LS, and compensated density against simulations with MCNP and density values for the assumed model. For 2D perturbations resulting from shoulder-bed effects combined with mudcake or tool standoff, the iterative refinement technique accurately approximates density measurements to less than a 0.03 g/cm^3 difference with respect to MCNP. **Figure 3.20** compares MCNP simulations to those obtained with the rapid approximation across low and high porosity water- and gas-saturated formation layers. In this case, the numerical uncertainty in the Monte Carlo simulations results in larger differences with respect to the rapid approximations. Results for 1-inch mudcake represent an extreme case. For smaller effects, the accuracy of the approximation improves. In this particular exercise, MCNP simulations required 384 hours of CPU time for 96 sample points and two detectors, whereas the rapid approximation technique required 1.11 minutes.

3.7 CONCLUSIONS

We introduced a new approximation for the fast numerical simulation of neutron and density borehole measurements. The method is based on first-order Born approximations in conjunction with an iterative refinement procedure that adapts the weighting function to local spatial variations of formation properties. The approximations used Monte Carlo-derived flux sensitivity functions for specific tool configurations. In this chapter, we introduced the new approximation and successfully tested the iterative refinement method for neutron and density measurements acquired in vertical wells. Simulations included variations of formation petrophysical properties in the vertical (layering) and radial (invasion) directions. In addition, the approximations included basic borehole environmental effects (mudcake and tool standoff).

The influence of key borehole environmental effects and of spatial variations of formation petrophysical properties on nuclear measurements was characterized with flux sensitivity functions. Sensitivity analyses of the flux sensitivity functions for a wide range of base-case formations confirmed that the density FSF is much less affected by variations of formation properties than that of neutron measurements. However, significant perturbations can result in the radial J-factor (up to 1.2 inches) of density measurements due to large contrasts of formation density or in the presence of mudcake or tool standoff. The impact of mudcake on the density FSF depends on both thickness and density contrast between formation and mudcake. Variations of radial length of investigation are critical to the fast simulations of density measurements in the presence of invasion or mudcake. Simulations of neutron FSFs showed significant variations of

the vertical geometric factor in addition to variations of up to 4.1 inches of the radial J-factor.

Linear iterative refinement was implemented to approximate spatial variations of FSFs due to perturbations of formation petrophysical properties and presence of borehole environmental effects. In the presence of non-homogeneous formations the linear iterative refinement method locally adjusts a pre-selected base-case FSF_B to one associated with an equivalent (effective) local medium. This linear technique enables fast and accurate neutron simulations in cases of large contrasts of material properties wherein the relationship between migration length and detector count rate is highly nonlinear.

For 1D perturbations in the vertical direction (shoulder-bed effects), fast simulations of density measurements yielded differences of less than 0.02 g/cm^3 with respect to Monte Carlo simulations. Iterative refinement simulations of neutron measurements across large contrasts of porosity and saturating fluids (migration length), including shoulder-bed effects, resulted in maximum differences of 1.6% porosity or 8% error with respect to MCNP simulations. Similarly, for 1D perturbations in the radial direction (invasion of water into a 30% porosity gas-saturated sand), iterative refinement simulations exhibited maximum differences of 0.019 g/cm^3 and 2.45% porosity for density and neutron measurements, respectively.

The capability of linear iterative refinement to approximate spatial FSF variations due to shoulder beds, invasion, and borehole environmental effects enables fast and reliable neutron and density simulations in vertical wells. Approximations improve the

quantitative interpretation of combined neutron and density measurements acquired in vertical wells across thin laminated sequences of contrasting porosities and fluid saturations. **Figure 3.21** describes iterative refinement simulations of neutron and density measurements across a long depth interval in a multi-layer formation model. These simulations would required several days of CPU time with MCNP as opposed to approximately 15 minutes with iterative refinement approximations. Chapter 4 verifies the reliability of the approximations in high-angle and horizontal wells. Additionally, linear iterative refinement approximations with FSFs can be applied to gamma-ray simulations (**Appendix B**) and potentially to thermal neutron decay and nuclear spectroscopy logs.

For simulations of neutron borehole measurements we considered migration length as the appropriate weighted formation property because we include both fast and thermal neutrons in the detector count rate. Future work will implement the linear iterative refinement approximation considering separate diffusion length and slowing-down length for thermal and fast neutrons, respectively.

Results discussed in this chapter were based on the assumption of generic tool models (Mendoza et al., 2007, b), which are close to commercial logging tool designs. For use with field logs, it would be necessary to implement flux sensitivity functions obtained for commercial logging tool configurations. The iterative refinement approximation with FSFs allows rapid simulations of neutron and density measurements without requiring proprietary nuclear tool design information. However, nuclear tool design information is required to generate base-case FSFs.

Table 3.1: Petrophysical properties of the base-case formations assumed for the calculation of neutron and density flux sensitivity functions in homogeneous formations with and without key borehole environmental effects.

Base case	Volumetric composition [v/v]	Formation density [g/cm^3]	Mudcake density [g/cm^3]	Mudcake thickness [in]	Migration length, L_m [cm]
DOLO40	0.40 H_2O, 0.60 $CaMg(CO_3)_2$	2.1040	-	0	**10.74**
DOLO30	0.30 H_2O, 0.70 $CaMg(CO_3)_2$	2.2880	-	0	11.98
DOLO20	0.20 H_2O, 0.80 $CaMg(CO_3)_2$	2.4720	-	0	13.88
DOLO10	0.10 H_2O, 0.90 $CaMg(CO_3)_2$	2.6560	-	0	17.20
DOLO05	0.05 H_2O, 0.95 $CaMg(CO_3)_2$	2.7480	-	0	20.18
DOLO00	0.00 H_2O, 1.00 $CaMg(CO_3)_2$	2.8400	-	0	26.46
DOLO40G	0.40 CH_4, 0.60 $CaMg(CO_3)_2$	1.7111	-	0	36.45
DOLO30G	0.30 CH_4, 0.70 $CaMg(CO_3)_2$	1.9933	-	0	33.11
DOLO20G	0.20 CH_4, 0.80 $CaMg(CO_3)_2$	2.2756	-	0	30.44
LIME40	0.40 H_2O, 0.60 $CaCO_3$	2.0260	-	0	10.93
LIME30	0.30 H_2O, 0.70 $CaCO_3$	2.1970	-	0	12.20
LIME20	0.20 H_2O, 0.80 $CaCO_3$	2.3680	-	0	14.13
LIME10	0.10 H_2O, 0.90 $CaCO_3$	2.5390	-	0	17.54
LIME05	0.05 H_2O, 0.95 $CaCO_3$	2.6245	-	0	20.72
LIME00	0.00 H_2O, 1.00 $CaCO_3$	2.7100	-	0	28.34
LIME40G	0.40 CH_4, 0.60 $CaCO_3$	1.6331	-	0	37.83
LIME30G	0.30 CH_4, 0.70 $CaCO_3$	1.9023	-	0	34.60
LIME20G	0.20 CH_4, 0.80 $CaCO_3$	2.1716	-	0	32.05
SAND40	0.40 H_2O, 0.60 SiO_2	2.0000	-	0	11.49
SAND35	0.35 H_2O, 0.65 SiO_2	2.0725	-	0	12.19
SAND35a	0.35 H_2O, 0.65 SiO_2	2.0725	1.0000	1	12.19
SAND35b	0.35 H_2O, 0.65 SiO_2	2.0725	1.0000	0.5	12.19
SAND35c	0.35 H_2O, 0.65 SiO_2	2.0725	1.0000	0.25	12.19
SAND35d	0.35 H_2O, 0.65 SiO_2	2.0725	2.7400	1	12.19
SAND35e	0.35 H_2O, 0.65 SiO_2	2.0725	2.7400	0.5	12.19
SAND35f	0.35 H_2O, 0.65 SiO_2	2.0725	2.7400	0.25	12.19
SAND30	0.30 H_2O, 0.70 SiO_2	2.1550	-	0	13.03
SAND20	0.20 H_2O, 0.80 SiO_2	2.3200	-	0	15.41
SAND20a	0.20 H_2O, 0.80 SiO_2	2.3200	1.0000	1	15.41
SAND20b	0.20 H_2O, 0.80 SiO_2	2.3200	1.0000	0.5	15.41
SAND20c	0.20 H_2O, 0.80 SiO_2	2.3200	1.0000	0.25	15.41
SAND20d	0.20 H_2O, 0.80 SiO_2	2.3200	2.7400	1	15.41
SAND20e	0.20 H_2O, 0.80 SiO_2	2.3200	2.7400	0.5	15.41
SAND20f	0.20 H_2O, 0.80 SiO_2	2.3200	2.7400	0.25	15.41
SAND10	0.10 H_2O, 0.90 SiO_2	2.4850	-	0	19.80
SAND05	0.05 H_2O, 0.95 SiO_2	2.5675	-	0	24.07
SAND05a	0.05 H_2O, 0.95 SiO_2	2.5675	1.0000	1	24.07
SAND05b	0.05 H_2O, 0.95 SiO_2	2.5675	1.0000	0.5	24.07
SAND05c	0.05 H_2O, 0.95 SiO_2	2.5675	1.0000	0.25	24.07
SAND05d	0.05 H_2O, 0.95 SiO_2	2.5675	2.7400	1	24.07
SAND05e	0.05 H_2O, 0.95 SiO_2	2.5675	2.7400	0.5	24.07
SAND05f	0.05 H_2O, 0.95 SiO_2	2.5675	2.7400	0.25	24.07
SAND00	0.00 H_2O, 1.00 SiO_2	2.6500	-	0	35.24
SAND40G	0.40 CH_4, 0.60 SiO_2	1.5971	-	0	**44.87**
SAND30G	0.30 CH_4, 0.70 SiO_2	1.8603	-	0	41.50
SAND20G	0.20 CH_4, 0.80 SiO_2	2.1236	-	0	38.88

Table 3.2: Petrophysical properties of the layers included in neutron and density simulations and quantitative comparison of neutron porosities simulated with the rapid approximation and MCNP. Layers are labeled (from the bottom up) I through V in **Figures 3.12**, **3.15**, **3.16**, **3.20**, and **3.21**.

Layer	Volumetric composition [v/v]	Formation density [g/cm^3]	*Migration length, L_m* [cm]	NPHI , SO = 0" MCNP / Approx. [%]	NPHI, SO=0.5" MCNP / Approx. [%]	NPHI, SO=1" MCNP / Approx. [%]	Maximum difference, MCNP – Approx. [%]
I	0.05 H_2O 0.50 $Al_2Si_2O_5(OH)_4$ 0.40 SiO_2 0.05 FeS_2	2.6655	12.74	33.75 / 34.82	34.50 / 35.73	**35.80 / 37.64**	**-1.8400**
II	0.05 H_2O 0.95 SiO_2	2.5675	24.07	4.98 / 4.79	6.53 / 6.96	**7.33 / 9.65**	**-2.3200**
III	0.30 H_2O 0.70 SiO_2	2.1550	13.03	**29.60 / 28.82**	30.35 / 29.98	31.64 / 31.98	**+0.7800**
IV	0.30 CH_4 0.70 SiO_2	1.8603	41.50	-1.09 / -0.95	-0.65 / 0.26	**-0.17 / 2.13**	**+2.300**
V	0.05 CH_4 0.95 SiO_2	2.5184	35.98	-0.17 / -0.20	0.69 / 1.27	**1.63 / 3.39**	**-1.76**

Table 3.3: Comparison of SS detector density simulations obtained with the rapid approximation and MCNP. Results include light mudcake of density 1.00 g/cm^3 and heavy mudcake of density 2.74 g/cm^3. Refer to **Table 3.2** for additional details about the chemical composition of layers.

Layer	Formation density [g/cm^3]	Density MC = 0" - MCNP / Approx. [g/cm^3]	Density MC =0.5" *light* MCNP / Approx. [g/cm^3]	Density MC = 1" *light* MCNP / Approx. [g/cm^3]	Density MC =0.5" *heavy* MCNP / Approx. [g/cm^3]	Density MC = 1" *heavy* MCNP / Approx. [g/cm^3]	Maximum difference MCNP – Approx. [g/cm^3]
I	2.6655	**2.7378 / 2.6655**	2.0082 / 2.0077	1.4725 / 1.4677	1.7321 / 1.7308	2.7512 / 2.7489	**+0.0723**
II	2.5675	2.5819 / 2.5675	1.9493 / 1.9483	1.4272 / 1.4386	2.6520 / 2.6662	**2.6633 / 2.7284**	**-0.0651**
III	2.1550	2.1408 / 2.1550	1.6905 / 1.6985	1.3059 / 1.3154	2.4039 / 2.3960	**2.6201 / 2.6521**	**-0.032**
IV	1.8603	1.8486 / 1.8603	1.5202 / 1.5200	1.2332 / 1.2267	2.2024 / 2.2060	**2.5876 / 2.6149**	**-0.0273**
V	2.5184	2.4889 / 2.5184	1.9089 / 1.9186	1.4492 / 1.4240	2.6056 / 2.6338	**2.6858 / 2.7184**	**-0.0326**

Table 3.4: Comparison of LS detector density simulations obtained with the rapid approximation and MCNP. Results include light mudcake of density 1.00 g/cm^3 and heavy mudcake of density 2.74 g/cm^3. Refer to **Table 3.2** for additional details about the chemical composition of layers.

Layer	Formation density [g/cm^3]	Density MC =0" - MCNP / Approx. [g/cm^3]	Density MC =0.5" *light* MCNP / Approx. [g/cm^3]	Density MC = 1" *light* MCNP / Approx. [g/cm^3]	Density MC =0.5" *heavy* MCNP / Approx. [g/cm^3]	Density MC = 1" *heavy* MCNP / Approx. [g/cm^3]	Maximum difference MCNP – Approx. [g/cm^3]
I	2.6655	**2.6864 / 2.6654**	2.3581 / 2.3591	2.0619 / 2.0649	2.7012 / 2.7019	2.7160 / 2.7151	**0.021**
II	2.5675	2.5718 / 2.5674	2.2771 / 2.2788	2.0112 / 2.0073	2.6036 / 2.6069	**2.6018 / 2.6345**	**-0.0327**
III	2.1550	2.1526 / 2.1549	**1.9731 / 1.9409**	1.7895 / 1.7649	2.2308 / 2.2065	2.3191 / 2.2966	**+0.0322**
IV	1.8603	**1.8137 / 1.8602**	1.6988 / 1.6997	1.5881 / 1.5949	1.9217 / 1.9198	2.0491 / 2.0570	**-0.0465**
V	2.5184	2.5096 / 2.5183	2.2363 / 2.2386	1.9793 / 1.9784	**2.5462 / 2.5593**	2.5857 / 2.5942	**-0.0131**

Table 3.5: Comparison of compensated density simulations obtained with the rapid approximation and MCNP results. Results include light mudcake of density 1.00 g/cm^3 and heavy mudcake of density 2.74 g/cm^3. Refer to **Table 3.2** for additional details about the chemical composition of layers.

Layer	Formation density [g/cm^3]	Density MC = 0" - MCNP / Approx. [g/cm^3]	Density MC =0.5" *light* MCNP / Approx. [g/cm^3]	Density MC = 1" *light* MCNP / Approx. [g/cm^3]	Density MC =0.5" *heavy* MCNP / Approx. [g/cm^3]	Density MC = 1" *heavy* MCNP / Approx. [g/cm^3]	Maximum difference MCNP – Approx. [g/cm^3]
I	2.6655	**2.6530 / 2.6660**	2.5722 / 2.5753	2.5580 / 2.5670	2.6813 / 2.6834	2.6932 / 2.6932	**-0.013**
II	2.5675	2.5657 / 2.5686	2.4636 / 2.4686	**2.5025 / 2.4846**	2.5711 / 2.5683	2.5618 / 2.5735	**+0.0179**
III	2.1550	2.1471 / 2.1555	**2.1055 / 2.0296**	2.1740 / 2.1072	2.1199 / 2.0856	2.1323 / 2.0786	**+0.0759**
IV	1.8603	**1.7912 / 1.8608**	1.7304 / 1.7321	1.8087 / 1.8257	1.7466 / 1.7415	1.7355 / 1.7389	**-0.0696**
V	2.5184	2.5008 / 2.5189	2.4223 / 2.4154	**2.4172 / 2.4418**	2.5076 / 2.5108	2.5207 / 2.5138	**-0.0246**

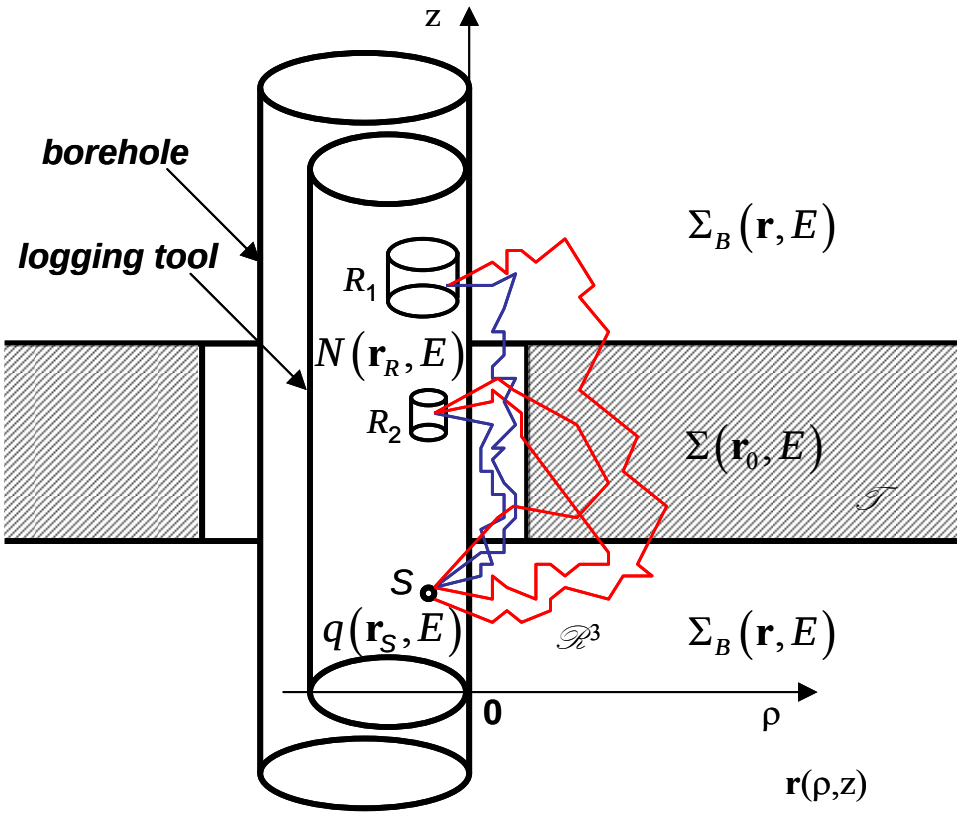

Figure 3.1: Schematic diagram of the geometrical components of the nuclear logging tool, the borehole, and the formation model assumed in the general formulation. We assume neutron and density tool models consisting of a short-spaced (near) and a long-spaced (far) detector at locations R_2 and R_1, respectively, and a radioactive source located at S. The response at each detector (count rate) is given by $N(\mathbf{r}_R,E)$ whereas the point source at S is described by $q(\mathbf{r}_S,E)$. Blue lines describe the path of particles that solely interact with the assumed fixed medium, $\mathscr{R}^3$, of energy-dependent cross-section $\Sigma_B(\mathbf{r},E)$. Red lines describe the path of particles that interact with both the assumed fixed medium and the scatterer region, $\mathscr{T}$, energy-dependent cross-section $\Sigma(\mathbf{r}_0,E)$.

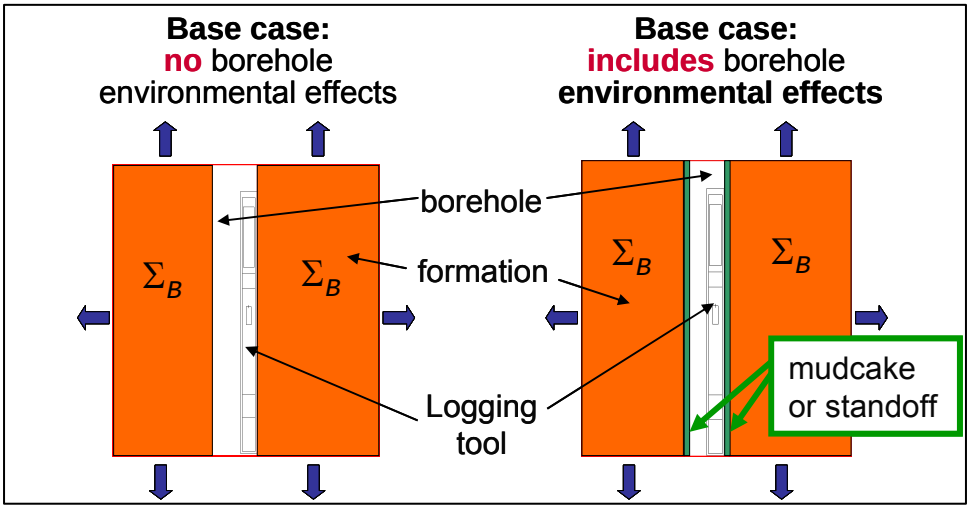

Figure 3.2: Graphical description of the base-case formation assumed in the calculation of flux sensitivity functions (FSFs). The linear iterative refinement technique used for the rapid simulation of borehole measurements includes a library of FSFs pre-computed in homogeneous formations (that include both borehole and tool) of spatially constant energy-dependent cross-section, Σ_B (shown on the left). In addition, in the presence of key borehole environmental effects, the FSFs include mudcake or tool standoff (shown on the right). In both situations, the formation is assumed infinite in the directions away from the borehole and the tool location.

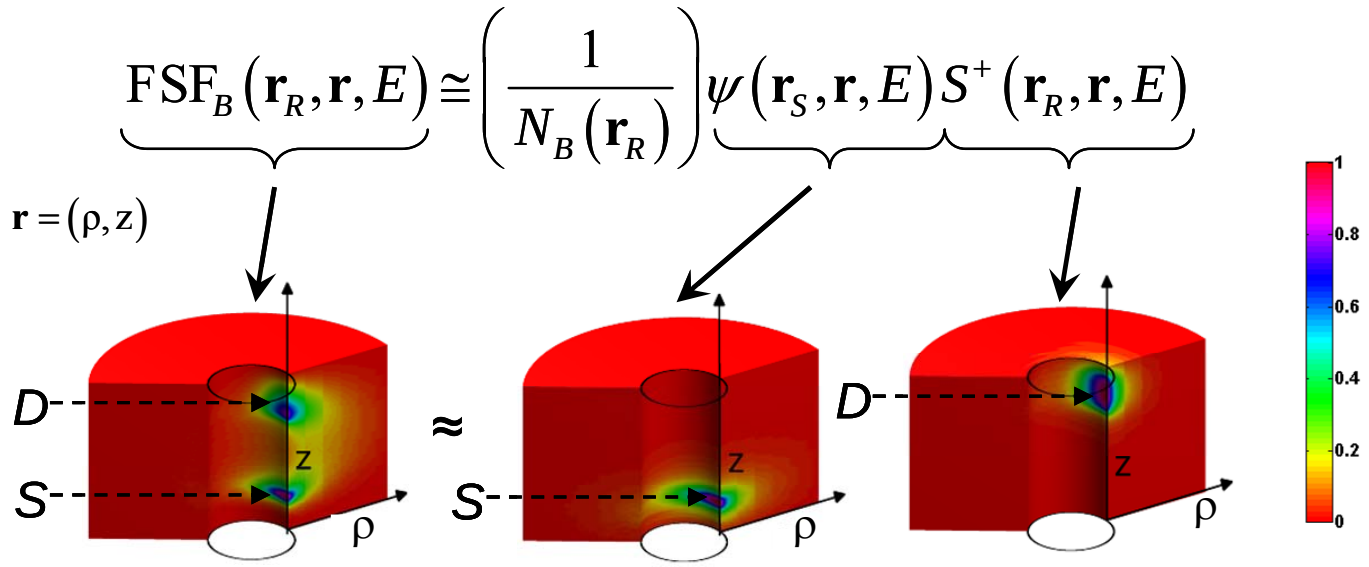

Figure 3.3: Description of the calculation of flux sensitivity function (FSF_B) for a given base-case formation and for the far detector of a neutron tool. The center figure shows a 3D quantitative representation of the neutron flux spatially distributed and centered about the source. The right figure is a similar description of the corresponding detector response function centered at the vicinity of the detector. The figure on the left shows the resulting 3D geometrical FSF. Each of the figures described above is normalized with respect to its maximum value. Colors describe spatial sensitivity of each function. Refer to Figure 1 for additional details about source-sensor model conventions, and **Table 3.1** for descriptions of base-case formations.

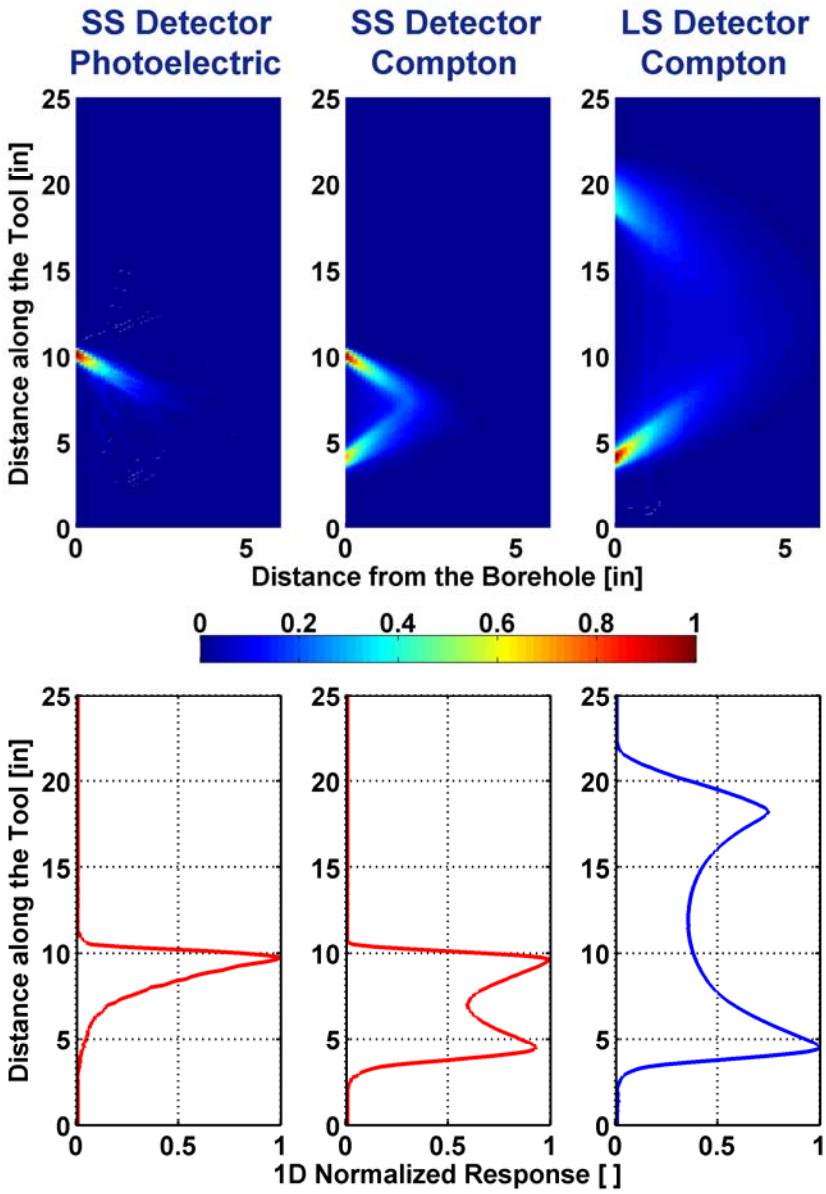

Figure 3.4: Flux sensitivity functions of PEF and density (Compton scattering) for the short- (SS) and long-spaced (LS) detectors of a density tool in a base-case formation. Top-left panels show 2D plots for the SS detector, and bottom-left panels show the corresponding 1D plots along the axis of the borehole integrated in the radial direction. Top- and bottom-right panels, respectively, show similar plots for the LS detector. Functions are normalized with respect to corresponding maximum values. Colors in 2D plots describe spatial sensitivity of PEF and density measurements where maximum sensitivity equals 1. Refer to **Figure 3.1** for additional details about source-sensor conventions and **Table 3.1** for details about base-case formations. Simulations assume an 8-in borehole diameter.

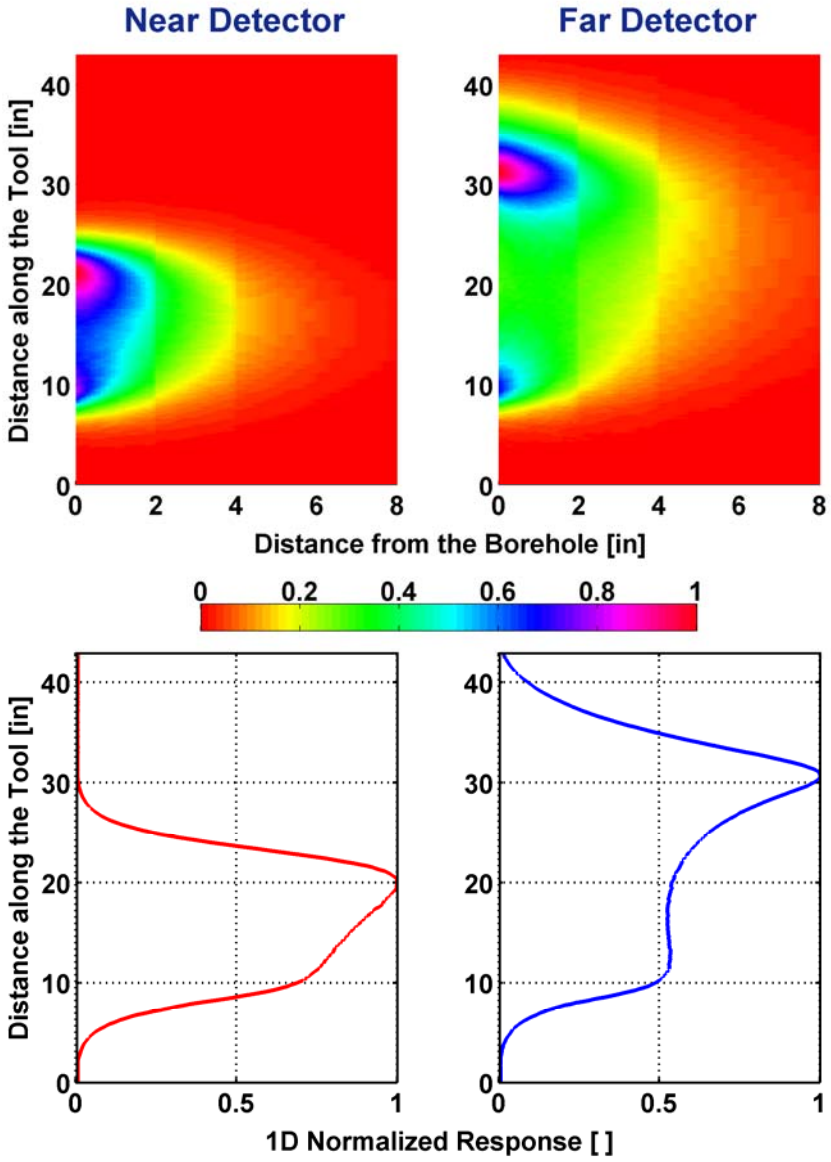

Figure 3.5: Flux sensitivity functions corresponding to neutron measurements acquired with near and far detectors. Top panels show 2D plots for the FSF, and bottom panels show the corresponding 1D plots along the axis of the borehole, integrated in the radial direction. Functions are normalized with respect to corresponding maximum values. Colors in 2D plots describe spatial sensitivity of neutron measurements where maximum sensitivity equals 1. Refer to **Figure 3.1** for additional details about source-sensor conventions and **Table 3.1** for details about base-case formations. Simulations assume an 8-in borehole diameter.

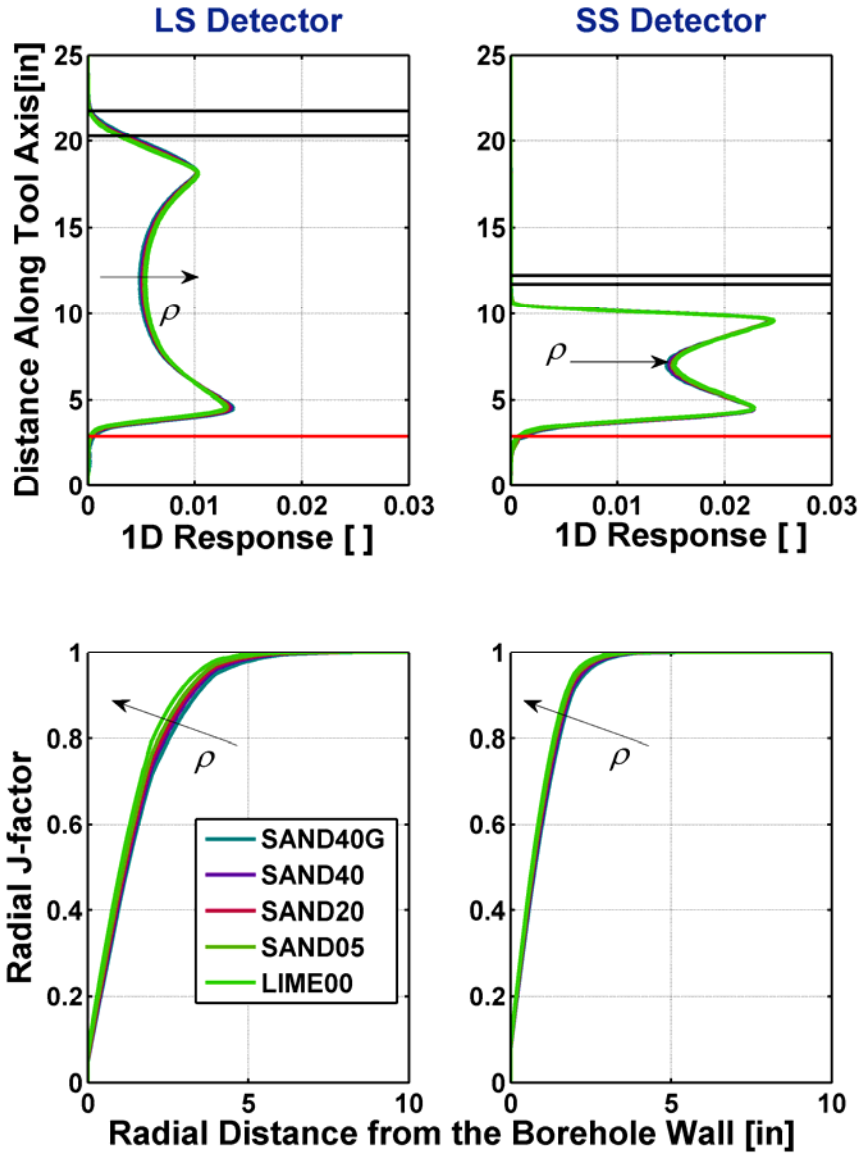

Figure 3.6: Spatial sensitivity of the density geometrical response to formation mass density for the SS and LS detectors. Top panels describe 1D FSFs (integrated in the radial direction) of the SS and LS detectors of a density tool. Bottom panels are similar 1D plots of the radial J-factors of the FSF. Colored curves describe geometric factors for several homogeneous formations with a wide range of mass density values. The horizontal red line identifies the approximate location of the radioactive source, and horizontal black lines indicate the detector position. Refer to **Figure 3.1** and **Table 3.1** for additional details about source-sensor conventions and formation properties. Simulations assume an 8-in borehole diameter.

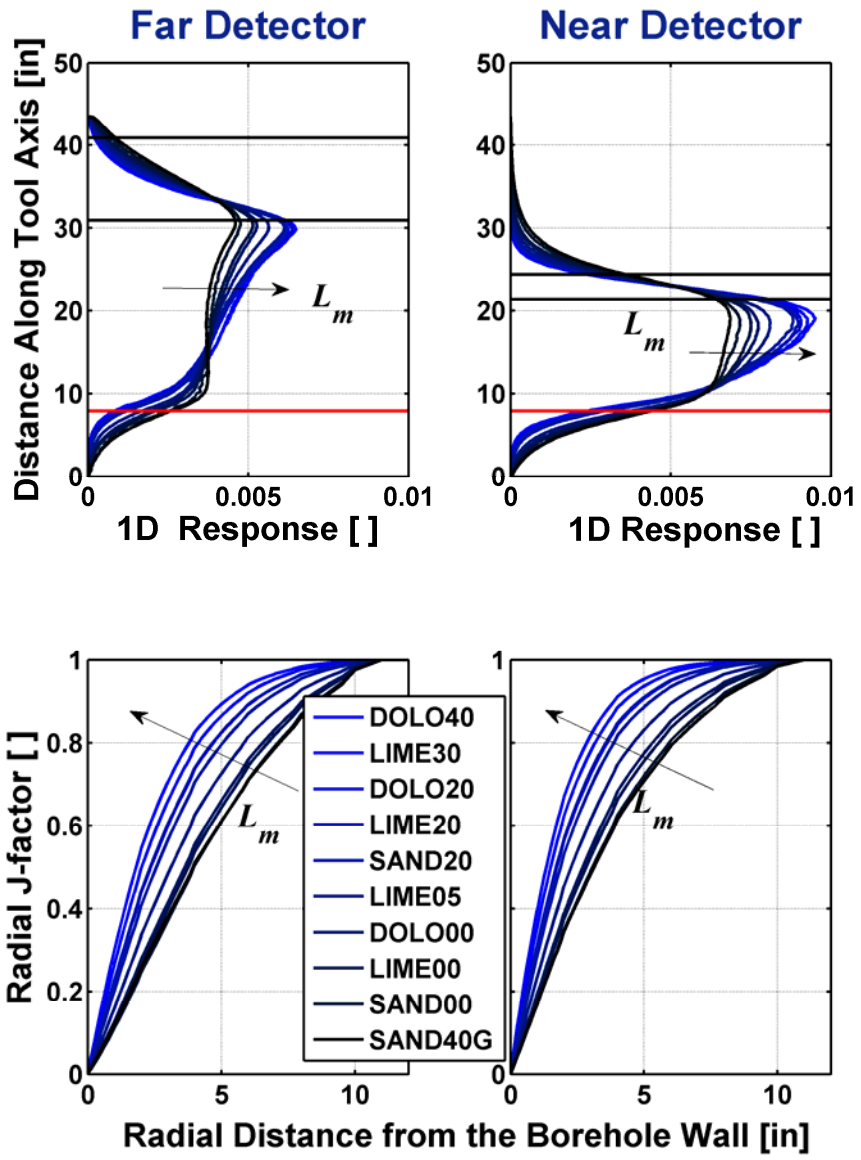

Figure 3.7: Spatial sensitivity of the neutron geometrical response to formation migration length for near- and far-detectors. Top panels describe 1D FSFs (integrated in the radial direction) of the near and far detectors of a neutron tool. Bottom panels are similar 1D plots of the radial J-factors of the geometrical response. Colored curves describe FSFs for several base-case formations with a wide range of migration length values. The horizontal red line identifies the approximate location of the radioactive source, and horizontal black lines indicate the detector position. Refer to **Figure 3.1** and **Table 3.1** for additional details about source-sensor conventions and formation properties (labels). Simulations assume an 8-in borehole diameter.

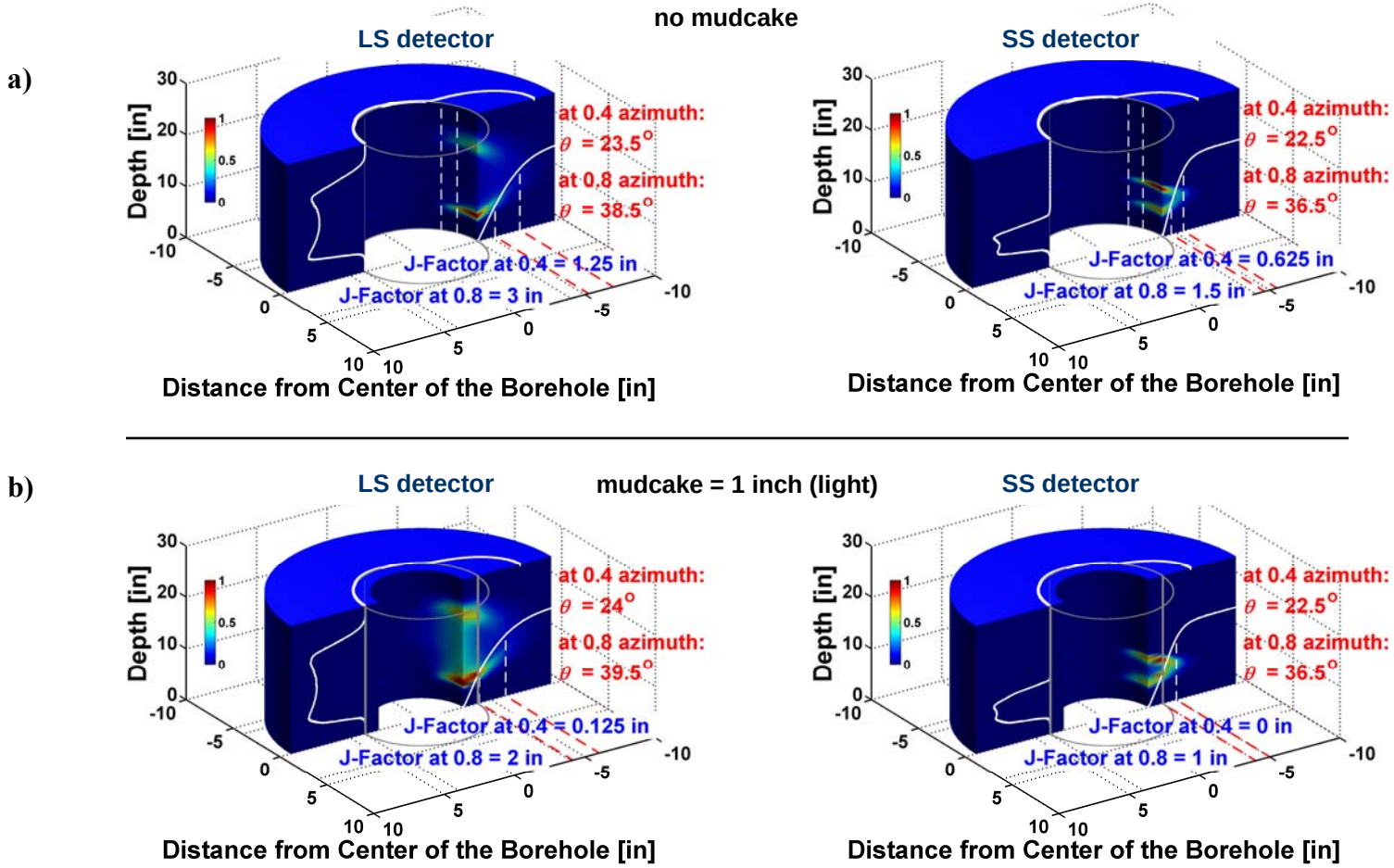

Figure 3.8: Flux sensitivity functions of the LS and SS detectors of a density logging tool. Solid white lines represent the 1D projection of the geometrical factors in the radial (J-factor), vertical, and azimuthal directions. Panel **(a)** shows the density response functions for the case of no tool standoff in a 20% porosity water-filled limestone formation. Panel **(b)** shows the case of an 8-inch borehole with 1-inch of tool standoff (mudcake of density 1 g/cm^3) in the same formation. Tool standoff effects cause discrepancies in the J-factors while the azimuthal and vertical geometric factors remain nearly invariant. Functions are normalized with respect to corresponding maximum values. Colors in plots describe 3D spatial sensitivity of density measurements where maximum sensitivity equals 1.

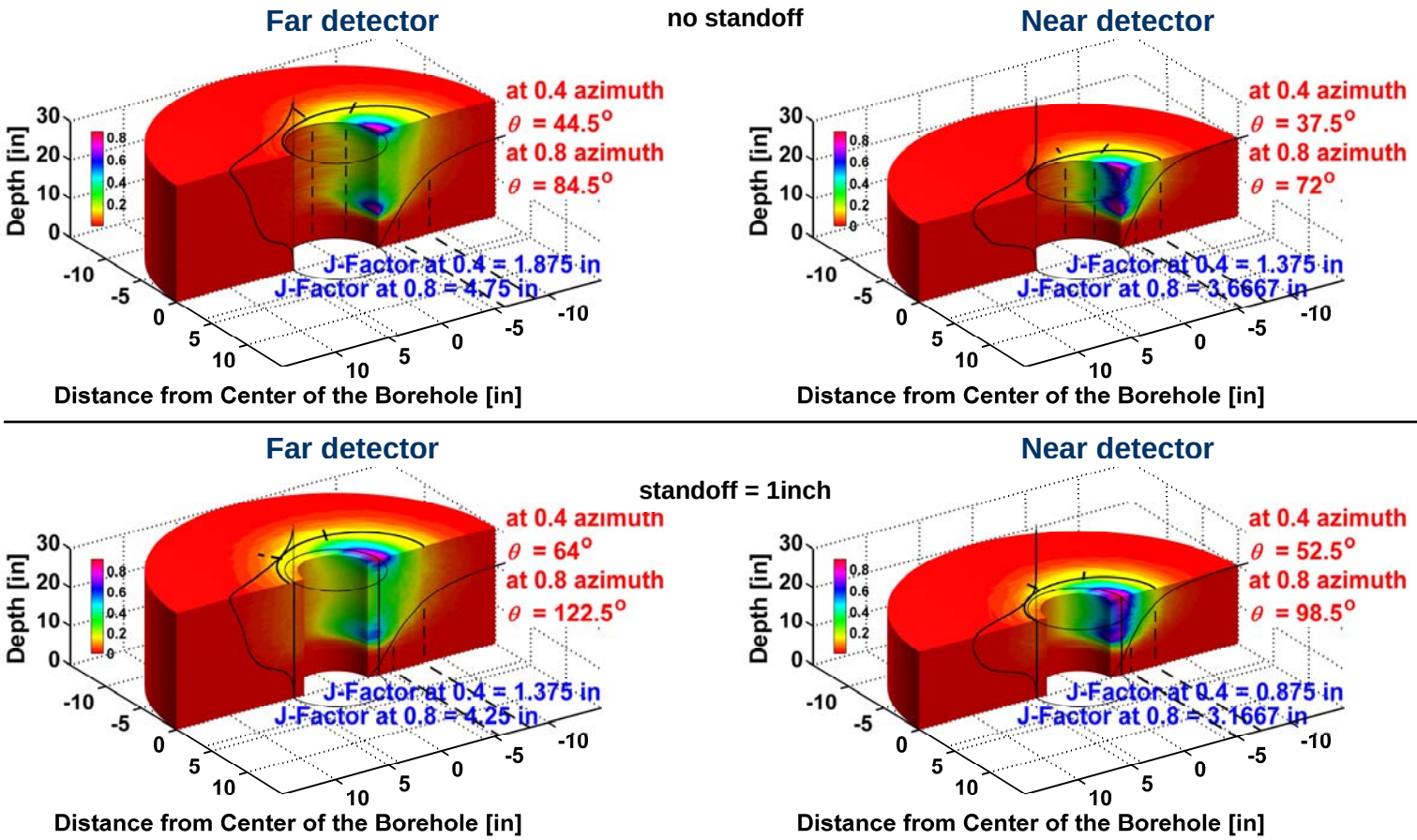

Figure 3.9: Flux sensitivity functions of the far and near detectors of the assumed neutron logging tool model. Solid black lines represent the 1D projection of the geometrical factors in the radial (J-factor), vertical, and azimuthal directions. Panel **(a)** shows the neutron response functions for the case of no tool standoff for fresh water mud in a 20% porosity water-filled limestone formation. Panel **(b)** shows the case of an 8-inch borehole with 1-inch of tool standoff in the same formation. Standoff effects cause large discrepancies in both the J-factor and the azimuthal geometric factor. Functions are normalized with respect to corresponding maximum values. Colors in plots describe 3D spatial sensitivity of density measurements where maximum sensitivity equals 1.

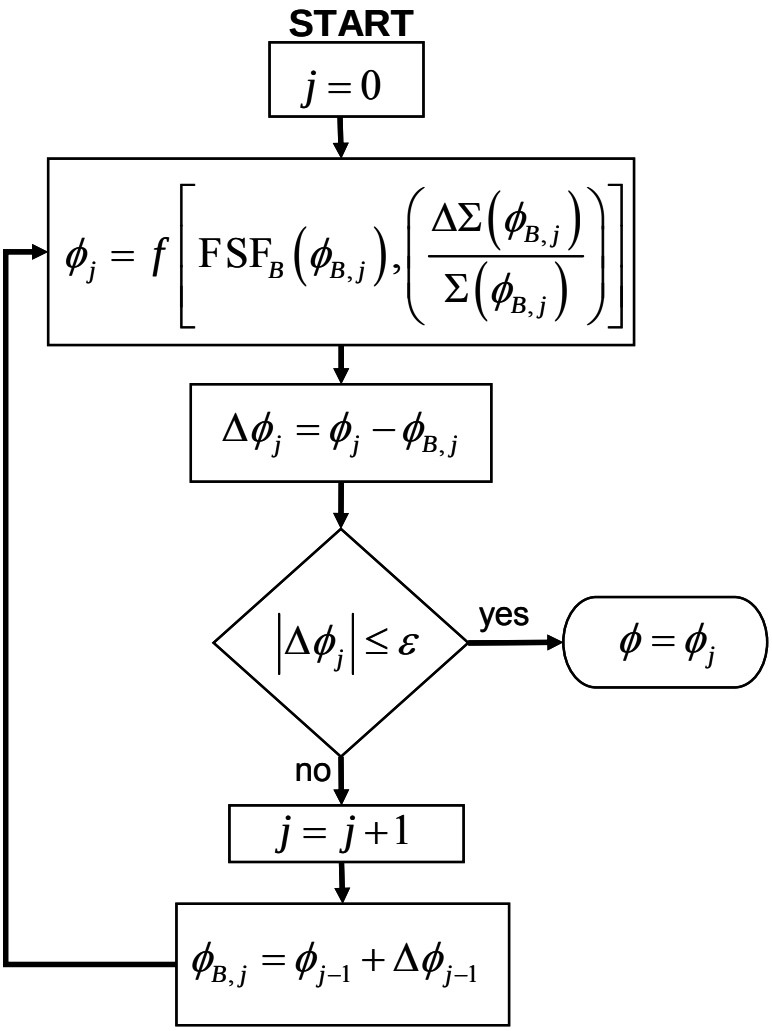

Figure 3.10: Flow chart of the linear iterative refinement procedure used to approximate nuclear borehole measurements. The figure shows the steps included in the iterative procedure at one depth sample point (fixed-point iteration). The simulated porosity is labeled ϕ_j, where j is iteration number. Subscript B denotes the selected reference base-case formation porosity, FSF is the flux sensitivity function (which depends on the porosity value), and the cross-section Σ represents a perturbed formation property of the formation. The symbol ε describes a pre-specified threshold used to assess convergence.

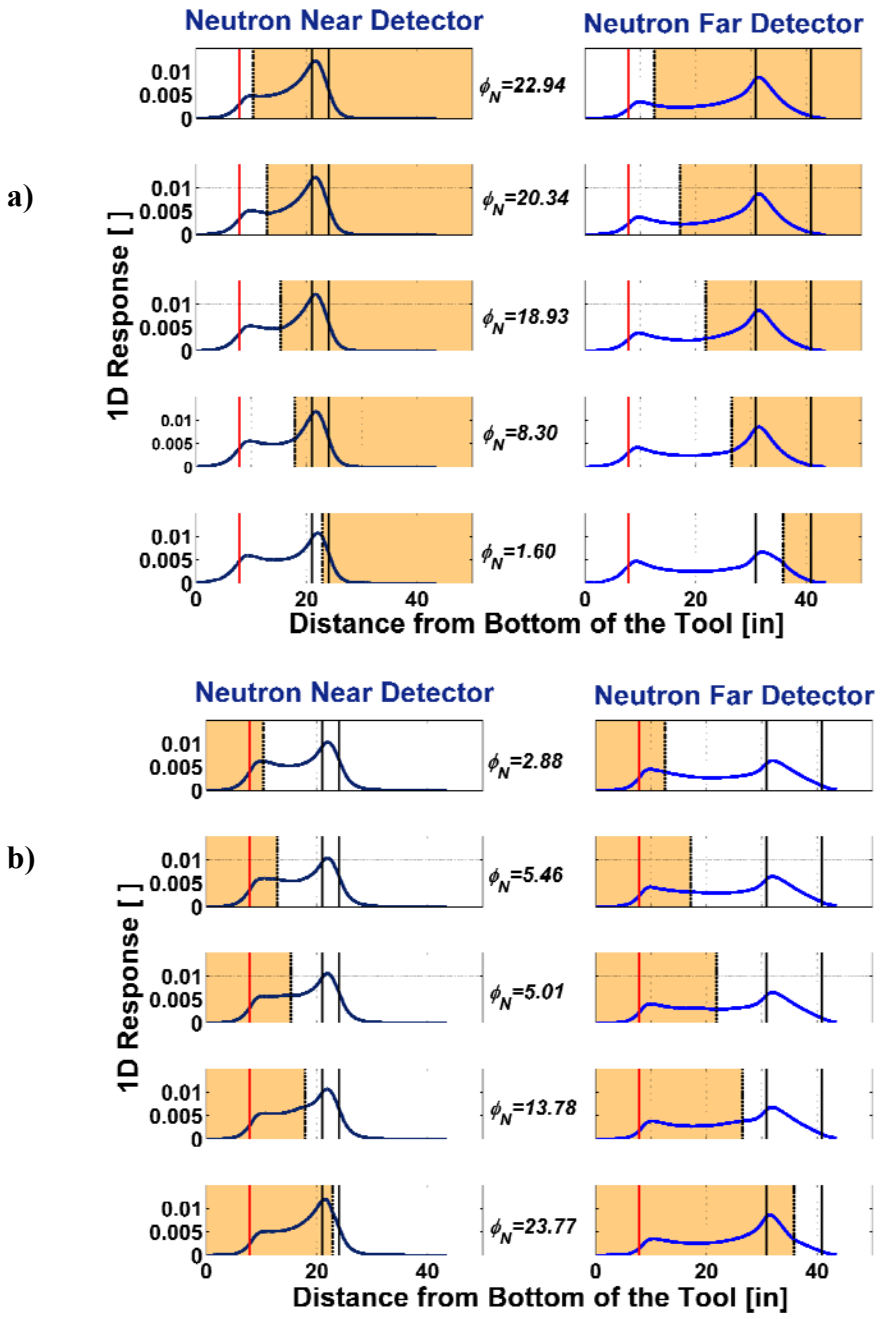

Figure 3.11: Comparison of simulated neutron measurements (1D axial neutron FSF) across the boundary between two water-saturated sandstone formations. Colored blocks represent 25% porosity, and white blocks indicate 2% porosity. The vertical red line describes the approximate location of the radioactive source, whereas vertical black lines indicate the position of the detector. Neutron porosity values, in the center of panels **(a)** and **(b)**, correspond to the near-to-far detector ratio at source-detector positions with respect to the boundary identified in the left and right panels.

a)

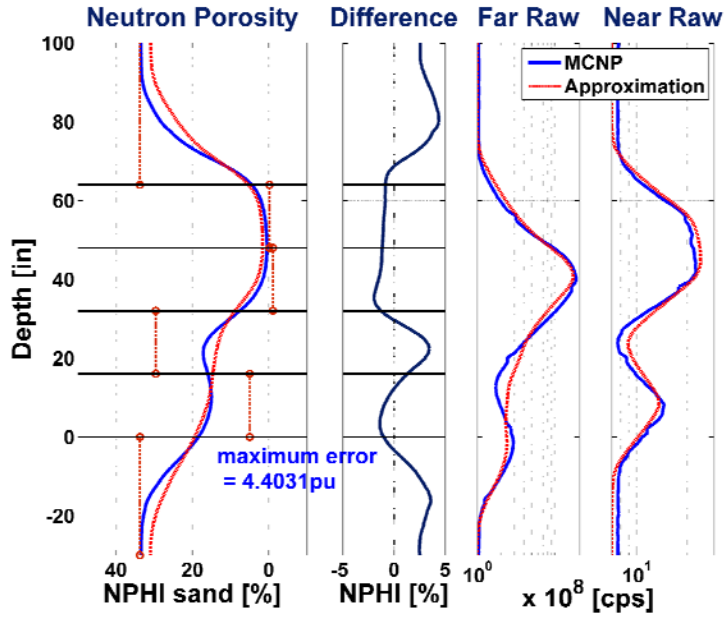

b)

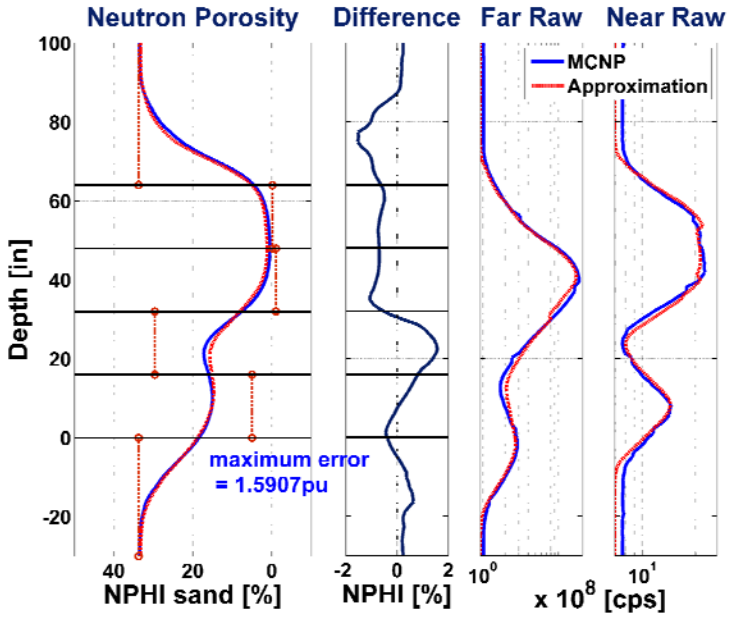

Figure 3.12: Comparison of the rapid approximation of neutron borehole measurements against Monte Carlo (MCNP) simulations with 1D vertical perturbations (shoulder-bed effects), **(a)** without the implementation of iterative refinement, and **(b)** with the use of iterative refinement. Solid blue curves describe MCNP simulations while red curves describe rapid approximation results. Right panels show the near- and far-detector count rates, whereas the left panel shows the resulting neutron porosity calculated from the detector ratio. The dark blue curve in the center panel shows the neutron porosity difference between MCNP simulations and the rapid approximation. Refer to **Table 3.2** for a description of the assumed layer properties.

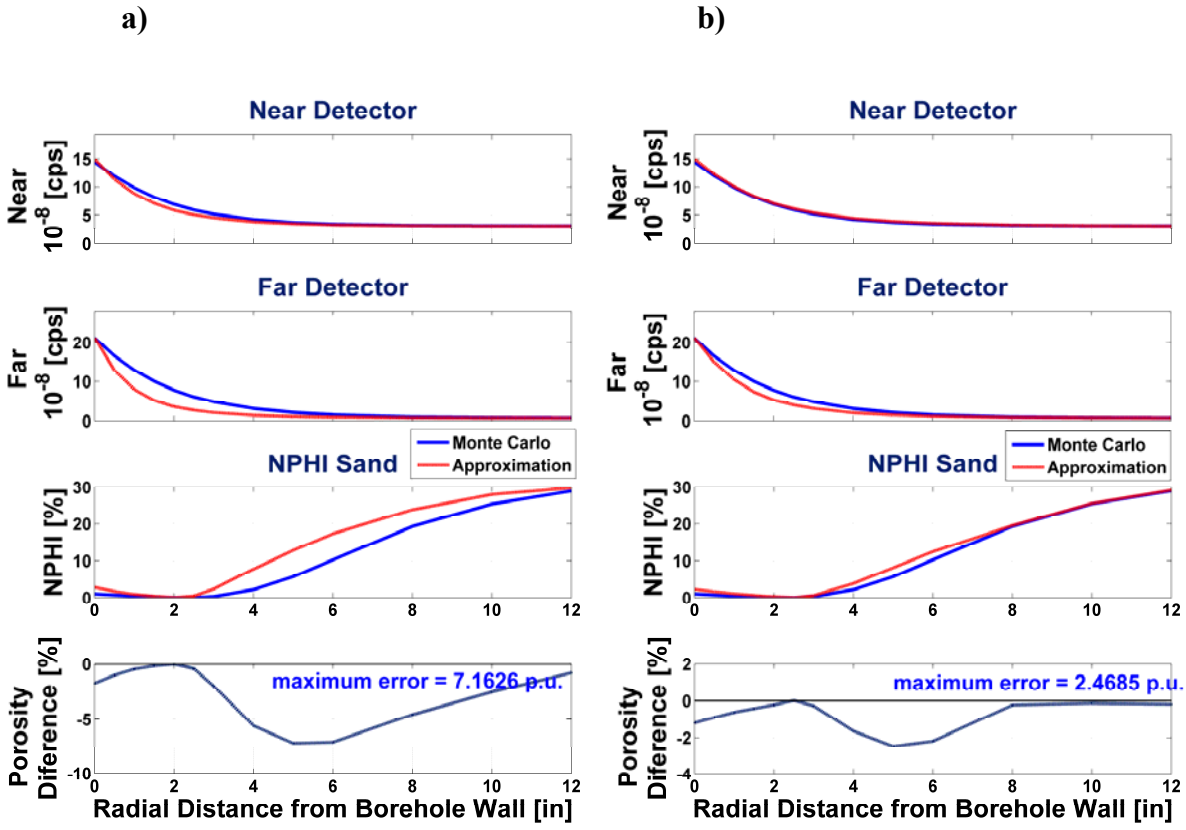

Figure 3.13: Comparison of the rapid approximation of neutron measurements against Monte Carlo (MCNP) simulations with 1D radial perturbations (piston-like invasion), **(a)** without the implementation of iterative refinement, and **(b)** with the use of iterative refinement**.** Solid blue curves describe MCNP simulations whereas red curves describe rapid approximation results. Top panels show the near- and far-detector count rates. Bottom panels show the neutron porosity calculated from the detector ratio. The dark blue curves show the neutron porosity difference between MCNP and rapid approximation simulations. The horizontal axis describes radial distance from the borehole wall to a front of water invading a gas-saturated 30% porosity sandstone. Simulations assume that invading water displaces 100% of the gas in place (zero residual gas saturation). Refer to **Table 3.1** for details about the formation properties.

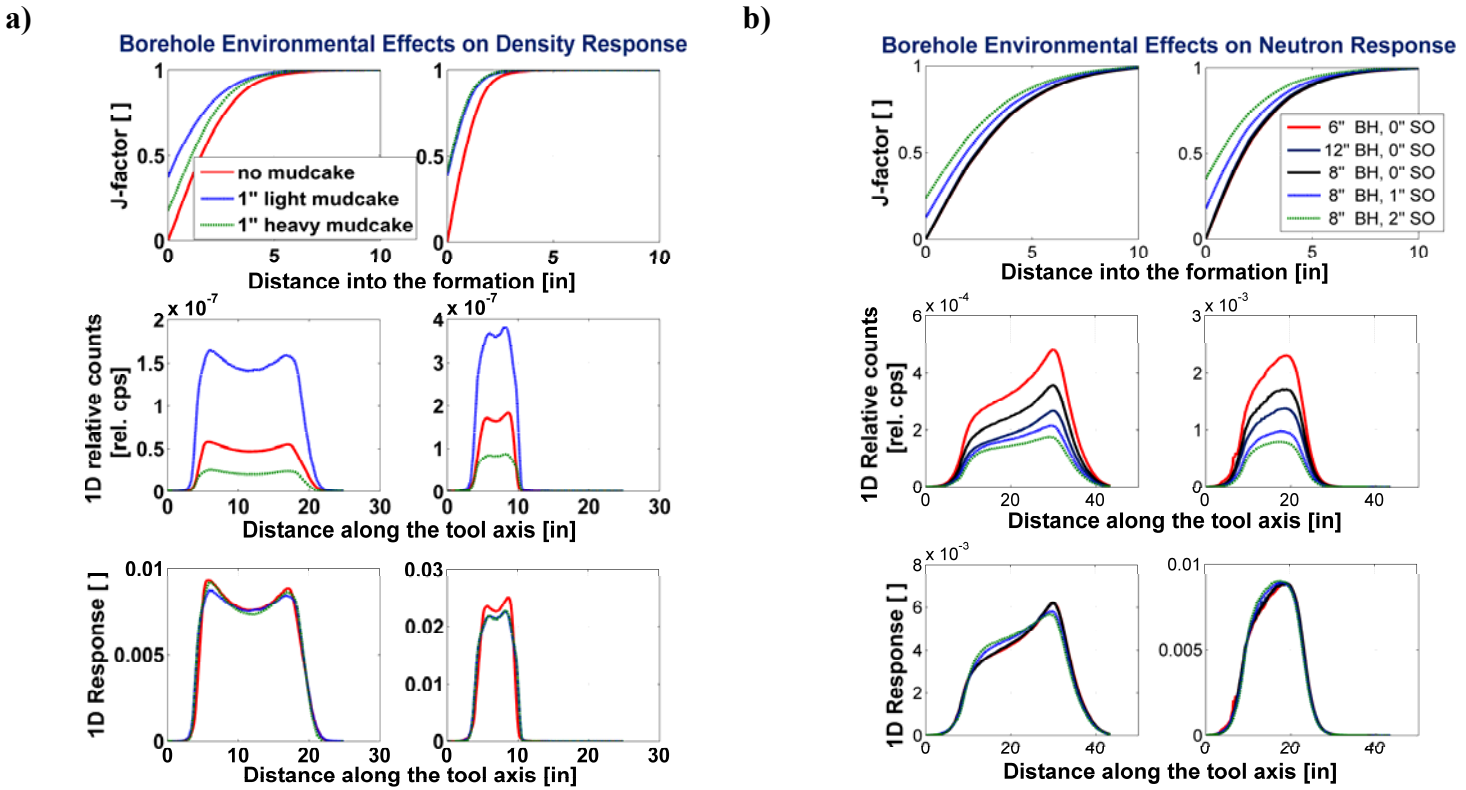

Figure 3.14: **(a)** Comparison of radial and vertical geometric factors of the LS (left panels) and SS detector (right panels) of the assumed density logging tool in the presence of no mudcake, 1-inch light (1 g/cm^3) mudcake, and 1-inch heavy (2.74 g/cm^3) mudcake. Top panels show significant variations in the J-factors that depend on the density contrast between mudcake and formation (20% porosity limestone, 2.37 g/cm^3). **(b)** Comparison of the radial and vertical geometric factors of the near- (right panels) and far-detector (left panels) of a neutron logging tool. Top panels show significant variations in the presence of tool standoff and different borehole size. For both neutron and density, center and bottom panels show that, although the magnitude of the count rate is significantly different, the shape of the vertical geometric factors remains nearly constant under these conditions of borehole environmental effects. Refer to **Table 3.1** for details about the formation properties.

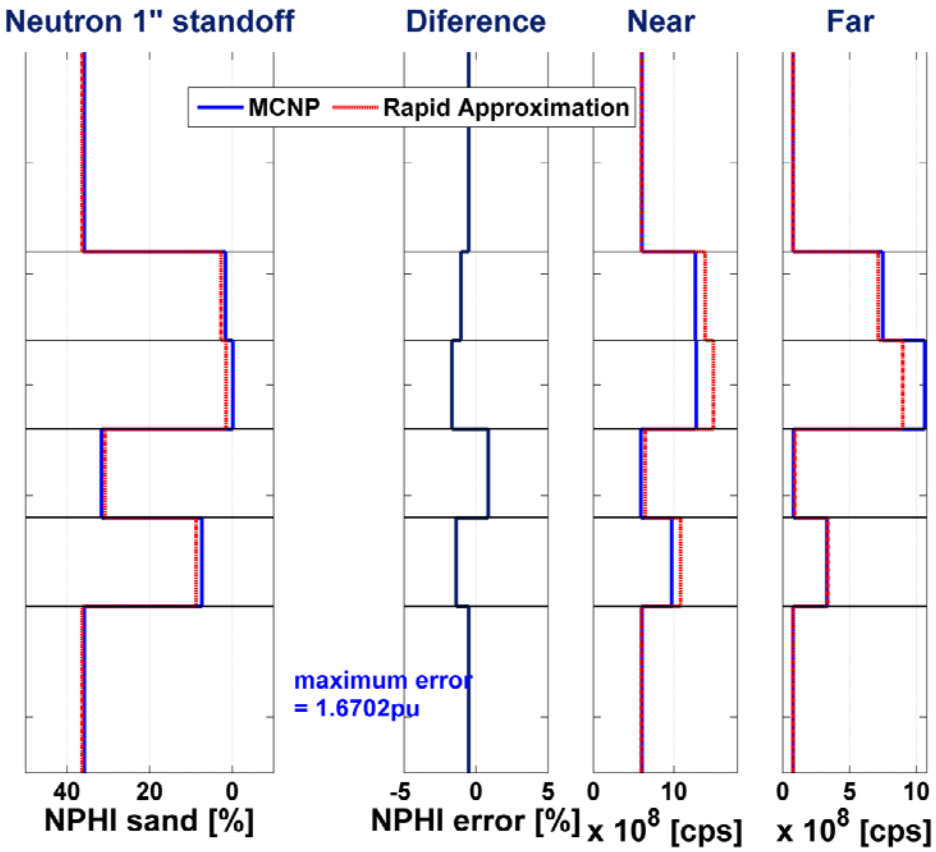

Figure 3.15: Comparison of the rapid approximation of neutron measurements against Monte Carlo (MCNP) simulations with a 1D radial perturbation (1-inch standoff). Piecewise-constant plots describe results corresponding to layers of infinite thickness. From bottom to top, properties of each case are as follows: shale density=2.67 g/cm^3, 5% porosity water-saturated sand density=2.57 g/cm^3, 30% porosity water-saturated sand density=2.16 g/cm^3, 30% porosity gas-saturated sand density=1.86 g/cm^3, 5% porosity gas-saturated sand density=2.52 g/cm^3. Refer to **Table 3.2** for a description of formation properties for each case.

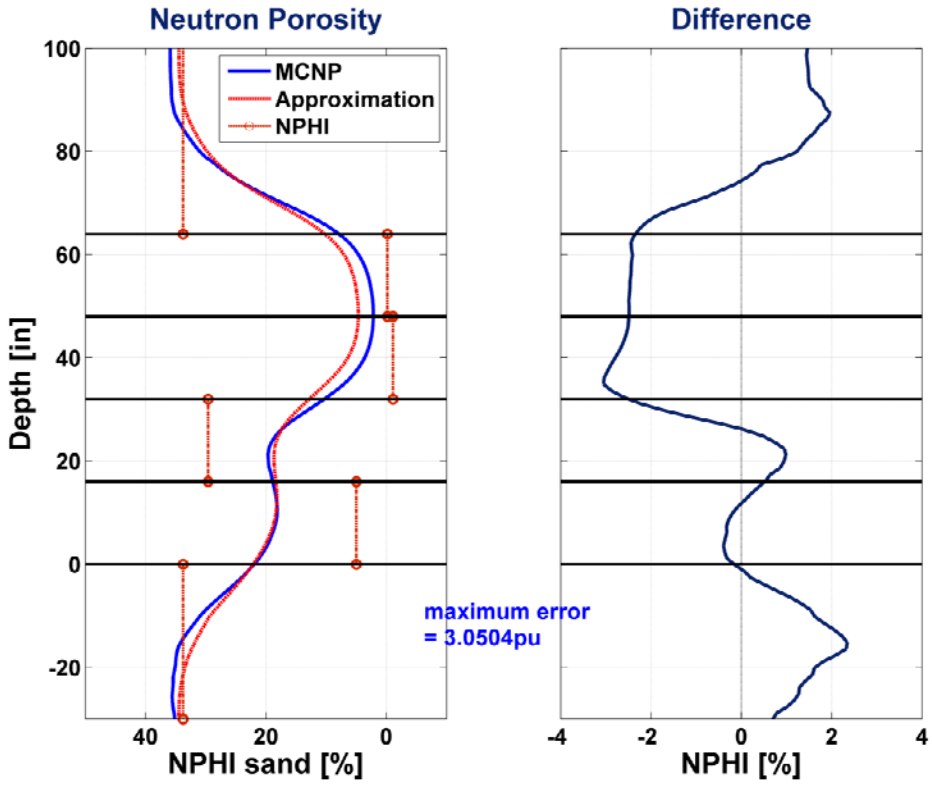

Figure 3.16: Comparison of rapid approximations of neutron measurements against Monte Carlo (MCNP) simulations with 2D radial and vertical perturbations (1-inch tool standoff and shoulder-bed effects). Solid blue and red curves identify MCNP simulations and rapid approximation results, respectively. The right panel shows the neutron porosity difference between MCNP simulations and rapid approximations. Refer to **Table 3.2** and **Figure 3.15** for a description of the properties of each layer.

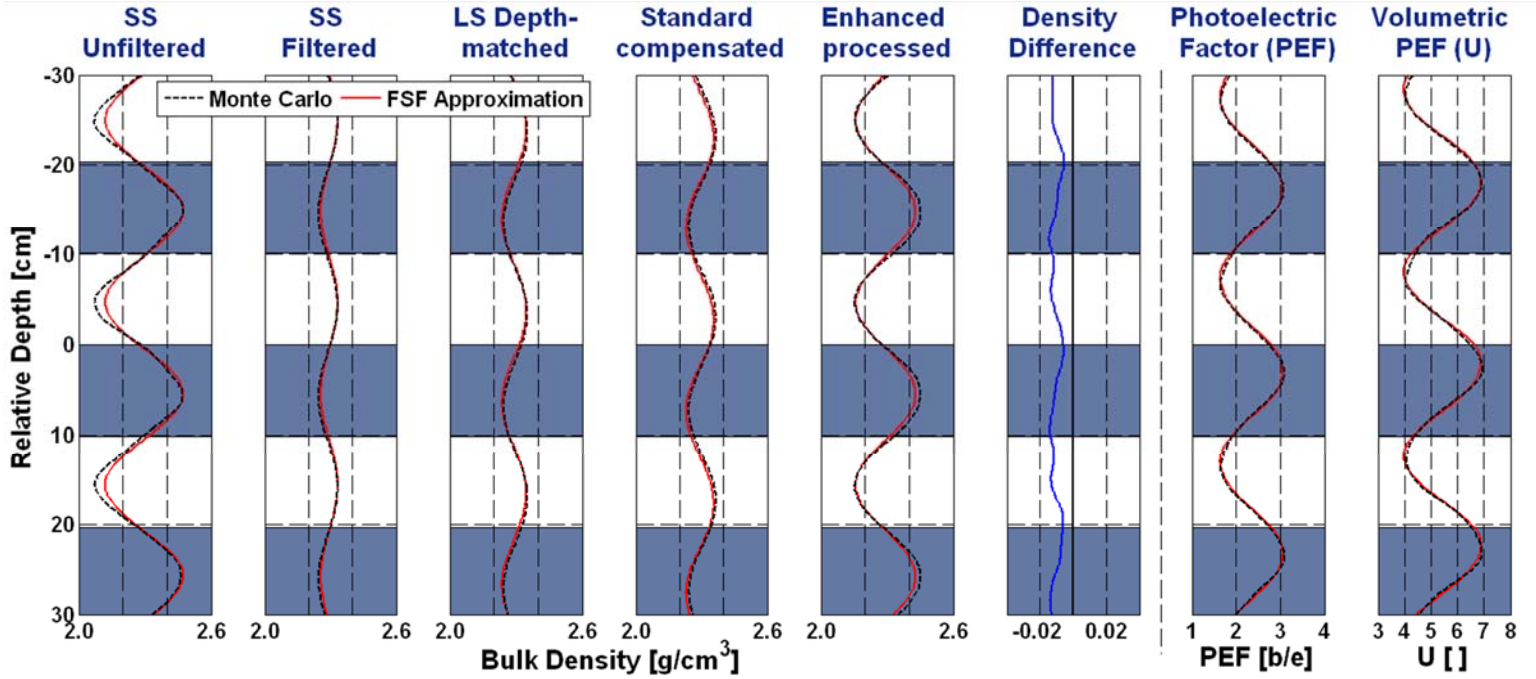

Figure 3.17: Comparison of Monte Carlo (MCNP) simulations and rapid approximation results of density measurements across periodic 4-inch layers of mass densities equal to 2.0 g/cm^3 and 2.6 g/cm^3. Solid red and dashed black curves identify rapid approximations and MCNP simulations, respectively. Left-hand panels describe simulations of raw single-detector measurements and standard compensated density. The solid blue line describes the difference in compensated density between rapid approximations and MCNP simulations. Right-hand panels show the simulated photoelectric and volumetric photoelectric factors. Dark and white blocks identify the higher- and lower-density materials, respectively.

a)

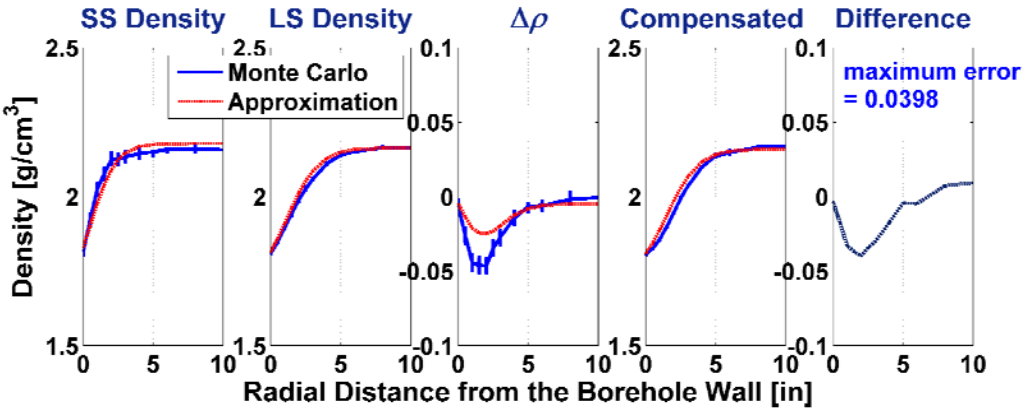

b)

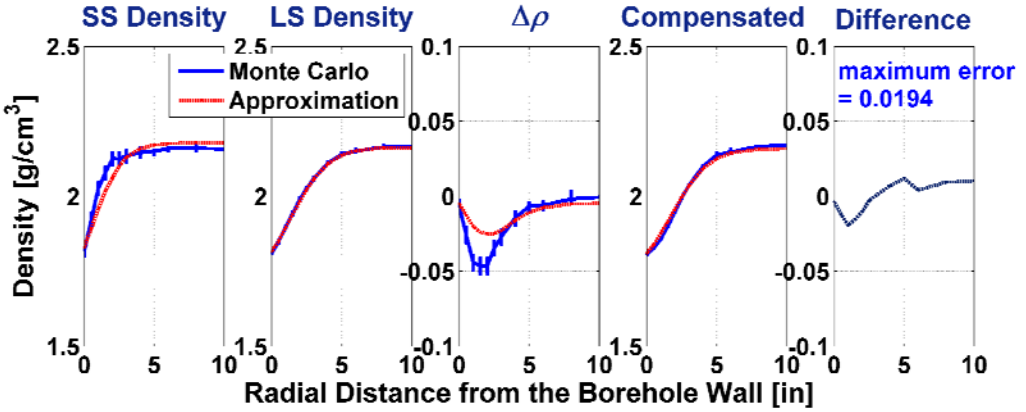

Figure 3.18: Comparison of Monte Carlo (MCNP) simulations and rapid approximation results of density measurements with 1D radial perturbations (piston-like invasion), **(a)** without the implementation of iterative refinement, and **(b)** with the use of iterative refinement**.** Solid blue and red curves identify MCNP simulations and rapid approximation results, respectively. Left panels show the SS and LS detector density. Right panels show the compensated density. Dark blue curves describe the compensated density difference between MCNP and rapid approximation simulations. The horizontal axis describes the radial distance from the borehole wall to the water saturation front invading a gas-saturated 30% porosity sandstone. Simulations assume that invading water displaces 100% of the gas in place (no residual gas saturation). Refer to **Table 3.1** for details about formation properties.

a)

b)

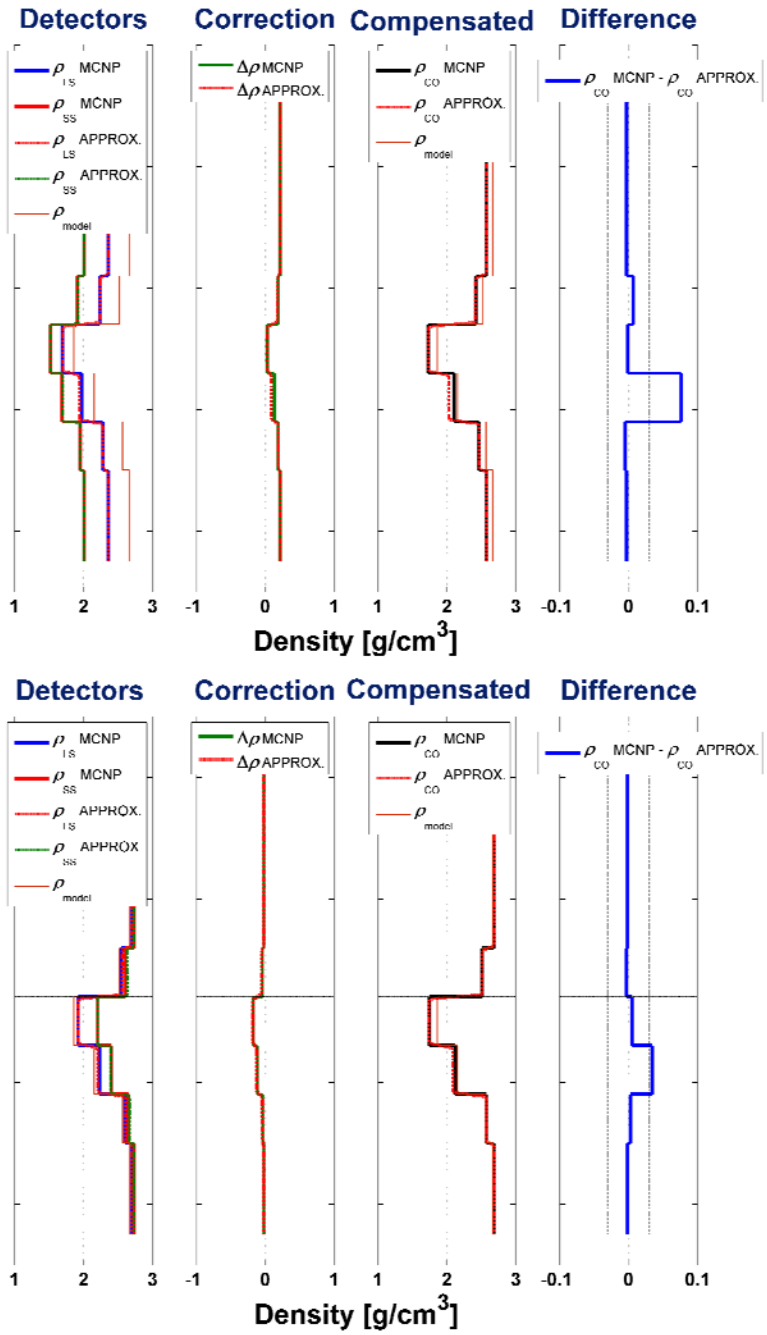

Figure 3.19: Comparison of Monte Carlo (MCNP) simulations and rapid approximation of (1D radial perturbation) density measurements against simulations with **(a)** 1-inch light mudcake, and **(b)** 1-inch heavy mudcake. From left to right, the first panel describes LS and SS density approximations in dashed lines and MCNP results in solid lines. The second and third panels describe $\Delta\rho$ and compensated density results, respectively. The fourth panel plots the difference between MCNP simulations and rapid approximations of compensated density in g/cm^3. Refer to **Table 3.2** and **Figure 3.15** for a description about assumed layer properties.

a)

b)

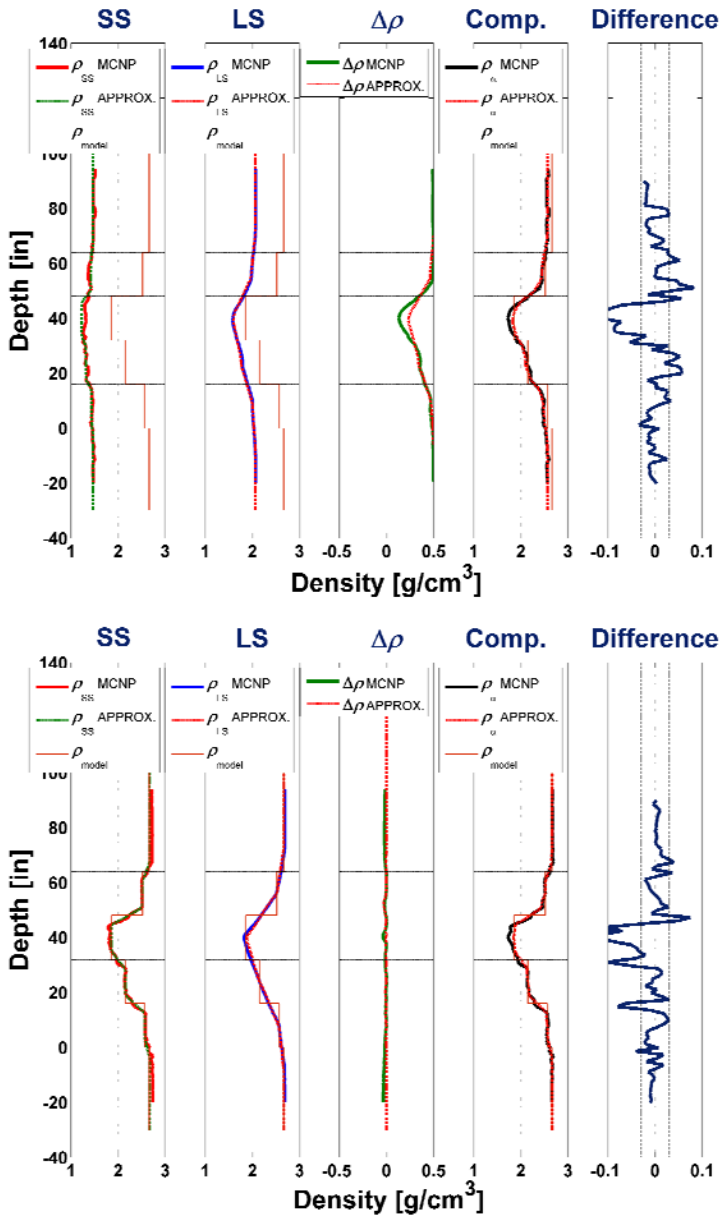

Figure 3.20: Comparison of Monte Carlo (MCNP) simulations and rapid approximation of (2D radial and vertical) density measurements and simulations with **(a)** 1-inch light mudcake, and **(b)** no mudcake in the presence of shoulder-bed effects. Panels describe simulations for 16-inch thick layers. Refer to **Table 3.2** and **Figure 3.15** for a description about layer properties. From left to right, the first panel describes SS density approximations and MCNP simulations in dashed and solid curves, respectively. The second panel shows LS density simulations, the third panel displays the $\Delta\rho$ results, and the forth panel describes compensated density results. The fifth panel describes differences between MCNP simulations and rapid approximations of compensated density in g/cm^3. The maximum error in porosity units (including the statistical uncertainty of MCNP simulations) is equal to 0.11.

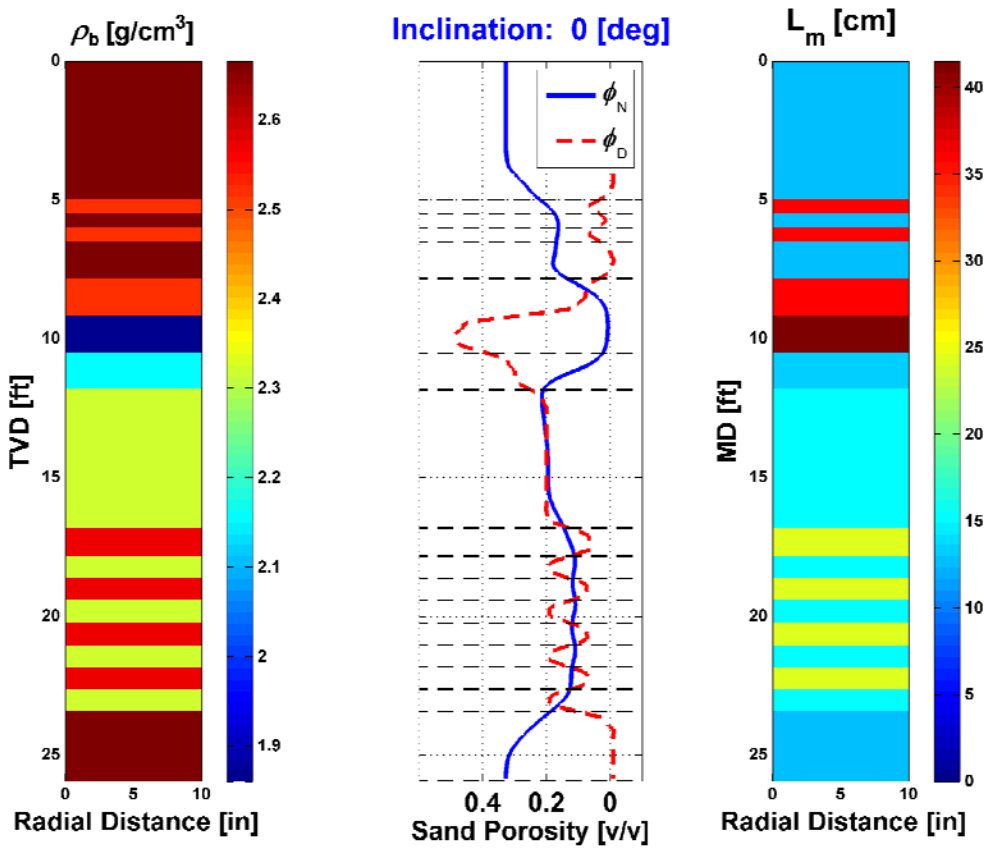

Figure 3.21: Neutron and density logs simulated with linear iterative refinement. Panels show, from left to right: the formation bulk density model in g/cm^3, the simulated neutron and density porosity logs across horizontal layers of different petrophysical properties, and the migration length (L_m) of the model used in the simulation of neutron measurements. A neutron-density gas crossover appears near the top where the model includes gas-saturated sands. The bottom section is a laminated sequence of alternating 20% and 5% porosity water-saturated beds. Differences in resolution between neutron and density measurements cause a small false gas effect (neutron-density cross-over) in the lower water zone.

Chapter 4: Linear Iterative Refinement Technique for the Rapid Simulation of Borehole Nuclear Measurements Acquired in High-Angle and Horizontal Wells

In vertical wells, the vertical resolution of nuclear logging tools determines the minimum stratigraphic thickness that can be resolved with a measurement. Presence of invasion and borehole environmental effects (i.e., mudcake or tool standoff) can have a substantial influence on the measurement depending on the radial length of investigation of the tool. By contrast, in high-angle and horizontal (HA/HZ) wells, because formation layering is not perpendicular to the borehole axis, both detection of bed boundaries and porosity estimation are influenced by vertical (axial) resolution, radial length of investigation, and azimuthal sensitivity of the measurements.

In the case of neutron measurements, petrophysical properties of the formation influence the resolution limits of the tool. Therefore, asymmetry of formation and fluid distributions around the perimeter of the borehole may perturb the spatial sensitivity of neutron measurements. This effect does not occur in density logs primarily because of their focused measurement design and the fact that, unlike neutrons, gamma rays do not exhibit significant preferential paths in formations with relatively low hydrogen index. Combined quantitative interpretation of neutron and density measurements in HA/HZ wells requires numerical simulation of formation and environmental effects.

The approximations described in Chapter 3 considered two-dimensional (2D) spatial properties of Monte Carlo-derived flux sensitivity functions (FSFs) to simulate

neutron and density measurements acquired across formations with horizontal layering. In this Chapter, we implement the linear iterative refinement technique incorporating the three-dimensional (3D) spatial properties of FSFs to approximate nuclear borehole measurements. The central objective is to validate the linear iterative refinement technique for the simulation of neutron and density measurements acquired in HA/HZ wells.

4.1 INTRODUCTION

Previously, we developed an iterative refinement procedure that approximates spatial variations of flux sensitivity functions (FSFs) due to contrasts of formation properties and key borehole environmental effects in vertical wells (Mendoza et al., 2009). In this chapter, we implement the linear iterative refinement technique for the rapid simulation of neutron and density measurements acquired in HA/HZ wells. The method incorporates the 3D (radial, vertical and azimuthal) spatial capabilities of FSFs in the approximation of nuclear measurements across horizontal layers penetrated by deviated wells. Comparison of the approximations against MCNP simulations validates the reliability and accuracy of the iterative refinement technique in HA/HZ wells.

Knowledge of the 3D spatial resolution limits of nuclear measurements is critical for the accurate interpretation of neutron and density porosity logs acquired in HA/HZ wells. We make use of the Monte Carlo code MCNP (X-5 Monte Carlo Team, 2003) to simulate 3D neutron and density FSFs for quantitative appraisal of the resolution limits and spatial variations of nuclear measurements acquired in HA/HZ wells.

Numerical simulations indicate that neutron and density measurements can be biased in deviated wells because of the influence of adjacent layers of large contrasts of petrophysical properties. Ellis and Chiaramonte (2000) indicated that the difference in depth of investigation between compensated neutron and density measurements may lead to abnormal responses such as a false apparent-gas effect (cross-over between neutron and density logs) in the proximity of a thin bed of high hydrogen index. Furthermore, Monte Carlo simulations of density measurements acquired in HA/HZ wells emphasize the differences between single-detector and compensated density measurements in detection of bed boundaries and for dip-angle estimation (Radtke, et al., 2006; Uzoh, et al., 2007; Badruzzaman et al., 2007; Guo, et at., 2008). Moreover, numerical simulations of density measurements suggest modified compensation techniques in HA/HZ wells (Yin, et al., 2008; Uzoh et al., 2008).

Because nuclear-log simulations in HA/HZ wells entail large computational requirements, a fast and reliable simulator is essential for quantitative integration of neutron and density measurements, as well as for inversion. Conventional compensation algorithms of nuclear borehole measurements were designed for vertical wells. An efficient and accurate modeling technique of nuclear logs can be a powerful tool in the design of new post-processing techniques that are appropriate for measurements acquired in HA/HZ wells. Numerical inversion of neutron and density measurements has not been implemented before because of the lack of fast simulation methods. The objective of this chapter is to validate the efficiency and accuracy of the 3D spatial capabilities of the

previously developed linear iterative refinement technique for simulation of borehole nuclear measurements acquired in highly-deviated wells.

At the outset, we simulate neutron-porosity measurements at an interface between two layers of high contrasting petrophysical properties for a range of borehole inclination angles. Subsequently, for the case of neutron simulations, we consider a multi-layer model of high contrasts in petrophysical properties penetrated by wells deviated 60, 75, and 85 degrees from the vertical. For the case of density, we simulate measurements in vertical and 75-degree deviated wells. The multi-layer model includes water- and gas-saturated formations of contrasting porosity values bounded by shale shoulder-beds. In both, neutron and density simulations for various wellbore deviation angles, linear iterative refinement approximations show variations of effective vertical resolution that match MCNP simulations.

4.2 BED BOUNDARY EFFECTS ON FLUX SENSITIVITY FUNCTIONS IN HA/HZ WELLS

Variations of formation density are small relative to contrasts of formation energy-dependent cross-section. For this reason, the spatial distribution of the flux that eventually contributes to the detector count rate is nearly invariant to variations of formation density. Hence, in the absence of borehole environmental effects (i.e., mudcake or tool standoff), density FSFs of a particular tool remain nearly invariant to perturbations of formation density (Mendoza et al., 2009). For different tool designs, the FSFs would be different, but again invariant to variations of formation properties. This limited sensitivity of density FSFs to variations of formation density indicates that a small set of

base cases would be necessary to secure reliable approximations in non-homogeneous formations. Conversely, neutron measurements can be significantly affected by variations of formation properties. Contrasts of migration length relative to energy-dependent cross-section variations of formation rock-fluid mixtures can be large and non-linear in nature. Moreover, the dependency of neutron FSFs on formation properties indicates that measurement resolution limits can change across bed boundaries. Substantial differences between the volume of investigation of neutron and density measurements may also bias the estimation of porosity with combined neutron-density measurements acquired in laminated sequences penetrated by HA/HZ wells.

Figure 4.1 shows section views (radial and azimuthal) of the volume of investigation of neutron and density measurements in high- and low-porosity formations. Although the 2D neutron volume of investigation (axially-integrated FSF) shows favorable spatial sensitivity near the location of the tool and radially away from the wellbore, the flux sensitivity extends around the perimeter of the borehole. **Figure 4.1 (a)** also shows that the neutron measurement volume of investigation expands in low porosity (larger L_m) formations. By contrast, **Figure 1 (b)** shows that the density flux sensitivity is focused in the region of the formation near the tool location and is nearly invariant to contrasts of formation density.

The proximity of an adjacent bed in HA/HZ wells may have a measurable effect on the neutron radial length of investigation (radial geometric factor) referred to as J-factor (Sherman and Locke, 1975), as well as on the vertical and azimuthal geometric factors. To appraise the effect of adjacent layers of contrasting petrophysical properties

(i.e. migration length, L_m) on the neutron geometrical response factors, we consider the case of a single measurement point at a bed-boundary intersection in HA/HZ wells. We construct 3D FSFs of the near and far detectors of a neutron tool pressed against the bottom side of an 8-inch borehole. Simulations consider the case of a boundary between two layers of 5% and 30% porosity water-saturated sandstones (L_m = 24.07 cm and L_m = 13.03 cm, respectively) penetrated by wells of inclination angles ranging from 45 to 90 degrees from the vertical. In addition, simulations consider depth-matching of the near and far detectors at the location of the intersection between the bed boundary and the axis of the borehole.

Figure 4.2 shows the case of a well deviated 65 degrees from the vertical and the case of a horizontal well (90 degrees from the vertical) where the location of the low porosity layer is in close proximity to the neutron tool (top layer). **Figure 4.3** shows a quantitative summary of the spatial (radial and azimuthal) variations of neutron FSFs as functions of well inclination. For this particular location of bed boundary with respect to the axis of the borehole, and when the low porosity layer is in close proximity to the measuring tool, the J-factor variation is as large as 1.42 inches for both near and far detectors at 80% of the response. For the same situation, azimuthal response variations are as large as 20 and 57 degrees for the near and far detectors, respectively (**Table 4.1**). Similarly, for the reverse order of porosities (high porosity layer in close proximity to the measuring tool) and 80% of the response, J-factor variations are as large as 1.75 and 2.17 inches for the near and far detectors, respectively. Azimuthal response variations are as large as 4.5 and 15.5 degrees (**Table 4.2**).

Figure 4.4 confirms that adjacent layers with high contrasts of migration length, $L_{m,}$ (contrasting values of hydrogen index) can have a significant impact on the neutron volume of investigation due to streaming of neutrons through beds of longer L_m (Ellis and Singer, 2007). In addition to J-factor variations of neutron measurements, **Figures 4.1** and **4.4** indicate significant perturbations in the azimuthal geometric factor due to contrasts in formation migration length. Consequently, a 2D approximation would not be sufficient to secure reliable simulations of neutron-porosity logs acquired in HA/HZ wells. To account for simultaneous variations of formation properties in the radial, vertical, and azimuthal directions, we implement 3D flux sensitivity functions in the rapid approximation of neutron measurements. The linear iterative refinement technique considered in this chapter includes the 3D spatial properties of the FSFs in the rapid simulation of nuclear measurements acquired in HA/HZ wells.

4.3 METHOD

We use the Monte Carlo code MCNP to simulate neutron and density flux sensitivity functions in homogeneous formation base cases (Mendoza, et al., 2009). Simulations include the 3D spatial distribution of the flux that contributes to detector count rate. Starting with a set of pre-computed 3D flux sensitivity functions, we construct a library that includes a wide range of porosity-matrix-fluid mixtures (base cases). Subsequently, we incorporate the 3D spatial capabilities of FSFs in a linear iterative refinement procedure to approximate neutron and density borehole measurements acquired in HA/HZ wells. We use MCNP simulations as benchmark to appraise the reliability of the approximations of neutron and density measurements.

Figure 4.5 describes the linear iterative procedure implemented to approximate the neutron and density porosity logs. Firstly, the procedure selects a flux sensitivity function that corresponds to an assumed base-case (constant L_m or ρ for neutron or density, respectively). Secondly, we convolve the flux sensitivity function for the assumed base-case formations (FSF_B) with the nuclear sensitivity parameter (ΔL_m or $\Delta\rho$, for neutron or density, respectively) to approximate the change of detector response (ΔN) via fist-order Born approximations (Mendoza et al., 2009). Sensitivity parameters constitute spatial variations from the assumed base-case in a perturbed region (i.e., $\Delta L_m = L_{mB} - L_m$ and $\Delta\rho = \rho_B - \rho$). A third step updates the value of the initially-assumed base-case parameter based on ΔL_m or $\Delta\rho$ for neutron or density, respectively. A new FSF_B that corresponds to the updated parameter is used to approximate a new value of ΔN. This procedure is repeated at each depth sample point until ΔN is within a tolerance minimum value (ΔL_m<0.01 cm or $\Delta\rho$< 0.01 g/cm^3 for neutron or density, respectively) or up to three iterations. In most cases two iterations are sufficient to achieve convergence and advance to the next depth point. Because the migration length and density of materials are not necessarily correlated, we implement the neutron and density linear iterative refinements separately.

4.4 RESULTS AND DISCUSSION

As a staring point, we use MCNP to simulate neutron-porosity measurements acquired with a tool pressed against the bottom side of an 8-inch borehole that intersects a horizontal boundary between two layers of water-saturated sandstone of 5% and 30%

porosity (**Figure 4.2**). Neutron-porosity simulations consider a single depth point (at the borehole intersection with a bed boundary) and borehole inclination angles ranging from 45 to 90 degrees. Subsequently, we implement the linear iterative refinement technique described in the previous section for the rapid approximation of neutron measurements in the same formation-borehole geometries.

A first set of results considers the case in which the low-porosity layer is closest to the borehole and a second set considers the reverse order of porosities. MCNP neutron-porosity simulations are reference values used to assess the accuracy of the approximations. When the low-porosity layer is closest to the borehole, approximations match MCNP simulations with a difference of up to 1% porosity for the case of the 85-degree well. The reverse order of porosities yields a maximum difference of 2% porosity between approximations and MCNP simulations (**Figure 4.6**). These results were obtained for the particular case of a bed boundary between layers of 5% and 30% porosity sandstone intersecting the borehole at the same point in vertical depth. The precision of the approximated neutron-porosity will differ with distinct contrasts of petrophysical properties of layers, and with different depths of intersection between the borehole axis and the bed boundary. However, the agreement between the MCNP-simulated neutron porosity and the rapid approximation in this case confirms that the azimuthal discretization of the geometrical response functions (**Appendix C**) is sufficient to secure accurate simulations in HA/HZ wells.

For the approximation of neutron porosity measurements, the FSF simulated in a homogeneous formation is not an exact match of an FSF calculated in a perturbed

formation. However, an FSF_B calculated in a particular homogeneous matrix-fluid mixture (base-case) approximates the 3D spatial characteristics of an FSF corresponding to a non-homogeneous formation. The selection of optimal FSF_B by the linear iterative refinement procedure enables reliable approximations of neutron and density measurements acquired in HA/HZ wells.

To appraise the accuracy of neutron measurement simulations across layers penetrated by HA/HZ wells, we consider a multi-layer case of large contrasts in petrophysical properties (**Figure 4.7**). The model consists of sandstone layers of 5% and 30% porosity bounded by shale shoulder beds. Sand beds are water-saturated in the lower zone and gas-saturated in the upper zone. At the outset, we use MCNP to simulate neutron porosity measurements for wells deviated 0, 60, 75, and 85 degrees from the vertical. **Figure 4.7** shows that the 16-inch sandstone beds are thinner than the vertical resolution of the neutron tool, and that with increasing well inclination shale shoulder-bed effects decrease in the low-porosity water sand at the bottom. However, shoulder-bed effects in the 16-inch, 30% porosity water-saturated sand, bounded at the bottom by a 5% porosity water-saturated sand and at the top by a 30% gas-saturated sandstone, increase at higher well inclinations. This effect is due to the preferential response of neutron measurements to formations of longer migration length (low hydrogen-index) and the fact that the azimuthal resolution is broadly affected by adjacent layers at high well deviations from the vertical. (**Figure 4.4**). Hence, in this particular situation the resolution of neutron measurements across a thin high-porosity layer, bounded by beds of significantly lower hydrogen-index, decreases at higher deviation angles.

Subsequently, we simulate neutron measurements in the same multi-layer formation penetrated by HA/HZ wells with the use of the linear iterative refinement approximation. **Figure 4.8** compares the rapid approximation of neutron measurements against MCNP simulations for the case of wells deviated 60, 75 and 85 degrees from the vertical. The maximum difference between the two simulation methods across the complete depth interval in the case of a 60-degree well is equal to 2.4% porosity, which corresponds to approximately 10% of the simulated neutron porosity value. For the cases of 75- and 85-degree wells, the difference between MCNP and the fast simulations is 4.3% and 4.1% porosity, respectively. For all the cases, the maximum error occurred at the location of the high porosity (30%) water-saturated sand bounded by beds of long migration length. In addition to the small thickness of sand beds, this example describes a situation of extreme contrasts in layer properties. For more moderate contrasts of petrophysical properties of layers or reduced shoulder-bed effects (thicker layers), the accuracy of the iterative refinement simulation of neutron measurements improves. **Table 4.3** summarizes the porosity differences and required CPU time for both MCNP simulations and the fast approximations.

In contrast to neutron measurements, shoulder-bed effects in HA/HZ wells can be different for the case of density measurements. Because of its more focused azimuthal geometric factor and the fact that the spatial shape of the density FSFs are nearly invariant to changes of formation density, shoulder-bed effects decrease at higher angles of well inclination. In addition to depth shifts of inflection points of density measurements with respect to bed boundary locations, the resolution of the measurement

increases at higher well inclinations (Radtke et al., 2006, Mendoza et al., 2006, Uzoh et al., 2007, Badruzzaman et al., 2007). For benchmark, we simulate density measurements with MCNP across the multi-layer formation model considered for neutron simulations in HA/HZ wells. **Figure 4.9** compares fast simulations of density measurements against MCNP-simulated density logs in a vertical well and for the case of a 75-degree deviated well. Both simulation methods of single-detector and compensated density exhibit a significant increase in the resolution of formation layering. However, MCNP simulations entail numerical uncertainty inherent to the statistical characteristics of the Monte Carlo method. Hence, differences between MCNP simulations and rapid approximations would include the relative error of the Monte Carlo results. For the case of the 75-degree deviated well, MCNP simulations required 653 hours of CPU time for 98 sample points and two detectors. By contrast, the linear iterative refinement technique required 1.28 minutes of CPU time for 124 sample points and two detectors.

4.5 CONCLUSIONS

We validated the linear iterative refinement technique for the simulation of neutron and density borehole measurements acquired in HA/HZ wells. At the outset, we constructed 3D flux sensitivity functions of neutron and density measurements in the proximity of bed boundaries between layers of large porosity contrasts penetrated by highly-deviated wells. Simulations provided important insights to the response of nuclear measurements acquired in HA/HZ wells. They confirmed that the volume of investigation (i.e., spatial resolution) of density measurements remains nearly invariant to contrasts of formation properties. By contrast, simulations show that the volume of investigation of

neutron measurements is significantly modified when contrasting layers are nearly tangent to the borehole axis. We quantified these effects to appraise the reliability of FSF approximations of neutron and density measurements in HA/HZ wells. To that end, we considered the case of a boundary between two layers of 5% and 30% porosity water-saturated sandstones penetrated by wells of inclination angles ranging from 45 to 90 degrees from the vertical. For one particular location of the bed boundary, at 80% of the response, variations of neutron measurements radial and azimuthal geometric factors were as large as 2.17 inches and 57 degrees, respectively. For the same bed boundary location, spatial resolution variations of neutron measurements due to well inclination angle were different depending on the relative location of the low porosity layer.

Measurement of spatial resolution limits (i.e., volume of investigation) of neutron and density measurements indicated that linear iterative refinement approximations require 3D spatial properties of FSFs to secure reliable simulations in HA/HZ wells. We simulated neutron measurement across laminated sequences of large contrasts of formation properties. Comparison of neutron approximations against MCNP simulations yielded maximum porosity differences of 4.3% in horizontal wells. This maximum difference occurred in simulations across a thin high-porosity (30%), water-saturated layer bounded by shoulder beds of 5% porosity and 30% porosity gas-saturated sandstones. Such a situation represents an extreme contrast of migration length. Simulations in wells with smaller inclination angles improve with respect to MCNP results. More moderate contrasts of petrophysical properties between adjacent layers also improve the accuracy of linear iterative refinement approximations in HA/HZ wells.

Density measurements simulated across laminated sequences penetrated by HA/HZ wells exhibited increased resolution with respect to vertical wells in measured depth. Simulations considered a multi-layer model consisting of 16-inch thick layers. The vertical (axial) resolution and radial length of investigation of the assumed tool configuration estimate the actual layer density values. Both, the linear iterative refinement approximations and MCNP simulations exhibited the same formation geometrical effects on simulated density measurements acquired in HA/HZ wells. However, the numerical uncertainty inherent to MCNP simulations results in differences with respect to the approximations

Simulations with linear iterative refinement can be used for quantitative integration of neutron and density logs in laminated formations where differences in measurement resolution may result in unexpected responses such as false, apparent gas effects (neutron-density log cross-over). **Figure 4.10** is an example of the simulation of neutron and density measurements over a long depth interval in vertical and highly-deviated wells. These simulations incorporate the 3D spatial capabilities of the neutron and density FSF approximations. Nuclear measurement simulations across a similar depth interval would require several days of CPU time with MCNP compared to 18 minutes with the fast approximations.

Table 4.1: Comparison of neutron radial J-factor and azimuthal geometric factor for 80% of the response of the near and far detectors as a function of well inclination. Simulated values assume the case of a well intersecting a bed-boundary at different inclination angles at one particular depth point. The layer at the top (closest to the tool) is a low-porosity sandstone (L_m = 24.07 cm). Refer to **Figures 4.2** and **4.3** for a description of the borehole and formation geometry and for a graphical representation of the results.

Well inclination [degrees]	Near-detector radial J-factor [inches]	Far-detector radial J-factor [inches]	Near-detector azimuthal geometric factor [degrees]	Far-detector azimuthal geometric factor [degrees]
0	5.25	6.67	80.00	88.50
45	5.25	6.33	80.00	92.00
60	5.00	6.00	81.00	98.50
65	4.75	5.75	82.50	100.50
70	4.75	5.75	84.00	105.50
75	4.50	5.50	85.50	112.50
80	4.25	5.25	90.50	122.50
85	3.83	5.25	95.50	133.00
90	3.83	5.25	100.00	145.50

Table 4.2: Comparison of neutron radial J-factor and azimuthal geometric factor for 80% of the response of the near and far detectors as a function of well inclination. Simulated values assume the case of a well intersecting a bed-boundary at different inclination angles at one particular depth point. The layer at the top (closest to the tool) is a high-porosity sandstone (L_m = 13.03 cm). Refer to **Figures 4.2** and **4.3** for a description of the borehole and formation geometry and for a graphical representation of the results.

Well inclination [degrees]	Near-detector radial J-factor [inches]	Far-detector radial J-factor [inches]	Near-detector azimuthal geometric factor [degrees]	Far-detector azimuthal geometric factor [degrees]
0	3.50	4.50	71.50	85.00
45	3.50	4.75	72.00	83.00
60	3.67	5.00	71.50	79.50
65	3.67	5.25	70.50	77.50
70	3.83	5.75	69.50	73.50
75	4.25	6.00	68.00	70.50
80	4.75	6.33	65.00	67.50
85	5.00	6.67	65.00	67.00
90	5.25	6.67	67.00	69.50

Table 4.3: Comparison of the relative error and CPU time associated with the rapid approximation of neutron measurements with respect to MCNP simulations. Refer to **Figure 4.8** for additional details about the multi-layer model and neutron simulations.

Well inclination [degrees]	**Number of simulated sample points [ ]**	**CPU time MCNP [minutes]**	**CPU time Approximation [minutes]**	**Maximum Porosity difference MCNP – Approximation [%]**
0	120	9,600	1.27	**1.59**
60	120	9,600	3.09	**2.42**
75	120	9,600	2.97	**4.29**
85	120	9,600	2.99	**4.09**

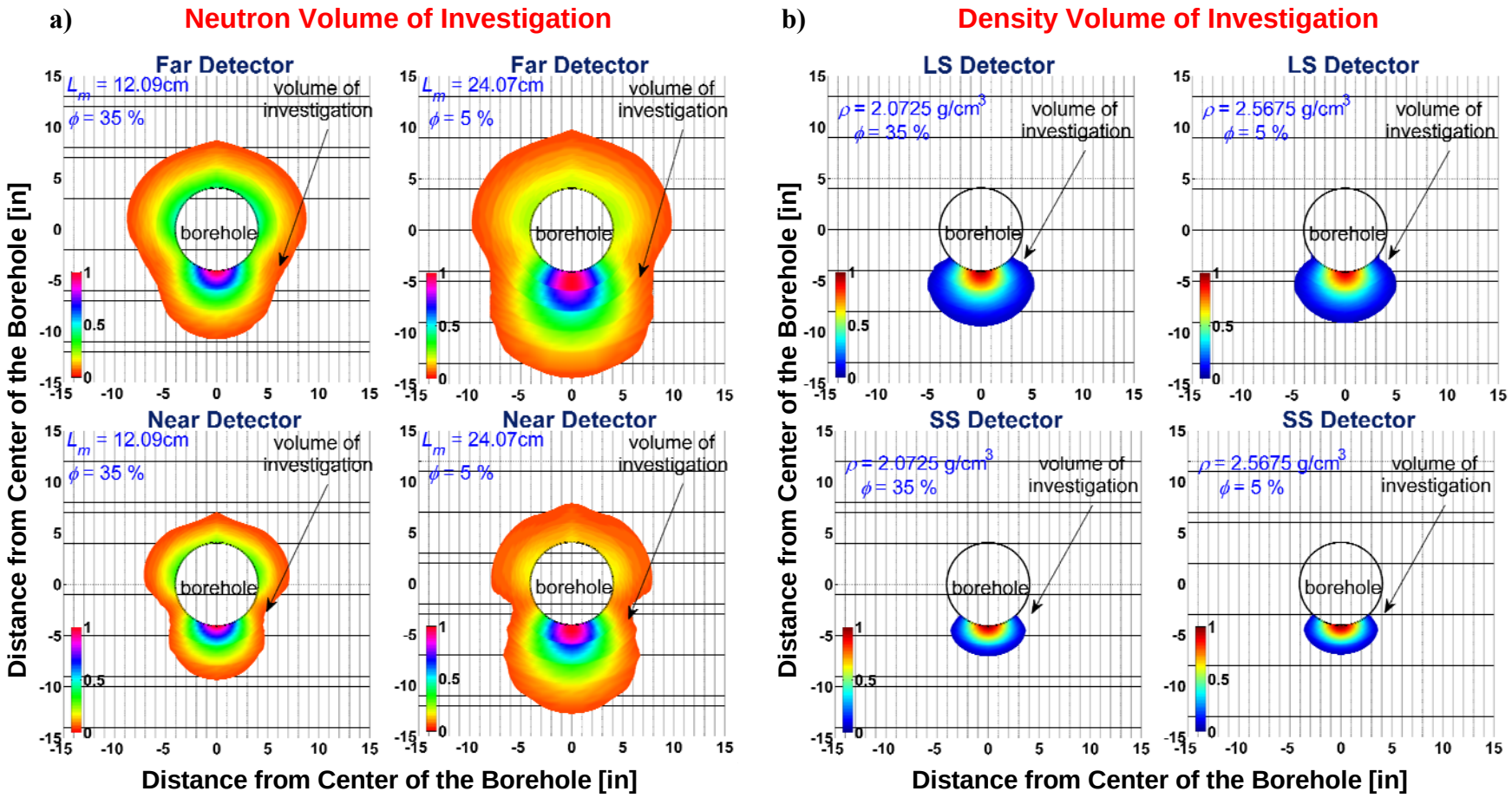

Figure 4.1: Comparison of the simulated volume of investigation of neutron and density measurements around the perimeter of an 8-inch borehole. **a)** Section views of the axially-integrated flux sensitivity function of near and far detectors of a neutron tool. **b)** Section views of the axially-integrated flux sensitivity function of short-spaced (SS) and long-spaced (LS) detectors of a density tool. In both neutron and density simulations, the tool is pressed against the bottom side of the borehole wall. Simulations show results for the cases of 5% and 35% water-saturated sandstone formations.

(a)

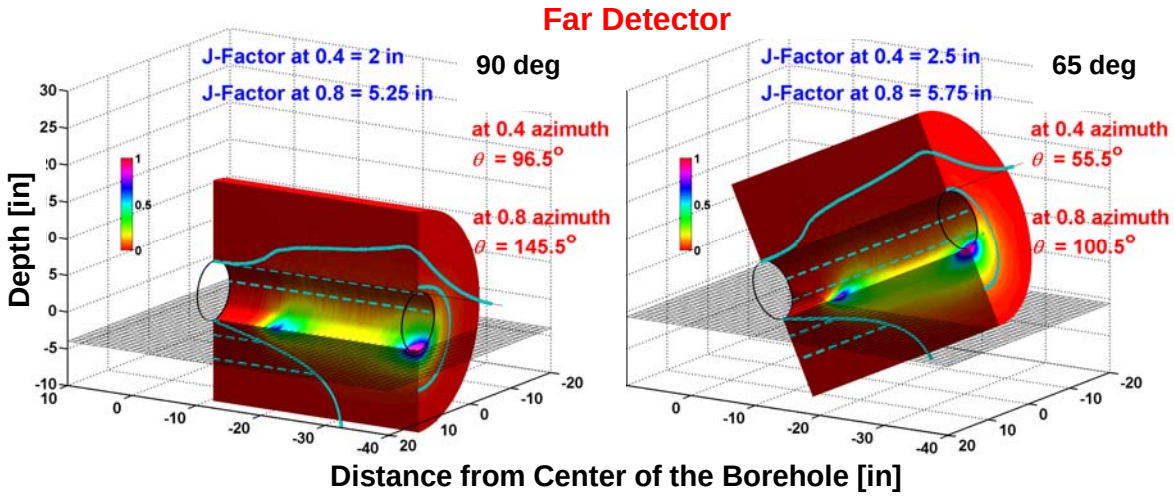

(b)

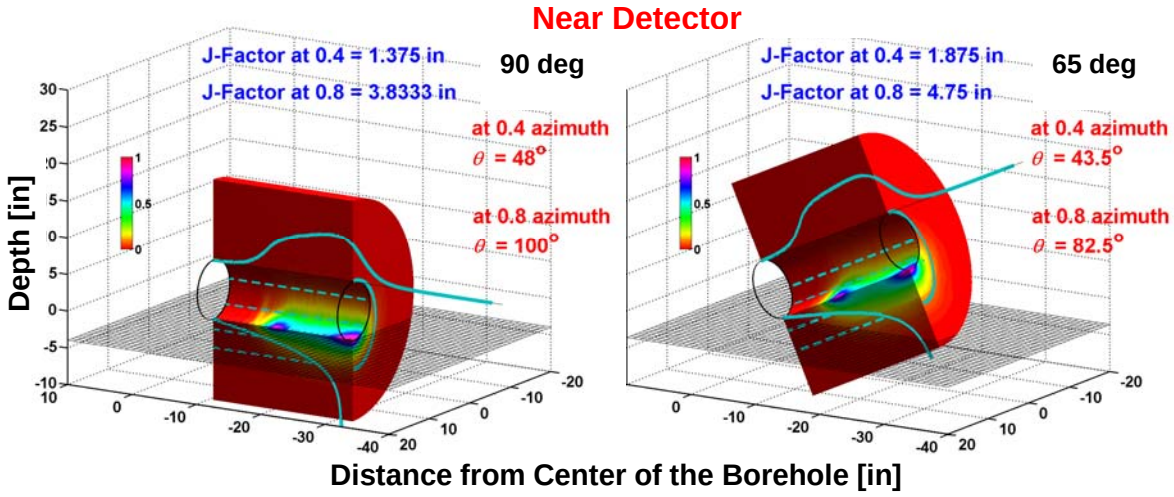

Figure 4.2: Spatial flux sensitivity functions (FSFs) of the **(a)** far and **(b)** near detectors of a neutron tool across a bed boundary between two layers of contrasting porosity values in HA/HZ wells. Solid cyan lines represent the 1D projection of the FSF in the radial (J-factor), vertical, and azimuthal directions. The tool is pressed against the bottom side of an 8-inch borehole between two water-saturated layers of 30% (bottom layer) and 5% (top layer) porosity sandstone. Spatial variations of the FSFs also depend on the relative location and contrast of the high- and low-porosity layers (**Figure 4.3**).

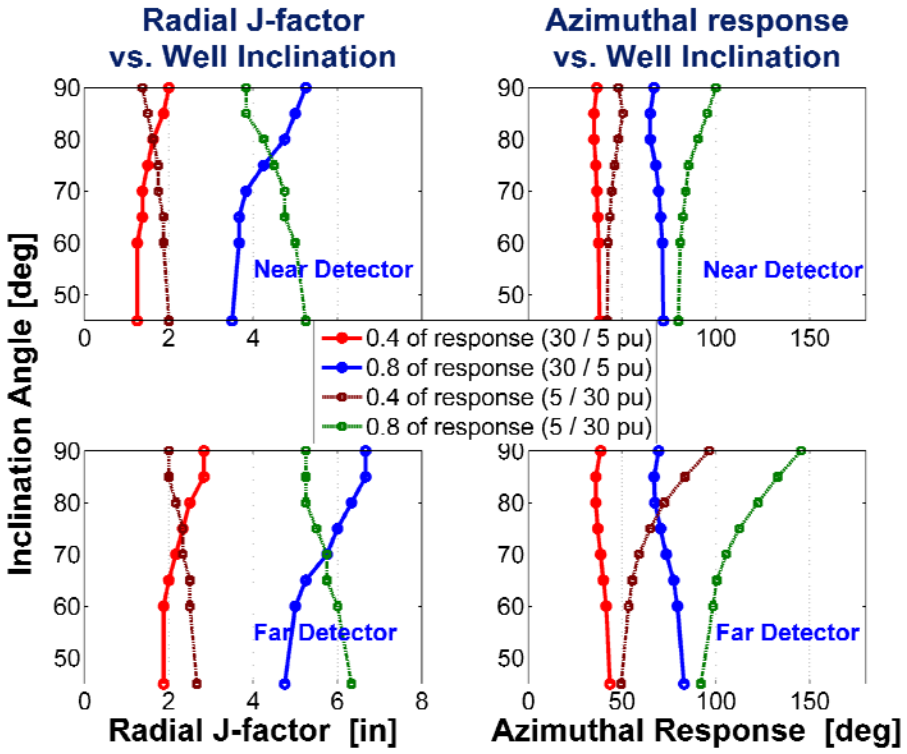

Figure 4.3: Comparison of the variation of the radial J-factor and azimuthal geometric factor at 40% (red and brown curves) and 80% (blue and green curves) of the neutron flux sensitivity as a function of well inclination. The tool is pressed against the bottom side of an 8-inch borehole across two water-saturated layers of 30% and 5% porosity sandstone**.** Results assume that the location of the low-porosity layer is at the top (solid curves) and at the bottom (dashed curves). Refer to **Figure 4.2** for additional details about the assumed geometrical properties.

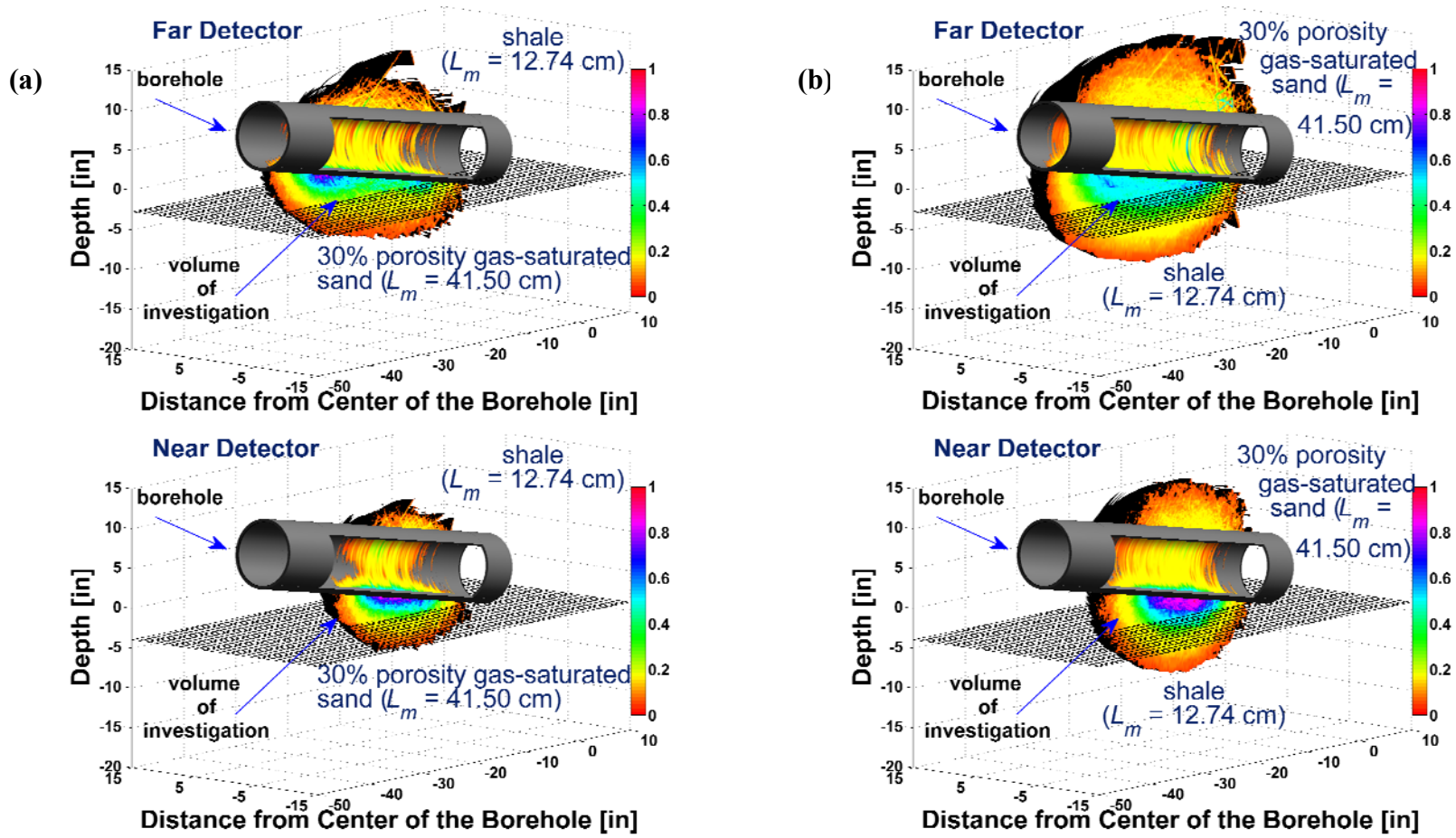

Figure 4.4: Volume of investigation of neutron measurements acquired in an 80-degree well intersecting a boundary between two horizontal layers of extreme contrasts of migration length. **(a)** The top panel shows the Monte Carlo-simulated flux sensitivity function (FSF) of the far-detector across a 30% porosity gas-saturated sandstone bounded on the top by a shale layer. The bottom panel shows the corresponding results for the depth-matched near-detector. **(b)** FSFs of near- and far-detectors assuming that the gas-saturated layer is located at the top. Volumes of investigation show one half of the perimeter of the borehole. The color scale describes the sensitivity of the response normalized with respect to its maximum value (i.e., maximum spatial sensitivity is 1 in the color scale).

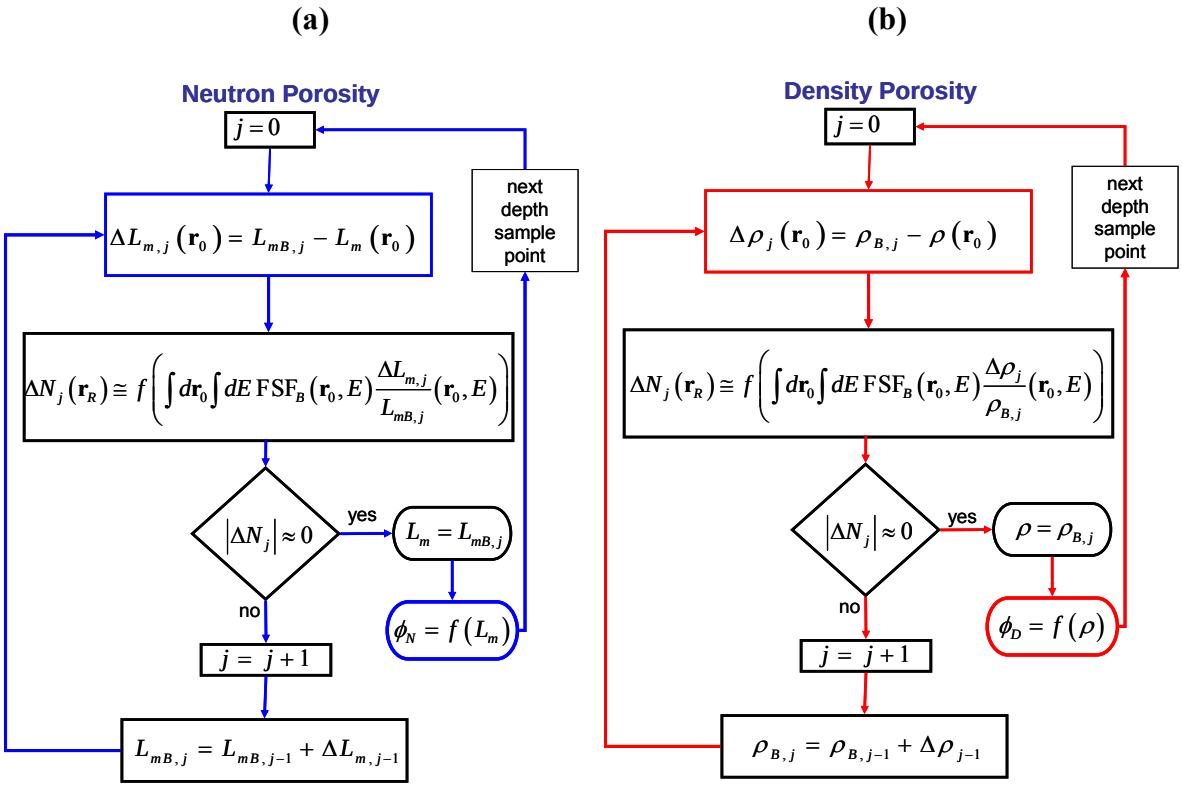

Figure 4.5: Flow chart of the linear iterative refinement technique implemented in the simulation of borehole neutron and density measurements. **(a)** Linear iterative refinement procedure for the approximation of neutron measurements. **(b)** Linear iterative refinement procedure for the approximation of density measurements. The optimization technique initially assumes a base-case (i.e., L_{mB} or ρ_B for neutron or density, respectively). At each depth measurement point, the procedure iteratively updates the flux sensitivity function, FSF_B, for a base-case that best approximates the properties of the formation. The iterative refinement procedure stops when an optimum FSF is used in the simulation, thereby proceeding to the simulation of a subsequent depth measurement point. Neutron- and density-porosity are labeled ϕ_N and ϕ_D, respectively. ΔN is the excess or perturbed response at the detector (located at $\mathbf{r}_R$). The iteration index is labeled j and the subscript B denotes the selected base-case. E and $\mathbf{r}_0$ denote energy and perturbed space, respectively.

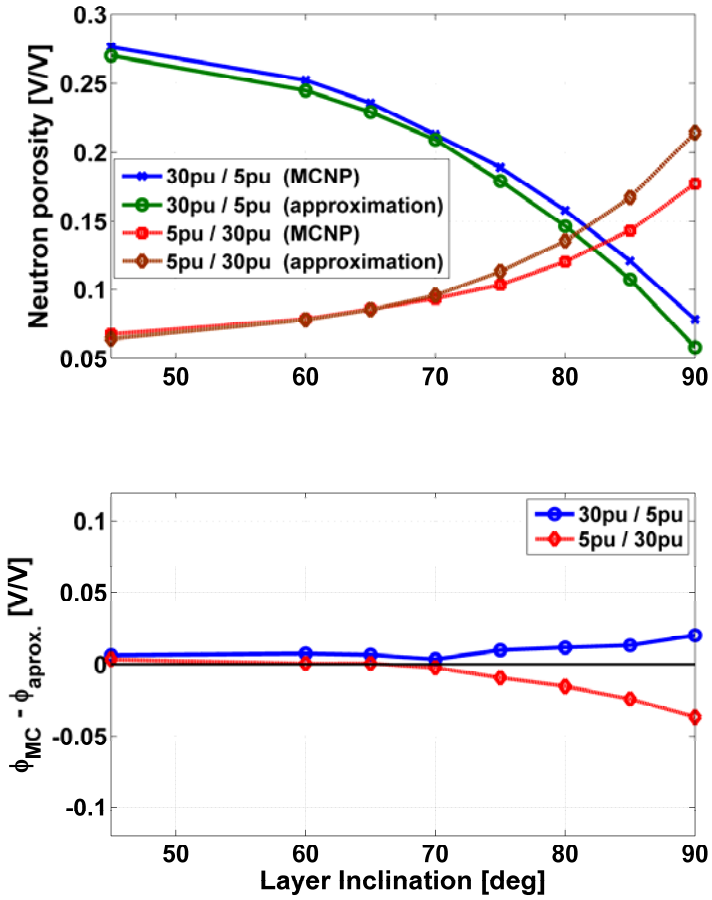

Figure 4.6: Comparison of MCNP-simulated neutron porosity values and linear iterative refinement approximations as a function of well inclination across a bed boundary between the two layers described in **Figure 4.2**. The top panel shows MCNP-simulated neutron porosity values (red curve) for cases where the low-porosity layer is closest to the borehole and neutron porosity values simulated with the linear iterative refinement approximation (brown curve). The top panel also compares MCNP simulations in the reverse order of porosities (blue curve) to the rapid approximation (green curve). The bottom panel describes the difference in porosity units (pu) between MCNP simulations and the corresponding linear iterative refinement approximations.

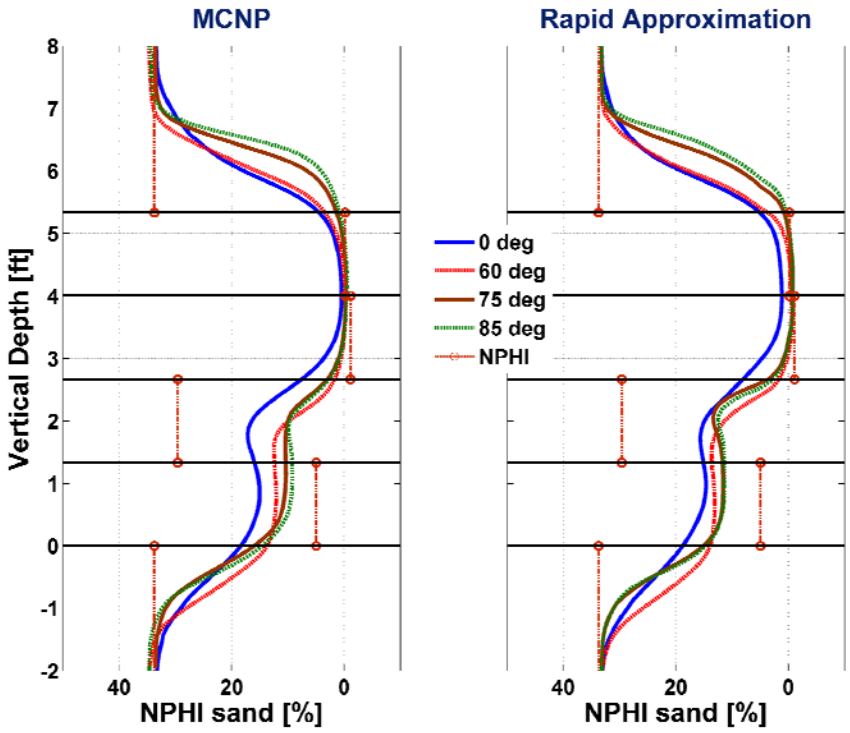

Figure 4.7: Comparison of neutron-log simulations across a multi-layer formation penetrated by wells at different inclination angles. The left panel shows neutron logs simulated with MCNP for a vertical well and for wells deviated 60, 75, and 85 degrees from the vertical. The left panel shows neutron logs simulated with the linear iterative refinement technique for the same cases. From bottom to top, the properties of each of the 16-inch thick layers are as follows: shale of density 2.67 g/cm^3 (L_m = 12.74 cm), 5% porosity water-saturated sand of density 2.57 g/cm^3 (L_m = 24.07 cm), 30% porosity water-saturated sand of density 2.16 g/cm^3 (L_m = 13.03 cm), 30% porosity gas-saturated sand of density 1.86 g/cm^3 (L_m = 41.50 cm), 5% porosity gas-saturated sand of density 2.52 g/cm^3 (L_m = 35.98 cm).

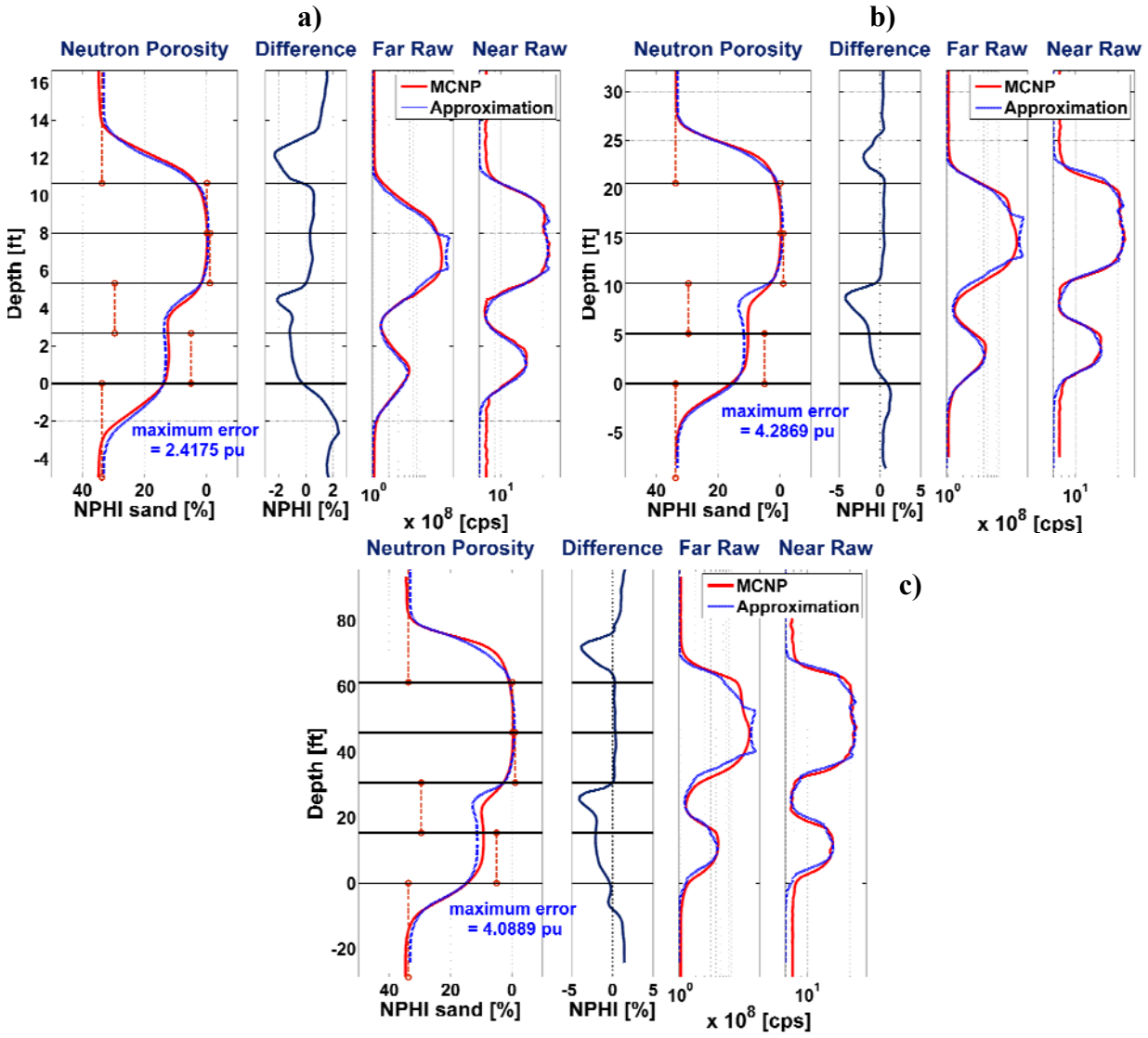

Figure 4.8: Comparison of approximated neutron measurements against Monte Carlo (MCNP) simulations for a well deviated **(a)** 60 degrees, **(b)** 75 degrees, and **(c)** 85 degrees with respect to the vertical. From left to right, the first panel shows the neutron porosity log in measured depth simulated with MCNP (solid red curve) and the neutron-porosity log simulated with the linear iterative refinement technique (dashed blue curve). Dashed red lines identify the actual neutron porosity value of each layer in the absence of shoulder-bed effects. The second panel shows the percent porosity difference between MCNP simulations and the corresponding approximations. The third and forth panels compare, respectively, the near and far raw neutron count rates between MCNP and the rapid approximation. Refer to **Table 4.1** for details about the CPU time and relative error of the simulations.

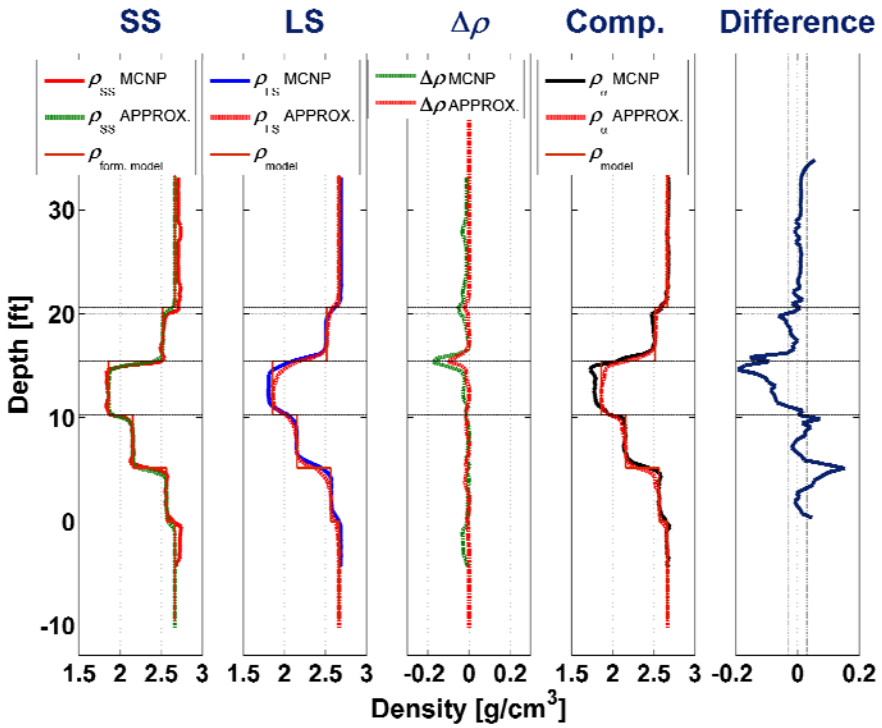

Figure 4.9: Comparison of rapid approximations (dashed curves) of density measurements against Monte Carlo (MCNP) simulations (solid curves) in a well deviated 75 degrees with respect to the vertical. Refer to **Figure 4.7** for a description of the properties of each layer. From left to right, the first panel shows SS density approximations and MCNP simulations. The second panel shows LS density results, the third panel displays the density correction, $\Delta\rho$, and the forth panel shows compensated density results. The fifth panel shows the difference between MCNP simulations and rapid approximations of the compensated density in g/cm^3.

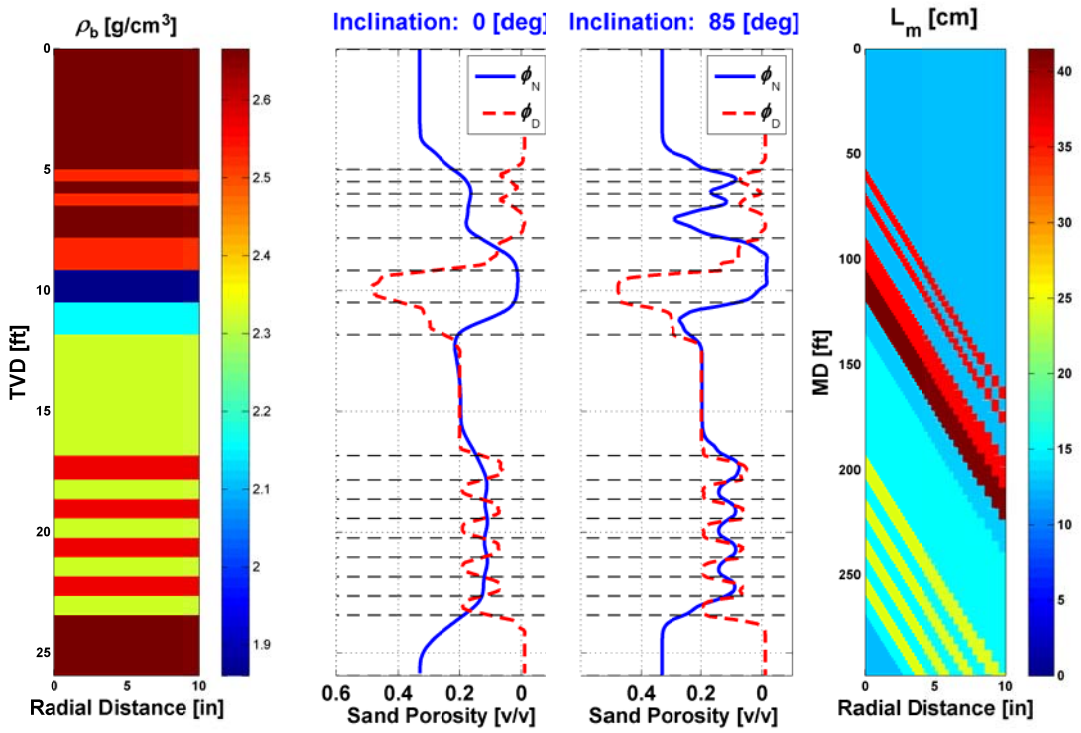

Figure 4.10: Neutron and density logs simulated with the linear iterative refinement approximation. From left to right, panels show: formation bulk density model in g/cm^3, simulated neutron and density porosity logs in a vertical well across horizontal layers of different petrophysical properties, simulated neutron and density porosity logs in a well deviated 85 degrees from the vertical, and the migration length (L_m) of the model used for the simulation of the neutron log. A neutron-density gas cross-over occurs near the top, where the model includes gas-saturated sands. An interesting observation is a small false apparent gas cross-over effect across the thin layers near the bottom. This bottom section is a laminated sequence of 20% and 5% porosity water-saturated beds. The false gas effect is caused by the difference in resolution between neutron and density measurements in both the vertical and deviated well cases (Ellis and Chiaramonte, 2000).

Chapter 5: Inversion of Sector-Based Density Measurements Acquired in Laminated Sequences Penetrated by High-Angle and Horizontal Wells

This chapter shows that inversion processing improves the petrophysical interpretation of logging while drilling (LWD) density measurements acquired in high-angle and horizontal (HA/HZ) wells. Inversion was not implemented in the past primarily because of the lack of fast and reliable simulation capabilities of density measurements. We introduce new post-processing methods of azimuthal density measurements in HA/HZ wells based on two-dimensional (2D) inversion and using the concept of Monte Carlo-derived response functions described in Chapter 3. These methods estimate layer thickness and density from sector-based density measurements.

We consider three independent inversion techniques. The first two techniques consist of 2D inversion of azimuthal single-detector density data with the use of geometrical response factors derived for a commercial LWD density tool. Inversion is implemented with both filtered and unfiltered SS-detector measurements in conjunction with LS measurements. A third technique uses only fully-compensated azimuthal densities. To verify the reliability and applicability of the proposed inversion methods, we first use forward simulations to generate synthetic density images from a model constructed from field data. Furthermore, to evaluate the individual performance of inversion methods in practice, we implement them on field data.

5.1 INTRODUCTION

Conventional processing of LWD density measurements acquired across thin laminations penetrated by HA/HZ wells may result in unreliable petrophysical interpretations. Numerical simulations show that density measurements exhibit depth offsets that vary azimuthally and depend on relative dip angle (angle between the borehole and formation layering) and effective penetration length (*EPL*) of each sensor (Uzoh et al., 2007). These depth shifts may result in inaccurate estimations of true stratigraphic thickness (TST) of porous layers. In addition, standard compensation (spine-and-rib method) of mono-sensor density measurements acquired in thin laminations may not yield results with sufficient resolution to estimate actual layer density. It has been demonstrated that enhanced-resolution processing does not always improve the resolution of compensated density in HA/HZ wells (Radtke et al., 2006; Mendoza et al., 2006). For wells deviation angles greater that 60 degrees, where commercial enhanced-resolution processing does not improve density measurements resolution, inversion reduces shoulder bed effects.

Accurate estimation of TST and porosity is essential for reliable calculations of net pay. Because existing standard and enhanced-resolution compensation methods were designed for vertical wells, there is a need for compensation techniques suitable for HA/HZ wells. Recent publications on Monte Carlo simulation of azimuthal density

measurements acquired across thin laminations in HA/HZ wells propose alternative post-processing techniques of raw density image data (Uzoh et al., 2009; Yin et al, 2008).

Inversion methods can improve petrophysical interpretations of nuclear borehole measurements. These techniques reduce shoulder-bed effects in the presence of noisy measurements and improve the estimation of formation properties, i.e. density, porosity, and fluid saturation, based on simulations of the response of nuclear measurements. However, the lack of fast and reliable numerical simulation methods constraints the applicability of inversion methods for interpretation of nuclear measurements. Patchett and Wiley (1994) used an iterative inverse modeling procedure to determine porosity, water saturation, and lithology with a forward modeling algorithm that simulated nuclear log responses based on elemental composition of the rocks and fluids. Similarly, Aristodemou et al., (2003 and 2005) introduced an interpretation method based on neural networks for the estimation of porosity, salt concentration, and oil saturation. Liu et al., (2007) implemented 1D inversion of density and resistivity logs to improve the petrophysical interpretation of thinly-bedded formations in vertical wells. In HA/HZ wells, porosity, fluid saturation, mineral composition of the rock matrix, and shoulder-bed effects can significantly bias the calculations of net pay in thinly-laminated formations.

The objective of this chapter is to implement linear inversion methods to improve the estimation of layer densities and TST based on azimuthal density measurements acquired in HA/HZ wells. To that end, we make use of fast numerical simulation procedures that approximate the response of nuclear borehole measurements using the

concept of Monte Carlo-derived flux sensitivity functions (FSFs). It has been shown that the rapid simulation method accurately approximates density measurements for specific rock-fluid mixtures in the presence of shoulder beds and dipping layers (Mendoza et al., 2009b). We implement 2D inversion to account for simultaneous radial and vertical variations of formation density detected by measurements acquired in HA/HZ wells. Moreover, because LWD density measurements are acquired azimuthally around the perimeter of the borehole, we include multiple azimuthal sectors in the inversion. This method provides redundancy of measurements, hence yields more reliable estimations of layer density and thickness than from single-sector measurements. Likewise, inversion allows quantitative appraisal of the reliability and internal consistency of the measurements in the presence of noise.

As starting point, we select bed-boundaries from sector-based compensated and SS-detector density measurements. We use an algorithm that detects inflection points of density measurements as the location of bed boundaries. Subsequently, we use a correlation algorithm to estimate dip and azimuth from density-image measurements. With the estimated angles, we refine the location of the selected boundaries for each azimuthal sector. Next, we perform linear inversion of density for each layer based on three independent inversion procedures. The first two procedures assume as input data the raw and filtered sector-based combined SS- and LS-detector density measurements. The third technique uses only fully-compensated azimuthal density as input. Inversions performed with synthetic density images appraise the accuracy and reliability of the inversion methods. Furthermore, using field data we evaluate the practical

implementation of inversion of LWD density measurements. Inversion reduces shoulder-bed effects and enables the quantitative appraisal of the reliability and internal consistency of field measurements. Comparison of integrated porosity-feet from the various inversion methods quantifies the relative improvement with respect to conventional compensation techniques. For synthetic density measurements that did not include tool standoff effects, porosity-feet calculated from inversion results increased 3% with respect to that calculated from the synthetic compensated density measurements. For inversion of filed measurements that included borehole environmental effects and noise, depending on the azimuthal sectors included in the inversion, integrated porosity-feet values increased from 7% to 64% compared to porosity-feet calculated with compensated density.

5.2 METHOD

Numerical simulation of borehole density measurements invokes the concept of Monte Carlo-derived flux sensitivity functions and fast numerical approximations described by Mendoza et al. (2009a). Inversion methods introduced in this chapter focus on measurements acquired with a commercial LWD density tool. Accordingly, we consider an azimuthal binning scheme divided into 16 sectors, each subtending an angle of 22.5 degrees from the center of the tool (Radtke et al., 2003). Furthermore, we assume that a measurement acquired with a given sector represents the average angular LWD density measurement for that sector (Uzoh et al., 2007).

Inversion procedures consider four principal stages of analysis: (1) estimation of dip and azimuth, (2) selection of layer boundaries from sector-based compensated or SS-

detector density measurements, (3) linear inversion of layer densities, and (4) forward simulation of density measurements based on a model constructed from inverted densities and bed-boundaries. Comparison of simulations to original density measurements quantifies the accuracy and reliability of the inversion. The procedure can be repeated with a different selection of bed-boundaries. Agreement between simulated and measured densities quantifies the reliability of inversion results.

5.2.1 Dip-Angle Estimation

In analogy to dipmeter processing, used with microresistivity measurements, we implement a fixed-interval correlation technique to estimate dip from density images (Cameron et al., 1993). This method consists of cross-multiplication between pairs of curves in all possible positions within a specified window to ascertain maximum coherence. Maximum coherence follows from the minimization of residuals between pairs of density measurement sectors, i.e., $\left\| \bar{\mathbf{d}}_I - \bar{\mathbf{d}}_{II} \right\|^2$, where $\bar{\mathbf{d}}$ is the vector of density measurements and the subscripts designate sector number. The number of shift positions multiplied by the depth sampling rate of the measurements gives the corresponding depth offset between different sectors. In the first step, the top azimuthal sector is depth shifted against all other azimuthal density measurements to calculate the coherence per depth shift. Calculated depth offsets along with their calculated coherence between pairs of azimuthal sectors are stored in a matrix. The second step consists of searching for depth shifts that yield the maximum coherence. These depth shifts form a sinusoid whose amplitude (A) is used to estimate the dip angle, θ, with the equation (Yin et al., 2006)

$$\theta = \tan^{-1}\left(\frac{A}{D+2EPL}\right), \tag{5.1}$$

where D is bit size and EPL is referred to as the effective penetration length. The correlation procedure requires the specification of several input variables including correlation depth interval, step distance, and search angle (**Figure 5.1**). Correlation depth interval is the depth window used in the comparison of logs for correlation. Step distance is the depth shift implemented for multiple correlation intervals. Search angle controls the length of the maximum displacement between pairs of azimuthal measurements. In the presence of highly-laminated sequences, the above processing parameters must include depth intervals that encompass several bed boundaries and a search angle that allows sufficient vertical displacement between sectors.

5.2.2 Bed boundary Detection

Bed boundaries are determined from density measurements (compensated or SS) by calculating the variance of the log within a sliding window, and by placing a bed boundary wherever the variance increases above a threshold value (Uzoh et al., 2007). Subsequently, depth shifts that vary azimuthally and depend on relative dip angle, together with the EPL of each sensor, refine the previously selected bed boundaries (Uzoh et al., 2009). These depth-shifts are calculated in true vertical depth (TVD) with the equation

$$\Delta TVD = \cos(\beta) LS_{mp} + \frac{\cos(\beta) EPL}{\tan(\theta)}, \tag{5.2}$$

where LS_{mp} is the measurement point of the LS-detector. **Figure 5.2 (a)** shows the geometrical conventions assumed for the modeling log-based boundary TVD shifts, where β is borehole inclination angle, and θ is formation dip angle. **Figure 5.2 (b)** shows the total TVD shift applied to the SS-detector density log-based boundary location to correlate with that of the LS-detector density, where $\Delta TVD_1 = \cos(\beta)\left(LS_{mp} - SS_{mp}\right)$. In the case that dip angle (θ) equals zero (layering parallel to the borehole axis), the total TVD shift is equal to the corresponding *EPL*. Depth shifts vary per sector by $\cos(\alpha)$, where α is azimuthal angle (Uzoh et al., 2009).

5.2.3 Inversion

The objective of inversion is to estimate layer-by-layer density values of the model previously constructed with bed-boundary location and dip angle estimation. Sector-based inversion of mono-sensor density measurements is posed as the minimization of a quadratic cost function, given by

$$C(\bar{\mathbf{x}}) = \frac{1}{2}\left\{\left\|\bar{\mathbf{e}}(\bar{\mathbf{x}})\right\|^2 + \lambda^2 \left\|\bar{\mathbf{x}} - \bar{\mathbf{x}}_0\right\|^2\right\}, \tag{5.3}$$

where $\bar{\mathbf{x}}$ is the vector of unknown layer densities, and λ is a stabilization parameter that controls the weight given to the residual norm relative to a prescribed reference model $\bar{\mathbf{x}}_0$. The value of λ increases for smaller well inclination angles across thinly-laminated sequences where non-uniqueness in the solution of $\bar{\mathbf{x}}$ increases. In this case, $\bar{\mathbf{x}}_0$ is a vector with constant and equal entries equal to the value of measured density averaged over the depth interval considered for inversion. The term $\left\|\bar{\mathbf{x}} - \bar{\mathbf{x}}_0\right\|^2$ incorporates *a-priori*

assumptions about the expected solution in order to reduce non-uniqueness (Hansen, P. C., 1998). Entries of the unknown vector of layer densities,

$$\bar{\mathbf{x}} = \begin{bmatrix} x_1 \\ \vdots \\ x_t \\ \vdots \\ x_T \end{bmatrix}, \tag{5.4}$$

are bounded as $0 \le x_t \le \varepsilon$, where x_t is the *m*-th density layer, ε is the maximum value of density allowed in the solution, and the subscript *T* designates the total number of layers. The vector of residuals $\bar{\mathbf{e}}(\bar{\mathbf{x}})$ is written as

$$\bar{\mathbf{e}}(\bar{\mathbf{x}}) = \begin{bmatrix} e_1(\bar{\mathbf{x}}) \\ \vdots \\ e_m(\bar{\mathbf{x}}) \\ \vdots \\ e_M(\bar{\mathbf{x}}) \end{bmatrix} = \begin{vmatrix} d_1(\bar{\mathbf{x}}) - d_1^0 \\ \vdots \\ d_m(\bar{\mathbf{x}}) - d_m^0 \\ \vdots \\ d_M(\bar{\mathbf{x}}) - d_M^0 \end{vmatrix} = \bar{\mathbf{d}}(\bar{\mathbf{x}}) - \bar{\mathbf{d}}^0, \tag{5.5}$$

where the entry $d_m(\bar{\mathbf{x}})$ is the *m*-th value of density simulated from a model $\bar{\mathbf{x}}$ constructed from inverted layer densities, and d_m^0 is the *m*-th density measurement. The term $\bar{\mathbf{d}}(\bar{\mathbf{x}})$ is the vector of numerically simulated density values. Accordingly, the vector of measurements $\bar{\mathbf{d}}^0$ contains blocks of indexed density measurements acquired by SS and LS detectors and includes all azimuthal sectors. For each azimuthal sector, blocks containing indexed LS-density measurements follow similar blocks of SS-density values i.e.,

$$\bar{\mathbf{d}}(\bar{\mathbf{x}}) = \begin{bmatrix} \begin{bmatrix} \rho_{SS,j,m} \\ \vdots \\ \rho_{SS,J,m} \end{bmatrix} \\ \begin{bmatrix} \rho_{LS,j,m} \\ \vdots \\ \rho_{LS,J,m} \end{bmatrix} \\ \vdots \\ \begin{bmatrix} \rho_{SS,j,M} \\ \vdots \\ \rho_{SS,J,M} \end{bmatrix} \\ \begin{bmatrix} \rho_{LS,j,M} \\ \vdots \\ \rho_{LS,J,M} \end{bmatrix} \end{bmatrix} \cong \bar{\bar{\mathbf{K}}} \cdot \bar{\mathbf{x}}, \tag{5.6}$$

where the subscripts j and m designate the j-th azimuthal sector and the m-th measured density value, respectively. The sub-index J designates the total number of azimuthal sectors and is equal to 16. Similarly, M denotes the total number of data points. Because of the assumption of linearity between measurements and densities, we have $\bar{\mathbf{d}}(\bar{\mathbf{x}}) \cong \bar{\bar{\mathbf{K}}} \cdot \bar{\mathbf{x}}$, where the matrix $\bar{\bar{\mathbf{K}}}$ is constructed with flux sensitivity functions (FSFs) that weigh the vector of unknown layer densities, $\bar{\mathbf{x}}$. Blocks containing integrated 2D FSFs for SS- and LS-detectors oriented in the direction of each azimuthal sector are included as rows in $\bar{\bar{\mathbf{K}}}$ (**Appendix** D) that weigh the vector $\bar{\mathbf{x}}$ to reproduce indexed density measurements included in vector $\bar{\mathbf{d}}^0$. The solution of Equation (5.3) is given by

$$\left[\bar{\bar{\mathbf{K}}}^{\mathrm{T}} \cdot \bar{\bar{\mathbf{K}}} + \lambda^2 \bar{\bar{\mathbf{I}}} \right] \cdot \bar{\mathbf{x}} - \lambda^2 \bar{\bar{\mathbf{I}}} \cdot \bar{\mathbf{x}}_0 = \bar{\bar{\mathbf{K}}}^{\mathrm{T}} \cdot \bar{\mathbf{d}}^0, \tag{5.7}$$

where the superscript T indicates transposition.

5.2.4 Forward Simulation

Equation (5.7) yields a multi-layer density model constructed from inverted density values entered in $\bar{\mathbf{x}}$ and layer boundary locations determined *a-priori*. We simulate azimuthal density measurements for the inverted model with the fast linear FSF approximations described by Mendoza et al. (2009a). To that end, we use Monte Carlo-derived SS- and LS-detector FSFs for a commercial LWD density tool. Simulations use 2D FSFs (radial and vertical) integrated azimuthally to weigh the angular average density of every sector at each fixed depth-point. We assume that the tool is pressed against the wall of an 8.5-inch borehole for all tool locations around the perimeter of the wellbore. Subsequently, we use commercial post-processing of mono-sensor densities to calculate compensated and enhanced (alpha-processed) densities. Accordingly, with simulated azimuthal density measurements we construct images for SS- and LS-detector measurements as well as for compensated densities. Comparison of images constructed from simulations to those constructed from original data quantifies the ability of inversion to reproduce density values for each azimuthal sector along a depth interval.

Figure 5.3 is a flow chart of the linear inversion procedure implemented with simulated raw SS- and LS-detector density measurements. For field density measurements where mono-detector densities are filtered, we implement a similar inversion procedure that incorporates density averaging over a depth interval that is proportional to the size of commercial filters (**Figure 5.4**). For inversion of fully-compensated density measurements, an iterative procedure of forward simulations yields

density values of layers, which are determined from the location of bed boundaries (**Figure 5.5**).

5.3 RESULTS

This section describes examples of inversion of azimuthal density measurements with the procedures described above. Inversions were carried out both with synthetic and field measurements.

5.3.1 Benchmark Examples

In order to quantify accuracy of the inversion technique described in the previous section, we first perform inversion of density from simulated azimuthal density measurements. To that end, we consider a multi-layer formation model consisting of alternating 2.0 and 2.6 g/cm^3 density layers of varying thickness. Simulations of density measurements with the FSF approximations across the multi-layer formation consider wells of 60, 70, and -80 degrees of inclination with respect to the vertical. Negative angles indicate simulations for down-dip direction of drilling and positive angles correspond to up-dip LWD simulations. We use the simulated densities for each case as input synthetic data for inversion.

Figure 5.6 shows inversion results obtained from density measurements simulated across a measured-depth section of the multi-layer formation model penetrated by a 60-degree deviated well. **Figures 5.7** and 5.**8** describe inversion results obtained across similar measured-depth sections in the same formation model penetrated by wells deviated 70 and -80 degrees, respectively. Common observations about the three inversion cases are that, in general, inversion improves the assessment of layer densities

across thicker layers and higher well inclination angles. Because the number of measurements decreases across thin layers and smaller well inclination angles, non-uniqueness increases for the solution of layer densities. Therefore inversion of density measurements across thin layers requires larger values of the regularization parameter λ in order to control the smoothness of the solution.

To appraise the reliability of inversions, we calculate percent errors between simulations and synthetic data averaged over a measured depth section. **Figure 5.9** compares residuals between inversion-based simulations and original synthetic data in percent for azimuthal sectors. For both SS- and LS-detectors, simulations for the 80-degree down-dip well exhibit smaller differences compared to simulations for 60- and 70-degree wells. Average percent errors for 60- and 70-degree well simulations vary across azimuthal sectors ranging from 1.6% to 4.3% and 0.8% to 1.8% for the SS- and LS-detectors, respectively. Percent errors for simulations for the -80-degree well have maximum values of 1.8% and 0.9% for the SS-and LS-detectors, respectively. In general, maximum differences for SS-detector inversion-based simulations are under 5% and for the LS-detector; residuals are under 2%.

Simulations confirm that in HA/HZ wells, compensated and alpha-processed (Flaum, et at., 1987) densities are practically the same (Uzoh et al., 2007). Alpha processing imposes the vertical resolution of the short-spaced detector onto the compensated density over an interval of measured depth. Because in HA/HZ wells, the smaller radial geometric factor governs effective vertical resolution, effective resolutions of both SS-detector and compensated density are not as dissimilar in HA/HZ wells as

they are in vertical wells. Similarly, filtering of SS- and LS-detector density averages the measurements over a relatively small measured-depth interval. Consequently, the influence of filtering is not significant for inversion. In the following sections we concentrate on field measurements processed with standard commercial compensation techniques.

5.3.2 Field Case Study

To verify the reliability and applicability of inversion methods described in previous sections, we first perform inversions on simulated density measurements from a synthetic model constructed from field data. Subsequently, we perform the inversion on LWD field data images. The case under analysis corresponds to a field located in West Africa. In the log section under study, we select a depth interval located below the free oil-water contact. The formation consists of alternating 1 to 2-foot true vertical thickness (TVT) laminations of siltstones, argillaceous siltstones, and calcite cemented siltstones. **Figure 5.10** displays LWD measurements acquired in a highly-deviated well across the depth section under analysis in true vertical depth (TVD). Measurements shown in **Figure 5.10** include gamma-ray (GR), resistivity, bottom-sector photoelectric effect (PEF), bottom-sector compensated density, well inclination, and compensated density image. Density measurements were acquired with the same commercial LWD density tool assumed in our inversions and simulations. For this interval, the well inclination fluctuates between 78 and 82 degrees from the vertical, the direction of drilling is up-dip, and bit size is equal to 8.5 inches.

5.3.2.1 Inversion of Field-Based Modeled Density

As the outset, we construct a model from bottom-sector compensated density measurements. Due to gravity, in HA/HZ wells the tool makes better contact with the borehole wall at the bottom-sector location. As a result, the bottom-sector compensated density measurements are the least affected by borehole environmental effects and are closer to true bed densities. Track 4 of **Figure 5.10** describes measured compensated density (blue curve) and the constructed model (piece-wise constant red line). We use a procedure called zonation to obtain layer density values. Firstly, this procedure detects bed-boundary locations in the measured density whenever the variance, calculated within a sliding window, increases above a threshold value. Secondly, density values for each layer included in the model are calculated based on the selected bed-boundary location. These layer density values are either maximum, minimum, or average density across beds, depending on the variability of density measurements within each bed.

We use the multi-layer model constructed from compensated density measurements to simulate LWD SS- and LS-detector density images. In so doing, we use linear approximation procedures for fast simulation of density measurements (Mendoza et al., 2009a). Simulations use FSFs constructed for the commercial LWD density tool that acquired the field measurements used for inversion. Subsequently, we obtain compensated density, enhanced-resolution density, and density correction ($\Delta\rho$), using commercial post-processing techniques of mono-sensor densities.

Numerical simulations obtained for the field-based model are used as input measurements for inversion. Accordingly, inversion procedures described above assume

synthetic density data as the vector of measurements $\bar{\mathbf{d}}^0$ which is constructed from all azimuthal sectors and SS- and LS-density values. Minimization of the quadratic cost function described by Equation (5.3) yields azimuthal layer density values, $\bar{\mathbf{x}}$, which are subsequently used as input model for fast forward simulations of density images.

Density images are constructed from the combination of sector density measurements around the perimeter of the wellbore. **Figures 5.11** through 5.**14** compare density-derived images displayed in measured depth, for SS-detector, LS-detector, compensated, and density correction, respectively. Figures display images, in the following order from left to right: field density measurements, synthetic density, inversion results, simulated density, density difference, and percent difference between simulated and synthetic density images. Colors describe density values corresponding to simulations and measurements. Sectors located in the upper sides of the borehole are displayed in the left and right sides of the images, whereas bottom sectors are displayed in the center of the images.

Density images constructed with SS-and LS-detector field measurements exhibit lower layer density values in upper sectors due to tool standoff. Because simulations of synthetic density images do not include tool standoff, layer densities are more continuous across azimuthal sectors. The density image constructed from inversion exhibits continuous boundaries and density values for each bed across azimuthal sectors. In addition, inversion shows higher density contrast between layers of varying densities and thicknesses. Compensated, SS-and LS-detector density images show sinusoids of larger amplitude than inversion. This effect is due to apparent shifts in detection of bed

boundary locations caused by differences in radial length of investigation that vary azimuthally around the perimeter of the borehole.

Percent errors between simulations and field-based synthetic data quantify the capability of simulations (that are based on inversion) to reproduce input measurements. **Figure 5.15** shows that maximum differences between simulated and synthetic SS-detector density images averaged over the measured-depth interval under analysis are 1%. Similarly, for LS-detector and compensated density images, maximum average differences are 0.5% and 0.6%, respectively. Comparison of simulated SS- and LS-detector density images to original synthetic images show better results in upper sectors than side and bottom sectors. Errors in upper sectors (sectors 1 and 16) are equal to 0.85% and 0.65%, for SS and LS detectors, respectively.

Figure 5.16 shows that inversion improves porosity-feet estimations compared to compensated density. Because inversion exhibits continuous bed boundaries (bed thickness) around azimuthal sectors, the calculated value of porosity-feet is constant for measured depth intervals. By contrast, azimuthal variations of the detected location of bed boundaries by the compensated density yield azimuthally variable porosity-feet. Values of integral porosity-feet across the selected measured depth interval, averaged over azimuthal sectors, are equal to 25.44 and 26.18 feet for compensated density and for inversion, respectively.

5.3.2.2 Inversion of Field Density Measurements

Using the same inversion procedures described above for synthetic density data, we perform inversion directly on field measurements. We consider the same depth

interval described in **Figure 5.10**. By comparison to synthetic density measurements numerically simulated from a field-based model, field measurements include noise and are biased by borehole environmental effects (i.e. mudcake and tool standoff) primarily in the upper azimuthal sectors. Due to gravity, the LWD density tool is preferentially eccentered toward the bottom side of the borehole. Hence, mono-sensor density measurements yield density values that vary azimuthally depending on the radial length of investigation of the tool. Because bottom sector density measurements are the least affected by tool standoff, inversion should preferentially weigh density measurements acquired with these sectors.

Because our simulations do not include tool standoff, we perform several inversions winnowing out sectors that are most affected by tool standoff. The first case includes only density measurements acquired with bottom sectors (sectors 8 and 9). For comparison, additional cases include sectors 6 through 11 and all azimuthal sectors. To that end, we construct the vector of measurements $\bar{\mathbf{d}}^o$ in Equation (5.6) with SS- and LS-density values from the selected azimuthal sectors. In all cases, we assume a constant well inclination angle of 77.28 degrees calculated from field measurements using the correlation technique described earlier.

Figures 5.17 through 5.**20** show inversion results for the case that includes only bottom sectors (sectors 8 and 9). The density image derived from inversion exhibits azimuthally continuous layer thicknesses and densities. Simulated SS- and LS-detector density images neglect borehole environmental effects. Consequently, mono-sensor and compensated density images simulated from inversion show more azimuthally

continuous layers than field measurements. This effect indicates that some sectors are not reproduced accurately with respect to the measured density images. **Figure 5.15** shows that simulations from inversion of field density measurements acquired with bottom sectors (sectors 8 and 9) yield minimum depth-averaged errors of 3% and 1.5% for SS- and LS-detector density images, respectively. These minimum percent errors are associated with the sectors included for inversion. Density simulations across sectors where field measurements are most affected by tool standoff (upper sectors) yield maximum errors. These errors are as large as 25% and 9% for SS- and LS-detectors, respectively. Large errors reflected on the SS-detector correspond to measurements of low density affected by tool standoff. By comparison, compensated density images simulated from inversion yield maximum average percent errors of 2.5% with respect to field measurements.

Figures 5.21 through 5.**23** show inversion results for the case that includes bottom, right, and left sectors (sectors 6 through 11), and **Figures 5.24** through 5.**26** show results for the case that includes all azimuthal sectors. Comparison of inversion results that increasingly weigh measurements in the upper azimuthal sectors of the borehole emphasize the relative improvement of the results due to inclusion of additional measurements affected by borehole environmental effects. Salient observations from the above inversion exercise are that presence of density measurements affected by environmental effects or noise result in biased inverted values of density and layer thickness. **Figure 5.27** compares average percent errors of simulated density images from inversion to images inverted from field measurements. Inclusion of upper sector density

measurements that are affected by tool standoff in the input data set for inversion increases percent errors in the simulated compensated density images. The integrated value of porosity-feet shows similar results for cases that include only bottom sectors, and a false apparent increase of porosity-feet in the case when inversion is performed with all sectors (**Figures 5.28**, **5.29**, and **5.30**). This latter false increase of porosity-feet is due to erroneous low values of density resulting from tool standoff.

5.4 CONCLUSIONS

We developed and successfully tested a new inversion method for the interpretation of sector-based azimuthal density measurements acquired in laminated sequences penetrated by HA/HZ wells. Inversion was implemented with a recently-developed fast numerical simulation method for nuclear borehole measurements based on Monte Carlo-derived flux sensitivity functions. Firstly, we used a correlation algorithm to estimate dip and azimuth and detected bed boundaries based on inflection points of density measurements. Subsequently, using the estimated values of dip and azimuth as well as *EPL* for each density detector, we refined the location of detected bed boundaries. Secondly, we performed inversion of azimuthal density measurements by constructing a vector of measurements that included measurements from several azimuthal sectors acquired with both SS- and LS-detectors. Thirdly, we performed forward simulations of azimuthal density measurements based on layer densities calculated from inversion and compared them to input measurements to appraise least-squares data residuals and goodness of fit.

As benchmark examples, we performed inversion on synthetic density measurements that were simulated assuming a commercial tool configuration and considering a multi-layer model of various bed thicknesses and alternating density values of 2.0 and 2.6 g/cm^3. Because inversions assumed the same tool configuration and 2D geometrical characteristics of the model as did the simulations of synthetic density measurements, the accuracy of the inversion depended solely on *a-priori* estimated parameters (i.e., boundary location and dip angle) and non-uniqueness of the unknown layer-density values. Simulations of synthetic density measurements did not incorporate borehole environmental effects. Estimated dip angles for these simulations yielded maximum differences of 0.5 degrees with respect to actual values. Simulations based on inversion results in wells deviated 60, 70 and -80 degrees reproduced SS-detector azimuthal density with less than 5% difference with respect to input measurements. Simulations for LS-detector density reproduced all azimuthal sector densities with less than 2% error. Because of increased measurements per layer in HA/HZ wells, redundancy of data decreases non-uniqueness for inversion thereby improving the estimation of layer densities. Inversion reduced shoulder-bed effects, and enabled the quantitative assessment of the reliability and internal consistency of the measurements.

Inversion of synthetic density images simulated from a model constructed from field measurements yielded accurate simulations of density images. The field-based model was constructed from bottom-sector compensated density measurements, which were close to values of formation density, and did not include borehole environmental effects. Comparison of inversion-based density image simulations to assumed density

measurements yielded percent errors of less than 1% for SS-, LS-detectors, and compensated density. Simulations from the field-based model inversion yielded smaller errors compared to the case of the multi-layer model of alternating 2.0 and 2.6 g/cm^3 density layers primarily because of the relatively larger thickness of layers included in the field-based model. Additionally, integrated porosity-feet calculated from the filed-based inversion increased by 3% with respect to that calculated with the synthetic compensated density.

Finally, we used field measurements for inversion of density images. Field density measurements were acquired with the same LWD tool used in our simulations. Because density images constructed from mono-sensor field measurements were influenced by borehole environmental effects, and simulations do not include tool standoff, inversion preferentially weighed azimuthal sectors that were the least affected by tool standoff. Density images simulated from inversion results that included only bottom sectors reproduced these sectors with less than 3% error with respect to field measurements. Simulations of mono-sensor density across the upper sectors yielded large values of data misfit because tool standoff was not included in the inversion. However, compensated density images simulated from inversion results yielded errors smaller than 2.5% across all azimuthal sectors. Incorporating additional sectors of field measurements that exhibit non-zero tool standoff effects did not, in general, improve inversion results. The reduction of shoulder-bed effects with inversion enabled quantitative appraisal of the reliability and internal consistency of the field measurements. Future work would include the effect of tool standoff in density measurements simulations and inversion.

Calculations of integrated porosity-feet over the analyzed measured depth interval quantified the relative improvement between inversion and standard compensated post-processing of mono-sensor density images. In all cases, inversion yielded a constant value of porosity-feet across azimuthal sectors while compensated density yielded an azimuthally variable one. Integrated porosity-feet values averaged over azimuthal sectors from compensated density images were approximately 2 feet or 7% less than values from inversion results that included only bottom sectors across the same measured depth interval. By comparison, integrated porosity-feet calculated from inversion results that included additional azimuthal sectors increased by 27% and 64% with respect to that calculated from the compensated density measurements. Including density measurements with large tool standoff effects in the inversion may result in biased porosity-feet estimations. For best practice, it is recommended that those sectors not be included in the inversion.

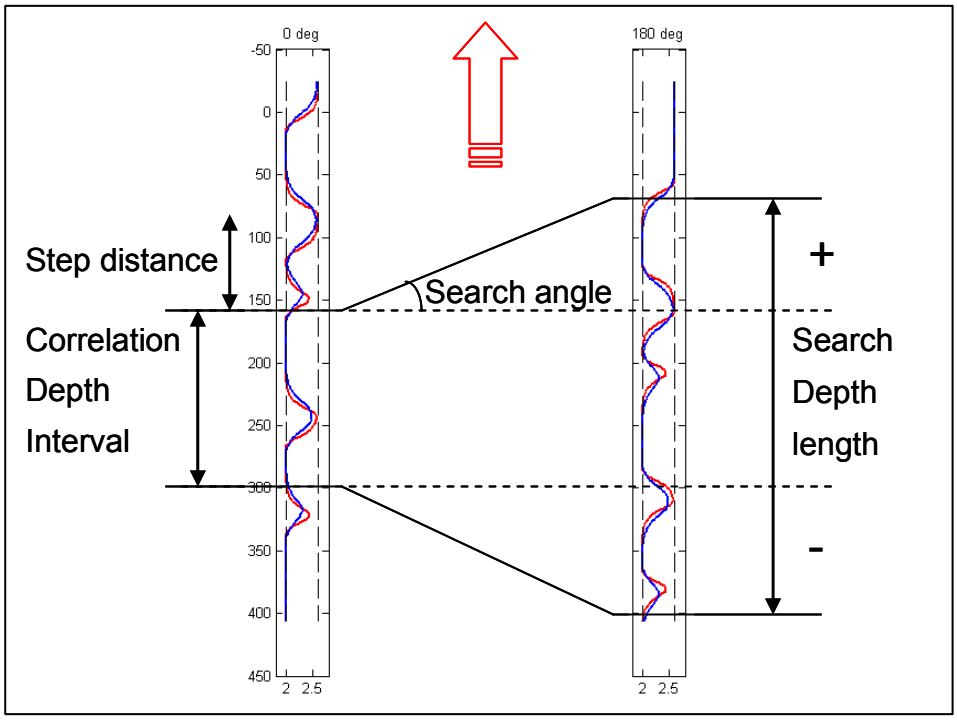

Figure 5.1: Schematic of the variables included in the fixed-interval correlation technique for dip angle estimation. The correlation depth interval is a selected depth section used for maximum coherence. Search angle controls the amplitude of the maximum offset angle between azimuthal sectors. Search length includes the total depth interval of azimuthal sectors searched for maximum coherence. Step distance defines the number of depth points where an angle is estimated across a section (Cameron et al., 1993).

(a)

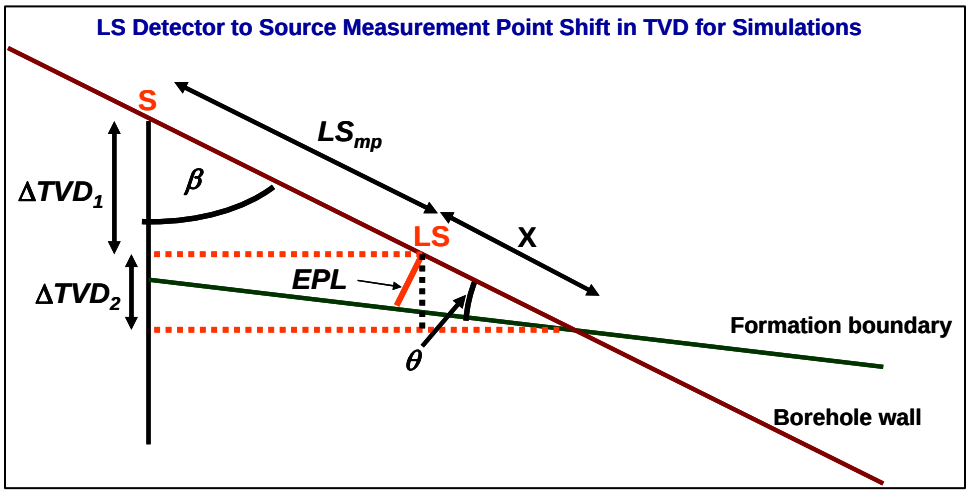

(b)

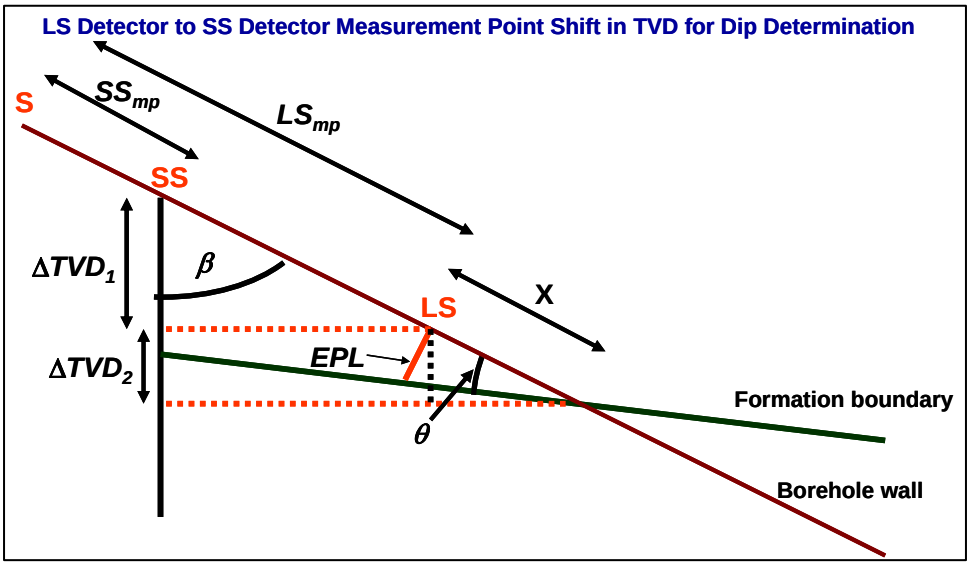

Figure 5.2: Geometrical conventions for the detection of bed boundaries based on dip angle, effective penetration length (*EPL*), and source-detector spacing. In the figure, S is source location, and LS and SS are the locations of measurement points for long- and short-spaced detectors, respectively. The subscript *mp* designates measurement points. β is borehole inclination angle and θ is formation dip angle. ΔTVD_1 and ΔTVD_2 are true vertical depth-shifts from **(a)** source to LS-detector measure point and LS-detector measure point to the intersection between a boundary and the borehole, respectively, and **(b)** from SS-detector to LS-detector, and from LS-detector to the intersection between a boundary and the borehole, respectively. The figure assumes measurements acquired with a bottom azimuthal sector.

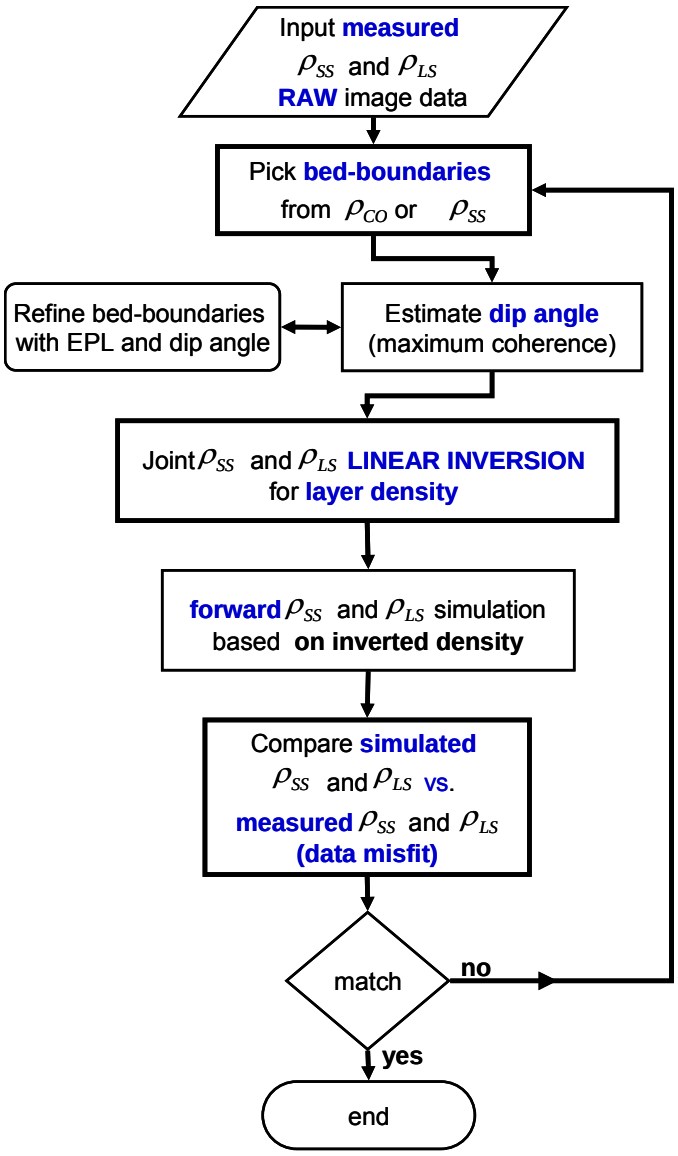

Figure 5.3: Flow chart of the sector-based inversion procedure for estimating layer densities from raw mono-sensor azimuthal density measurements. The procedure starts by selecting boundaries and estimating dip angle, followed by linear inversion, and forward simulation of density images based on the layer densities estimated from inversion.

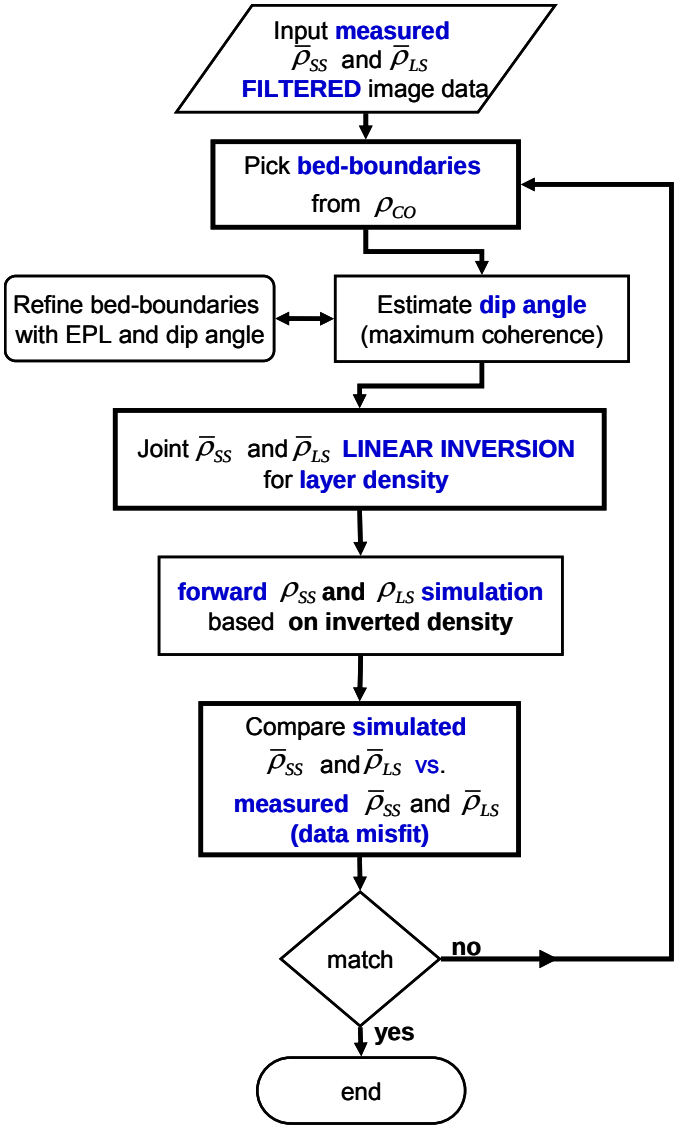

Figure 5.4: Flow chart of the sector-based inversion procedure for estimating layer densities from filtered mono-sensor azimuthal density measurements. The procedure starts by selecting boundaries and estimating dip angle, followed by linear inversion, and forward simulation of density images based on the layer densities estimated from inversion.

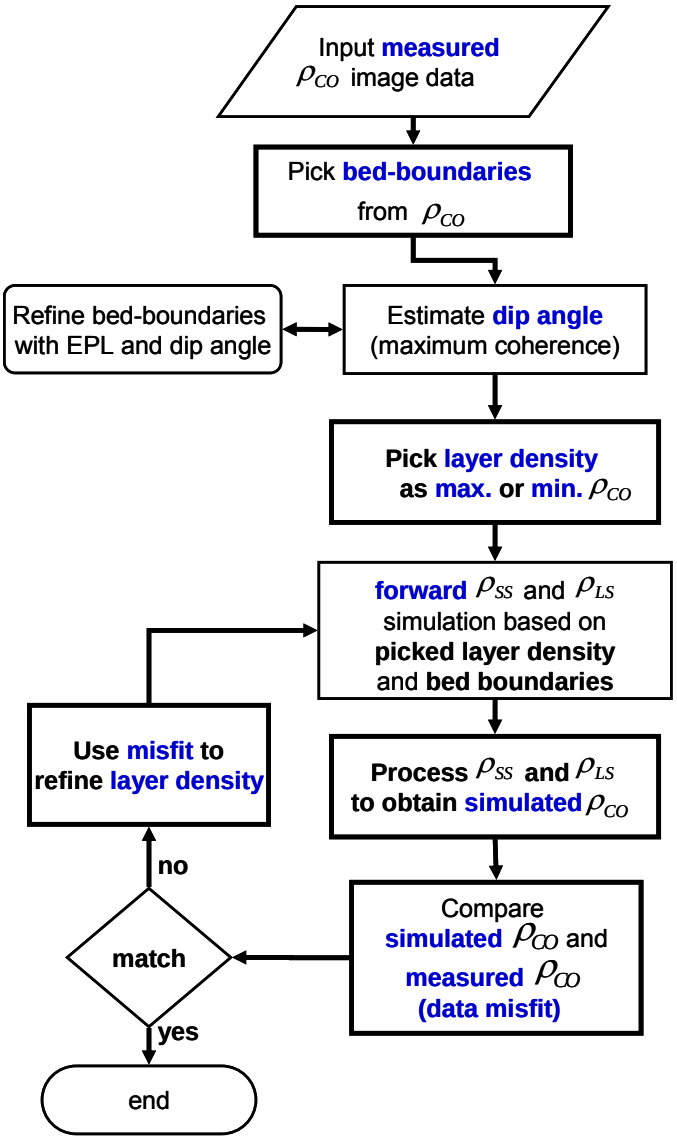

Figure 5.5: Flow chart of the iterative sector-based inversion procedure for estimating layer densities from compensated azimuthal density measurements. The procedure starts by selecting boundaries and estimating dip angle, followed by the construction of a model based on field measurements, and forward simulation of density images based on the multi-layer model. Residuals between simulations and field measurements (data misfits) are used to refine layer density values and to repeat the simulations until securing an acceptable data misfit.

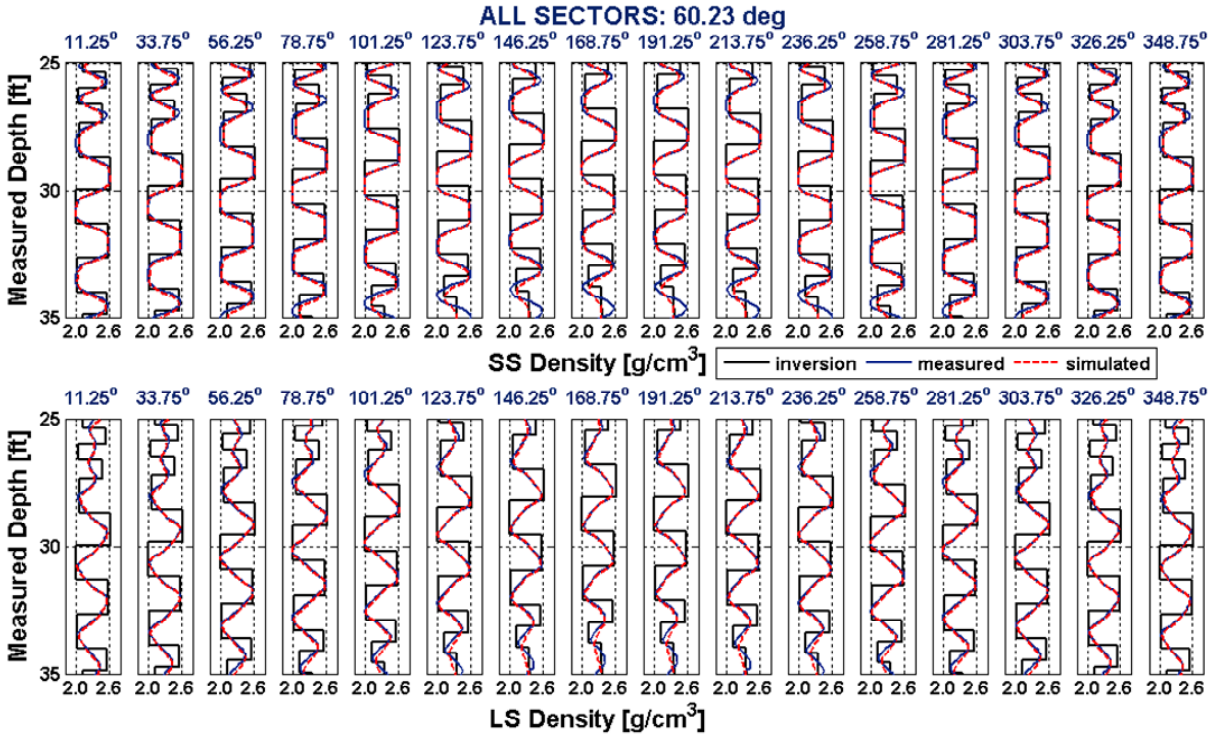

Figure 5.6: Example of inversion of synthetic measurements for the case of a 60-degree deviated well: Measured density is assumed from simulated density measurements across a multi-layer model consisting of thin layers of 2.0 and 2.6 g/cm^3 alternating density values. The assumed borehole diameter is 8.5 inches and the direction of drilling is up-dip. Estimated well inclination angle was 60.23 degrees. Curves describe: azimuthal sector density from inversion (piece-wise constant black line), simulations based on inversion (dashed red curves), and assumed measurements (continuous blue curve). Top panels show results from SS-detector inversion and simulations. Bottom panels correspond to LS-detector density inversion and simulations. Blue numbers describe azimuthal location around the perimeter of the borehole of each sector. The regularization parameter, λ, equals 0.8 and controls the amplitude of inversion across the thinner layers. A prescribed constant model, $\bar{\mathbf{x}}_0$, was assumed equal to 2.3 g/cm^3. Refer to Equations (5.3) through (5.5) for details about the inversion method.

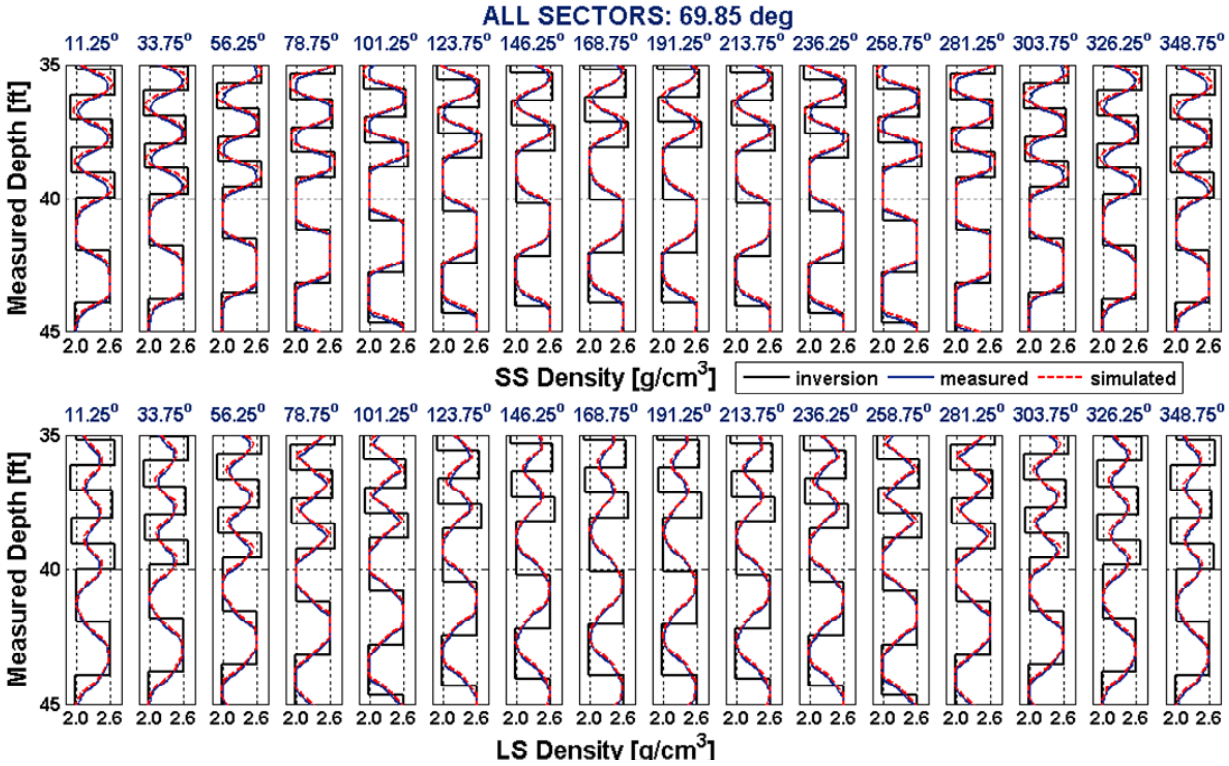

Figure 5.7: Example of inversion of synthetic measurements for the case of a 70-degree deviated well: Measured density is assumed from simulated density measurements across a multi-layer model consisting of thin layers of 2.0 and 2.6 g/cm^3 alternating density values. The assumed borehole diameter is 8.5 inches and the direction of drilling is up-dip. Estimated well inclination angle was 69.85 degrees. Curves describe: azimuthal sector density from inversion (piece-wise constant black line), simulations based on inversion (dashed red curves), and assumed measurements (continuous blue curve). Top panels show results from SS-detector inversion and simulations. Bottom panels correspond to LS-detector density inversion and simulations. Blue numbers describe azimuthal location around the perimeter of the borehole of each sector. The regularization parameter, λ, equals 0.4 and controls the amplitude of inversion across the thinner layers. A prescribed constant model, $\bar{\mathbf{x}}_0$, was assumed equal to 2.3 g/cm^3. Refer to Equations (5.3) through (5.5) for details about the inversion method.

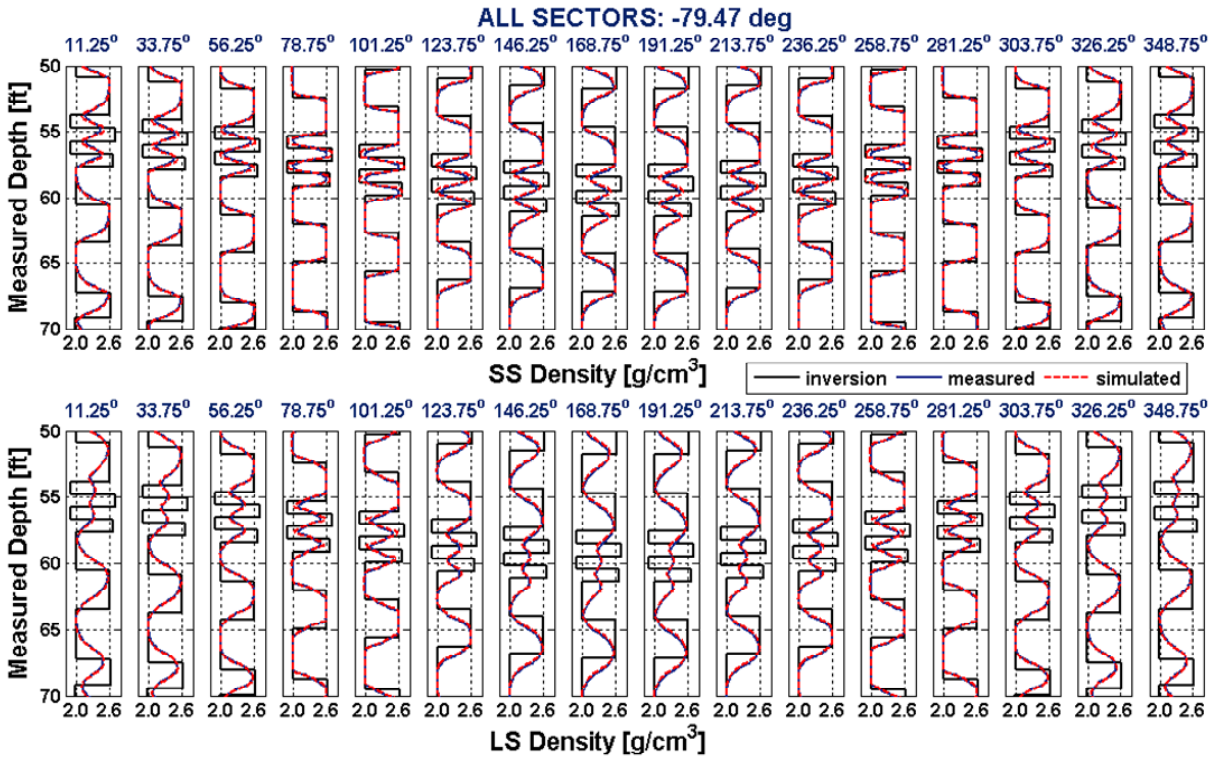

Figure 5.8: Example of inversion of synthetic measurements for the case of an 80-degree deviated well: Measured density is assumed from simulated density measurements across a multi-layer model consisting of thin layers of 2.0 and 2.6 g/cm^3 alternating density values. The assumed borehole diameter is 8.5 inches and the direction of drilling is down-dip. Estimated well inclination angle was -79.47 degrees. Curves describe: azimuthal sector density from inversion (piece-wise constant black line), simulations based on inversion (dashed red curves), and assumed measurements (continuous blue curve). Top panels show results from SS-detector inversion and simulations. Bottom panels correspond to LS-detector density inversion and simulations. Blue numbers describe azimuthal location around the perimeter of the borehole of each sector. The regularization parameter, λ, equals 0.2 and controls the amplitude of inversion across the thinner layers. A prescribed constant model, $\bar{\mathbf{x}}_0$, was assumed equal to 2.3 g/cm^3. Refer to Equations (5.3) through (5.5) for details about the inversion method.

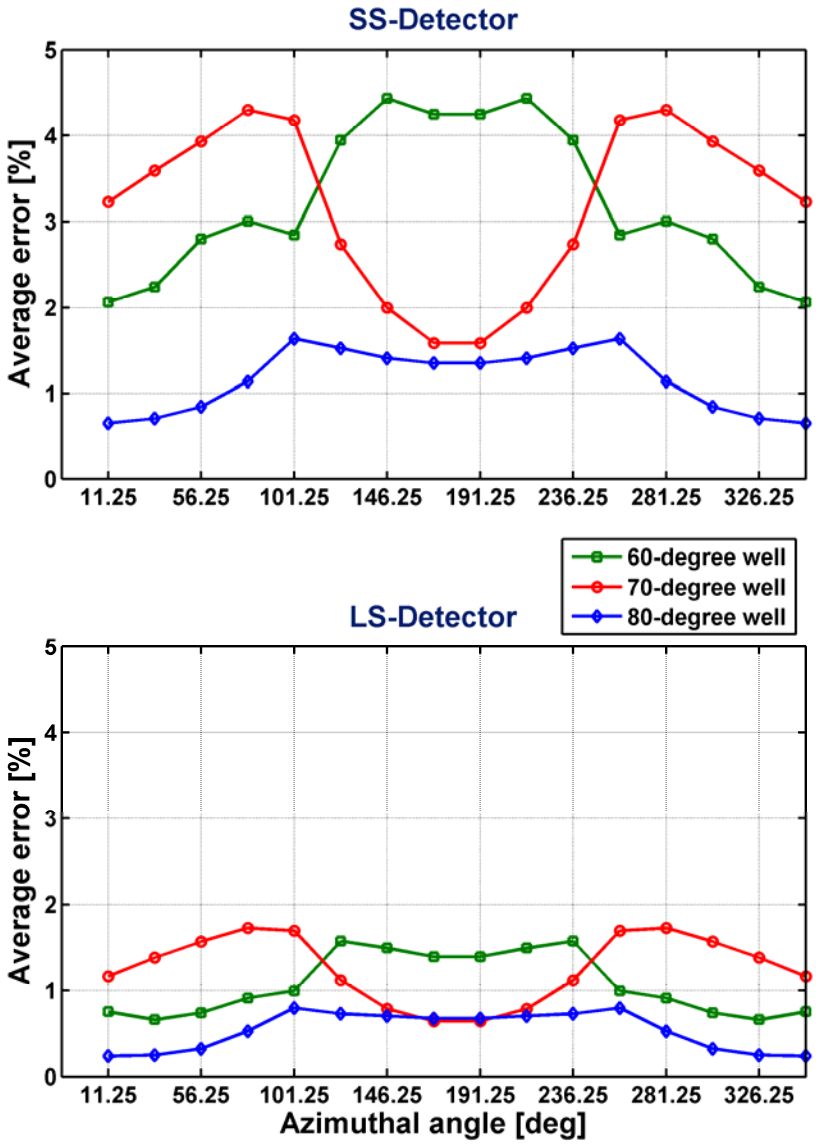

Figure 5.9: Comparison of sector-based inversion results across azimuthal sectors for cases of synthetic density measurements acquired in wells of 60, 70, and -80 degrees of inclination. Colored curves show percent differences between azimuthal density simulations from inversion and density azimuthal measurements averaged across the same depth interval. Refer to Figures 5.5 through 5.7 for details about the assumed multi-layer model and inversion parameters.

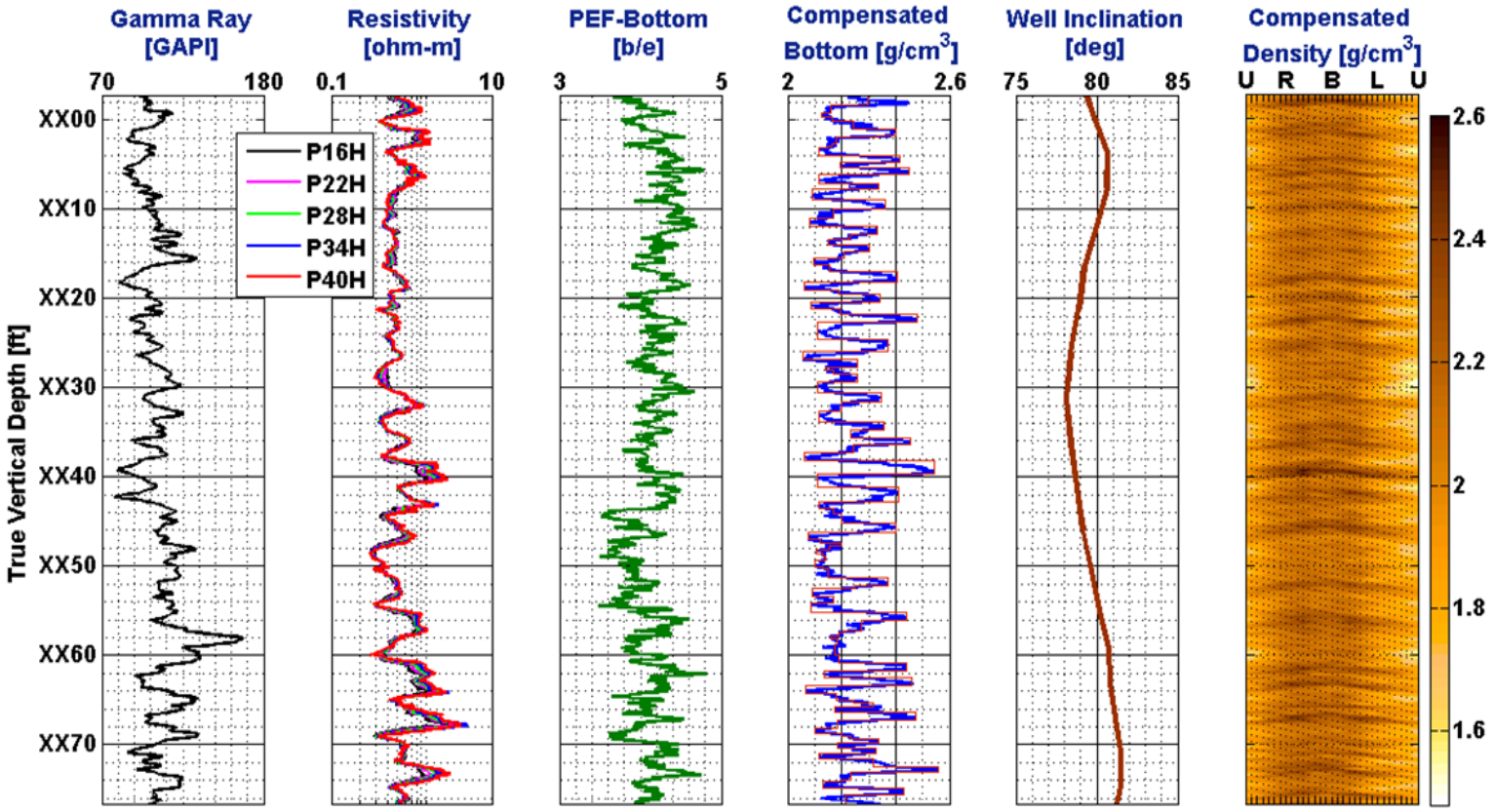

Figure 5.10: Logging while drilling (LWD) measurements acquired in a highly deviated well displayed in true vertical depth (TVD). Measurements were acquired with the same commercial tool assumed in the inversion and simulation examples considered in this paper. Starting from the left, panel 4 shows compensated bottom sector density measurements (blue curve) used for the construction of a field-based model (piece-wise constant red line). Well inclination in panel 5 fluctuated between 78 and 82 degrees and the direction of drilling is up-dip. Panel 6 shows a density image constructed from compensated density measurements.

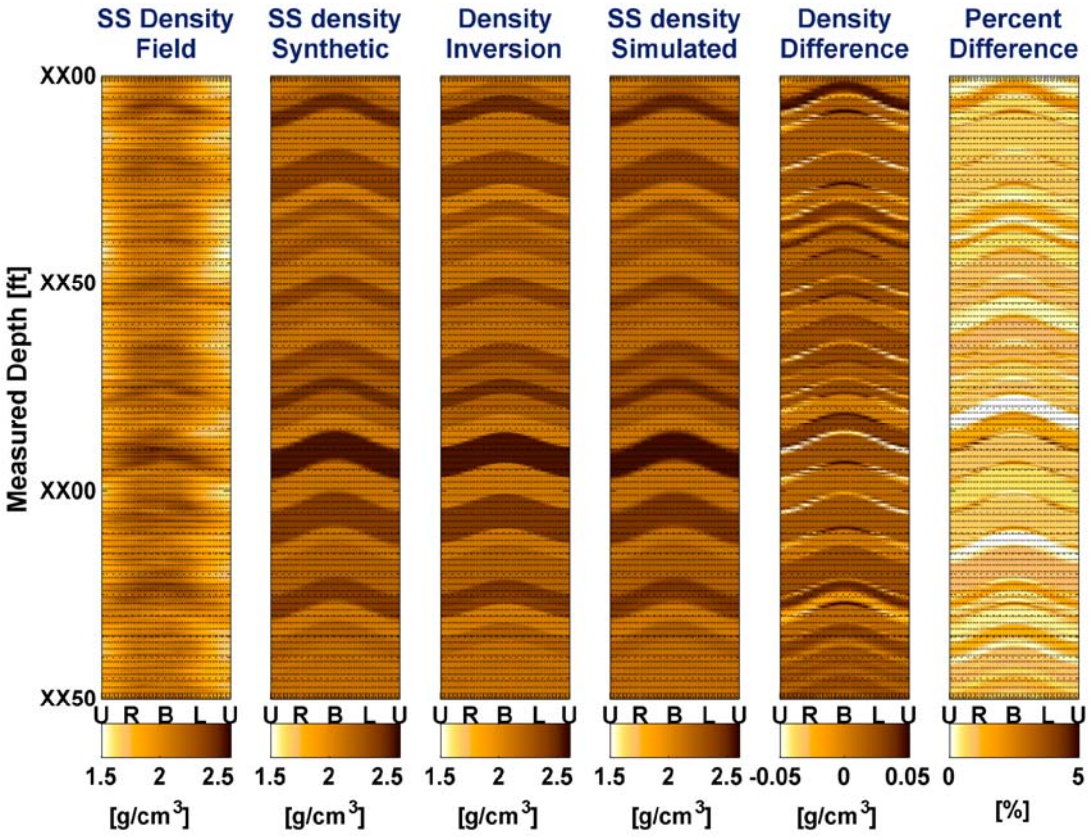

Figure 5.11: Density image obtained from short-spacing (SS) detector density azimuthal measurements. From left to right, panels describe: field-measurement image, synthetic density image (simulated from a model constructed from field measurements), density inversion image (constructed from sector-based layer density inverted from synthetic density image), density image simulated from the inversion image, and percent difference between synthetic density and simulated density images.

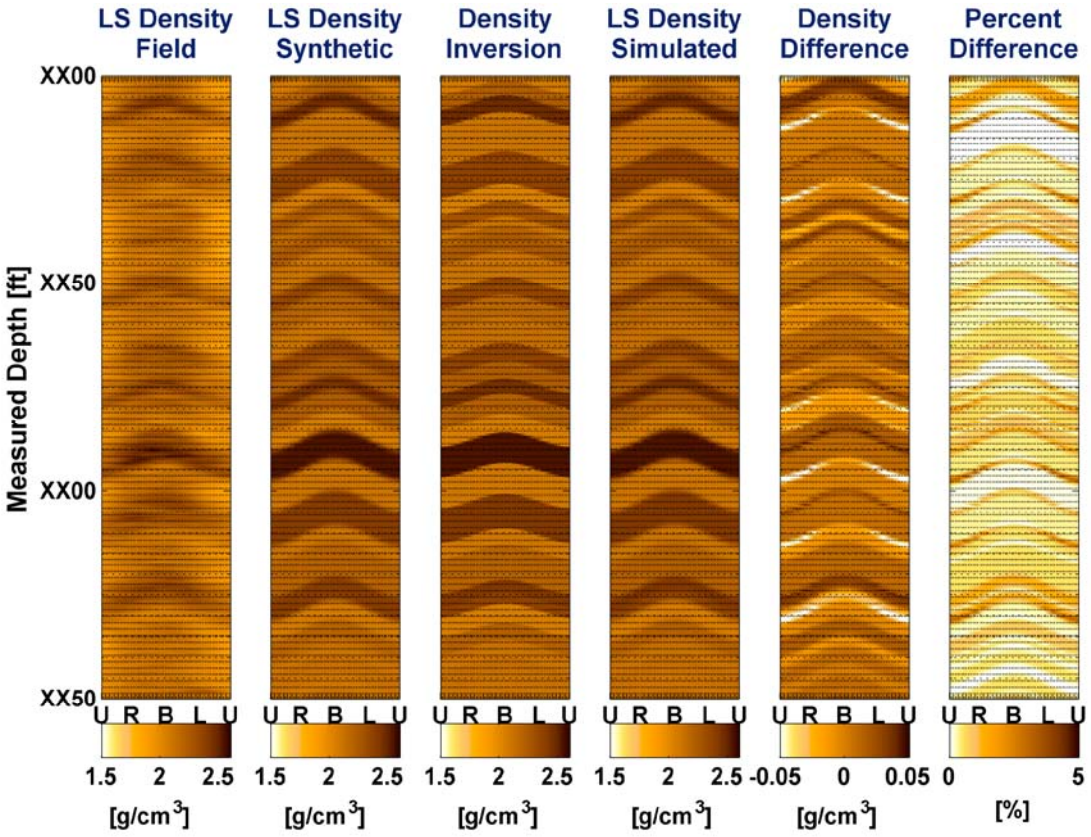

Figure 5.12: Density image obtained from long-spacing (LS) detector density azimuthal measurements. From left to right, panels describe: field-measurement image, synthetic density image (simulated from a model constructed from field measurements), density inversion image (constructed from sector-based layer density inverted from synthetic density image), density image simulated from the inversion image, and percent difference between synthetic density and simulated density images.

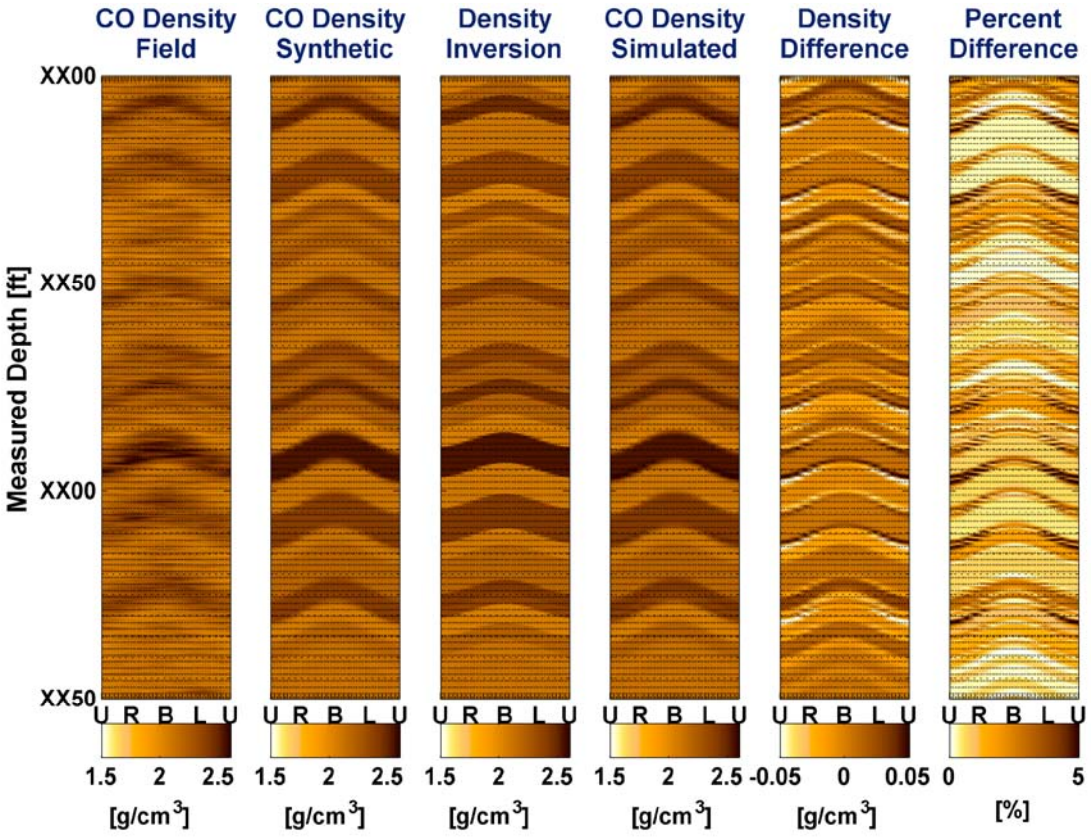

Figure 5.13: Density image obtained from compensated density azimuthal measurements. From left to right, panels describe: field-measurement image, synthetic density image (simulated from a model constructed from field measurements), density inversion image (constructed from sector-based layer density inverted from synthetic density image), density image simulated from the inversion image, and percent difference between synthetic density and simulated density images.

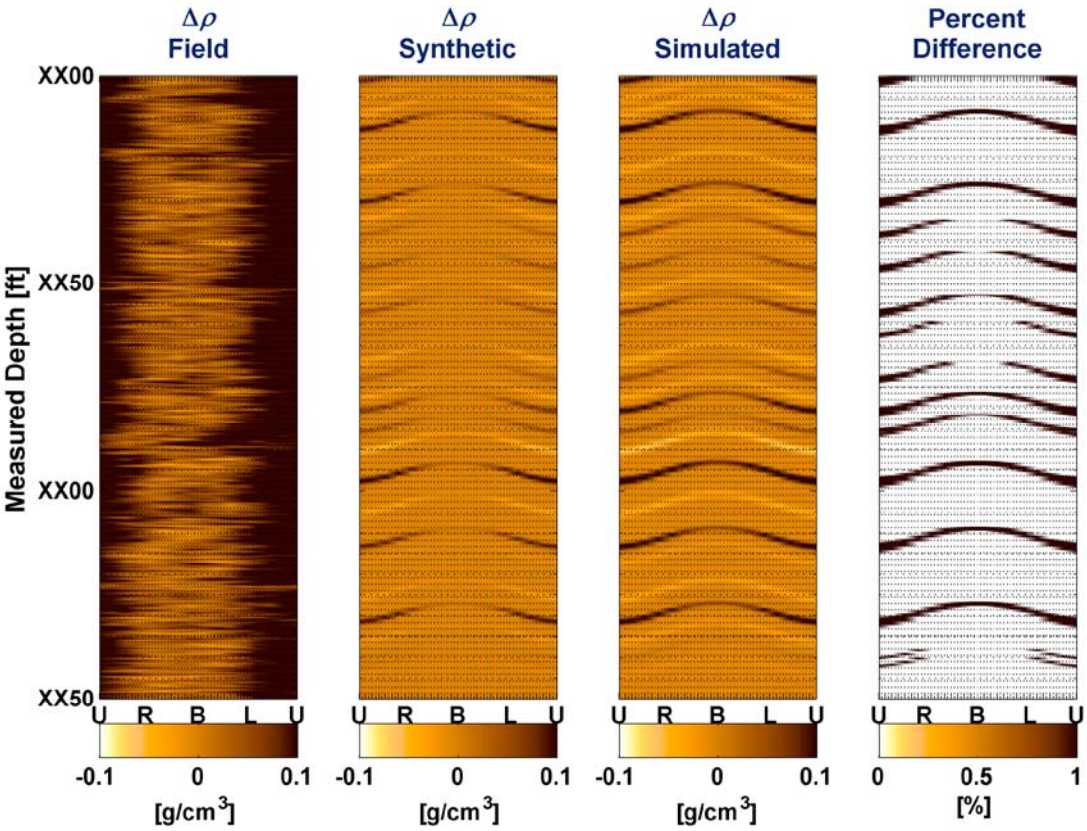

Figure 5.14: Density image obtained from density correction azimuthal measurements. From left to right, panels describe: field measurement image, synthetic density correction image (simulated from a model constructed from the field measurements), density image simulated from the inversion image, and percent difference between synthetic and the simulated density images.

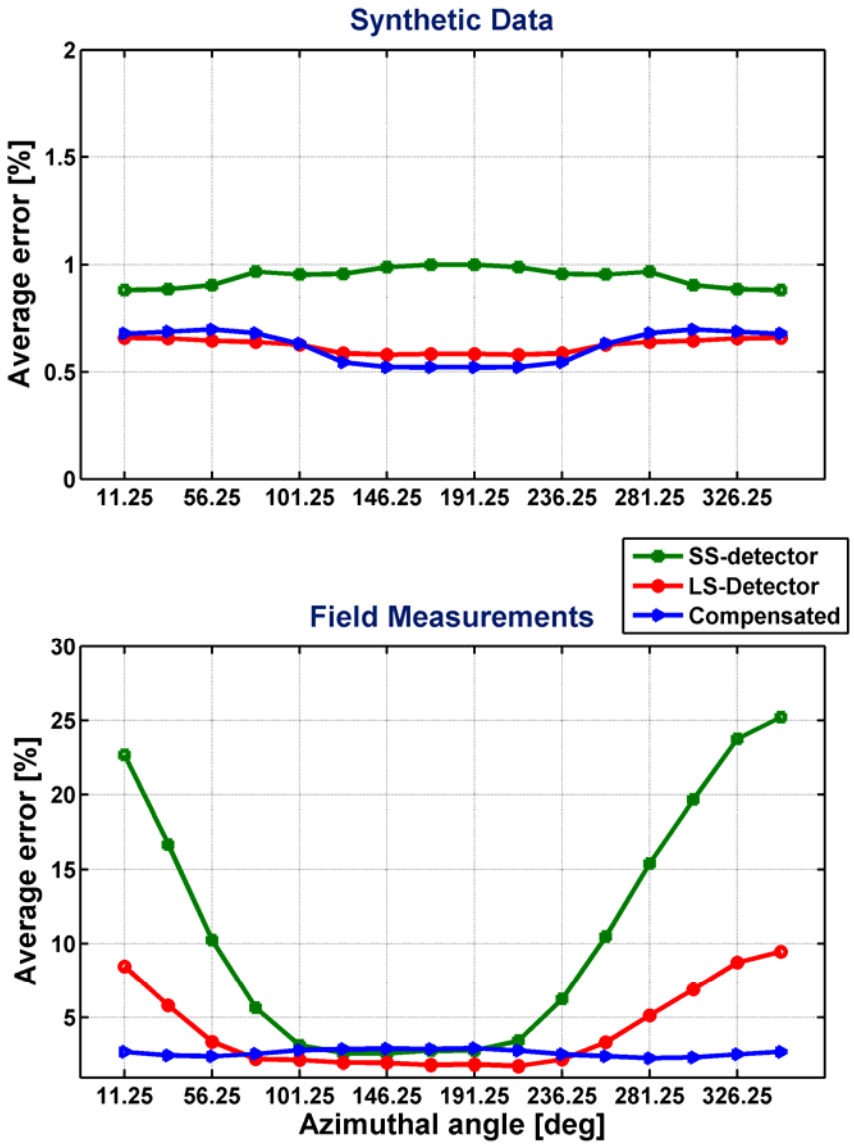

Figure 5.15: Comparison of sector-based inversion across azimuthal sectors. The top panel shows the case of synthetic density measurements simulated from a model constructed from field measurements. The Bottom panel shows the case of inversion from field measurements. Colored curves show percent differences between azimuthal density simulations from inversion and density azimuthal measurements averaged across the same depth interval. Refer to Figures 5.11 through 5.13 for details about the density images.

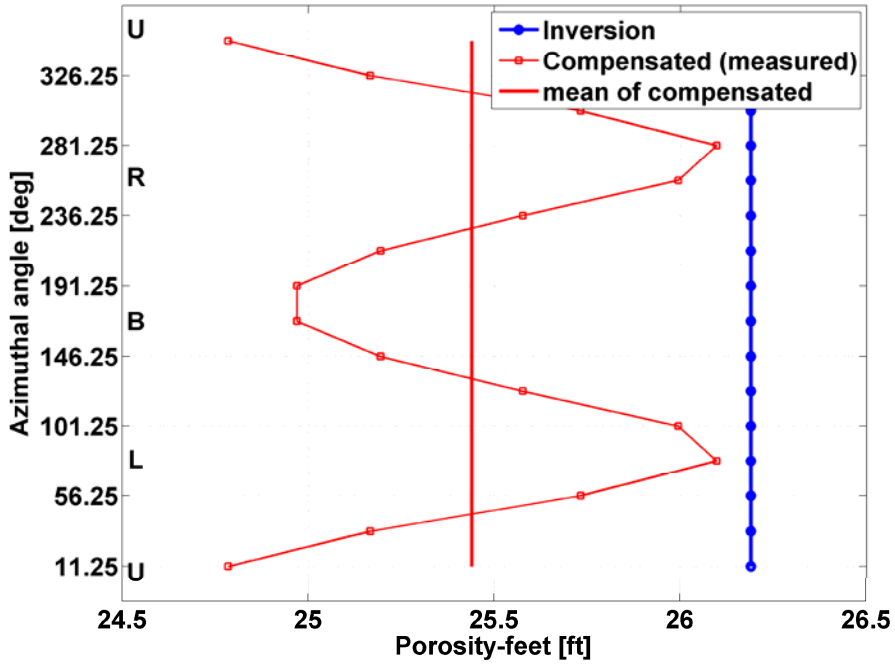

Figure 5.16: Comparison of integrated values of porosity-feet calculated from inversion and from compensated density for the case of synthetic azimuthal density simulated from a model constructed from field data. The blue line describes integrated porosity-feet calculated from inversion, and the straight red line describes the azimuthally-averaged integral porosity-feet calculated from synthetic compensated density. Letters along the vertical axis designate upper sectors (U), right sectors (R), bottom sectors (B), and left sectors (L). Refer to Figures 5.11 through 5.13 for details about inversions and simulations.

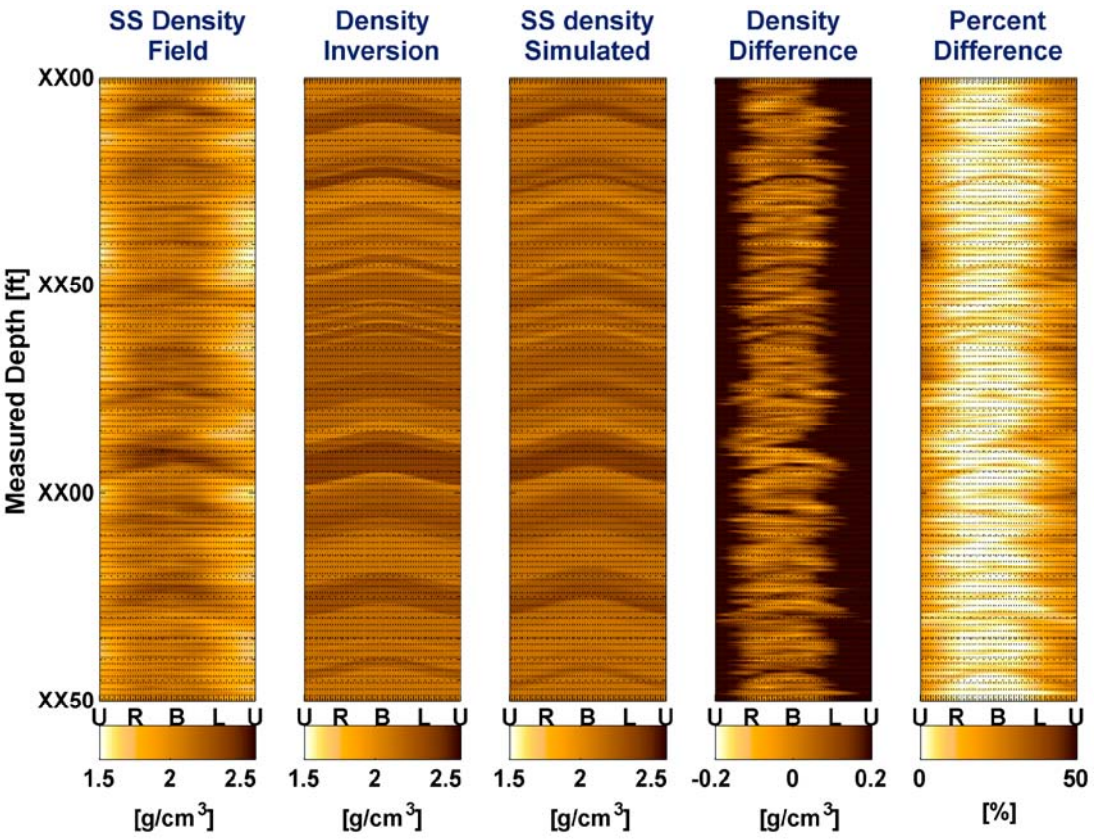

Figure 5.17: Density image obtained from short-spacing (SS) detector density azimuthal field measurements. From left to right, panels describe: field measurement image, density inversion image (constructed from sector-based layer density inverted from the field density image), density image simulated from the inversion image, and percent difference between field density and simulated density images. Inversion was performed with bottom sectors only (sectors 8 and 9).

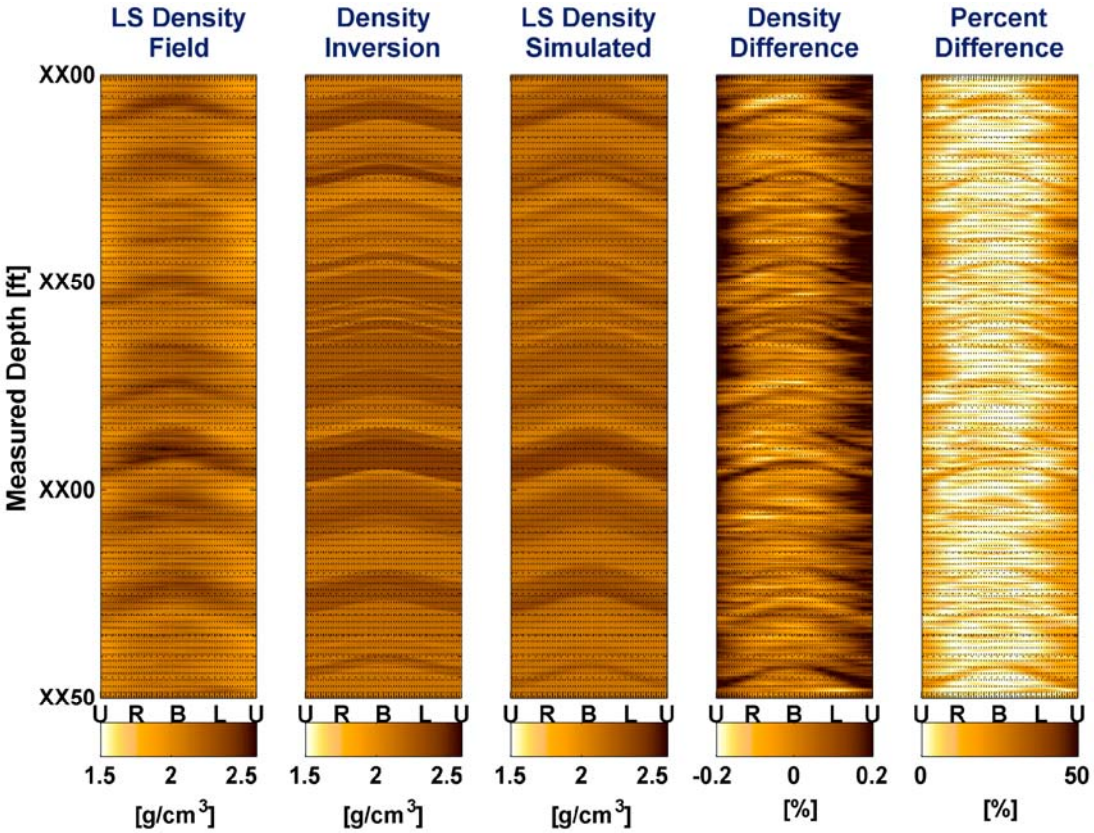

Figure 5.18: Density image obtained from long-spacing (LS) detector density azimuthal field measurements. From left to right, panels describe: field measurement image, density inversion image (constructed from sector-based layer density inverted from the field density image), density image simulated from the inversion image, and percent difference between field density and simulated density images. Inversion was performed with bottom sectors only (sectors 8 and 9).

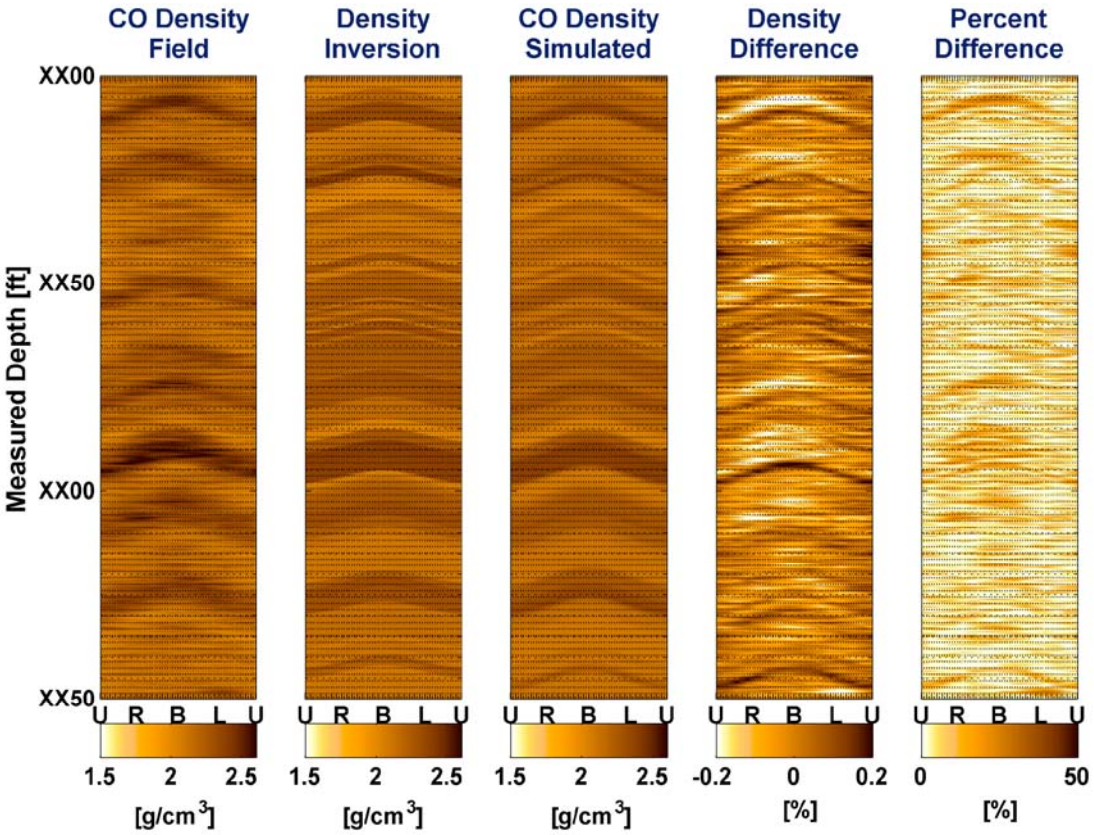

Figure 5.19: Density image obtained from compensated density azimuthal field measurements. From left to right, panels describe: field measurement image, density inversion image (constructed from sector-based layer density inverted from the field density image), density image simulated from the inversion image, and percent difference between field density and simulated density images. Inversion was performed with bottom sectors only (sectors 8 and 9).

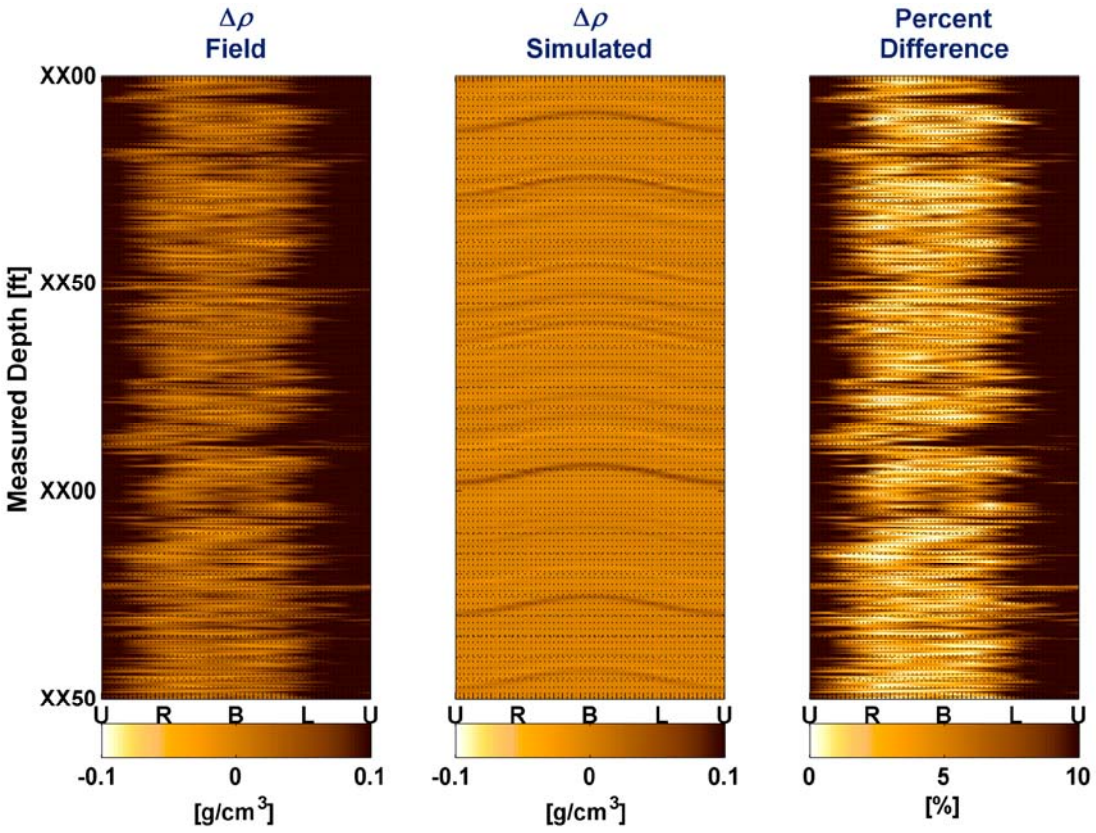

Figure 5.20: Density correction images obtained from density azimuthal field measurements. From left to right, panels describe: field measurement density correction image, density correction image simulated from the inversion image, and percent difference between field and the simulated density images. Inversion was performed with bottom sectors only (sectors 8 and 9).

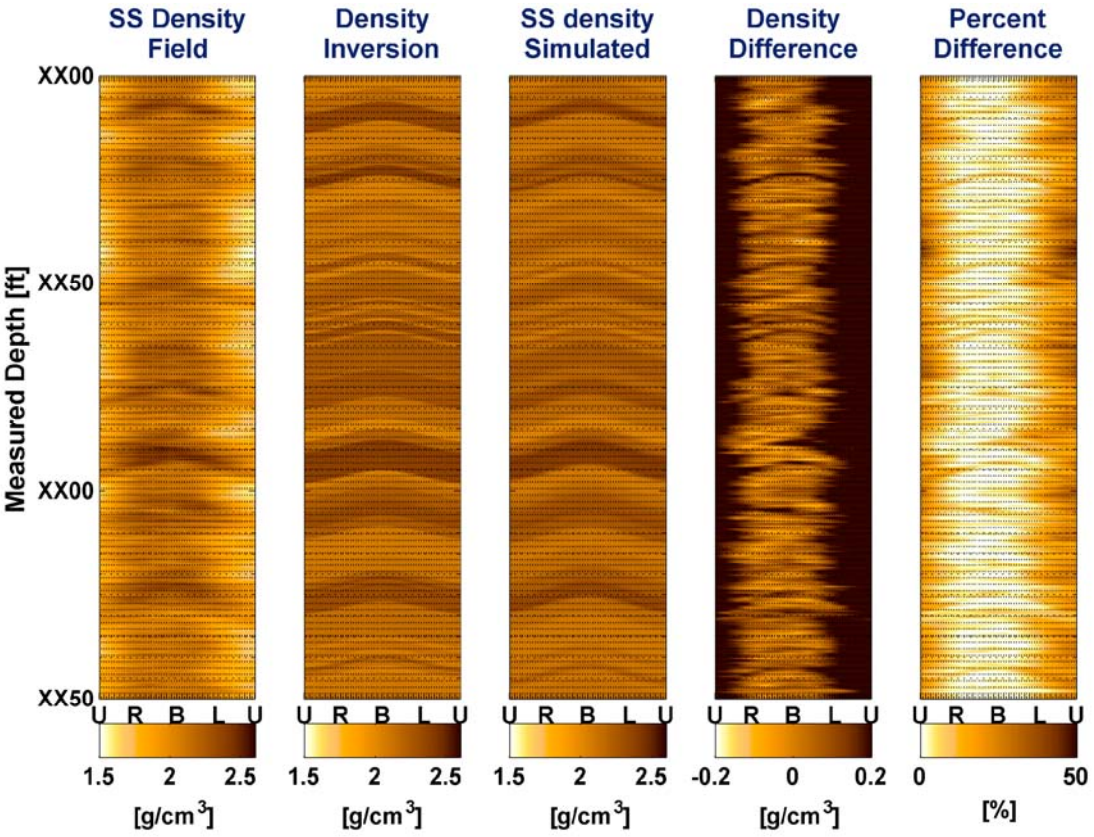

Figure 5.21: Density image obtained from short-spacing (SS) detector density azimuthal field measurements. From left to right, panels describe: field measurement image, density inversion image (constructed from sector-based layer density inverted from the field density image), density image simulated from the inversion image, and percent difference between field density and simulated density images. Inversion was performed with bottom and side sectors (sectors 6 through 11).

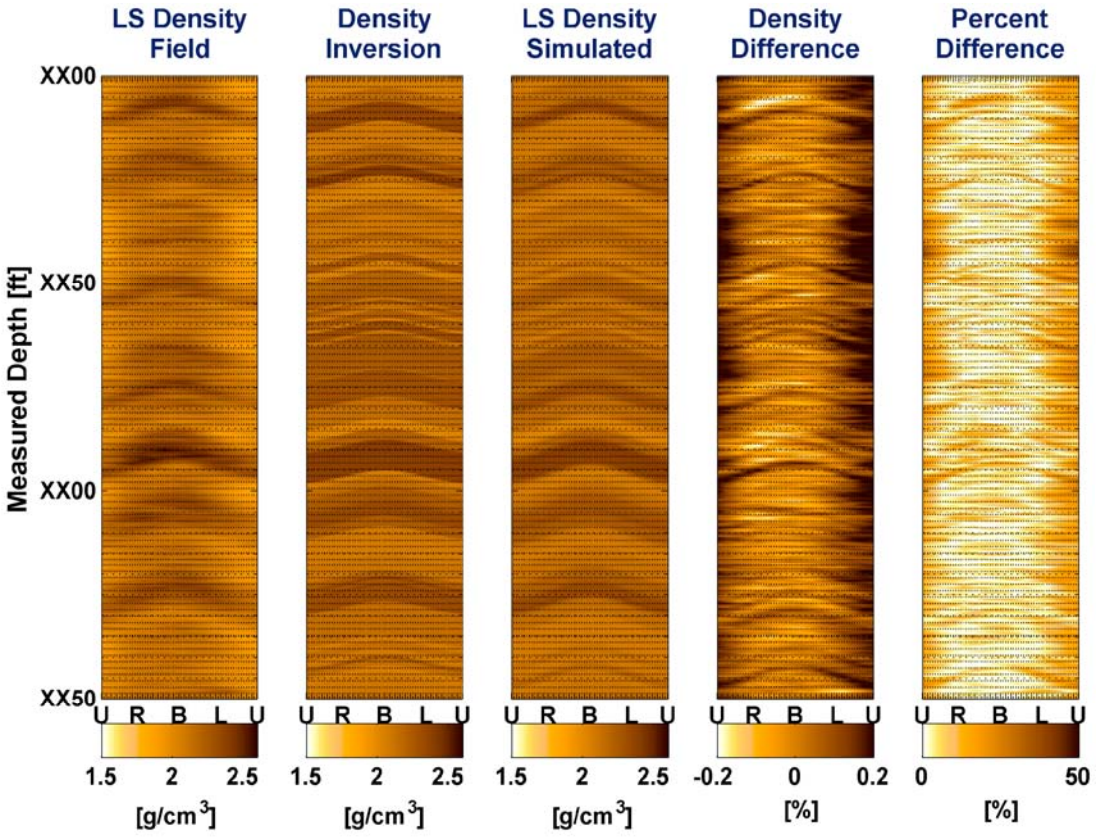

Figure 5.22: Density image obtained from long-spacing (LS) detector density azimuthal field measurements. From left to right, panels describe: field measurement image, density inversion image (constructed from sector-based layer density inverted from the field density image), density image simulated from the inversion image, and percent difference between field density and simulated density images. Inversion was performed with bottom and side sectors (sectors 6 through 11).

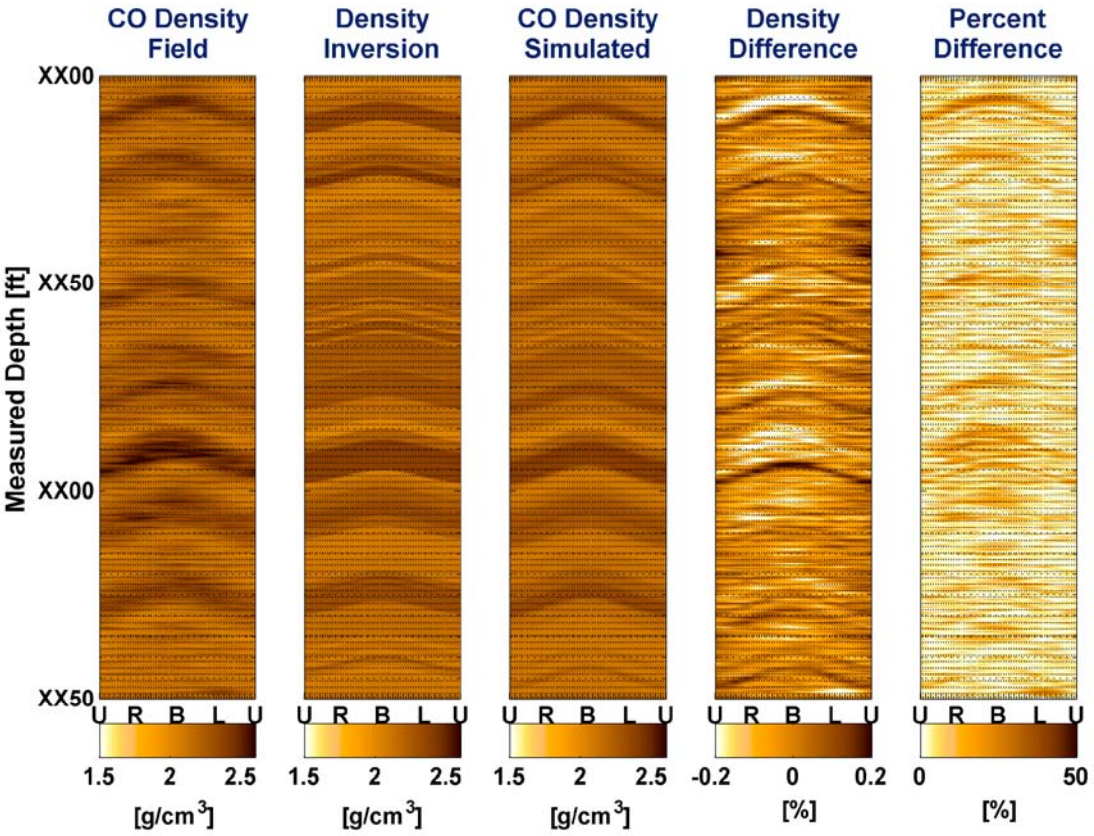

Figure 5.23: Density image obtained from compensated density azimuthal field measurements. From left to right, panels describe: field measurement image, density inversion image (constructed from sector-based layer density inverted from the field density image), density image simulated from the inversion image, and percent difference between field density and simulated density images. Inversion was performed with bottom and side sectors (sectors 6 through 11).

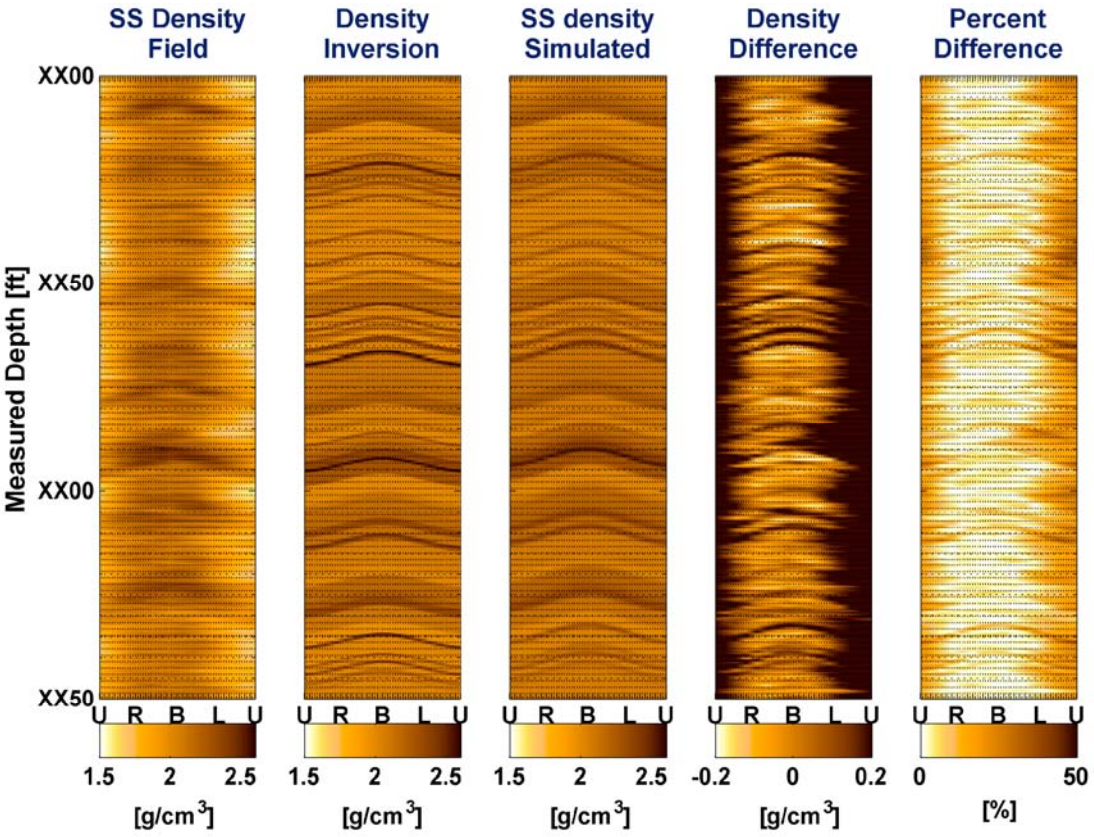

Figure 5.24: Density image obtained from short-spacing (SS) detector density azimuthal field measurements. From left to right, panels describe: field measurement image, density inversion image (constructed from sector-based layer density inverted from the field density image), density image simulated from the inversion image, and percent difference between field density and simulated density images. Inversion was performed with all azimuthal sectors (sectors 1 through 16).

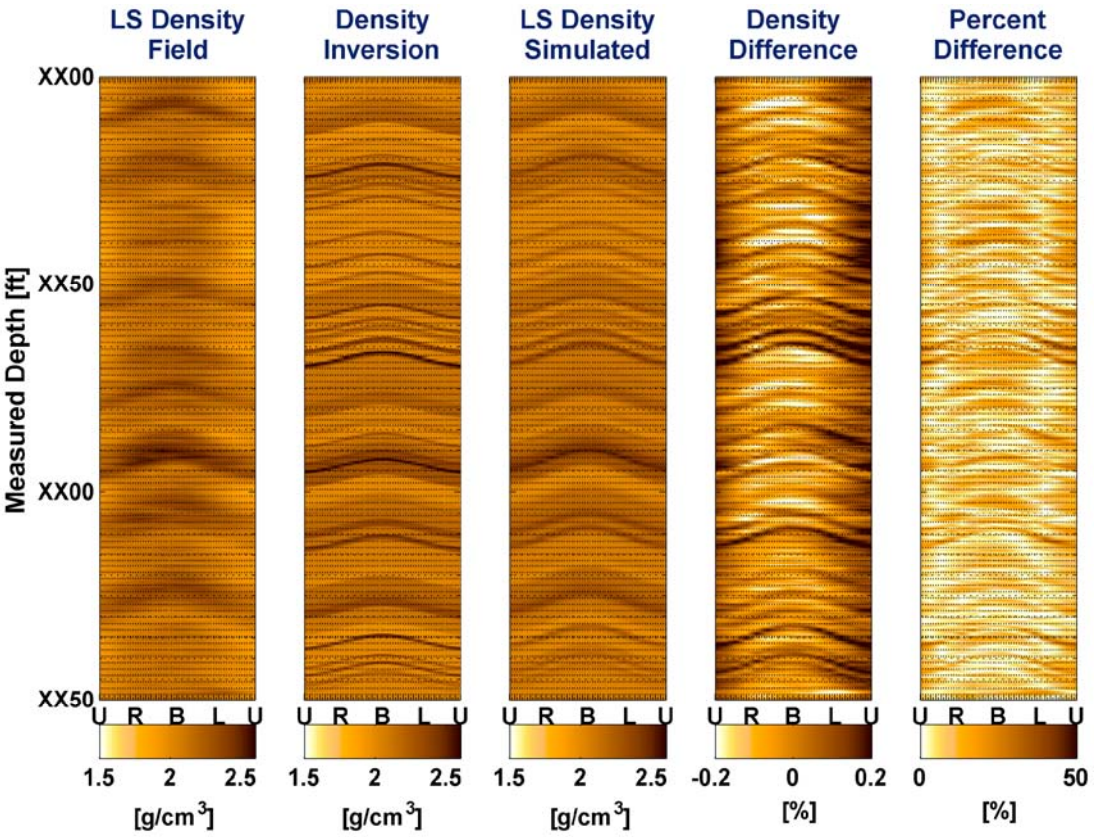

Figure 5.25: Density image obtained from long-spacing (LS) detector density azimuthal field measurements. From left to right, panels describe: field measurement image, density inversion image (constructed from sector-based layer density inverted from the field density image), density image simulated from the inversion image, and percent difference between field density and simulated density images. Inversion was performed with all azimuthal sectors (sectors 1 through 16).

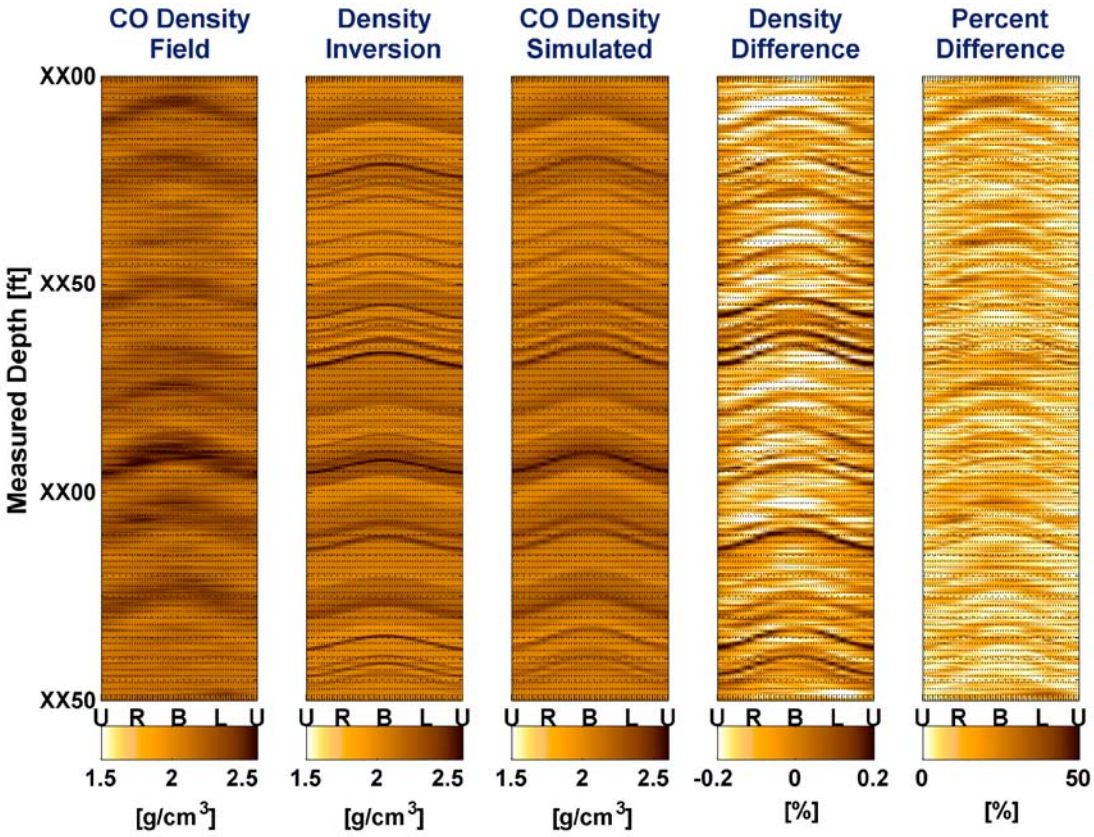

Figure 5.26: Density image obtained from compensated density azimuthal field measurements. From left to right, panels describe: field measurement image, density inversion image (constructed from sector-based layer density inverted from the field density image), density image simulated from the inversion image, and percent difference between field density and simulated density images. Inversion was performed with all azimuthal sectors (sectors 1 through 16).

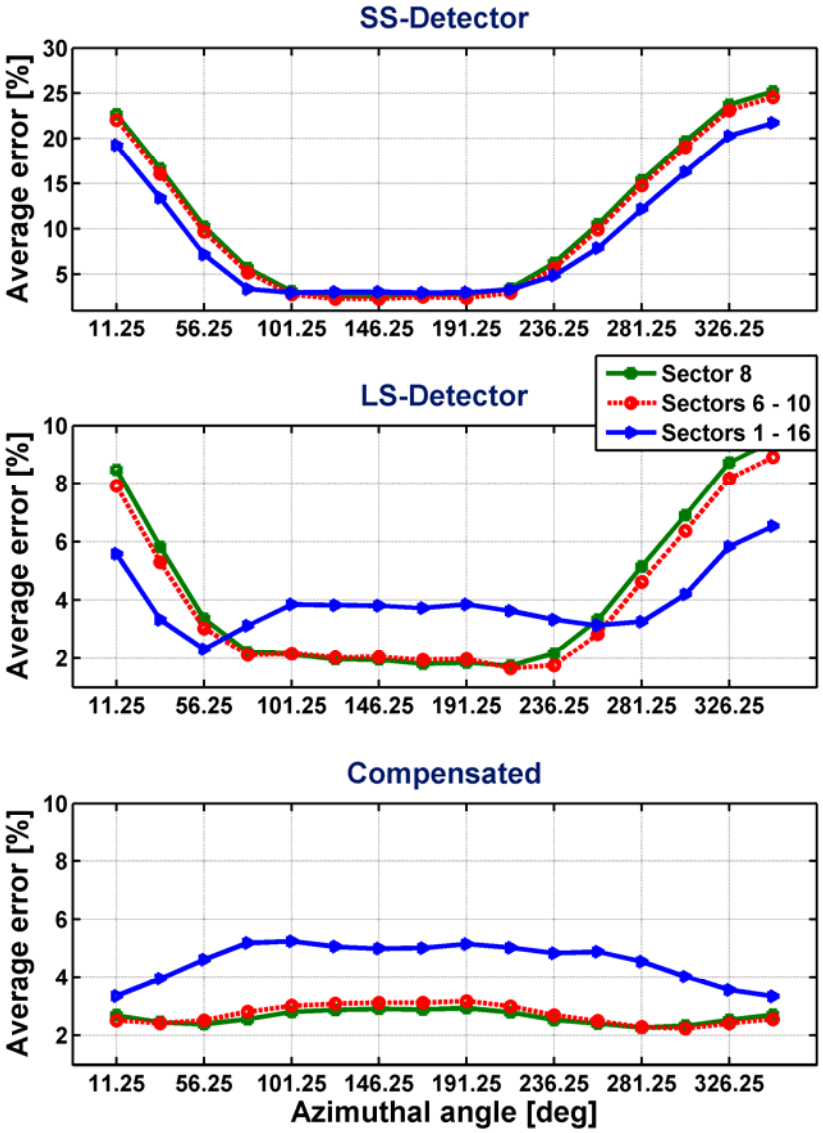

Figure 5.27: Comparison of sector-based inversion from field measurements across azimuthal sectors. From top to bottom, panels show: simulations for SS-detector density, simulations for LS-detector density, and simulations for compensated density. Colored curves show percent differences between azimuthal density simulations from inversion and density measurements, averaged across the same depth interval. Green curves describe inversion including bottom sectors only. Red and blue curves describe inversion including bottom and side sectors and including all sectors, respectively. Refer to Figures 5.17 through 5.26 for details about the density images.

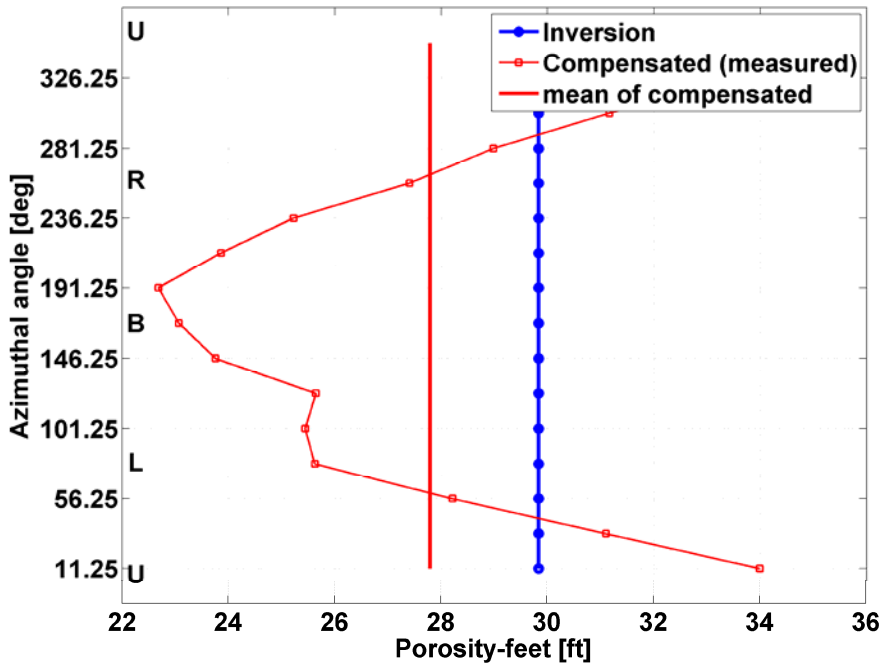

Figure 5.28: Comparison of integrated values of porosity-feet calculated from inversion and from compensated density for the case of inversion performed with only bottom sectors in the vector of measurements. The blue line describes integrated porosity-feet calculated from inversion, and the straight red line describes the azimuthally-averaged integral porosity-feet calculated from field compensated density. Letters along the vertical axis designate upper sectors (U), right sectors (R), bottom sectors (B), and left sectors (L). Refer to Figures 5.17 through 5.20 for details about inversions and simulations.

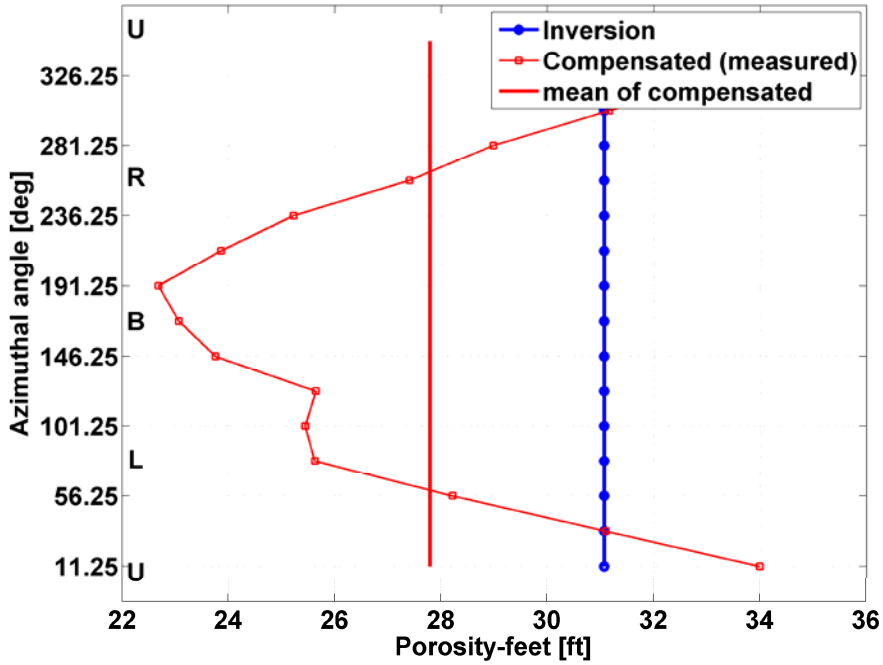

Figure 5.29: Comparison of integrated values of porosity-feet calculated from inversion and from compensated density for the case of inversion performed with bottom and side sectors in the vector of measurements. The blue line describes integral porosity-feet calculated from inversion, and the straight red line describes the azimuthally-averaged integrated porosity-feet calculated from field compensated density. Letters along the vertical axis designate upper sectors (U), right sectors (R), bottom sectors (B), and left sectors (L). Refer to Figures 5.21 through 5.23 for details about the inversion method and simulations.

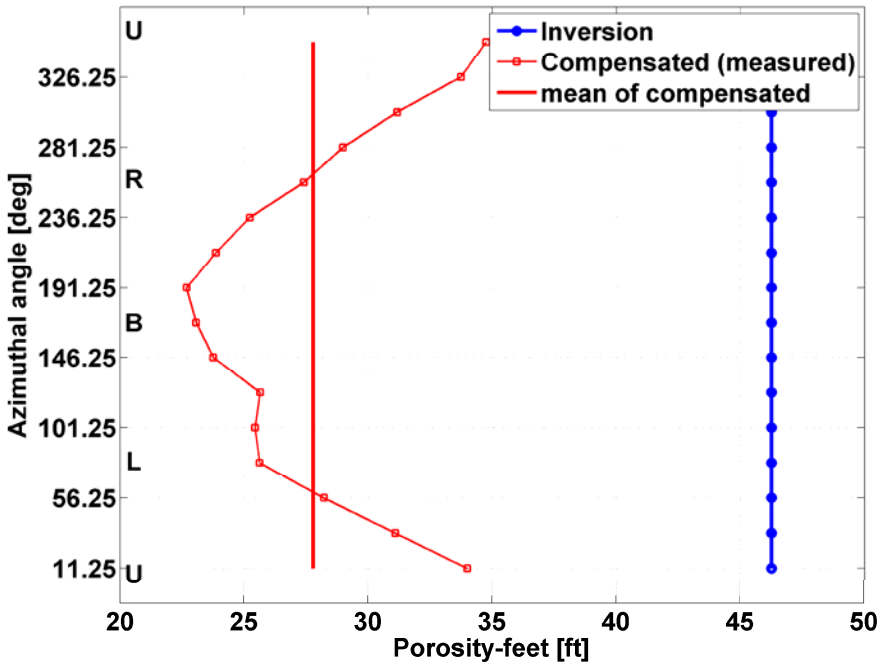

Figure 5.30: Comparison of integrated values of porosity-feet calculated from inversion and from compensated density for the case of inversion performed with all sectors in the vector of measurements. The blue line describes integral porosity-feet calculated from inversion, and the straight red line describes the azimuthally-averaged integrated porosity-feet calculated from field compensated density. Letters along the vertical axis designate upper sectors (U), right sectors (R), bottom sectors (B), and left sectors (L). Refer to Figures 5.24 through 5.26 for details about the inversion method and simulations.

Chapter 6: Summary, Conclusions, and Recommendations

This final chapter summarizes the main contributions of the work described in the dissertation, states the general conclusions, and provides recommendations for potential future research work.

6.1 SUMMARY

The objective of this dissertation was two-fold: (1) to develop a numerical procedure to rapidly and accurately simulate nuclear borehole measurements, and (2) to simulate nuclear borehole measurements in conjunction with inversion techniques.

The central focus of the dissertation was the development of fast simulation procedures for neutron and density measurements. The purpose was to enable the implementation of inversion techniques for improved interpretation of borehole nuclear field measurements. The rapid and accurate simulation of nuclear borehole measurements also enabled the combined quantitative interpretation of neutron and density logs.

The first stage of the dissertation quantified effects of thinly-laminated formations on neutron and density measurements acquired in highly-deviated wells. Monte Carlo simulations were used to quantify in a systematic manner the effect of petrophysical and environmental variables on neutron and density measurements acquired in sand-shale laminations penetrated by high-angle and horizontal wells. The need for fast simulation methods and improved interpretation techniques suitable for nuclear borehole measurements acquired in high-angle and horizontal wells motivated subsequent research work.

In the second stage of the dissertation, I developed and successfully tested a new linear iterative refinement technique to accurately and rapidly simulate nuclear borehole measurements. To that end, I used the Monte Carlo method to construct flux sensitivity functions for specific neutron and density tool configurations that were close to commercial designs. I used first-order Born approximations to simulate variations of detector response due to spatial variations of formation properties. The linear iterative refinement technique used a library of pre-computed flux sensitivity functions to approximate effects of spatial variations of formation properties on neutron and density measurements. First, I implemented and tested the linear iterative refinement method in vertical wells under the assumption of axial-symmetry about the axis of the borehole. Next, I validated the linear iterative refinement technique for the simulation of neutron and density measurements acquired in high-angle and horizontal wells.

Finally, I successfully implemented a 2D inversion procedure to interpret sector-based azimuthal density measurements into layer-by-layer density values. The inversion was tested on LWD density measurements acquired across laminated sequences penetrated by high-angle and horizontal wells. This method enabled quantitative appraisal of the reliability of azimuthal density measurements in highly-laminated sequences and in the presence of noise.

6.2 CONCLUSIONS

The following sections state the conclusions stemming from specific research themes included in the dissertation.

6.2.1 Environmental and petrophysical effects on density and neutron porosity logs acquired in highly deviated wells

i. Individual detector responses for neutron and density measurements are spatially complex. Each of these responses exhibits different vertical resolutions and radial lengths of investigation. Accounting for such properties of nuclear measurements is essential for estimating actual formation porosity. In the case of highly deviated wells, optimal combination of multi-detector responses is a more complicated process than in the case of vertical wells.

ii. At high angles of deviation, the response of both neutron and density measurements was sharper than for the case of a vertical well. I observed an apparent enhancement in vertical resolution. These effects are attributed to the much longer distance along the borehole of the response compared to the case of a vertical well.

iii. Because of their sensitivity to hydrogen index, neutron porosity measurements are substantially more affected than density measurements by the combined effects of gas saturation and geometrical factors between the wellbore and laminated formations.

iv. Rotation of the tool around the borehole caused a geometrical shift in bed-boundary detection from simulated neutron and density logs. However, the vertical resolution remained approximately constant for both neutron and density measurements.

6.2.2 Linear iterative refinement technique for the rapid simulation of borehole nuclear measurements acquired in vertical wells

i. I introduced a new approximation for the fast numerical simulation of neutron and density borehole measurements. The method is based on first-order Born approximations in conjunction with an iterative refinement procedure that adapts the weighting function to local spatial variations of formation properties.

ii. Sensitivity analyses of the flux sensitivity functions for a wide range of base-case formations confirmed that the density FSF is much less affected by variations of formation properties than that of neutron measurements. However, significant perturbations can result in the radial J-factor (up to 1.2 inches) of density measurements due to large contrasts of formation density or in the presence of mudcake or tool standoff. The impact of mudcake on density simulation depends on both thickness and density contrast between formation and mudcake.

iii. The linear iterative refinement technique enables fast and accurate neutron simulations in cases of large contrasts of material properties wherein the relationship between migration length and detector count rate was highly nonlinear.

iv. For shoulder-bed effects, fast simulations of density measurements yielded differences of less than 0.02 g/cm^3 with respect to Monte Carlo simulations. Iterative refinement simulations of neutron measurements

across large contrasts of porosity and saturating fluids, including shoulder-bed effects, resulted in maximum differences of 1.6% porosity or 8% error with respect to MCNP simulations.

v. In the radial direction, for piston-like invasion of water into a 30% porosity gas-saturated sand, iterative refinement simulations exhibited maximum differences of 0.019 g/cm^3 and 2.45% porosity for density and neutron measurements, respectively.

vi. The developed approximations improved the quantitative interpretation of combined neutron and density measurements acquired in vertical wells across thinly-laminated sequences of contrasting porosities and fluid saturations.

vii. Simulations of neutron and density measurements across long depth intervals (hundreds of measurement points) would required several days of CPU time with MCNP as opposed to minutes with iterative refinement approximations.

viii. Results discussed in this dissertation were based on the assumption of generic tool models, which are close to commercial logging tool designs. For use with field logs, it would be necessary to implement flux sensitivity functions obtained for commercial logging tool configurations.

6.2.3 Linear iterative refinement technique for the rapid simulation of borehole nuclear measurements acquired in high-angle and horizontal wells

i. Simulations confirmed that the volume of investigation (i.e., spatial resolution) of density measurements remains nearly invariant in the presence of variable contrasts of formation properties whereas the volume of investigation of neutron measurements is significantly modified when contrasting layers are nearly tangent to the borehole axis.

ii. Spatial resolution variations of neutron measurements due to well inclination angle can be different depending on the relative location of low porosity layers.

iii. I validated the linear iterative refinement technique using 3D spatial properties of FSFs for the simulation of neutron and density borehole measurements acquired in HA/HZ wells. Comparison of neutron approximations against MCNP simulations yielded maximum porosity differences of 4.3% in horizontal wells.

iv. The linear iterative refinement approximations and MCNP simulations exhibited the same formation geometrical effects on simulated density measurements acquired in HA/HZ wells.

6.2.4 Inversion of sector-based density measurements acquired in laminated sequences penetrated by high-angle and horizontal wells

i. I developed and successfully tested a new inversion method for the interpretation of sector-based azimuthal density measurements acquired in laminated sequences penetrated by HA/HZ wells.

ii. Because of the increased number of measurements per layer in HA/HZ wells, redundancy of data decreases non-uniqueness of the inversion and, consequently, inverted density values improve with respect to those of standard density correction.

iii. The inversion preferentially weighted azimuthal sectors that were the least affected by tool standoff because density images constructed from mono-sensor field measurements were influenced by borehole environmental effects.

iv. Reduction of shoulder-bed effects with inversion enabled the quantitative appraisal of the reliability and internal consistency of field measurements.

6.3 RECOMMENDATIONS

The following list itemizes recommendations for future research aimed at expanding the technical topics considered in this dissertation:

i. The linear iterative refinement approximations with flux sensitivity functions described in this dissertation can be applied to spontaneous gamma-ray simulations and, potentially, to thermal neutron decay and nuclear spectroscopy logs.

ii. For simulations of neutron borehole measurements, this dissertation considered migration length as the appropriate weighted formation

property because I included both fast and thermal neutrons in the detector count rate. Future work could implement the linear iterative refinement approximations by splittin neutron count rate for diffusion length and slowing-down length for thermal and fast neutrons, respectively.

iii. This dissertation quantified borehole environmental effects on the spatial properties of flux sensitivity functions. Such effects were included in the iterative refinement technique for simulations of neutron and density measurements acquired in vertical wells with the assumption of axial-symmetry about the borehole. For LWD measurements acquired in high-angle and horizontal wells, mudckae or tool standoff effects on nuclear measurements depend on the azimuthal location of the tool. Further research is necessary to validate the linear iterative refinement method with non-symmetric borehole environmental effects (variable tool standoff) in high-angle and horizontal wells.

iv. I implemented inversion of sector-based density measurements. Simulations confirmed that a 2D approach was suitable for density inversions and simulations. This was possible because of its spatially focused measurement properties. However, a 3D approach would be required for inversion of measurements whose volume of investigation exhibits large angular sensitivity around the perimeter of the borehole (i.e., neutron and gamma ray measurements). Further research is necessary for

the implementation of inversion techniques of neutron and spontaneous gamma-ray measurements.

APPENDIX A: Dependence of Energy-Dependent Cross-Section on Nuclear Properties

The migration length, L_m, is the nuclear formation property used for the rapid approximation of neutron measurements in place of Σ in Equations (3.4) and (3.5) and is given by

$$L_m = \sqrt{L_s^2 + L_d^2} \ ,$$

where L_s is the neutron slowing-down length and L_s is the thermal diffusion-length (McKeon and Scott, 1989).

We choose L_m as the appropriate formation property because it is related to the capture formation energy-dependent cross-section, Σ, (**Figure A.1 (a)**) and incorporates neutrons of all energies. The relation between the reciprocal of L_m and the detector count rate is independent of formation rock type (**Figure A.1 (b)**). Similarly, for the rapid simulation of density measurements with Equations (3.4) and (3.5), we choose formation mass density as the formation property. **Figure A.2** shows the exponential correlation between formation mass density and detectors count rate for water-saturated sandstone, limestone, and dolomite formations. The count rate response for variations of formation density is independent of formation rock type. The formation density can be determined from an observed detector count rate (Ellis and Singer, 2007).

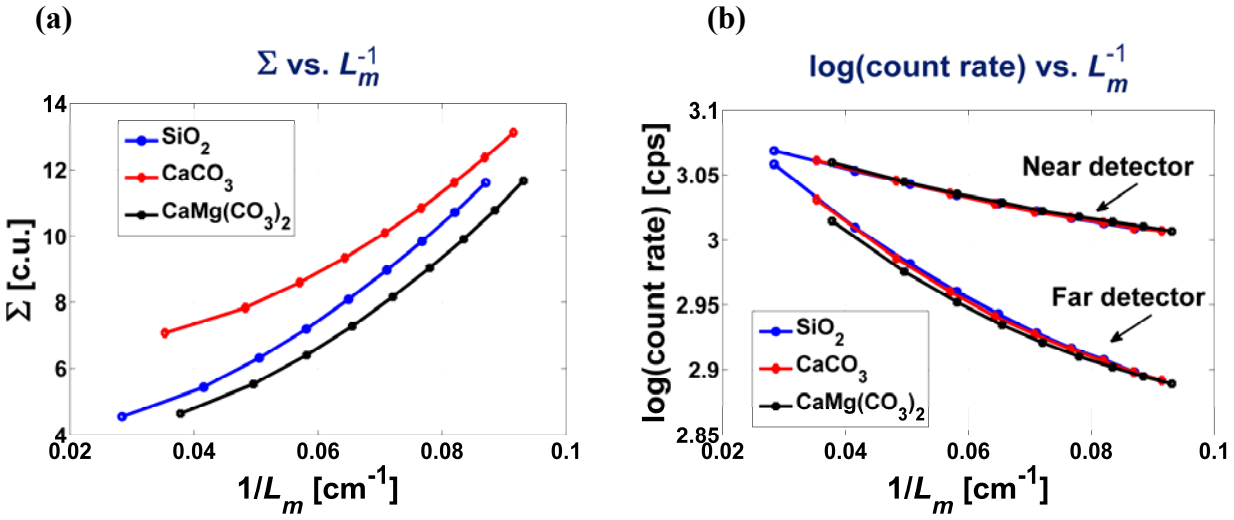

Figure A.1: **(a)** Correlation between capture cross-section and the reciprocal of migration length of water-saturated sandstone (blue), limestone (red) and dolomite (black) of porosity values ranging from 0% to 40%. **(b)** Correlation between the logarithm of count rate at neutron detectors and the reciprocal of migration length.

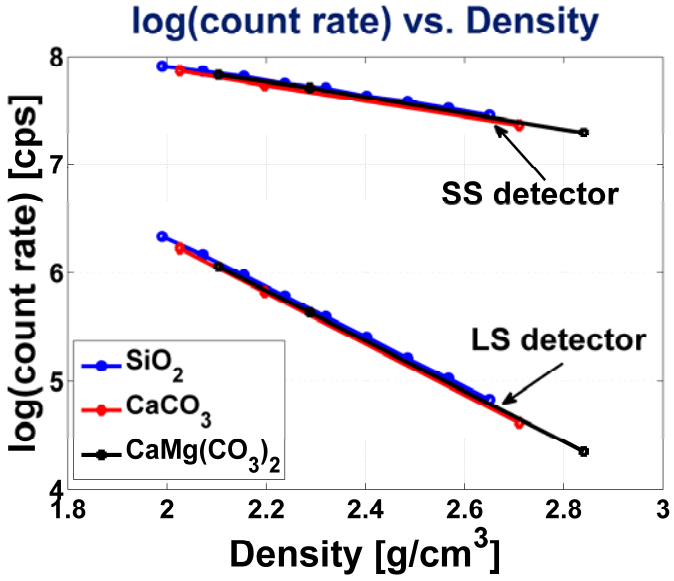

Figure A.2: Correlation between logarithm of count rate of gamma-ray at detectors and formation mass density of water-saturated sandstone (blue), limestone (red) and dolomite (black) of porosity values ranging from 0% to 40%.

APPENDIX B: Fast Numerical Simulation of Spontaneous Gamma-Ray Measurements

Figures B.1 (a) and **(b)** show simulations of spontaneous gamma-ray measurements across sand-shale laminations penetrated by a vertical and a horizontal well, respectively. Simulations are performed with the rapid approximations validated in this paper for HA/HZ wells. The API gamma-ray response is obtained from the linear combination of radioactive isotope concentrations weighted by the corresponding sensitivity coefficients (Ellis and Singer, 2007), namely,

$$GR_{API} = A\,{}^{238}U_{ppm} + B\,{}^{232}Th_{ppm} + C\,{}^{39}K_{\%}, \tag{B.1}$$

where GR_{API} is the gamma-ray response in API units, ${}^{238}U_{ppm}$ and ${}^{232}Th_{ppm}$ are the concentrations of uranium and thorium in ppm, respectively, and ${}^{39}K_{\%}$ is the percent concentration of potassium. For specific tool designs, the sensitivity coefficients (*A*, *B*, and *C*) that weigh the isotope concentrations in Equation (B.1) can be calculated with numerical simulations (Mendoza et al., 2006).

(a)

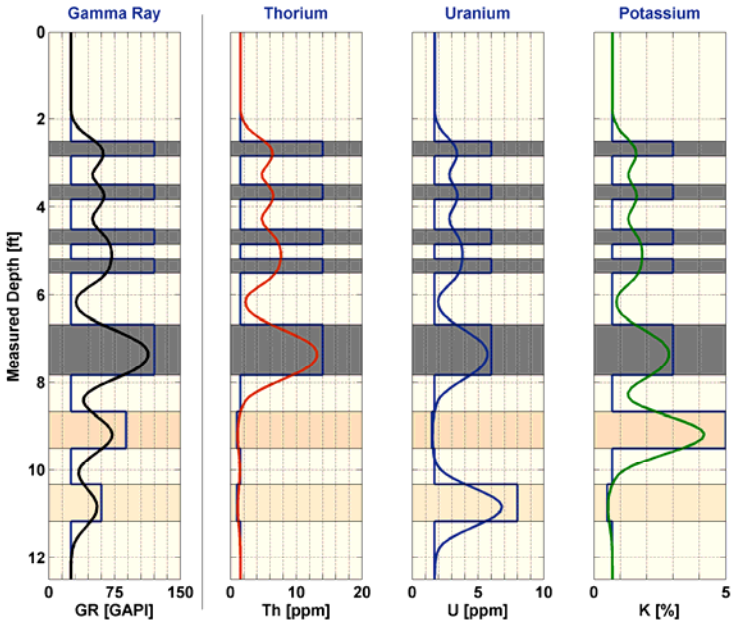

(b)

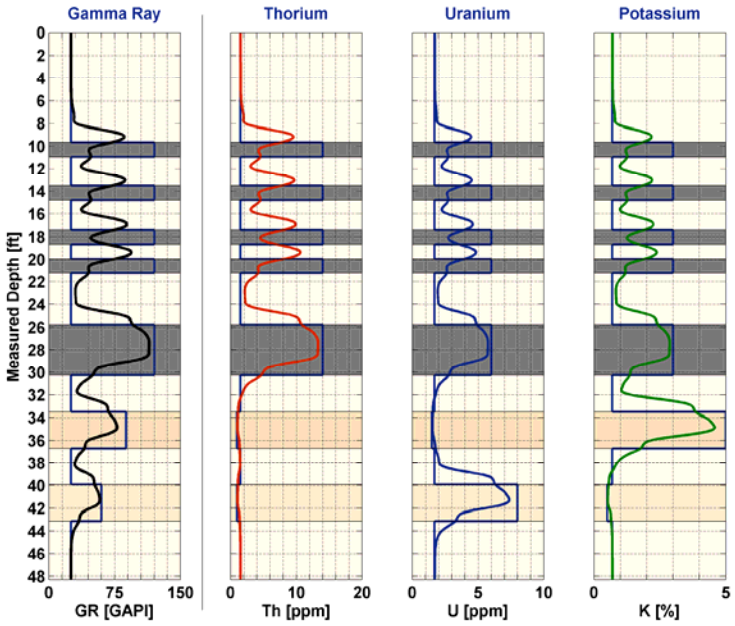

Figure B.1 Rapid approximation of spectral gamma-ray measurements across a sand-shale sequence of various bed thicknesses **(a)** penetrated by a vertical well, and **(b)** penetrated by a 75-degree deviated well. Panels above show gamma-ray simulations of Th (red curve), U (blue curve), and K (green curve) concentrations. Left panels show the resulting API gamma-ray measurement (black curve). Solid squared blue lines describe the actual gamma-ray and isotope concentration values assumed in the model.

APPENDIX C: Discretization of the Flux Sensitivity Functions and Tool Description

Figures C.1 (a) and **(b)** illustrate the spatial grid used to calculate neutron and density flux sensitivity functions in a cylindrical coordinate system. The figures show MCNP top (ρ vs. ρ) and side (z vs. ρ) sections of the super-imposed mesh used for the calculation of the functions. Simulations include the borehole, the nuclear tool (**Tables C.1** and **C.2**), and formation geometry and material composition. In both neutron and density simulations, the radial grid is coarsened every two inches away from the borehole wall as follows: 1/8-inch, 1/6-inch, 1/4-inch, 1/2-inch, and 1-inch. Along the z axis, the grid spacing is constant at 1/8-inch intervals. In the azimuthal direction, neutron simulations include five sectors of 24 degrees in the proximity of the tool and four 60-degree sectors along the rest of the perimeter of the wellbore. Density simulations include 45-degree sectors in the front and back of the tool and two 135-degree sectors on the sides. Refer to **Figures 4.1**, **4.2**, and **4.4** for additional details about the spatial distribution of the volume of investigation of the measurements.

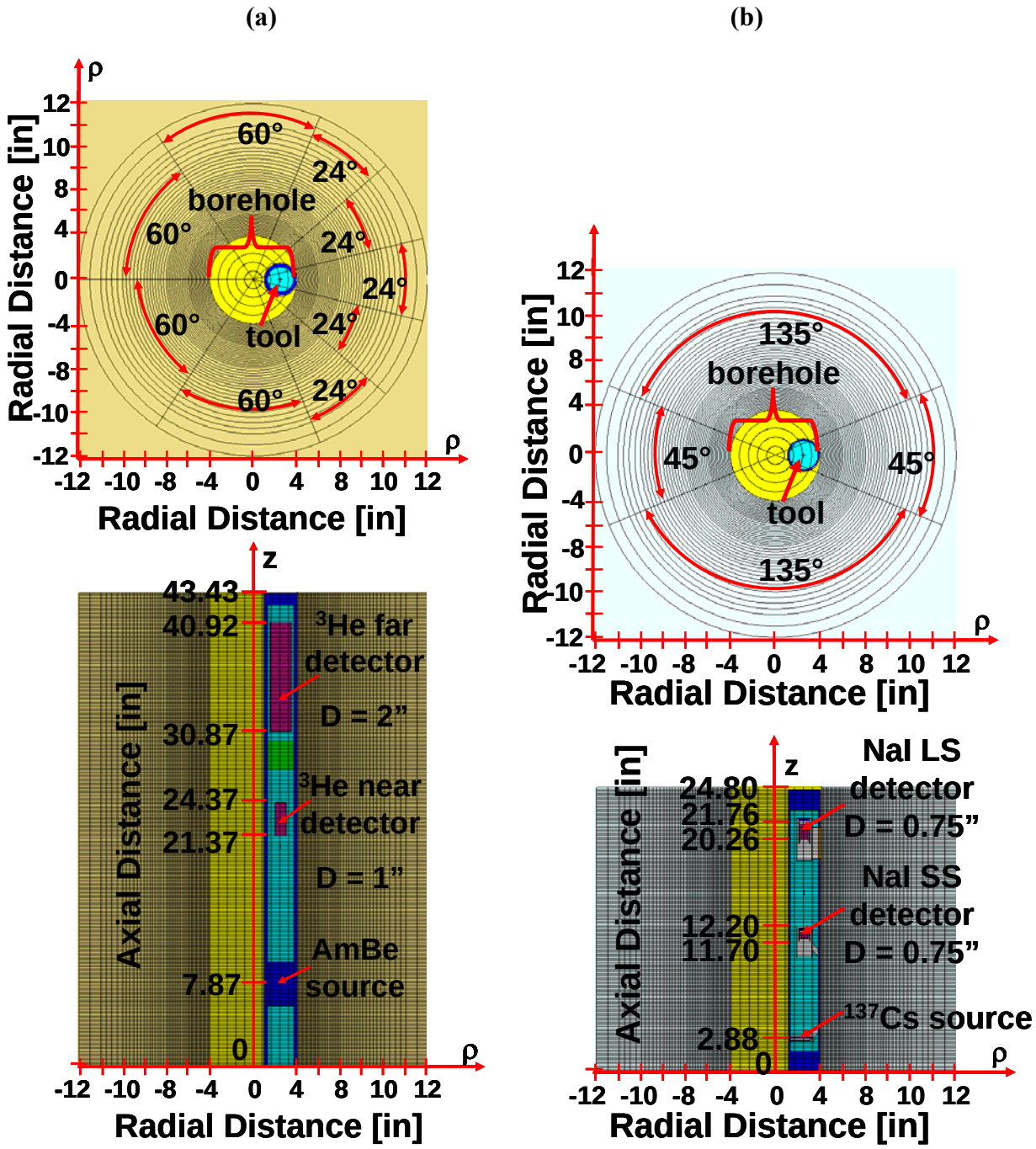

Figure C.1: **(a)** Spatial mesh used for the calculation of MCNP neutron flux sensitivity functions. **(b)** Spatial mesh used for the calculation of MCNP density flux sensitivity functions.

Table C.1: Geometrical properties of the assumed density porosity tool. Distances are measured with respect to the lower end of the tool.

Variable	Units	Value
LS-detector distance (center point)	in	18
SS-detector distance (center point)	in	9
LS-detector diameter	in	0.75
LS-detector length	in	1.5
SS-detector diameter	in	0.75
SS-detector length	in	0.51
LS-photomultiplier tube diameter	in	1.34
SS-photomultiplier tube diameter	in	1.34
LS-photomultiplier tube length	in	3.74
SS-photomultiplier tube length	in	2.76
Tungsten pad housing diameter	in	2.56
Tungsten pad housing length	in	21.26
Tool diameter	in	2.87
Tool length	in	24.8
Location of the ^{137}Cs source	in	2.85
Source window diameter	in	0.47
SS-detector window diameter	in	0.47
LS-detector window length	in	2.76
LS-detector window width	in	1.44

Table C.2: Geometrical properties of the assumed thermal neutron porosity tool. Distances are measured with respect to the lower end of the tool.

Variable	Units	Value
Far detector distance (center point)	in	28
Near detector distance (center point)	in	15
Far detector diameter	in	2
Far detector length	in	10
Near detector diameter	in	1
Near detector length	in	3
^{3}He Detectors fill pressure	psi	58.78
Tool diameter	in	3
Tool length	in	43
Location of the AmBe source	in	7.87

APPENDIX D: Structure of the Coefficient Matrix

The matrix of coefficients included in Equations (6) and (7) was constructed with integrated 2D flux sensitivity functions (FSFs) specifically calculated for commercial LWD density measurements. Entries of the coefficient matrix $\overline{\overline{\mathbf{K}}}$ exhibit the following structure:

$$\overline{\overline{\mathbf{K}}} = \begin{bmatrix} \begin{bmatrix} FSF^{SS}_{1,1,1} & \cdots & FSF^{SS}_{1,1,t} & \cdots & FSF^{SS}_{1,1,T} \\ \vdots & \ddots & \vdots & & \vdots \\ FSF^{SS}_{j,1,1} & \cdots & FSF^{SS}_{j,1,t} & \cdots & FSF^{SS}_{j,1,T} \\ \vdots & & \vdots & \ddots & \vdots \\ FSF^{SS}_{J,1,1} & \cdots & FSF^{SS}_{J,1,t} & \cdots & FSF^{SS}_{J,1,T} \end{bmatrix} & \cdots & \overline{\overline{0}} \\ \begin{bmatrix} FSF^{LS}_{1,1,1} & \cdots & FSF^{LS}_{1,1,t} & \cdots & FSF^{LS}_{1,1,T} \\ \vdots & \ddots & \vdots & & \vdots \\ FSF^{LS}_{j,1,1} & \cdots & FSF^{LS}_{j,1,t} & \cdots & FSF^{LS}_{j,1,T} \\ \vdots & & \vdots & \ddots & \vdots \\ FSF^{LS}_{J,1,1} & \cdots & FSF^{LS}_{J,1,t} & \cdots & FSF^{LS}_{J,1,T} \end{bmatrix} & & \\ \vdots & \ddots & \vdots & & \\ \overline{\overline{0}} & & \begin{bmatrix} FSF^{SS}_{1,M,1} & \cdots & FSF^{SS}_{1,M,t} & \cdots & FSF^{SS}_{1,M,T} \\ \vdots & \ddots & \vdots & & \vdots \\ FSF^{SS}_{j,M,1} & \cdots & FSF^{SS}_{j,M,t} & \cdots & FSF^{SS}_{j,M,T} \\ \vdots & & \vdots & \ddots & \vdots \\ FSF^{SS}_{J,M,1} & \cdots & FSF^{SS}_{J,M,t} & \cdots & FSF^{SS}_{J,M,T} \end{bmatrix} \\ & \cdots & \begin{bmatrix} FSF^{LS}_{1,M,1} & \cdots & FSF^{LS}_{1,M,t} & \cdots & FSF^{LS}_{1,M,T} \\ \vdots & \ddots & \vdots & & \vdots \\ FSF^{LS}_{j,M,1} & \cdots & FSF^{LS}_{j,M,t} & \cdots & FSF^{LS}_{j,M,T} \\ \vdots & & \vdots & \ddots & \vdots \\ FSF^{LS}_{J,M,1} & \cdots & FSF^{LS}_{J,M,t} & \cdots & FSF^{LS}_{J,M,T} \end{bmatrix} \end{bmatrix}.$$

In the above expression, superscripts *SS* and *LS* designate short- and long-spaced detectors, respectively. Likewise, subscripts *j*, *m*, and *t* designate *j*-th sector number, *m*-th measurement data, and *t*-th layer, respectively. Additionally, Subscripts *J*, *M*, and *T* designate total number of sectors , total number of measurement points, and total number of layers, respectively. The *m*-th pair of *SS* and *LS* FSF blocks included as rows describes coefficients used for the solution of vector $\bar{\mathbf{x}}$ by minimizing least-squares residuals for *m*-th measurement i.e., $d_m\left(\bar{\mathbf{x}}\right)-d_m^0$. Each entry (*j*,*m*,*t*) in the matrix $\bar{\bar{\mathbf{K}}}$ is the *SS* or *LS* FSF integrated over the measured depth across the *t*-th layer, azimuthally oriented to the *j*-th sector, and located at the depth of the *m*-th measurement. Because the depth location of the measurement point of the FSF progressively shifts with increasing *m* or rows, $\bar{\bar{\mathbf{K}}}$ includes off diagonal null spaces, $\bar{\bar{0}}$.

Acronyms and Nomenclature

E' : Energy of the incoming particle [eV].

E : Energy of the scattered particle [eV].

FSF : Flux sensitivity function [1/cm^3-eV].

FSF_B : Flux sensitivity function for an assumed base-case background formation [1/cm^3-eV].

GAPI : Gamma-ray American Petroleum Institute Units.

GR : Gamma-ray [GAPI].

HA : High-angle.

HZ : Horizontal.

LS : Long-spaced.

L_m : Migration length [cm].

L_{mB} : Migration length of a homogeneous base-case formation [cm].

N : Detector response [particles/cm^2].

N_B : Detector response for an assumed base-case formation [particles/cm^2].

PEF : Photoelectric factor [b/e].

q : Source [particles/cm^3-ster-eV].

$\mathbf{r}_0$: Position vector inside a scatterer region of $\Sigma(\mathbf{r}_0, E) \neq \Sigma_B(\mathbf{r}, E)$.

$\mathbf{r}$: Position vector in 3D space.

$\mathbf{r}_R$: Position vector at the observation point, R (detector location).

R : Observation point location (detector location).

S : Point-source location.

SS : Short-spaced.

S_B^+ : Detector response function for an assumed base-case background formation [1/cm^3].

U : Volumetric photo electric factor. U=ρ_ePEF [ ].

z : Vertical direction [in].

$\Delta\phi$: Porosity difference from a homogeneous formation base-case value of porosity [%].

ΔL_m : Migration length difference from a homogeneous formation base-case value of migration length [cm].

$\Delta\Sigma$: Excess total macroscopic cross-section for all interactions of particles of energy E at **r** [1/cm].

ΔN : Excess detector response [particles/cm^2].

$\Delta\rho$: Density correction [g/cm^3].

ϕ : Porosity [%].

ϕ_D : Density-porosity [%].

ϕ_N : Neutron-porosity [%].

ϕ_B : Porosity of a homogeneous formation base-case [%].

$\mathbf{\Omega}'$: Unit direction of incoming particles [ ].

$\mathbf{\Omega}$: Unit direction of scattered particles [ ].

ψ : Angular flux at **r** of energy E and direction $\mathbf{\Omega}$ [particles/cm^2-ster-eV].

ψ_B : Angular flux for an assumed base-case at **r** of energy *E* and direction **Ω** [particles/cm^2-ster-eV].

ψ^+ : Importance function [ ].

θ : Azimuthal angle [degrees]

ρ : Radial direction [in].

ρ : Mass density [g/cm^3].

ρ_B : Mass density of a homogeneous formation base-case [g/cm^3].

ρ_e : Electron density [g/cm^3].

ρ_b : Bulk density [g/cm^3].

ρ_{CO} : Compensated density [g/cm^3].

ρ_{model} : Model density [g/cm^3].

ρ_{SS} : Short-spaced detector density [g/cm^3].

ρ_{LS} : Long-spaced detector density [g/cm^3].

Σ : Total macroscopic cross-section for all interactions of particles of energy *E* at $\mathbf{r}_0$ [1/cm].

Σ_B : Total macroscopic cross-section of an assumed base-case for all interactions of particles of energy *E* at **r** [1/cm].

Σ_s : Macroscopic scattering cross-section for particles of energy *E* at **r** [1/cm].

Σ_t : Total macroscopic cross-section for all interactions of particles of energy *E* at **r** [1/cm].

References

Aristodemou, E., Pain, C., de Oliveira, C., Goddard, T., and Harris, C., 2003, Subsurface properties determination from nuclear well-logging data using neural networks, in Transactions of the SPWLA 44th Annual Logging Symposium, Galveston, Texas, June 22 - 25.

Aristodemou, E., Pain, C., de Oliveira, C., Goddard, T., and Harris, C., 2005, Inversion of nuclear well-logging data using neural networks, *Geophysical Prospecting*, vol. 53, pp. 103 - 120.

Aristodemou, E., Pain, C., de Oliveira, C., Umpleby, A., Goddard, T., and Harris, C., 2006, Energy group optimization for forward and inverse problems in nuclear engineering: application to downwell-logging problems, *Geophysical Prospecting*, vol. 54, March, pp. 99-120.

Badruzzaman, A., Mendoza, A., Stockhausen, E. J., and Reik, B. A., 2007, Density measurement sensitivity to varying borehole angle and tool azimuth in medium to thin beds, paper J, in Transactions of the SPWLA 48th Annual Logging Symposium, Austin, TX, June 3 - 6.

Bigelow, E.L., 1995, Introduction to Wireline Log Analysis: Western Atlas International, Inc., Houston, Texas.

Booth, T. E., and Hendricks, J. S., 1984, Importance estimation in forward Monte Carlo calculations, *Nuclear Technology / Fusion*, vol. 5, pp. 90 – 100.

Couët, B., and Watson, C. C., 1992, Application of Monte Carlo differential neutron sensitivity calculations to geophysical measurements, in Transaction of The American Nuclear Society, vol. 65, suppl. 1, pp. 5.

Couët, B., and Watson, C. C., 1993, Monte Carlo differential neutron sensitivity calculations for nuclear well logging, IEEE Transactions on Nuclear Science, vol. 40, no. 4, pp. 928 - 932.

Case, C., Watson, C. C., and Lawrence, R., 1994, Sensitivity function technique for modeling nuclear tools, United States Patent 5,334,833.

Cameron, G. I. F., Collinson, J. D., Rider, M. H., and Xu, L., 1993, Analogue dipmeter logs through a prograding deltaic sandbody, *Advances in Reservoir Geology*, Geological Society Special publication No. 69, pp. 195 – 217.

Dodge, W.S., 1994, Quantifying HIRES Nuclear Tool Resolution in Thinly Bedded Reservoirs Using Time Series Analysis, SPE-28797, SPE Asia Pacific Oil and Gas Conference: Society of Petroleum Engineers. Melbourne, Australia.

Ellis, D.V., 2003, Formation Porosity Estimation from Density Logs: *Petrophysics*, v. 44, no. 5, September-October, p. 306 -316.

Ellis, D. V., Flaum, C., Galford, J. E., and Scott, H. D., 1987, The effect of formation absorption on the thermal neutron porosity measurement, SPE 16814 in SPE Annual Technical Proceedings held in Dallas, TX Sept. 27-30.

Ellis, D. V., and Singer, J. M., 2007, Well Logging for Earth Scientists, Springer, The Netherlands.

Ellis, D. V., and Chiaramonte, J. M., 2000, Interpreting neutron logs in horizontal wells: a forward modeling tutorial, *Petrophysics*, vol. 41, no. 1, pp. 23 -32.

Evans, M., Best, D., Holenka, J., Kurkoski, P., ans Sloan, W., 1995, Improved formation evaluation using azimuthal porosity data while drilling, SPE 30546, in SPE Annual Technical Conference Proceedings, Society of Petroleum Engineers, Dallas, Texas, October 22 – 25.

Flaum, C., Galford, J. E., and Hastings, S., 1987, Enhanced vertical resolution processing of dual detector gamma-gamma density logs, paper M, in Transactions of the SPWLA 38th Annual Logging Symposium, London, England, June 29 – July 2.

Flaum, C., Galford, J.E., and Hastings, A., 1989, Enhanced Vertical Resolution Processing of Dual Detector Gamma-Gamma Density Logs: *The Log Analyst*, v. 30, no. 3, May-June, p. 139-148.

Flaum, C., Holenka, J. M., and Case, C. R., 1991, Eliminating the rugosity effect from compensated density logs by geometrical response matching, *SPE Formation Evaluation*, June, pp. 252 – 258.

Galford, J.E. Flaum, C., Glichrist Jr., W.A., and Duckett, S.W., 1986, Enhanced Resolution Processing of Compensated Neutron Logs, SPE-15541, in SPE Annual Technical Conference Proceedings: Society of Petroleum Engineers. New Orleans, Louisiana, October 5-8.

Gardner, R. P., and Liu, L., 1999, Monte Carlo simulation of neutron porosity oil well logging tools: combining the geometry-independent fine-mesh importance map and one-dimensional diffusion model approaches, *Nuclear Science and Engineering*, 133, pp. 80 - 91.

Greenspan, E., 1976, Developments in perturbation theory, *Advances in Nuclear Science and Technology*, vol. 9, Academic Press, inc., New York, NY.

Guo, P., Mendoza, A., and Yin, H., 2008, Impact on density tool depth of investigation on dip determination in high-angle and horizontal wells, in Transactions of the SPWLA 49th Annual Logging Symposium, Edinburgh, Scotland, May 25 – 28.

Habashy, T. M., Groom, R. W., and Spies, B. R., 1993, Beyond the Born and Rytov approximations: a non-linear approach to electromagnetic scattering, Journal of Geophysical Research, vol. 98, No. B2, pp. 1759 – 1775, February 10.

Hansen, P. C., 1998, Rank-deficient and discrete ill-posed problems: numerical aspects of linear inversion, SIAM, TheUnited States of America.

Hendricks, J. S., 1982, A code-generated Monte Carlo importance function: Reactor Physics Methods, *Trans. Am. Nucl. Soc*., 41, 307.

Lewins, J., 1965, Importance- the adjoint function- the physical basis of the variational and perturbation theory in transport and diffusion problems: Pergamon Press Ltd, London.

Liu, L., and Gardner, R. P., 1997, A geometry independent fine-mesh-based Monte Carlo importance generator, *Nuclear Science and Engineering*, 125, pp. 188 – 195.

Liu, Z., Torres- Verdín, C., Wang, G. L., Zhu, P., Mendoza, A., and Terry, R., 2007, Joint inversion of density and resistivity logs for the improved petrophysical assessment of thinly-bedded clastic rock formations, paper VV, in Transactions of the SPWLA 48th Annual Logging Symposium, Austin, Texas, June 3 - 6.

McCall, D.C., Allen, D.F., and Culbertson, J.S., 1987, High-Resolution Logging: The Key to Accurate Formation Evaluation, SPE 16769, in SPE Annual Technical Conference Proceedings: Society of Petroleum Engineers. Dallas, Texas, September 27-30.

McKeon, D. C., and Scott, H. D., 1989, SNUPAR – a nuclear parameter code for nuclear geophysics applications: IEEE Transactions on Nuclear Geoscience, vol. 36, no. 1, February, pp. 1215–1219.

Mendoza, A., Preeg, W., Torres-Verdin, C., and Alpak, O., 2005, Monte Carlo Modeling of Nuclear Measurements in Vertical and Horizontal Wells in the Presence of Mud-Filtrate Invasion and Salt Mixing, paper PP, in 46th Annual Logging Symposium Transactions: Society of Professional Well Log Analysts. New Orleans, Louisiana, June 26 – 29.

Mendoza, A., Torres-Verdín, C., and Preeg, W. E., 2006, Environmental and petrophysical effects on density and neutron porosity logs acquired in highly deviated wells, paper EEE, in Transactions of the SPWLA 47th Annual Logging Symposium, Veracruz, Mexico, June 4 - 6.

Mendoza, A., Ellis, D. V., Rasmus, J. C., 2006, Why the LWD and wireline gamma ray measurements may read different values in the same well, SPE 101718, presented at the

Society of Petroleum Engineers First International Oil Conference and Exhibition, Cancun, Mexico, August 31 – September 2.

Mendoza, A., Torres-Verdín, C., and Preeg, W. E., 2007, Rapid simulation of borehole nuclear measurements with approximate flux scattering functions, paper O, in Transactions of the SPWLA 48th Annual Logging Symposium, Austin, Texas, June 3 – 6.

Mendoza, A., Preeg, W. E., and Torres-Verdín, C., 2007, Monte Carlo modeling of borehole nuclear measurements in vertical and horizontal wells in the presence of mud-filtrate invasion and salt mixing, *Petrophysics*, vol. 48, no. 1, pp. 28 - 44.

Mendoza, A., Torres-Verdín, C., and Preeg, W.E., 2009, Linear iterative refinement technique for the rapid simulation of borehole nuclear measurements, Part I: vertical wells, submitted for publication.

Mendoza, A., Torres-Verdín, C., and Preeg, W.E., 2009, Linear iterative refinement technique for the rapid simulation of borehole nuclear measurements, part II: HA/HZ wells, submitted for publication.

Mickael, M. W., 1992, Importance estimation in Monte Carlo modeling of neutron and photon transport, *Nuclear Geophysics*, vol. 6, no. 3, pp. 341 – 350.

Passey, Q.R., Yin, H., Rendeiro, C.M., and Fitz, D.E., 2005, Overview of High-Angle and Horizontal Well Formation Evaluation: Issues, Learnings, and Future Directions, paper A, in 46th Annual Logging Symposium Transactions: Society of Professional Well Log Analysts. New Orleans, Louisiana, June 26 – 29.

Parsons, R., J., 1983, The use of steady state neutron flux measurement to determine the size of an invaded region following fluid injection, The International Journal of Applied Radiation Isotopes, vol. 34, no. 1, pp. 129 – 135.

Patchett, J. G., and Wiley, R., 1994, Inverse modeling using full nuclear response functions including invasion effects plus resistivity: paper H, in 35th Annual Logging Symposium Transactions: Society of Professional Well Log Analysts. Tulsa, Oklahoma, June 19-22.

Radtke, R. J., Adolph, R. A., Climent, H., and Ortenzi, L., 2003, Improved formation evaluation through image-derived density, paper P, in Transactions of the SPWLA 44th Annual Logging Symposium, Galveston, Texas, June 22 - 25.

Radtke, R. J., Evans, M., Rasmus, J. C., Ellis, D. V., Chiaramonte, J. M., 2006, LWD density response to bed laminations in horizontal and vertical wells, paper ZZ, in Transactions of the SPWLA 47th Annual Logging Symposium, Veracruz, Mexico, June 4 - 6.

Sherman, H., and Locke, S., 1975, Depth of investigation of neutron and density sondes for 35 percent porosity sand, paper Q, in Transactions of the SPWLA 16th Annual Logging Symposium, New Orleans, LA, June 4 – 7.

Torres- Verdín, C., and Habashy, T. M., 2001, Rapid numerical simulation of axisymmetric single-well induction data using the extended Born approximation, Radio Science, vol. 36, no. 6, pp. 1287 – 1306, November – December.

Uzoh, E. A., Mendoza, A., Torres-Verdín, C., Preeg, W. E., and Stockhausen, E. J., 2007, Quantitative studies of relative dip angle and bed thickness effects on LWD density images acquired in high-angle and horizontal wells, paper M, in Transactions of the SPWLA 48th Annual logging Symposium, Austin, Texas, june 3 – 6.

Uzoh, E. A., Mendoza, A., Torres-Verdín, C., Preeg, W. E., and Stockhausen, E. J., 2009, Quantitative studies of relative dip angle and bed thickness effects on LWD density images acquired in high-angle and horizontal wells, submitted to *Petrophysics*.

Watson, C. C., 1984, Monte Carlo computation of differential sensitivity functions, in Transaction of The American Nuclear Society, vol. 46, pp. 655.

Watson, C. C., 1992, A spatial sensitivity analysis technique for neutron and gamma-ray measurements: *Trans. Am Nucl. Soc*., vol. 65, Suppl. 1, pp. 3

X-5 Monte Carlo Team. MCNP., 2003 – A General Monte Carlo N-Particle Transport Code, Version 5. Volume III: Developer's Guide. University of California, Los Alamos National Laboratory. Los Alamos, New Mexico.

Yin, H., Han., H., Xu, L., Guo, W., Shehata, A., and Gardner, R. P., 2006, Field and benchmark studies of LWD nuclear tool response in high angle and horizontal wells, paper AAA, in Transactions of the SPWLA 47th Annual Logging Symposium, Veracruz, Mexico, June 4 – 6.

Yin, H., Guo, P., Mendoza, A., 2008, Comparison of processing methods to obtain accurate bulk density compensation and azimuthal density images from dual-detector gamma density measurements in high-angle and horizontal wells, paper M, in Transactions of the SPWLA 49th Annual Logging Symposium, Edinburgh, Scotland, May 25 – 28.

Vita

Alberto Mendoza Chávez was born in the capital city of the State of Chihuahua, México on February 14, 1979, the third son of Rogelio Mendoza Árce and Margarita Chávez de Mendoza. He received B.Sc. and M.Sc. degrees in Petroleum Engineering from The University of Texas at Austin in 2002 and 2005, respectively. Alberto worked for Schlumberger Oilfield Services as a Well-testing Field Engineer from 2002 to 2003. He was a research assistant with the Formation Evaluation Group in the Department of Petroleum and Geosystems Engineering at The University of Texas at Austin between August 2003 and December 2008. In the summers of 2005 through 2007 he was a research intern with Schlumberger Doll-Research, Chevron Energy-Technology Company, and ExxonMobil Upstream Research Company. Upon completion of his Doctoral degree Alberto will join ExxonMobil to work in Formation Evaluation.

Permanent address:

Bosque de San Marcos # 1813
Col. Sicomoros
Chihuahua, Chih. 31250
Mexico

This dissertation was typed by the author.